

Springer Theses

Recognizing Outstanding Ph.D. Research

Enrique Abad

Energy Level Alignment and Electron Transport Through Metal/Organic Contacts

From Interfaces to Molecular
Electronics

 Springer

Springer Theses

Recognizing Outstanding Ph.D. Research

For further volumes:
<http://www.springer.com/series/8790>

Aims and Scope

The series “Springer Theses” brings together a selection of the very best Ph.D. theses from around the world and across the physical sciences. Nominated and endorsed by two recognized specialists, each published volume has been selected for its scientific excellence and the high impact of its contents for the pertinent field of research. For greater accessibility to non-specialists, the published versions include an extended introduction, as well as a foreword by the student’s supervisor explaining the special relevance of the work for the field. As a whole, the series will provide a valuable resource both for newcomers to the research fields described, and for other scientists seeking detailed background information on special questions. Finally, it provides an accredited documentation of the valuable contributions made by today’s younger generation of scientists.

Theses are accepted into the series by invited nomination only and must fulfill all of the following criteria

- They must be written in good English.
- The topic should fall within the confines of Chemistry, Physics, Earth Sciences, Engineering and related interdisciplinary fields such as Materials, Nanoscience, Chemical Engineering, Complex Systems and Biophysics.
- The work reported in the thesis must represent a significant scientific advance.
- If the thesis includes previously published material, permission to reproduce this must be gained from the respective copyright holder.
- They must have been examined and passed during the 12 months prior to nomination.
- Each thesis should include a foreword by the supervisor outlining the significance of its content.
- The theses should have a clearly defined structure including an introduction accessible to scientists not expert in that particular field.

Enrique Abad

Energy Level Alignment and Electron Transport Through Metal/Organic Contacts

From Interfaces to Molecular Electronics

Doctoral Thesis accepted by
the Autonomous University of Madrid, Spain

 Springer

Author

Dr. Enrique Abad
Autonomous University of Madrid
Madrid
Spain

Supervisor

Prof. Dr. Fernando Flores Sintas
Autonomous University of Madrid
Madrid
Spain

ISSN 2190-5053

ISBN 978-3-642-30906-9

DOI 10.1007/978-3-642-30907-6

Springer Heidelberg New York Dordrecht London

ISSN 2190-5061 (electronic)

ISBN 978-3-642-30907-6 (eBook)

Library of Congress Control Number: 2012940947

© Springer-Verlag Berlin Heidelberg 2013

This work is subject to copyright. All rights are reserved by the Publisher, whether the whole or part of the material is concerned, specifically the rights of translation, reprinting, reuse of illustrations, recitation, broadcasting, reproduction on microfilms or in any other physical way, and transmission or information storage and retrieval, electronic adaptation, computer software, or by similar or dissimilar methodology now known or hereafter developed. Exempted from this legal reservation are brief excerpts in connection with reviews or scholarly analysis or material supplied specifically for the purpose of being entered and executed on a computer system, for exclusive use by the purchaser of the work. Duplication of this publication or parts thereof is permitted only under the provisions of the Copyright Law of the Publisher's location, in its current version, and permission for use must always be obtained from Springer. Permissions for use may be obtained through RightsLink at the Copyright Clearance Center. Violations are liable to prosecution under the respective Copyright Law.

The use of general descriptive names, registered names, trademarks, service marks, etc. in this publication does not imply, even in the absence of a specific statement, that such names are exempt from the relevant protective laws and regulations and therefore free for general use.

While the advice and information in this book are believed to be true and accurate at the date of publication, neither the authors nor the editors nor the publisher can accept any legal responsibility for any errors or omissions that may be made. The publisher makes no warranty, express or implied, with respect to the material contained herein.

Printed on acid-free paper

Springer is part of Springer Science+Business Media (www.springer.com)

*To my parents,
it could not have been anybody else*

Inspect every piece of pseudoscience and you will find a security blanket, a thumb to suck, a skirt to hold. What does the scientist have to offer in exchange? Uncertainty! Insecurity!

Isaac Asimov

Nature is a merciless and harsh judge of the theorist's work. In judging a theory, it never rules "Yes" in best case says "Maybe", but mostly "No". In the end, every theory will see a "No"

Albert Einstein

All our science, measured against reality, is primitive and childlike—and yet it is the most precious thing we have

Albert Einstein

Supervisor's Foreword

The growing field of organic electronics relies on the use of organic conjugated molecules as components of multilayer devices, whose performance depends critically on the energy barriers controlling the carrier transport between layers. Those barriers are determined by the relative alignment of the molecular levels between the materials forming the contacts, either a Metal/Organic or an Organic–Organic interface. This thesis work is focused on analyzing theoretically the energy level alignment of different Metal/Organic interfaces.

The organic molecule/metal interaction is, in principle, amenable to density functional theory (DFT) calculations; however, using local density approximation (LDA) or generalized gradient approximation (GGA) for the exchange–correlation potential tends to yield for the organic molecule transport energy gaps that are too small by several eVs. This problem is related to the fact that Kohn–Sham eigenvalues (as calculated in those approximations) are not a proper representation of the quasiparticle excitation energy: in conjugated organic molecules the difference between the HOMO and LUMO Kohn–Sham eigenvalues is significantly smaller than the transport energy gap measured experimentally due to the self-interaction correction that arises because the Kohn–Sham LDA–DFT (or GGA–DFT) gap refers to a N -electron calculation, while the experimental transport gap is related to the total energy differences of the molecule ground states with $N + 1$, N and $N - 1$ electrons.

Another problem limiting the application of DFT to Metal/Organic interfaces is related to the importance in these systems of van der Waals interactions which are, in many cases, necessary to get an accurate description of the organic molecule adsorption distance and energy. The reason is that van der Waals is a non-local and long-range interaction, while exchange–correlation functionals in standard DFT methods are local and short range, with a typical exponential decay. Therefore, in many Organic/Metal interfaces one has to introduce corrections to standard DFT methods in order to get an accurate description of the Metal/Organic interaction.

In this thesis work, these two problems have been addressed introducing in the standard LDA approach corrections in the direction of increasing the organic molecule energy gap and of including an appropriate van der Waals interaction.

Regarding the energy gap problem, it has been shown how the Kohn–Sham energy gap of the molecule has to be corrected by its charging energy: this quantity is calculated from the charge transfer between the metal and the molecule, and the energy level shift of the LUMO and HOMO levels as obtained from a consistent LDA calculation; in this consistent approach, the molecule energy gap is finally calculated by means of a scissor operator that introduces the appropriate charging energy in those levels. Regarding the van der Waals interaction, a kind of corrected-LDA calculation has been introduced which combines a weak chemical interaction between the metal and the organic molecule with a semiempirical van der Waals attraction. The way of calculating the weak chemical interaction tries to avoid the double counting that would appear including both the exchange correlation energy provided by a conventional LDA approach and the correlation energy associated with the long-range van der Waals potential introduced independently.

All these ideas have been combined in this thesis work in a full calculation of different Metal/Organic interfaces; in particular the following systems have been considered: C₆₀/Au(111), benzene/Au(111), pentacene/Au(111), TTF/Au(111) and TCNQ/Au(111), at the molecular level and for an organic monolayer.

All these results have also been interpreted within the Unified-Induced Density of Interface States (IDIS) model, whereby the Metal/Organic level alignment is controlled by the potentials created by the charge transfer between the two materials and by the “pillow” effect associated with the Pauli principle applied to the overlap between the charges of both materials. It has been found that the Unified-IDIS model is valid not only for the Metal/Organic interface but also in the molecular limit, with a lonely molecule adsorbed on a metal.

Madrid, Spain, March 2012

Prof. Dr. Fernando Flores Sintas

Acknowledgments

It is curious that in all theses only one author is mentioned, when actually, they come from the coordinated work of a lot of people. The author is the one that has contributed the most, of course, but this thesis would not have been successful without the collaboration of other people. This is the place to take all these people into account.

First, I would like to acknowledge this work to my Ph.D. advisors: Fernando Flores and José Ortega. Fernando showed me the way a physicist thinks. It is amazing how this “physical intuition” that professors try so hard to teach us during undergraduate courses, is innate in his case. His skill for taking the most relevant parts of a physical problem, make reasonable approximations, and give some physical sense to hours and hours of computational time is incredible; as it is his dedication to this work. Despite his long career, he still gets excited, like a freshman physics undergraduate student, when facing a new problem. José has taken care of the “ends” of my formation. Both from the point of view of the technical issues—his guidance through the FIREBALL code, and the physical meaning of its approximations—and from the point of view of what being a scientist means—to be critical with other peoples’ work, and with the own work; but also knowing that although a result is not exact or perfect, this does not mean that we cannot learn a lot about it. Also, for his aid during my visit to the US during fall 2008.

The help from Cesar González has also been critical. He had to answer the huge quantity of questions that I made to him during my first two years of this thesis, and he had a critical reading of the manuscript (moreover, he was my host in Prague in 2008). Also, it has been helpful to know Pavel Jelínek, and all his work on FIREBALL and to work with him during May 2008 (and via online during the rest of my thesis). The work of Dani González both in FIREBALL and in “xeo”, as well as his guidance during the first year of my thesis is acknowledged too. I also want to thank James Lewis, to introduce me in his group during fall 2008, and allow me to collaborate in the new version of the code. The collaboration with José Ignacio Martínez these last two years is greatly acknowledged, as part of this

work would not have been possible without him (and without Barbara). Also, collaboration with Yannick Dappe in van der Waals calculations has been critical. Finally, I want to thank Pau Burset, for answering my “many-body” questions, Giulio Biddau for his particular point of view of C_{60} physics, Laura Cano and her thesis on organic conductors, which has helped me to put mine in perspective, Milica for her advice on the “research world” outside graduate school and for answering thousands of English language questions during my thesis writing, and Laura Ramos for her help with the bureaucracy that research involves. And of course to Jose Antonio Ibáñez, my physics teacher in High School, who discovered me my vocation, and Nerea Zabala from the Basque Country University, who introduced me to the research world. The financial support from the Consejería de Educación de la Comunidad de Madrid, and the Fondo Social Europeo through the “Ayudas para la realización de contratos de personal investigador de apoyo” program, and EU through the FP7 project MINOTOR (Grant FP7-NMP-228424). This research was also funded by the Comunidad de Madrid through projects S2009/MAT-1467, 0505/ MAT/0303, and Ministerio de Ciencia e Innovación through projects MAT2007-60966 and FIS2010-16046.

But there have been more than research in my life during these years. A lot of people have made my life more pleasant in the department. In particular, Floren, César, Michael and Barbara, my office mates; and all the “fifth floor” of “C-V”; the ones that have been “always” there (Pau, Laura, Alfonso, Diego, Juan Antonio, Linda, Stefan, Rafa...), the ones that left (Yannick, Antonio, Sebas, Giulio, César, Remi, Dani...) and the “new” people (Nacho, Milica, Delia, Lucía, Blanca...). Concerning my life outside the department (there is life outside!) I could not forget José Angel (we are the exception, where sharing a flat had made us better friends instead of turning us into enemies), Kike, Rocío and their couples: Gema and Pedro. People from my old theater troupe (Gemma, Sara, Eva) and from the new one (Nines, Pilar, Jose María, María, Sole, Alicia... and of course, Pilar, “the boss”). And my present and past flatmates, and “Torredebabel” users: Thomas, Josu, Guillaume, Michaela, Ruth, Maggie, Linda, Alessia, Roberto, María, Natalia, Sheila, Gorka, Diego.... Thank you all for making my life more satisfying in this city I have fallen in love with: Madrid.

I want to thank also the people who have been at my side, in spite of the distance. My group of friends: Tere, Idoia, Nuria, Rober, María, Andrea, Tania, Iratxe, Natxo.... in particular, my best friends: Igone and Eburne. I can't imagine my life without them, but I guess that it would have been less pleasant. Also, people from San Ciprián (Lete, Félix, Dani... and Olalla, that right now is “another one”). I want to thank Tanja for making 2010 nicer, and the first month of thesis writing.

And the best for the end. The ones who my thesis is dedicated to: my parents. For raising me, teaching me the ethics of hard work (without that, I wouldn't have been able to do this), and for supporting me in this adventure, even if this meant that their only child had to leave the nest. I want to thank also my grandmother and the rest of my family for their support and help.

At this point I only have to say: Thank you everybody!!!!

Contents

1	General Introduction	1
1.1	Limitations of Conventional Electronics	1
1.2	Nanotechnology	2
1.3	Organic Electronics	4
1.4	Experimental Setup	5
1.4.1	Photo-Electron Spectroscopy	5
1.4.2	Scanning Tunneling Microscope	8
1.4.3	Mechanically Controlled Break Junction	10
1.5	This Thesis	11
	References	13
2	Theoretical Foundation	17
2.1	Introduction	17
2.2	Statement of the Problem	17
2.2.1	Hartree Approximation	18
2.2.2	Hartree-Fock Approximation	19
2.2.3	Configuration Interaction	20
2.2.4	Møller-Plesset Perturbation Theory	21
2.2.5	Pseudopotential	21
2.3	Density Functional Theory	22
2.3.1	Kohn-Sham Equations	24
2.3.2	Exchange and Correlation Functional Approximations	27
2.4	The FIREBALL Method	28
2.4.1	Fireball Orbitals	29
2.4.2	The Harris Functional	30
2.4.3	Exchange and Correlation	31
2.4.4	Molecular Dynamics and Structure Relaxation	35
2.5	LCAO-OO Method	37
2.5.1	Local Density LCAO-OO	39
2.6	Calculation of Transport Properties	42

2.6.1	Current Equation	42
2.6.2	Stationary Current	44
2.6.3	Conductance with Two Electrodes	45
2.7	Corrections of DFT Deficiencies	47
2.7.1	Weak Chemical and Van der Waals Interaction	47
2.7.2	Underestimation of the Gap	48
2.7.3	Hybrid HF-LDA Functional	49
2.7.4	Koopmans' Shift	52
2.7.5	Scissor Operator	54
2.8	Other Methods for Correcting the Gap	55
2.8.1	GW Method	55
2.8.2	LDA+U Method	56
	References	58
3	Further Developments in IDIS Model	63
3.1	Introduction	63
3.2	Brief Introduction to Metal/Inorganic Semiconductor Interfaces	64
3.2.1	Schottky–Mott Limit	65
3.2.2	Bardeen Limit	67
3.2.3	Intermediate Case	67
3.2.4	Origin of Interface States	69
3.3	Brief Introduction to Metal/Organic Interfaces	70
3.3.1	Charge Transfer and Chemical Reactions	70
3.3.2	Image Effect and Surface Charge Rearrangement: “Pillow” Dipole	73
3.3.3	Intrinsic Molecular Dipole	74
3.3.4	Effects on Real Devices	74
3.3.5	The Integer Charge Transfer Model	75
3.4	IDIS Model for Metal/Organic Semiconductor Interfaces	76
3.4.1	Interface States and the Charge Neutrality Level	76
3.4.2	Level Alignment and Screening Parameter	78
3.4.3	Pillow Dipole	79
3.4.4	Intrinsic Molecular Dipole	81
3.4.5	Surface Dipole	81
3.5	Mind the Gap: C ₆₀ /Au(111) and Benzene/Au(111) Interfaces	82
3.5.1	Geometry	82
3.5.2	Interface Potential with LDA Gap Calculations	84
3.5.3	C ₆₀ /Au(111) Interface with a Larger Gap	86
3.5.4	Discussion	88
3.6	The Gap Problem	89
	References	90

4	The IDIS Model at the Molecular Limit	95
4.1	Introduction	95
4.2	C ₆₀ Molecule Over a Au(111) Surface	96
4.2.1	IDIS Based Calculation of Charging Energy	98
4.2.2	Practical Implementation	99
4.2.3	Calculation of Pillow and Surface Potential at Low Coverages	101
4.2.4	C ₆₀ /Au(111) Gap Calculation: Summary and Conclusions	101
4.3	Application of the IDIS Model at the Molecular Level: C ₆₀ Between Two Tips	102
4.3.1	Mechanical Study	102
4.3.2	Electronic Analysis: Unified IDIS Model and Self-Interaction Correction	105
4.3.3	Conclusions	106
4.4	Barrier Formation for a Tip/C ₆₀ /Au(111) Configuration	107
4.4.1	Geometry Calculations	107
4.4.2	Barrier Formation and Charging Energy	109
4.4.3	Pillow Potential	111
4.4.4	Conclusions	111
4.5	Conclusions	112
	References	112
5	Results for Various Interfaces: C₆₀, Benzene, TTF, TCNQ and Pentacene over Au(111)	115
5.1	Introduction	115
5.2	C ₆₀ /Au(111) Interface at Various Coverages	115
5.2.1	Geometry	116
5.2.2	The $2\sqrt{3} \times 2\sqrt{3}R30^\circ$ Monolayer	117
5.2.3	IDIS Parameters for Various Coverages	118
5.2.4	Charging Energy for High Coverages	121
5.2.5	Extrapolation to the C ₆₀ /Ag(111) and C ₆₀ /Cu(111) Interfaces	123
5.2.6	Conclusions	125
5.3	Benzene/Au(111) Revisited: Realistic Gap and Benzene/Au Distance	126
5.3.1	Interaction Energy and Van der Waals Forces	126
5.3.2	Molecular Limit: U and δU	127
5.3.3	Benzene Monolayer Interface Dipole	130
5.3.4	Extrapolation to Benzene/Ag, Cu Interfaces	131
5.3.5	Discussion	132
5.3.6	Conclusions	134
5.4	TTF/Au(111) Interface	134
5.4.1	Calculation Details	135

5.4.2	STM Images and TTF Geometry	136
5.4.3	Interface Properties	137
5.4.4	Discussion and Conclusions	140
5.5	TCNQ/Au(111) Interface: Molecular Dipole	141
5.5.1	Calculation Details and Geometry	142
5.5.2	Theoretical STM Images	143
5.5.3	Electronic Structure and Interface Potential	144
5.5.4	Conclusions	147
5.6	Pentacene/Au(111) Interface: Hybrid Method in Practice	147
5.6.1	Geometry	148
5.6.2	Density of States, Interface Dipole and Charging Energy	149
5.6.3	Discussion and Conclusions	152
5.7	Conclusions	155
	References	156
6	General Conclusions and Future Work	159
6.1	Conclusions	159
6.2	Future work	161
	References	161
	Appendix A: Introduction to Second Quantization	163
	Appendix B: Different Approximations for a Simple Benzene Model: Hybrid Functionals	177
	Appendix C: Spin Dependent Extension of McWEDA and Hybrid Functionals	189
	Curriculum Vitae	195

Acronyms

CNL	Charge Neutrality Level
DFT	Density Functional Theory
DOS	Density of States
GGA	Generalized Gradient Approximation
HOMO	Highest Occupied Molecular Orbital
HB	Herringbone
HF	Hartree-Fock
IDIS	Induced Density of Interface States
LCAO	Linear Combination of Atomic Orbitals
LDA	Local Density Approximation
LUMO	Lowest Unoccupied Molecular Orbital
MD	Molecular Dynamics
ML	Monolayer
MO	Metal/organic
SIC	Self Interaction Correction
STM	Scanning Tunneling Microscope
STS	Scanning Tunneling Spectroscopy
OO	Orbital Occupancy
vdW	van der Waals
WCI	Weak Chemical Interaction

Chapter 1

General Introduction

1.1 Limitations of Conventional Electronics

In the second half of the 20th century, the field of electronics has suffered an outstanding progress. Since the invention of the transistor, in 1947, the speed and power of electronic devices has increased exponentially, while its size has decreased in the same proportion. The initially slightly idealistic Moore's law, which states that the number of transistors that can be placed inexpensively on an integrated circuit is doubled approximately every two years, remains true 45 years later (see Fig. 1.1).

However, limits of conventional silicon based electronics are close to be reached. In around 10 years transistors will reach the nanometer scale. At this size, standard semiconductor transistors theory, based on statistical physics and band structure theory [1] are no longer good approximations, and physics will be substantially changed. Pure quantum effects will appear or even govern electronics at that scale. A lot of effort is being made in understanding physics at the nanoscale [2–9] in order to be able to design and build mechanical, optical and electronic devices of that size.

Electronic devices at the molecular scale, such as diodes [10], electronic mixers [11], and switches [12] have been extensively investigated. This branch of electronics at this scale is called molecular electronics, and a lot of experimental and theoretical groups are trying hard to understand the physics and obtain devices with tailored properties that can be manufactured industrially [13–15].

On the other hand, in the field of “macroscopic” electronics, new materials with semiconducting properties have been introduced as a part of electronic devices. Both fundamental research and industry have aimed to organic semiconductors. They have the advantage of the high tunability of their properties (as well as being much cheaper and environment friendly than their inorganic counterparts). However, their electron mobility is lower than standard inorganic semiconductors. Besides, this kind of materials are very different than standard inorganic semiconductors, so a lot of effort needs to be made in order to understand their properties [16–20]. In particular, metal-organic interfaces, that appear in every connection of a semiconductor with the metallic circuit, have become difficult to understand. Due to the weak interaction

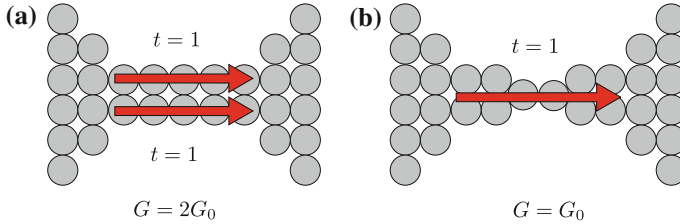


Fig. 1.2 Schematic view of a nanowire, illustrating the channel ballistic transport through nanoobjects. **a** A nanowire with a non-perturbed geometry, with two channels contributing to the wire conductance. **b** After a geometric relaxation (for example, during an stretching process), the channel structure has changed and only one contributes to the conductance. Note that this is just an oversimplified picture, so the fact that we have one or two atoms in a realistic chain does not mean that we have one or two channel (Color figure online)

behavior at that scale, since quantum phenomena govern these systems. In order to use circuits at the nanoscale, first we need to have an accurate vision of their mechanical, chemical and electrical properties. In the last two decades, with the invention of the scanning tunneling microscope (see Sect. 1.4.2) a great progress on this field has occurred both in theoretical and experimental research [2, 3, 22, 23].

One surprise of nanoscale physics is that metals, that are a homogeneous group in their macroscopic mechanical and electrical properties, behave very differently when they are of molecular size. For instance, when they are stretched in order to obtain nanowires, their conductance can change by more than 300%, and they can form long chains before they break [24] or just dimers [25]. At this scale, chemistry matters. Related to that, their chemical properties can be very different from their macroscopic ones. For instance, Au is a noble metal that barely reacts with other elements and compounds; however, gold at the nanoscale has an enhanced chemical reactivity [24, 26, 27].

However, there is still some universal behavior. Conductance of clean nanowires is usually a multiple of the quantum of conductance ($G_0 = 2e^2/h$), and there is a direct link between mechanical and electrical properties [25, 28].

The explanation for this fact is that the conductance is essentially ballistic for metallic nanowires. The seminal paper of Landauer [29] made people consider transport through nanoobjects as a transmission-reflection channel problem. Channels are just eigenvectors of the transmission matrix in a certain basis, and their physical meaning is that for this channel, the electrons move through the path given by the relative weight of the basis wavefunctions with a transmission t [30]. A complete transmission ($t = 1$) channel contributes with a quantum of conductance G_0 to the global conductance of the system. So in this particular case, the electron-electron and electron-phonon inelastic processes are not the source of finite conductance, but the limited number of transmissive channels (with $t \neq 0$). See Fig. 1.2.

This introduction is just a first glance to this enormous science, and aimed to the topics studied in this thesis. There are quite a lot of other fields within nanoscience; like photonics and metamaterials, graphene and carbon nanotubes,



Fig. 1.3 *Left* A wide range of electronic devices that use organic semiconductors are already being commercialized by technological corporations, like this LG@15EL9500 television with OLED technology. Copyright LG. Taken from [32]. *Right* Flexible organic display of 2.5 inch, 160×120 pixels manufactured by Sony®. It is able to reproduce 16.7 million colors (24 bits). Copyright Sony (2007). Taken from [33] (Color figure online)

coulomb blockade, shot noise and one electron transistors, self-assembling molecules, cluster physics. . . Just a brief abstract of all the physics at the nanoscale will need more than a chapter and will not be given.

1.3 Organic Electronics

We have already mentioned another discipline that has acquired much importance recently: organic electronics, i. e. the use of organic semiconductors in electronic devices. We stress here that the use of organic materials has important advantages with respect to conventional inorganic semiconducting materials. First of all, they are more *environmental friendly*, both in the fabrication and elimination processes. Moreover they consume less power and they are cheaper; so they are perfect candidates for relatively inexpensive and portable devices like mobile phones, displays and digital photo cameras. Organic displays have also improved brightness and contrast and a wider angle view.

The huge variety of organic molecules, and the possibility to add different functional groups, allows us to completely tailor our semiconductors properties; for instance, tuning the emitting wavelength of organic light emitting diodes (OLEDs), or using them as highly specific sensors (chemical, pressure, photons). This technology, although not completely revolutionary (it is based in macroscopic physics), is more mature industrially and organic electronic devices are not rare in the market (Fig. 1.3).

However, the industrial production of these devices does not imply that the physics of organic semiconductors is well understood. They are very different from their inorganic counterparts. They are molecular solids, with molecules bonded by weak Van der Waals forces; while conventional semiconductors are covalent solids, with atoms strongly tied by covalent (sometimes partially ionic) bonds. This makes that band theory used in inorganic semiconductors fail (see Sect. 3.1). A key aspect of these devices is the energy level alignment at metal/organic and organic/organic interfaces. It is closely related to the electron and hole injection barriers, and is critical in order to get good performance in these devices (see Sect. 3.1). Unfortunately, it is very complicated to be obtained theoretically with standard techniques because of intrinsic failures of density functional theory (see Sect. 2.7 and [19, 34]). However, our understanding of organic semiconductors and metal/organic interfaces have improved a lot in the last decade [16–20, 35], but some questions are still open. A more complete description of theoretical problems of organic semiconductors will be given in Sects. 3.1 and 3.3.

Finally, we point out that organic semiconductors are not only interesting in devices, but also as electricity *generators*. As conventional semiconductors are also used as solar cells, organic semiconductor solar cells are now being extensively researched [36]. The problem nowadays is that their performance is very low (they have a record on laboratory of around 8%, compared with the laboratory record of around 45% on standard GaAs inorganic semiconductor), but it is improving fast.

1.4 Experimental Setup

In this section we are going to give a brief summary of the main experimental techniques used to investigate metal/organic (MO) interfaces, as well as techniques to get atomic-size contacts or circuits. Most of these techniques are carefully explained at [18].

1.4.1 Photo-Electron Spectroscopy

This is the main experimental technique to obtain information of energy alignment at MO interfaces. The underlying physical idea is very simple. A sample is irradiated with a source of monochromatic photons, and the energy of these photons is employed in extracting electrons from the sample. These electrons arrive at a kinetic energy detector. Energy measurements allow us to extract a lot of information. Moreover, since the radiation penetration is around 5–30 Å, this technique is very surface sensitive.

The energy balance can be calculated as:

$$E_0 + h\nu = E_+^{(*)} + E_k \quad (1.1)$$

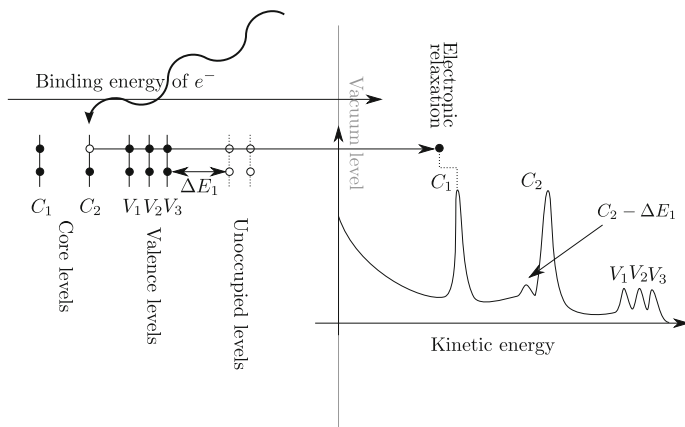


Fig. 1.4 Scheme of the physics of a photoemission spectrum, including some effects like electronic relaxation.

where E_0 is the initial energy of the molecule that absorbs the photon and $h\nu$ the energy of that photon. E_k is the energy of the collected electron and $E_+^{(*)}$ the energy of the positive molecular ion (usually in an excited state). One can measure the binding energy E_b^v of that electron as:

$$E_b^v = E_+^{(*)} - E_0 = h\nu - E_k \quad (1.2)$$

As Fig. 1.4 suggests, we can suppose that there is a one-to-one correspondence between the peaks in a photoelectron spectrum and the quasiparticle molecular levels in the neutral molecule. However there are some effects that break this simple picture. First of all, we need to take into account secondary electrons: the photoemitted electron can excite other electron and extract it from the sample; these two electrons are secondary electrons, and in this case, the picture is not that simple as the one shown in Fig. 1.4. Moreover, when an electron is emitted, there is an electronic intramolecular and intermolecular relaxation, that increases the electron energy. This energy is around 1–3 eV for valence electrons, but can be much larger in core levels [37, 38].

Depending on whether we are looking at the core or valence levels of molecules, we need to use X-ray or ultraviolet (UV) photons. The properties that can be obtained differ significantly between both so a brief summary of both techniques will be given.

X-ray Photoelectron Spectroscopy

In X-ray photoelectron spectroscopy (XPS) qualitative and even semiquantitative analysis of chemical composition in surface region is possible. Although core levels are not involved in chemical bonds, changes in the valence electron density will be reflected as small but detectable shifts in the core electron binding energies (chemical

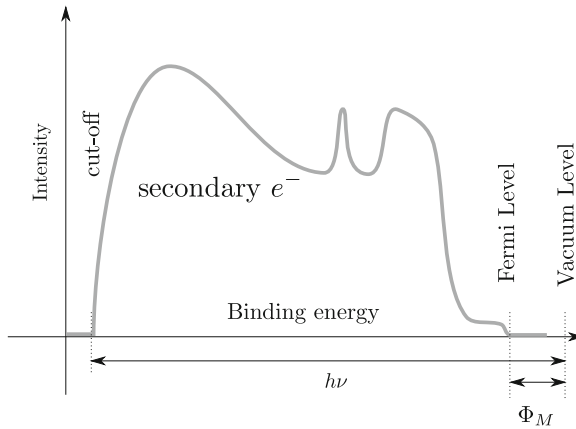


Fig. 1.5 Scheme of a typical UPS spectrum, illustrating the procedure to calculate the surface work function

shifts). XPS can also be used to study valence levels, but the cross section is lower than for UV photons. The photoemission spectroscopy is performed with reference to the Fermi level of the photoelectron spectrometer. So, when the Fermi level is shifted, it is necessary to take into account this change. This can be done combining XPS with ultraviolet spectroscopy (UPS) spectra as described in next paragraph.

Ultraviolet Photoelectron Spectroscopy

As stated before, this is the standard technique for the study of the valence band. UV photons have a greater cross section than X-ray ones, and the photon energy resolution is much higher. However, the natural linewidths in samples at room temperature can reach 1 eV, so a large part of the photon energy resolution is not fully appreciated [39].

Although photoelectron measurements are performed relative to the Fermi level, in some cases, it is important to obtain binding energies from the vacuum level (for example to interpret XPS chemical shifts or to measure change in vacuum level of the sample due to the appearance of dipoles). This energy is easy to find out just by looking at the cutoff of secondary electrons. The difference between the position of the Fermi energy and the vacuum level determines the work function of our system, as can be seen in Fig. 1.5.

Angle Resolved Photoelectron Spectroscopy

This technique does not only take into account the energy of the extracted electrons but also the direction in which these electrons are emitted (it gives us both the bond energy ε_n of the electrons and their momentum \mathbf{k}). This way we can obtain the complete band structure $\varepsilon_n(\mathbf{k})$ of the system. Like other photoelectron spectroscopies

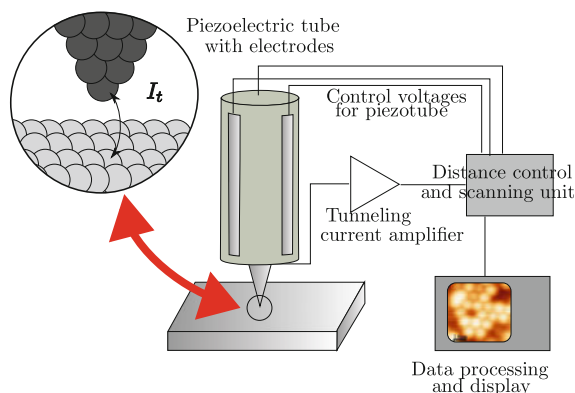


Fig. 1.6 Schematic view of an STM. The tunnel current between the tip and the sample is amplified, and used as a feedback for the tip-sample distance (in the constant current regime). In order to scan a finite region of the sample the tip is placed over a piezoelectric material, to move the tip via electronic control. Finally all data is sent to a computer, that creates the STM image and allows data processing (Color figure online)

techniques, some caution has to be taken when interpreting these results (secondary electrons, intraatomic relaxations, etc.)

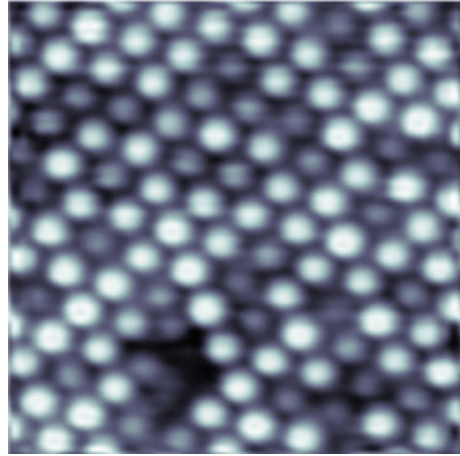
Inverse Photoelectron Spectroscopy

Inverse photoelectron spectroscopy (IPES) is closely related to the direct one. The sample is irradiated with low energy electrons (5–20 eV). The incident electrons decay into the empty molecular states, emitting a photon, that is detected. The energy of that state is the difference between the energy of the incident electron and the detected photon. By this way the conduction band can be studied. However, the resolution of this technique is lower than standard UPS. Anyway, combined UPS/IPES spectra can give us a reliable study of valence and conduction bands, crucial in MO interfaces.

1.4.2 Scanning Tunneling Microscope

As photoemission spectroscopy, the scanning tunneling microscope (STM) relies on a simple physical idea. When two conductors are separated by a vacuum gap, no current flows between them. But when the distance between them is reduced to a few angstroms, some electrons can flow by tunnel effect. If one of the conductors has a tip shape, this technique is *extremely* sensitive to the distance between the tip and the sample atoms, and resolutions lower than 1 Å (that is, *atomic* resolution) can be achieved. This is the basis of the STM [40, 41]. A simple scheme of the experimental setup is shown in Fig. 1.6, and an atomic resolution image is shown in Fig. 1.7.

Fig. 1.7 STM image with atomic resolution of a SiC(0001)- 3×3 -6H surface. Image has been taken at a constant current of 2 nA (height is the source of contrast), the bias applied is -3 V. The size shown in the figure is 10×10 nm. Courtesy of Pablo Merino (Color figure online)



This technique is suitable for studying topography at the atomic scale. However, interpretation of STM images is not trivial, because the current between tip and sample not only depends on distance but also on local density of states of tip and sample (sometimes a sudden change in current contrast is related to an abrupt change of the local density of states, while the topography remains constant). Moreover, not only topography can be measured. Different STM related techniques will be briefly explained.

Scanning Tunneling Spectroscopy

Scanning tunneling spectroscopy (STS) relies on the use of a STM to probe the local density of electronic states and band gap of surfaces and molecules deposited on surfaces at the atomic scale. As stated before, STM current also depends on the local density of states, so we can use it to measure this density. In a first approach the local density of states at point \mathbf{r} is $\text{LDOS}(\mathbf{r}) = \frac{dI}{dV}(\mathbf{r})$. So if we measure the current at a certain point at several voltages, we can have a reasonable estimation of the density of states at that point (Fig. 1.8).

Atomic Force Microscope and Kelvin Probe Microscope

Atomic force microscope (AFM) is another high-resolution scanning probe microscope. It consists on a cantilever (usually made of silicon) that is placed close enough to the surface sample that its dynamic has a measurable change due to the atomic forces between the surface and the cantilever.

There are two main modes: contact, and non-contact. In the contact mode forces are obtained by cantilever deflection measurement. There is usually an electronic feedback loop in order to have the height constant. In the non-contact mode, the cantilever is maintained oscillating at a given frequency ω by an electro-mechanical

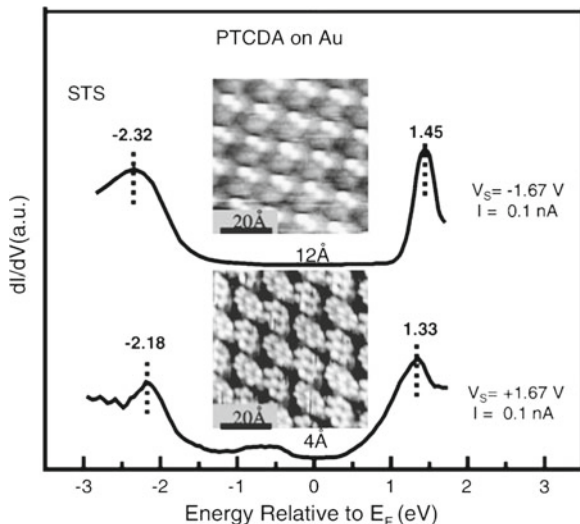


Fig. 1.8 $dI(V)/dV$ STS spectra of filled and empty states recorded for a monolayer (*bottom*) and a 2–3 molecular layer (*top*) film of PTCDA deposited on Au. The corresponding STM images of the films are shown. The curves were recorded at the same tunneling setpoints as the corresponding area scans. Reprinted from [42], Copyright (2002) with permission from Elsevier

circuit. When it is placed near the surface, the forces change the frequency or the phase shift between the input and the output signal; this change is used as the source of contrast.

The kelvin probe microscope [43] is a variant of the AFM, capable of measuring the work function of the surface locally. It is based on the macroscopic Kelvin Probe technique (see [44] and references therein). The AFM cantilever is a reference electrode that forms a capacitor with the surface. An AC+DC voltage is applied to the cantilever. Then an electrostatic force appears between the cantilever and the surface.

For a certain DC voltage, the vibration is minimal. A map of this minimal vibration voltage is used for imaging the work function of the surface. This technique is very important in order to study locally the work function change on metal-organic interfaces [18, 45].

1.4.3 Mechanically Controlled Break Junction

This technique allows to obtain very narrow metallic wires [3] so it is suitable for fabrication of metallic nanowires or molecular electronic devices [4, 46]. In this method, a metallic suspended bridge is fabricated by using electron beam lithography and shadow mask techniques. Using a pushing rod, the insulator platform is deformed and the wire is stretched (see Fig. 1.9) until it finally breaks. In the last stages of the

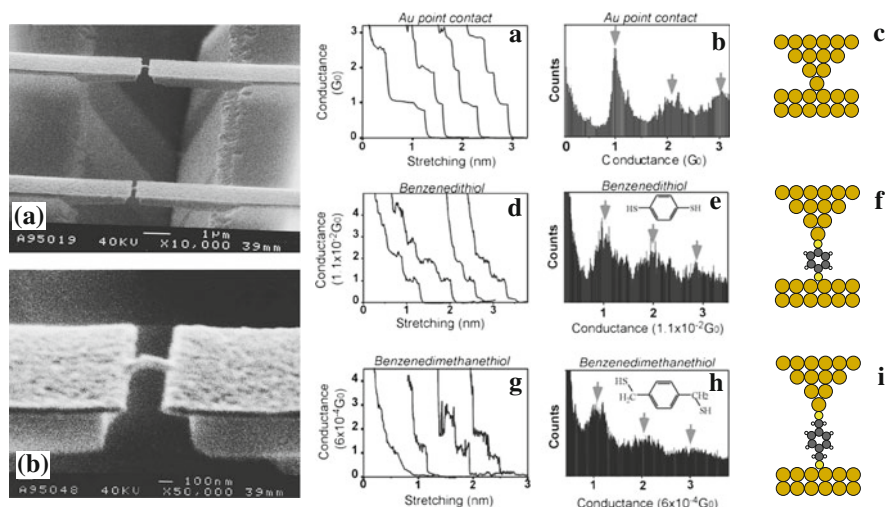


Fig. 1.9 *Left* (a) Electron microscopy image of two microfabricated bridges suspended above a triangular pit of silicon substrate. The close-up in (b) shows the two SiO_2 cantilevers, which are about 700 nm apart. The cantilevers are covered by a gold layer from which the final conducting bridge of about 100 nm wide is formed, and which is broken by bending of the silicon substrate. Reprinted with permission from [48] Copyright 1995 American Institute of Physics. *Right* Conductance (A) and conductance histogram (B) of a gold STM tip at contact regime (C), showing typical plateaus of conductance at integer multiples of G_0 that appear as peaks in the conductance histogram. When the experiment is conducted in a solution of benzenethiol, the conductance VS distance curve changes (D) and new peaks appear at $1\times$, $2\times$, and $3\times 0.011 G_0$ in the conductance histogram (E); that suggest that a molecular contact has been formed (F). When benzenethiol is substituted by benzenedimethanethiol, conductance (G) and conductance histogram (H) changes again; that confirms the idea that the molecule in solution attaches to the gold electrodes. Adapted with permission from [49]. Copyright (2004) American Chemical Society (Color figure online)

stretching process an atomic wire can be formed whose size varies from a dimer [25, 47] to several atoms [24].

During the last stages of stretching the wire can be exposed to gas phase molecules that are able to attach to the wire just after breaking, as shown in Fig. 1.9. Or, a self assembled monolayer can be formed in the metal surface and then the wire is stretched and broken, after that tips are brought together (see Fig. 1.10).

Molecular conductance can also be achieved using STM, placing the molecule between the tip and the surface [50, 51]. This method can also be used to obtain clean metallic nanowires [52, 53].

1.5 This Thesis

In this thesis we have analyzed several metal/organic interfaces from first principles in order to obtain realistic energy level alignment. Our results are interpreted in terms of the induced density of interface states (IDIS) model, that was developed in this

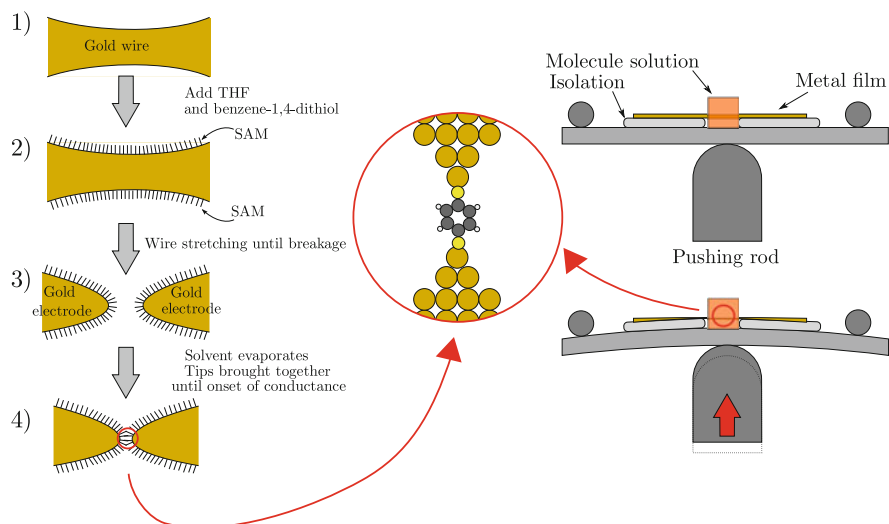


Fig. 1.10 *Left* Experimental setup for measuring conductance through a single molecule between two electrodes. (1) A gold wire is placed in a solution of the desired molecule. (2) Then, a self assembled monolayer of this molecule (SAM) is created over the gold surface. (3) The wires are stretched until breakage. (4) Tips are put back together, and sometimes, a molecule is anchored to both electrodes. *Right* Application of mechanically controlled break junction for study of molecular conductance. The stretched part of the wire is placed under a molecule solution. It is possible that, during the stretching and breaking process, one molecule is placed between electrodes. (Color figure online)

group in the late 1970s for inorganic semiconductors [54, 55] and extended in the last decade for organic semiconductors [35].

Our calculations employ density functional theory (DFT) techniques to simulate the whole system (the organic layer and the metal surface). In this thesis we show that the IDIS model is not useful only to understand the dipole formation at MO interfaces (for various coverages and different screening) but also at molecular contacts at the molecular level (that can be seen as the limit of MO interfaces with extremely low coverage). This allows us to use the IDIS model in a very different field: the field of molecular electronics.

Moreover, we have demonstrated on this thesis that within the theoretical framework of the IDIS model we can use DFT results in order to obtain the charging energy of the organic molecules, and *predict an accurate gap of the molecule*. Standard DFT techniques give underestimated energy gaps compared to real ones as the self-interaction correction (SIC) and the image potential are not taken into account. The value of this gaps is critical in order to obtain reliable values for the electron and hole injection barrier, that determine the performance of electronic devices both for macroscopic electronic devices and for molecular electronics.

This thesis is organized as follows:

In Chap. 2 we will introduce the main theoretical background: the general hamiltonian for condensed matter systems and the most common chemical and physical approximations, focusing on DFT. A small introduction to transport calculations is also given. After that we will show the deficiencies of DFT we have to deal with when working with metal/organic interfaces: the underestimation of the transport gap and the lack of van der Waals interaction; and how we can correct these deficiencies in order to have accurately characterized these kind of systems.

In the first part of Chap. 3 a small introduction to metal/semiconductor interfaces (both inorganic and organic) will be given. After that we present, with full detail, the IDIS model, necessary to interpret the results obtained in our thesis. In the second part, we will employ this model to characterize $C_{60}/Au(111)$ and benzene/ $Au(111)$ interfaces using standard DFT techniques, and we will show how the results are not good enough to obtain realistic interface potentials and electron and hole injection barriers. A brief discussion about the main problem (the underestimation of the DFT gap) will be given at the end of this section.

In Chap. 4 we will extend the IDIS model to molecular metal/organic contacts. Some proofs of the validity of the model at this level will be given (in Sect. 5.2 we will show that molecular organic contacts can be seen as the limit of low coverages of metal/organic interfaces). After that we will show that using IDIS parameters we can obtain an accurate estimation of the charging energy of a molecule interacting with a metal (including both self-interaction correction and image potential), and a reliable transport energy gap. Finally, we apply all these ideas to two nanosize systems: a C_{60} molecule between two gold tips and a C_{60} molecule between a tip and a gold surface (mimicking the experimental geometry of STM experiments).

In Chap. 5 we will apply all the techniques of Chap. 4 to the study of metal/organic interfaces. $C_{60}/Au(111)$ and benzene/ $Au(111)$ interfaces are revisited, with a realistic gap obtained using the ideas of Chap. 4 and the importance of vdW interaction will be discussed. TTF/Au, TCNQ/Au and pentacene/Au are also studied.

Finally in Chap. 6 we present the main conclusions of this thesis and suggest the future work inspired by this research work.

References

1. N.W. Ashcroft, N.D. Mermin, *Solid State Physics*, 1st edn. (Brooks Cole, New York, 1976)
2. S. Datta, *Electronic Transport in Mesoscopic Systems* (Cambridge University Press, Cambridge 1997)
3. N. Agrait, A. Yeyati, J.V. Ruitenbeek, Quantum properties of atomic-sized conductors. *Phys. Rep.* **377**(2–3), 81 (2003). doi:[10.1016/S0370-1573\(02\)00633-6](https://doi.org/10.1016/S0370-1573(02)00633-6)
4. B. Xu, N.J. Tao, Measurement of single-molecule resistance by repeated formation of molecular junctions. *Science* **301**(5637), 1221 (2003). doi:[10.1126/science.1087481](https://doi.org/10.1126/science.1087481)
5. A. Yeyati, F. Flores, A. Martín-Rodero, Transport in multilevel quantum dots: from the Kondo effect to the Coulomb blockade regime. *Phys. Rev. Lett.* **83**(3), 600 (1999). doi:[10.1103/PhysRevLett.83.600](https://doi.org/10.1103/PhysRevLett.83.600)

6. C. Gómez-Navarro, P.J. de Pablo, J. Gómez-Herrero, B. Biel, F.J. Garcia-Vidal, A. Rubio, F. Flores, Tuning the conductance of single-walled carbon nanotubes by ion irradiation in the Anderson localization regime. *Nat. Mater.* **4**(7), 534 (2005). doi:[10.1038/nmat1414](https://doi.org/10.1038/nmat1414)
7. G. Rubio-Bollinger, S. Bahn, N. Agrait, K. Jacobsen, S. Vieira, Mechanical properties and formation mechanisms of a wire of single gold atoms. *Phys. Rev. Lett.* **87**(2), 026101 (2001). doi:[10.1103/PhysRevLett.87.026101](https://doi.org/10.1103/PhysRevLett.87.026101)
8. J. Wang, Can man-made nanomachines compete with nature biomotors? *ACS nano* **3**(1), 4 (2009). doi:[10.1021/nm800829k](https://doi.org/10.1021/nm800829k)
9. N.J. Tao, Electron transport in molecular junctions. *Nat. Nanotechnol.* **1**(3), 173 (2006). doi:[10.1038/nnano.2006.130](https://doi.org/10.1038/nnano.2006.130)
10. R.M. Metzger, M.P. Cava. Rectification by a single molecule of hexadecylquinolinium tricyanoquinodimethanide. *Ann. N.Y. Acad. Sci.* **852**(1, Molecular electronics: science and technology), 95 (1998). doi:[10.1111/j.1749-6632.1998.tb09866.x](https://doi.org/10.1111/j.1749-6632.1998.tb09866.x)
11. J. Chen, M.A. Reed, A.M. Rawlett, J.M. Tour, Large on-off ratios and negative differential resistance in a molecular electronic device. *Science* **286**, 1550 (1999). doi:[10.1126/science.286.5444.1550](https://doi.org/10.1126/science.286.5444.1550)
12. C. Collier, E. Wong, M. Belohradský, F. Raymo, J. Stoddart, P. Kuekes, R. Williams, J. Heath, Electronically configurable molecular-based logic gates. *Science* **285**(5426), 391 (1999). doi:[10.1126/science.285.5426.391](https://doi.org/10.1126/science.285.5426.391)
13. J.C. Cuevas, E. Scheer, *Molecular Electronics An Introduction to Theory and Experiment* (World Scientific Publishing Co, Hackensack, 2010)
14. J.M. Tour, Molecular electronics. Synthesis and testing of components. *Acc. Chem. Res.* **33**(11), 791 (2000)
15. W. Lu, C.M. Lieber, Nanoelectronics from the bottom up. *Nat. Mater.* **6**(11), 841 (2007). doi:[10.1038/nmat2028](https://doi.org/10.1038/nmat2028)
16. W.R. Salaneck, S. Stafstrom, J.L. Bredas, *Conjugated Polymer Surfaces and Interfaces: Electronic and Chemical Structure of Interfaces for Polymer Light emitting Diodes*, (Cambridge University Press, Cambridge, 1996)
17. H. Ishii, K. Sugiyama, E. Ito, K. Seki, Energy level alignment and interfacial electronic structures at organic/metal and organic/organic interfaces. *Adv. Matter.* **11**(8), 605(1999)
18. W.R. Salaneck, K. Seki, A. Kahn, J.J. Pirauux (eds), *Conjugated Polymer and Molecular interfaces* (Dekker, New York, 2002)
19. F. Flores, J. Ortega, H. Vázquez, Modelling energy level alignment at organic interfaces and density functional theory. *Phys. Chem. Chem. Phys.* **11**(39), 8658 (2009). doi:[10.1039/b902492c](https://doi.org/10.1039/b902492c)
20. P. Samori, F. Cacialli (eds), *Functional Supramolecular Architectures: for Organic Electronics and Nanotechnology* (Wiley, Weinheim, 2010)
21. Transistor Count and Moore's Law. Image, http://commons.wikimedia.org/wiki/File:Transistor_Count_and_Moore%27s_Law-2011.svg. Accessed 13 May 2011
22. M. Brandbyge, J. Schiøtz, M. Sørensen, P. Stoltze, K. Jacobsen, J. Nørskov, L. Olesen, E. Laegsgaard, I. Stensgaard, F. Besenbacher, Quantized conductance in atom-sized wires between two metals. *Phys. Rev. B*, **52**(11), 8499 (1995). doi:[10.1103/PhysRevB.52.8499](https://doi.org/10.1103/PhysRevB.52.8499)
23. J. Gimzewski, R. Möller, Transition from the tunneling regime to point contact studied using scanning tunneling microscopy. *Phys. Rev. B* **36**(2), 1284 (1987). doi:[10.1103/PhysRevB.36.1284](https://doi.org/10.1103/PhysRevB.36.1284)
24. P. Jelínek, R. Pérez, J. Ortega, F. Flores, Hydrogen dissociation over Au nanowires and the fractional conductance quantum. *Phys. Rev. Lett.* **96**(4), 046803 (2006). doi:[10.1103/PhysRevLett.96.046803](https://doi.org/10.1103/PhysRevLett.96.046803)
25. P. Jelínek, R. Pérez, J. Ortega, F. Flores, Mechanical properties and electrical conductance of different Al nanowires submitted to a homogeneous deformation: a first-principles simulation. *Surf. Sci.* **566–568**, 13 (2004). doi:[10.1016/j.susc.2004.05.014](https://doi.org/10.1016/j.susc.2004.05.014)
26. B. Yoon, H. Häkkinen, U. Landman, A.S. Wörz, J.-M. Antonietti, S. Abbet, K. Judai, U. Heiz, Charging effects on bonding and catalyzed oxidation of CO on Au₈ clusters on MgO. *Science* **307**(5708), 403 (2005). doi:[10.1126/science.1104168](https://doi.org/10.1126/science.1104168)

27. M.S. Chen, D.W. Goodman, The structure of catalytically active gold on titania. *Science* **306**(5694), 252 (2004). doi:[10.1126/science.1102420](https://doi.org/10.1126/science.1102420)
28. T. Todorov, A. Sutton, Jumps in electronic conductance due to mechanical instabilities. *Phys. Rev. Lett.* **70**(14), 2138 (1993). doi:[10.1103/PhysRevLett.70.2138](https://doi.org/10.1103/PhysRevLett.70.2138)
29. R. Landauer, Spatial variation of currents and fields due to localized scatterers in metallic conduction. *IBM Journal of Research and Development* **32**(3), 306 (1988). doi:[10.1147/rd.323.0306](https://doi.org/10.1147/rd.323.0306)
30. D. Fisher, P. Lee, Relation between conductivity and transmission matrix. *Phys. Rev. B* **23**(12), 6851 (1981). doi:[10.1103/PhysRevB.23.6851](https://doi.org/10.1103/PhysRevB.23.6851)
31. Samsung®. Advertisement, http://www.samsung.com/es/experience/galaxys2/img/feature_img.png>. Accessed 12 Sept 2011
32. LG®. Advertisement, http://www.lg.com/uk/tv-audio-video/images/lg-tv-oled-EL9500-3_4view-01_large.png. Accessed 12 Sept 2011
33. Sony®. Press release image, <http://www.sony.co.jp/SonyInfo/News/Press/200705/07-053/01.jpg>. Accessed 24 May 2007
34. E. Abad, J. Ortega, F. Flores. Metal/organic barrier formation for a C₆₀/Au interface: from the molecular to the monolayer limit. *Phys. Status Solidi A* **209**, 636 (2012)
35. H. Vázquez, Energy level alignment at organic semiconductor interfaces. Ph.D. Thesis, Universidad Autónoma de Madrid, 2006
36. S. Günes, H. Neugebauer, N.S. Sariciftci, Conjugated polymer-based organic solar cells. *Chem. Rev.* **107**(4), 1324 (2007). doi:[10.1021/cr050149z](https://doi.org/10.1021/cr050149z)
37. N. Sato, K. Seki, H. Inokuchi. Polarization energies of organic solids determined by ultraviolet photoelectron spectroscopy. *J. Chem. Soc. Faraday Trans. 2* **77**(9), 1621 (1981). doi:[10.1039/f29817701621](https://doi.org/10.1039/f29817701621)
38. H.-J. Freund, R.W. Bigelow, Dynamic effects in VUV- and XUV-Spectroscopy of Organic Molecular Solids. *Phys. Scr.* **T17**, 50 (1987). doi:[10.1088/0031-8949/1987/T17/006](https://doi.org/10.1088/0031-8949/1987/T17/006)
39. C. Duke, W. Salaneck, T. Fabish, J. Ritsko, H. Thomas, A. Paton, Electronic structure of pendant-group polymers: Molecular-ion states and dielectric properties of poly(2-vinyl pyridine). *Phys. Rev. B* **18**(10), 5717 (1978). doi:[10.1103/PhysRevB.18.5717](https://doi.org/10.1103/PhysRevB.18.5717)
40. J.M. Blanco, F. Flores, R. Perez, STM-theory: Image potential, chemistry and surface relaxation. *Prog. Surf. Sci.* **81**(10–12), 403 (2006). doi:[10.1016/j.progsurf.2006.07.004](https://doi.org/10.1016/j.progsurf.2006.07.004)
41. C. Bai, *Scanning Tunneling Microscopy and Its Applications*, 2nd edn. Springer, New York, 2000)
42. E. Tsiper, Z.G. Soos, W. Gao, A. Kahn, Electronic polarization at surfaces and thin films of organic molecular crystals: PTCDA. *Chem. Phys. Lett.* **360**(1–2), 47 (2002). doi:[10.1016/S0009-2614\(02\)00774-1](https://doi.org/10.1016/S0009-2614(02)00774-1)
43. M. Nonnenmacher, M.P. O'Boyle, H.K. Wickramasinghe, Kelvin probe force microscopy. *Appl. Phys. Lett.* **58**(25), 2921 (1991). doi:[10.1063/1.105227](https://doi.org/10.1063/1.105227)
44. E. Moons, A. Goossens, T. Savenije, Surface Photovoltage of Porphyrin Layers Using the Kelvin Probe Technique. *J. Phys. Chem. B* **101**(42), 8492 (1997). doi:[10.1021/jp971071w](https://doi.org/10.1021/jp971071w)
45. H. Sugimura, K. Hayashi, N. Saito, O. Takai, N. Nakagiri, Kelvin probe force microscopy images of microstructured organosilane self-assembled monolayers. *Jpn. J. Appl. Phys.* **40**(Part 1, No. 6B), 4373 (2001). doi:[10.1143/JJAP.40.4373](https://doi.org/10.1143/JJAP.40.4373)
46. M. Kiguchi, O. Tal, S. Wohlthat, F. Pauly, M. Krieger, D. Djukic, J. Cuevas, J. van Ruitenbeek, Highly conductive molecular junctions based on direct binding of benzene to platinum electrodes. *Phys. Rev. Lett.* **101**(4), 46801 (2008). doi:[10.1103/PhysRevLett.101.046801](https://doi.org/10.1103/PhysRevLett.101.046801)
47. P. Jelínek, R. Pérez, J. Ortega, F. Flores, First-principles simulations of the stretching and final breaking of Al nanowires: Mechanical properties and electrical conductance. *Phys. Rev. B* **68**(8), 085403 (2003). doi:[10.1103/PhysRevB.68.085403](https://doi.org/10.1103/PhysRevB.68.085403)
48. C. Zhou, C.J. Muller, M.R. Deshpande, J.W. Sleight, M.A. Reed, Microfabrication of a mechanically controllable break junction in silicon. *Appl. Phys. Lett.* **67**(8), 1160 (1995). doi:[10.1063/1.114994](https://doi.org/10.1063/1.114994)
49. X. Xiao, B. Xu, N.J. Tao, Measurement of single molecule conductance: benzenedithiol and benzenedimethanethiol. *Nano Lett.* **4**(2), 267 (2004)

50. T. Albrecht, A. Guckian, J. Ulstrup, J.G. Vos, Transistor-like behavior of transition metal complexes. *Nano Lett.* **5**(7), 1451 (2005)
51. T. Albrecht, K. Moth-Poulsen, J.B. Christensen, A. Guckian, T. Bjørnholm, J.G. Vos, J. Ulstrup. In situ scanning tunnelling spectroscopy of inorganic transition metal complexes. *Faraday Discuss* **131**, 265 (2006). doi:[10.1039/b505451f](https://doi.org/10.1039/b505451f)
52. J.M. Blanco, C. González, P. Jelínek, J. Ortega, F. Flores, R. Pérez, First-principles simulations of STM images: From tunneling to the contact regime. *Phys. Rev. B* **70**(8), 085405 (2004). doi:[10.1103/PhysRevB.70.085405](https://doi.org/10.1103/PhysRevB.70.085405)
53. J.M. Blanco, Estudio teórico del microscopio de efecto túnel con métodos de primeros principios. Ph.D. Thesis, Universidad Autónoma de Madrid, 2004
54. C. Tejedor, F. Flores, E. Louis, The metal-semiconductor interface: Si (111) and zincblende (110) junctions. *J. Phys. C: Solid State Phys.* **10**, 2163 (1977). doi:[10.1088/0022-3719/10/12/022](https://doi.org/10.1088/0022-3719/10/12/022)
55. F. Flores, C. Tejedor, Energy barriers and interface states at heterojunctions. *J. Phys. C: Solid State Phys.* **12**, 731 (1979). doi:[10.1088/0022-3719/12/4/018](https://doi.org/10.1088/0022-3719/12/4/018)

Chapter 2

Theoretical Foundation

2.1 Introduction

Ab initio calculation of the electronic structure of molecules and solids have become one of the most important tools in solid state physics. These methods allow us to predict some properties (crystal structure, density, molecular geometry, adsorption and cohesive energies, among others) of condensed matter systems without need of any empirical parameters. By this way we can understand and calculate some properties of the systems that are very difficult or even impossible to measure experimentally. We can also gain insight in the origin of some effects that cannot be explained only with experimental data (such as conductance quantization in nanowires, or the origin of the dipole at metal/organic junctions). However, the price to pay is that a lot of computational effort is needed, compared with empirical or semi-empirical models. In order to reduce the computational time, a lot of approximations have been done in order to get the best accuracy/resources ratio. This chapter will guide through the state-of-the-art ab initio techniques necessary (some of them developed during this work) to successfully simulate the systems that have been studied during this thesis.

2.2 Statement of the Problem

Let us consider a system of n nuclei and N electrons. In order to calculate the properties of this system we should solve the following Schrödinger equation.

$$\left(- \sum_{\alpha} \frac{\hbar^2 \nabla_{\alpha}^2}{2M_{\alpha}} - \sum_i \frac{\hbar^2 \nabla_i^2}{2m} + \frac{1}{2} \sum_{\alpha, \beta} \frac{1}{4\pi \epsilon_0} \frac{Z_{\alpha} Z_{\beta} e^2}{|\mathbf{R}_{\alpha} - \mathbf{R}_{\beta}|} + \frac{1}{2} \sum_{i, j} \frac{1}{4\pi \epsilon_0} \frac{e^2}{|\mathbf{r}_i - \mathbf{r}_j|} - \sum_{\alpha, i} \frac{1}{4\pi \epsilon_0} \frac{Z_{\alpha} e^2}{|\mathbf{R}_{\alpha} - \mathbf{r}_i|} \right) \psi(\mathbf{R}_{\alpha}, s_{\alpha}, \mathbf{r}_i, s_i) = E \psi(\mathbf{R}_{\alpha}, s_{\alpha}, \mathbf{r}_i, s_i) \quad (2.1)$$

where $\mathbf{R}_\alpha = (R_{\alpha,x}, R_{\alpha,y}, R_{\alpha,z})$ are the spatial and s_α the spin coordinates of the nucleus α and \mathbf{r}_i are the spatial and s_i the spin coordinates of the electron i . This is a partial differential equation with $3N + 3n$ variables, clearly impossible to solve analytically or even numerically for the simplest system of interest. The first approximation to be done is the Born-Oppenheimer approximation. Due to the big mass difference between the heavy nuclei and the light electrons, we can decouple both equations of motion. The electronic structure relaxation is much faster than nuclei dynamics so we can consider that electrons “see” the ions as if they were frozen. The nuclei dynamics can be treated classically, considering that they are affected by a potential created by the electronic structure ($V(\mathbf{R}_\alpha) = -\nabla E_{gs}[\{\mathbf{R}_\alpha\}]$). So the equation we need to solve now is:

$$\left(-\sum_i \frac{\hbar^2 \nabla_i^2}{2m} + \frac{1}{2} \sum_{\alpha,\beta} \frac{1}{4\pi\epsilon_0} \frac{Z_\alpha Z_\beta e^2}{|\mathbf{R}_\alpha - \mathbf{R}_\beta|} + \frac{1}{2} \sum_{i,j} \frac{1}{4\pi\epsilon_0} \frac{e^2}{|\mathbf{r}_i - \mathbf{r}_j|} - \sum_{\alpha,i} \frac{1}{4\pi\epsilon_0} \frac{Z_\alpha e^2}{|\mathbf{R}_\alpha - \mathbf{r}_i|} \right) \psi(\mathbf{r}_i, s_i) = E \psi(\mathbf{r}_i, s_i) \quad (2.2)$$

that has “only” $3N$ variables. Although this equation seems very similar to (2.1), it is necessary to point out that in this case $\{\mathbf{R}_\alpha\}$ are parameters instead of variables, so for example, the nucleus-nucleus interaction is just a number. However, this equation is still impossible to solve. The main problem is the electron-electron interaction potential ($\widehat{V}_{ee} = \frac{1}{2} \sum_{i,j} \frac{1}{4\pi\epsilon_0} \frac{e^2}{|\mathbf{r}_i - \mathbf{r}_j|}$) that mix the position operators of the different electrons. Without this potential, the equation is separable in N equations of 3 variables. Most of the approximations made in order to solve this equation are aimed to transform this term and get separability of the problem. These approximations can be classified in two types: approximations based on the wave function (often used by chemists) or approximations based on the electron density (the most used, where the DFT is the most common). We are going to give the main ideas of the wave function methods on this section and we will explain in detail the DFT in the next one (for extensive monographs see [1–3]).

2.2.1 Hartree Approximation

Hartree approximation is the most simple one. It consists on treating the electron-electron interaction semiclassically, considering that each electron “see” a cloud of negative charge that is the square modulus of the electronic wavefunction.

The deduction of the equation for this approximation is very simple. First it’s necessary to realize that (2.2) can be derived [4] as the equation that makes stationary the following expression:

$$\langle \widehat{H} \rangle_\psi = \frac{\langle \psi | \widehat{H} | \psi \rangle}{\langle \psi | \psi \rangle} \quad (2.3)$$

The Hartree approximation relies in considering a fully separable solution for the Schrödinger equation $\psi(\{\mathbf{r}_i\}) = \prod_i \phi_i(\mathbf{r})$. Introducing this ansatz on (2.3) we get:

$$\left(-\sum_i \frac{\hbar^2 \nabla_i^2}{2m} + V_{nucl} + \widehat{V}_{ee}^H + \widehat{V}_{ext} \right) \phi(\mathbf{r}) = \varepsilon_i \phi(\mathbf{r}) \quad (2.4)$$

where $V_{nucl} = \frac{1}{2} \sum_{\alpha, \beta} \frac{1}{4\pi \varepsilon_0} \frac{Z_\alpha Z_\beta e^2}{|\mathbf{R}_\alpha - \mathbf{R}_\beta|}$ is the nucleus-nucleus interaction (just a number) and $\widehat{V}_{ext} = \sum_{\alpha, i} \frac{1}{4\pi \varepsilon_0} \frac{Z_\alpha e^2}{|\mathbf{R}_\alpha - \mathbf{r}_i|}$ is the interaction of the electrons with the electrostatic field created by the nuclei, and \widehat{V}_{ee}^H is the so-called *Hartree potential* that has the form of an electronic density cloud interacting with the electron:

$$\widehat{V}_{ee}^H = \frac{e^2}{4\pi \varepsilon_0} \int d^3 \mathbf{r}' \frac{\sum_i |\phi_i(\mathbf{r}')|^2}{|\mathbf{r} - \mathbf{r}'|} \quad (2.5)$$

where the sum is extended over the occupied orbitals. As we need $\{\phi_i\}$ to build \widehat{V}_{ee}^H , but only knowing the latter, the former can be obtained, we can only solve this equation in a selfconsistent manner: we choose some initial $\{\phi_i^{in}\}$ that seem not to be too different than the actual ones (for example, if we are calculating the electronic structure of a molecule, the wavefunctions of the free atoms that belong to it, is a good initial set). Then we calculate the Hartree potential and solve the Schrödinger equation, and we get $\{\phi_i^{out}\}$. Then we use this output as a new input (in fact, we use a combination of the $\{\phi_i^{in}\}$ and $\{\phi_i^{out}\}$, to avoid numerical instabilities), and obtain a new output. Use this output again as a new input, and so on. When the input and the output one-electron wave functions are very close to each other, we have found a *selfconsistent* solution, and we can use it to calculate the electronic properties of the system.

This simple approximation neglects *completely* any many-body effect (exchange and correlation), and does not give good numerical results even for systems where exchange and correlation are not very important. Moreover, it is very easy to see that the electronic wavefunction is not anti-symmetric, and we have to introduce the Pauli exclusion principle as an *ad-hoc* hypothesis. Despite the lack of accuracy of this approximation, it is very pedagogical as it introduces the idea of selfconsistency, and in the more sophisticated approximations the electron-electron interaction is of the form: $\widehat{V}_{ee} = \widehat{V}_{ee}^H + \text{other terms}$.

2.2.2 Hartree-Fock Approximation

The Hartree-Fock (HF) equation can be derived from Eq. (2.3), taking as an ansatz the simplest anti-symmetric wave-function: the Slater determinant:

$$\psi(\mathbf{r}_1, \dots, \mathbf{r}_n) = \frac{1}{\sqrt{n!}} \begin{vmatrix} \phi_1(\mathbf{r}_1) & \dots & \phi_1(\mathbf{r}_n) \\ \vdots & \ddots & \vdots \\ \phi_n(\mathbf{r}_1) & \dots & \phi_n(\mathbf{r}_n) \end{vmatrix} \quad (2.6)$$

If we introduce this expression into (2.3) we get the following integro-differential equation:

$$-\frac{1}{2}\nabla^2\phi_i(\mathbf{r})+V_{ext}(\mathbf{r})\phi_i(\mathbf{r})+V_{ee}^H(\mathbf{r})\phi_i(\mathbf{r})-\sum_j\int d^3\mathbf{r}'\frac{\delta_{s_i,s_j}}{|\mathbf{r}-\mathbf{r}'|}\phi_j^*(\mathbf{r}')\phi_j(\mathbf{r})\phi_i(\mathbf{r}')=\varepsilon_i\phi_i(\mathbf{r}) \quad (2.7)$$

This equation is considerably more complex than the Hartree one-electron Schrödinger-like equation (and more computationally “expensive” to solve). It is important to remark that it contains a non-local term (the last one), with the advantage of taking into account *exactly* the exchange, but no correlation effects at all, so the electronic repulsion will be overestimated. In order to introduce these effects, we have two choices: introduce them using a perturbative treatment (the Møller-Plesset (MPn) methods) or using a more general ansatz (a linear combination of Slater-like wave-functions) that is the basis of configuration interaction method.

2.2.3 Configuration Interaction

This method allow us to improve the HF results in a systematic (but expensive) way. It is based on the fact that the *exact* solution to the Schrödinger equation is a linear combination of Slater determinants.

$$|\psi\rangle = \sum_i a_i |\phi\rangle$$

where $\{|\phi\rangle\}$ is the infinite set of N -electron Slater determinants. Considering a subset of $\{|\phi\rangle\}$ we obtain better results than using Hartree-Fock (the bigger the subset, the closer to the exact energy). In order to obtain the eigen-energies and eigen-values we calculate the matrix equation:

$$\sum_j H_{ij} a_j = E a_i; \quad \text{where} \quad H_{ij} = \langle \phi_i | \hat{H} | \phi_j \rangle \quad (2.8)$$

This method is very expensive computationally, but the main problem is the scalability, because the time spent solving the equations grows as $N!$ with the number of electrons N , that limits this method for very small systems. It is also not suitable for extended systems (like solids) since for large N , the energy of the system $E \propto N^{1/2}$, violating the thermodynamic limit (unless we take the full—infinite—set of Slater determinants).

2.2.4 Møller-Plesset Perturbation Theory

It is based on time-independent perturbation theory.¹ We consider that we have a hamiltonian of the form $\widehat{H} = \widehat{H}_0 + \widehat{V}$ where $\widehat{V} = \widehat{H} - \widehat{H}_{HF} - \langle \psi_0 | \widehat{H} - \widehat{H}_{HF} | \psi_0 \rangle$ (ψ_0 is the ground state wave function of \widehat{H}_0), and solutions of $\widehat{H}_0 = \widehat{H}_{HF} + \langle \psi_0 | \widehat{H} - \widehat{H}_{HF} | \psi_0 \rangle$ are well known. It can be easily shown [5, 6] that corrections to the eigenvalues and energy at first order of perturbation theory are:

$$\begin{aligned} |\psi_i^{(1)}\rangle &= \sum_{j(j \neq i)} \frac{\langle \psi_j^{(0)} | \widehat{V} | \psi_i^{(0)} \rangle}{E_i^{(0)} - E_j^{(0)}} |\psi_i^{(0)}\rangle \\ E_i^{(1)} &= \langle \psi_i^{(0)} | \widehat{V} | \psi_i^{(0)} \rangle \\ E_i^{(2)} &= \sum_{j(j \neq i)} \frac{\langle \psi_i^{(0)} | \widehat{V} | \psi_j^{(0)} \rangle \langle \psi_j^{(0)} | \widehat{V} | \psi_i^{(0)} \rangle}{E_i^{(0)} - E_j^{(0)}} \end{aligned} \quad (2.9)$$

The Møller-Plesset methods [7] (MPn) calculate the energy at n -th order of perturbation theory. MP0 (no perturbation) is just Hartree-Fock, MP1 correction is Hartree-Fock also (the first order correction is zero), MP2 uses this second order equation for the energy, MP3 uses the third order and so on.

2.2.5 Pseudopotential

In most of the chemical or solid state physical systems only the valence electrons (i.e. the electrons in the outer shells) contribute to the bonding or band formation. The core electrons are so deep inside the atom, and so strongly bonded by the nucleus that they barely feel other atoms. So it is a waste of time to take into account a huge number of electrons that aren't important for obtaining the electronic properties of the system.

Pseudopotentials [8, 9] are used to avoid the use of core electrons in the calculation. They have the same scattering properties than the system formed by nucleus plus core electrons; and the wave functions of the valence electrons and the potential strength are the same as the all-electron system for a distance greater than some certain radius (r_c). At distances smaller than r_c , the pseudopotential is weaker than the bare nucleus potential (it doesn't diverge at $r = 0$ too), and the valence wave-functions are smoother (they don't need to have any nodes to be orthogonal to the core electrons).

So, not only pseudopotential simplify a N electron system by a $N - N_{core}$ one, it also allow us to work with well behaved and weaker potentials and smoother wave

¹ An excellent introduction of this theory, with some practical examples can be found in [5], Chap. XI.

functions, that numerical methods can handle much more efficiently. Moreover, some methods like plain wave-density functional theory methods (PW-DFT) will need a much smaller basis set in order to describe properly the systems under consideration.

Good pseudopotentials need to have some properties. The most important one is the *transferability*. That means that they have to reproduce the scattering properties of the nucleus plus core electrons in a lot of different chemical environments (isolated atom, molecules, crystals, etc.). It can be achieved just imposing norm conserving (that means that the pseudo-wavefunction integrals need to be the same as the actual ones) [10]. More sophisticated pseudopotentials are non-local (like the ones used in this thesis) and a different potential is used for each angular momentum [11–15]. Recently a new generation of ultra soft pseudopotentials have appeared in the literature. They are not norm-conserving; but they compensate this including different projectors in each angular moment [16, 17].

2.3 Density Functional Theory

The huge amount of theoretical ab initio research of very different materials (metal, semiconductors, organic molecules) in the second half of 20th century relies on the great simplification of the many-body Schrödinger equation due to the DFT and the Kohn–Sham equations [18, 19].

Despite of its known deficiencies (most of them related with the difficulty of finding a suitable exchange and correlation potential, see Sect. 2.3.2), the DFT has better computational resources/accuracy ratio than the other wave-function based methods (Hartree-Fock, configuration interaction, MP2...), so it is the suitable choice for the study of large systems (of more than one hundred, or even one thousand electrons). Although wave-function methods can be systematically improved (unlike DFT), usually don't work on extended systems (HF does not work well in metals, CI does not recover the thermodynamic limit, MP2 diverges for the homogeneous electron gas). That is another reason that encourage to use DFT in condensed matter systems, instead of other methods.

This theory is based on the Hohenberg-Kohn theorem [18]: The energy (and every observable) of a system of interacting electrons in a external potential (\widehat{V}_{ext}) is a functional *only* of the electronic density of the system $E = E[\rho(\mathbf{r})]$. Moreover, the minimum of this functional occurs when the electronic density is the electronic density of the ground state of the system ($\rho(\mathbf{r}) = \rho_{gs}(\mathbf{r})$). The proof is very simple.

Let \widehat{H} be the following hamiltonian:

$$\widehat{H} = \widehat{T} + \widehat{V}_{ext} + \widehat{V}_{ee} \quad (2.10)$$

where \widehat{T} is the kinetic energy of the electrons, \widehat{V}_{ext} the external potential, and \widehat{V}_{ee} the coulomb electron-electron interaction [20]. And let $V = \{\widehat{V}_{ext}\}$ be the set of all possible external potentials with the property that the solution of the many-body Schrödinger equation has a non degenerate ground state. If $\Psi = \{|\psi\rangle\}$ is the set of

all the possible ground states of \widehat{H} , then we can define the following application:

$$A : V \rightarrow \Psi$$

And if $N = \{\rho(\mathbf{r})\}$ is the set of the electronic densities of $\{|\psi\rangle\}$ $\rho(\mathbf{r}) = \int d^3\mathbf{r}_2 \dots d^3\mathbf{r}_N |\psi(\mathbf{r}, \mathbf{r}_2, \dots, \mathbf{r}_N)|^2$ then we can define another application:

$$B : \Psi \rightarrow N$$

The Hohenberg–Kohn theorem shows us that both applications are bijective. So let's show that A is surjective: If we have \widehat{V}_{ext} , and \widehat{V}'_{ext} with $\widehat{V}_{ext} \neq \widehat{V}'_{ext} + C$, and we assume that both have the same ground state

$$\begin{aligned} (\widehat{T} + \widehat{V}_{ee} + \widehat{V}_{ext})|\psi\rangle &= E|\psi\rangle \\ (\widehat{T} + \widehat{V}_{ee} + \widehat{V}'_{ext})|\psi\rangle &= E'|\psi\rangle \end{aligned} \quad (2.11)$$

subtracting both expressions:

$$(\widehat{V}_{ext} - \widehat{V}'_{ext})|\psi\rangle = (E - E')|\psi\rangle \Rightarrow (\widehat{V}_{ext} - \widehat{V}'_{ext}) = (E - E') \Rightarrow \widehat{V}_{ext} = \widehat{V}'_{ext} + C \quad (2.12)$$

that is against original assumption.

The proof of the surjectivity of the second application is the following. Let $|\psi\rangle$ and $|\psi'\rangle$ be two ground states of \widehat{H} and \widehat{H}' with densities $\rho(\mathbf{r})$ and $\rho'(\mathbf{r})$, that we consider to be the same. Due to both are ground states it is easy to see that:

$$\begin{aligned} E &= \langle \psi | \widehat{H} | \psi \rangle < \langle \psi' | \widehat{H} | \psi' \rangle = \langle \psi' | \widehat{H}' + \widehat{V}_{ext} - \widehat{V}'_{ext} | \psi' \rangle \Rightarrow \\ E &< E' + \int d^3\mathbf{r} \rho'(\mathbf{r})(V_{ext}(\mathbf{r}) - V'_{ext}(\mathbf{r})) \end{aligned} \quad (2.13)$$

If we repeat this for E' we find an analogous equation with primed and unprimed variables changed. Adding both expressions and taking into account that $\rho(\mathbf{r}) = \rho'(\mathbf{r})$ then:

$$E + E' < E' + E \quad (2.14)$$

that is impossible, so necessarily $\rho(\mathbf{r}) \neq \rho'(\mathbf{r})$.

The consequence of this theorem (as mentioned before) is that every observable, like the energy, is a functional of the density of the system. The definition of the ground state is the state that makes the energy of the hamiltonian a minimum. In the variational analysis language, the ground state is an extremal of the energy functional. This will allow us to deduce the Kohn–Sham equations.

2.3.1 Kohn–Sham Equations

We are going to separate from the energy functional the term due to the external potential:

$$E = E[\rho(\mathbf{r})] = F[\rho(\mathbf{r})] + \int d^3\mathbf{r} V_{ext}(\mathbf{r})\rho(\mathbf{r}) \quad (2.15)$$

where F is an universal functional that does not depend on the external potential. Kohn and Sham wrote, without loss of generality, the density as a sum of some orthonormal functions, $\psi_i(\mathbf{r})$, so that, $\rho(\mathbf{r}) = 2 \sum_{i=1}^{N/2} |\psi_i(\mathbf{r})|^2$ and divided this F functional in three terms with very easy physical interpretations.

$$\begin{aligned} F[\rho(\mathbf{r})] &= T_s[\rho(\mathbf{r})] + E_H[\rho(\mathbf{r})] + E_{xc}[\rho(\mathbf{r})] \quad \text{where} \\ T_s[\rho(\mathbf{r})] &= \sum_{i=1}^{N/2} \int d^3\mathbf{r} \psi_i^*(\mathbf{r}) \left(-\frac{\hbar^2}{2m} \nabla^2\right) \psi_i(\mathbf{r}) \\ E_H[\rho(\mathbf{r})] &= \int d^3\mathbf{r} d^3\mathbf{r}' \frac{\rho(\mathbf{r})\rho(\mathbf{r}')}{|\mathbf{r} - \mathbf{r}'|} \\ E_{xc}[\rho(\mathbf{r})] &= F[\rho(\mathbf{r})] - T_s[\rho(\mathbf{r})] + E_H[\rho(\mathbf{r})] \end{aligned} \quad (2.16)$$

It's clear that the T_s term can be considered as the kinetic energy of some hypothetical non-interacting particles, whose wavefunctions are $\psi_i(\mathbf{r})$, the E_H term is Hartree energy, and E_{xc} is the part of energy functional that we don't know. This equation means that we can consider this hypothetical non interacting particles as the electrons of the system, and the energy functional is the one-electron functional $E_{oe} = T_s + E_H + \int d^3\mathbf{r} V_{ext}(\mathbf{r})\rho(\mathbf{r})$, plus a term E_{xc} that contains all the many-body terms that we don't consider in the one-electron functional.

If the ground state is an extremal of the energy functional (the state where the energy is minimum), we can use variational analysis. We have a constraint on the total number of electrons $\int d^3\mathbf{r} \rho(\mathbf{r}) = N$, so we need to use a Lagrange parameter μ , that will be renamed as ε_i . Using the Euler-Lagrange equation:

$$\frac{\delta}{\delta\rho(\mathbf{r})} \left[T_s[\rho(\mathbf{r})] + E_H[\rho(\mathbf{r})] + E_{xc}[\rho(\mathbf{r})] + \int d^3\mathbf{r} V_{ext}(\mathbf{r})\rho(\mathbf{r}) + \varepsilon_i \left(N - \int d^3\mathbf{r} \rho(\mathbf{r}) \right) \right] = 0 \quad (2.17)$$

it is not difficult to get that:

$$\begin{aligned} \frac{\delta T_s[\rho(\mathbf{r})]}{\delta\rho(\mathbf{r})} &= -\frac{\hbar^2 \nabla^2}{2m} \\ \frac{\delta}{\delta\rho(\mathbf{r})} \left[\int d^3\mathbf{r} V_{ext}(\mathbf{r})\rho(\mathbf{r}) \right] &= V_{ext}(\mathbf{r}) \\ \frac{\delta E_H[\rho(\mathbf{r})]}{\delta\rho(\mathbf{r})} &= \int d^3\mathbf{r}' \frac{\rho(\mathbf{r}')}{|\mathbf{r} - \mathbf{r}'|} = V_{Hartree}(\mathbf{r}) \end{aligned}$$

$$\frac{\delta E_{xc}[\rho(\mathbf{r})]}{\delta \rho(\mathbf{r})} = V_{xc}(\mathbf{r}) \quad (2.18)$$

Putting all together we get [19]:

$$\left(-\frac{\hbar^2 \nabla^2}{2m} + V_{ext}(\mathbf{r}) + V_{Hartree}(\mathbf{r}) + V_{xc}(\mathbf{r}) - \varepsilon_i \right) \psi_i(\mathbf{r}) = 0 \quad (2.19)$$

We need to remember that these equations are *exact*. We haven't made any approximation up to this point. We have decoupled a partial differential equation with $3N$ variables to N partial differential Schrödinger-like equations of 3 variables. We need to remember here, that neither ε_i nor $\psi_i(\mathbf{r})$ have any physical meaning. They don't correspond to the electronic energy levels and considering them as that could result in misinterpretation of the calculation results.

However, this non-physical spectrum (eigen-energies and eigen-wavefunctions) compares reasonably well with the physical one and it is often treated as a reasonable approximation to the exact spectrum. Why these non-physical quantities turn out to be a good approximation for the physical ones?

Quasiparticles

This can be well understood if we introduce the idea of quasiparticles. Imagine that you have a jellium solid: that means, an homogeneous electron gas with an homogeneous positive background to neutralize the system. Then you add an electron to the system at a point \mathbf{r} . What will be the form of the potential created by this electron at a point \mathbf{r}' ?

If the electron does not interact with the electron gas, the potential will be simply $V_{coulomb} = e^2 / (4\pi \varepsilon_0) |\mathbf{r} - \mathbf{r}'|$.

This is considered in one-electron approaches like Hartree or Hartree-Fock. However, if the electron interact with the gas, things are not so simple. Physically, this interaction will repel other electrons on the surroundings (due to Coulomb repulsion and due to the Pauli exclusion principle). That means that the electron will be surrounded by a “lack” of negative charge (that implies a net positive charge due to the positive background, see Fig. 2.1). This is the so-called “exchange-correlation hole” (see Sect. 2.5.1). Now the potential created by the electron will be smaller, due to this exchange-correlation hole will screen the negative charge (see Fig. 2.1). So what will be the potential now? In simple dielectric theory, the potential is calculated using a dielectric constant $\varepsilon = \varepsilon_r \varepsilon_0$. A more accurate form of the potential can be written in a similar way:

$$W(\mathbf{r}, \mathbf{r}', \omega) = \int d\mathbf{r}'' \varepsilon^{-1}(\mathbf{r}, \mathbf{r}'', \omega) V_{coulomb}(\mathbf{r}', \mathbf{r}'') \quad (2.20)$$

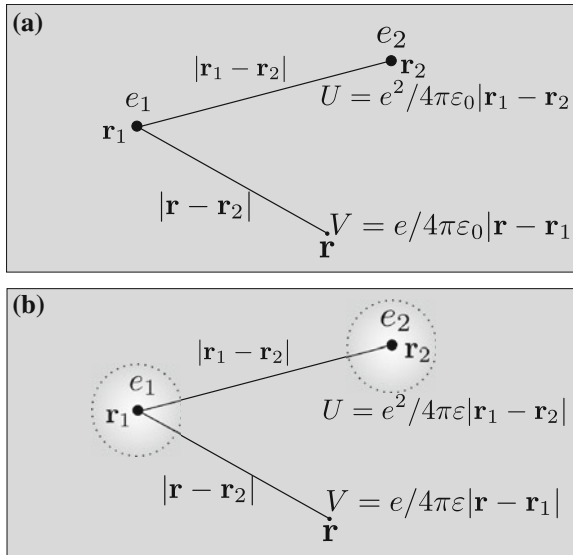


Fig. 2.1 Schematic figure of quasiparticles. In case **a**, there is no interaction of e_1 and e_2 with the surrounding electron gas. In case **b**, interaction between the electrons and the gas is working, creating a charge hole around them, so the effective coulomb interaction of the quasiparticle is lower. This allow to consider quasi-electrons as independent particles, explaining the good agreement of using KS orbitals as quasiparticle orbitals

where $\varepsilon^{-1}(\mathbf{r}, \mathbf{r}'', \omega)$ is the dielectric function. Its properties and different approximations for its calculation belong to the linear response theory in many-body physics. An extensive discussion about it can be found in [21, 22].

So instead of working with bare electrons (and holes), that are the ones that exists physically, we can take the electron and its positive charge cloud and treat it as a whole. This is not an actual particle but a *quasiparticle*. These quasiparticles can be considered, in good approximation, as nearly independent particles. That is the reason why the one-electron picture works pretty well. That is also the reason why, although they don't have in principle any physical meaning, Kohn–Sham eigenfunctions are treated as reliable eigenfunctions of the interacting system. They are the quasiparticle eigenvalues.

Despite this quasiparticle interpretation of the DFT spectra, in order to calculate the energy of the electrons at ground state we need to realize that it is not just $E = 2 \sum_{i=1}^{N/2} \varepsilon_i$ (factor 2 is due to spin multiplicity). There are terms that are not correctly included in this sum. For example, the electron-electron Hartree contribution is counted twice: in Hartree potential for atom i we include the $i-j$ interaction term, and in Hartree potential for atom j we include $i-j$ interaction too. This fact is commonly called 'double counting'. Also, the exchange and correlation energy E_{XC} is not correctly evaluated, because it is considered as $E_{XC} = \int d^3\mathbf{r} \rho(\mathbf{r}) V_{xc}(\mathbf{r})$ that is not true in general. So, the actual total energy is given by:

$$E[\rho(\mathbf{r})] = 2 \sum_{i=1}^{N/2} \varepsilon_i - \frac{1}{2} \int d^3\mathbf{r} d^3\mathbf{r}' \frac{\rho(\mathbf{r})\rho(\mathbf{r}')}{|\mathbf{r} - \mathbf{r}'|} + E^{xc}[\rho(\mathbf{r})] - \int d^3\mathbf{r} \rho(\mathbf{r}) V_{xc}(\mathbf{r}) \quad (2.21)$$

2.3.2 Exchange and Correlation Functional Approximations

When we want to put DFT in practice, we find a very important problem. We don't know the exact form of E^{xc} and $V_{xc}(\mathbf{r})$. So we need to do *approximations*, and our results will no longer be exact. There are several approximations to calculate the exchange-correlation energy (potential). The most common are:

Local Density Approximation (LDA)

It is the most simple one and it was proposed by Kohn and Sham in [19]. It relies on the approximation that the exchange and correlation interactions are entirely *local*; that means that exchange and correlation energy at the point \mathbf{r} *only* depends on the density at \mathbf{r} . Under this consideration, we can use the exchange-correlation energy for an homogeneous electron gas of density ρ (that is not, however, a trivial calculation [23, 24]) to calculate the E_{xc} functional:

$$E_{xc}[\rho(\mathbf{r})] = \int d^3\mathbf{r} \rho(\mathbf{r}) \varepsilon_{xc}(\rho = \rho(\mathbf{r})) \quad (2.22)$$

where $\varepsilon(\rho = \rho(\mathbf{r})) = f(\rho)$, (the exchange-correlation energy depends *only* on the density at each point).

Surprisingly this naive approximation works *pretty* well. However LDA has some deficiencies that cause systematic failures when computing some properties of the systems, such as:

- Bond lengths in LDA are systematically smaller than the ones found experimentally, i.e. LDA overestimates the attraction between atoms.
- Cohesive energies in LDA are systematically bigger than the ones found experimentally. This is related with the previous failure.
- It does not describe well the magnetic properties of some systems (for example LDA predicts for the iron a paramagnetic FCC structure, instead of the ferromagnetic BCC structure found experimentally).
- It does not describe well weak interactions (hydrogen bonds, Van der Waals interactions, etc.) so it is not suitable for calculations involving water, ice, biological molecules (proteins, DNA...), physisorbed molecules on metals, etc.
- V_{xc}^{LDA} decreases as $-\rho^{1/3}$ for atoms and clusters, instead of $-1/r$. Some anions are not stable in LDA.

Generalized Gradient Approximation (GGA)

This approximation corrects some of the deficiencies of the LDA, because it takes into account not only the density at some point, but also the gradient of the density. So the functional can be expressed as:

$$E_{xc}^{GGA}[\rho(\mathbf{r})] = \int d^3\mathbf{r} \rho(\mathbf{r}) \varepsilon_{xc}[\rho(\mathbf{r}), \nabla\rho(\mathbf{r})] \quad (2.23)$$

The exact form of the functional is found imposing several limits and scale and normalization rules. There are two types of GGA functionals: semiempirical [25, 26] (adjusted to reproduce good results in a big variety of molecules, but fail on non-localized systems) and non-empirical [27] (based on physical arguments, can handle a full variety of systems).

GGA correct some of the problems of LDA but not systematically.

- Reduces the error in formation energies, but not in bond length in molecules.
- It describes better hydrogen bonds.
- Tend (but not systematically) to reduce the error in energies and bond length in solids.
- It stabilizes the BCC magnetic iron.
- It still has some deficiencies: small bulk modulus in semiconductors, open gaps in transition metal oxides, etc.

Other Functionals

There are a full variety of other functionals apart from LDA and GGA. They can include exact exchange or second order derivatives [28], for example Meta-GGA. There are also hybrid methods that mix exact exchange (using Hartree-Fock) with E_{xc} . A new hybrid method is presented in this thesis (in the context of LCAO-OO) and will be carefully explained later (see 2.7.3).

There is an special family of functionals that uses the Kohn–Sham non-physical orbitals as an input, instead of charge density ($E_{xc} = E_{xc}[\{\phi_i(\mathbf{r})\}]$). For a extensive monograph of these functionals see [29].

2.4 The FIREBALL Method

The FIREBALL method is based on the work of Sankey and Niklewski [30]. It is an ab initio local orbital tight-binding method, using a self-consistent version [31] of the Harris-Foulkes functional [32, 33]. It has been implemented in a DFT code called FIREBALL [34, 35].

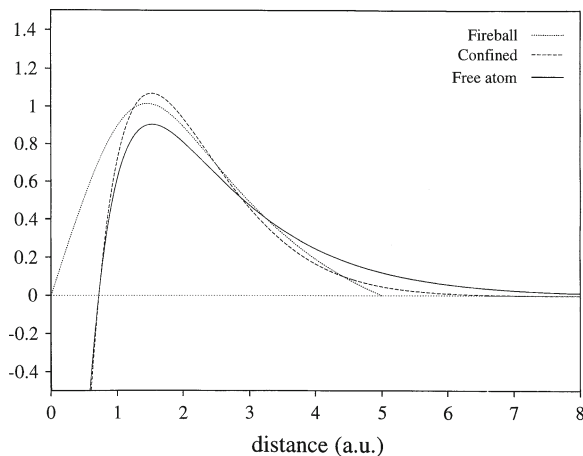


Fig. 2.2 Differences in the radial part of a 3p silicon fireball, free and confined orbitals. Reprinted from [36], Copyright (1998) with permission from Elsevier

2.4.1 Fireball Orbitals

The basis set used in the FIREBALL code are constructed using ‘fireball’ orbitals. They are atomic-like orbitals $\{\phi_{i\alpha}(\mathbf{r}_i)\}$ ($\alpha = nlm$) that are strictly zero beyond a certain cut-off radius (R_C) (Fig. 2.2). So the orbitals used in the code are slightly excited (this is the reason why they are called ‘fireball’ orbitals) but they reproduce better the shape of the orbitals inside a molecule or a lattice (due to orthonormalization they are more confined than free atomic ones). They also have the advantage of being strictly zero beyond R_C , so there are a finite number of interactions between the atoms in our system (even if they are extended systems like solids or surfaces). Although all electron calculations are possible in FIREBALL, usually calculations are carried out using only valence electrons: separable Kleinman–Bylander pseudopotentials [14] are used to take into account the effect of the nucleus and the core electrons.

Before any calculation is done we need to calculate the ‘fireball’ orbitals basis set. We have several degrees of freedom that give us a lot of flexibility in this choice:

- We can choose different R_C for each shell of each atomic species.
- We can choose a minimal basis (only $(2l + 1)$ orbitals for each l quantum number shell): an sp^3 basis or an sp^3d^5 basis.
- We can choose double basis set ($2(2l + 1)$ orbitals for l quantum number); the ground and the first excited wavefunction of the atomic hamiltonian (with the R_C condition) are used. There is no need to use both wavefunctions for all l , so it is possible to use double basis for some l and simple for the others (the use of a $sp^3d^5d^{*5}$ is common [37]).
- We can introduce an confinement potential, so the electronic tails would go smoothly to zero.

- We can mix ground state and excited state orbitals in order to construct an optimized minimal basis set [38]. Or we can even use ground state and excited orbitals from different calculations (such as ground state basis and ground state confined basis or even basis of different atoms).

In order to know if our basis is a good one for the element (or elements) under consideration, some tests are usually carried out: calculation of the lattice parameter of the crystal, bulk modulus, the volume band structure (comparing it with PW-LDA calculations [39]), surface properties, bond lengths, etc.

2.4.2 The Harris Functional

In Sect. 2.3 energy has been calculated using the Kohn–Sham functional, considering the output charge density $\rho^{out}(\mathbf{r})$, obtained after the diagonalization of the hamiltonian. Harris and Foulkes [32, 33] proved that the energy can be calculated approximately without self-consistent process. The Harris functional is formally the same as the Kohn–Sham functional, but using $\rho^{in}(\mathbf{r})$ instead of $\rho^{out}(\mathbf{r})$. The energy difference between the results obtained with the Kohn–Sham and the Harris functionals scale as the second order in the difference between the input and the self-consistent density.

$$E^{Harris} = E^{Kohn-Sham} + O^2(\rho^{in} - \rho^{sc}) \quad (2.24)$$

By this way we can choose an arbitrary input density to do our calculations. In FIREBALL, for computational convenience it has the form:

$$\rho^{in}(\mathbf{r}) = \sum_{i\alpha} n_{i\alpha}^{in} |\phi_{i\alpha}(\mathbf{r} - \mathbf{R}_i)|^2 \quad (2.25)$$

With this form of the input density, and the fact that the orbitals are confined, the hamiltonian matrix elements involve (at most) three center interactions (on the form $\langle \phi(\mathbf{r} - \mathbf{R}_i) | V(\mathbf{r} - \mathbf{R}_j) | \phi(\mathbf{r} - \mathbf{R}_k) \rangle$) and can be tabulated for several distances and angles [30] and interpolated for the distances and angles of our calculations. That means that no matrix elements' integral calculations are made during the simulations. That is one of the reasons why FIREBALL is so fast.

This combination of fireball orbitals and Harris functional works well in dimers and some solids but it fails in surfaces or in systems with big charge transfer between the atoms. In reference [31] a self-consistent version of the Harris functional is presented. In order to maintain the form of the input density in (2.25) to tabulate the interactions, an output $n_{i\alpha}^{out}$ are defined as:

$$n_{i\alpha}^{out} = \sum_n^{occ.} |\langle \psi_n | \phi_{i\alpha} \rangle|^2 \quad (2.26)$$

where ψ_n are the hamiltonian eigenvalues and $\varphi_{i\alpha}$ are the *Löwdin* orbitals [40]. These orbitals form an orthonormal basis set (the basis set of fireball orbitals is not orthonormal), that is the most similar to the fireball one [41]. These orbitals are calculated via:

$$\varphi_{i\alpha} = \sum_{j\beta} (S^{-1/2})_{i\alpha,j\beta} \phi_{j\beta}; \quad \text{where } (S)_{i\alpha,j\beta} = \langle \phi_{i\alpha} | \phi_{j\beta} \rangle \quad (2.27)$$

The $(S^{-1/2})$ matrix can be calculated by diagonalizing S and then taking the square root of the main diagonal elements [6]. So, we can calculate the $n_{i\alpha}$ numbers in a self consistent way $n_{i\alpha}^{in} = n_{i\alpha}^{out}$. These $n_{i\alpha}$ can be seen as the occupation numbers of the orbitals of our system, linking this approach to the LCAO-OO method, explained in Sect. 2.5.

We need to say here that the use of $n_{i\alpha}^{out}$ has an implicit approximation, due to the actual output density has the form:

$$\rho^{out}(\mathbf{r}) = \sum_{i\alpha,j\beta} n_{i\alpha,j\beta}^{out} \varphi_{i\alpha}^* \varphi_{j\beta}; \quad \text{where } n_{i\alpha,j\beta}^{out} = \sum_n^{occ.} \langle \psi_n | \varphi_{i\alpha} \rangle \langle \varphi_{j\beta} | \psi_n \rangle \quad (2.28)$$

and taking into account only $n_{i\alpha}^{out}$ means that we are considering that the non diagonal elements ($n_{i\alpha,j\beta}^{out}; j\beta \neq i\alpha$) are zero, that in general is not true. Moreover, note that in Eq. 2.28 the wavefunctions are the Löwdin φ instead of the non-diagonal ϕ that we use in (2.25). This is another approximation, motivated by the fact that φ are the orthonormal wavefunctions more similar to ϕ . Other choices for $n_{i\alpha}^{out}$ are available, but this is the one that gives better results.

In practice, for a calculation in FIREBALL there are always three steps. In the first step we calculate the atomic orbitals of the elements that are present at our system. In the second step we calculate and tabulate the two and three center integrals for different hamiltonian matrix elements. In the third step we use the tabulated elements to construct and diagonalize our hamiltonian until we find self-consistent occupation numbers. Then we calculate the energy using the Harris functional and the forces suffered by each atom, that allows us to do molecular dynamics (MD).

2.4.3 Exchange and Correlation

We want to tabulate the exchange-correlation potential as we have done for the Hartree and kinetic energy term. The problem is that this potential is not linear in the density (so if the density has the form $\rho = \sum_i \rho_i$, the potential cannot be written in the form $V^{xc}(\rho) = \sum_i V_i^{xc}(\rho_i)$). Some approximations are done in order to tabulate these interactions. Although LDA and GGA exchange-correlation functionals can be implemented in these approximations, only LDA is available for all approximations at the present version of the code.

The first one, Sankey-Niklewski (SN) approximation [30], is based on a Taylor expansion of exchange-correlation energy and potential. This approximation has been improved adding terms beyond first order Taylor expansion [42, 43].

Sankey–Niklewski

We want to calculate the matrix elements $\langle \phi_{i\alpha} | E_{xc} | \phi_{i\alpha} \rangle$, $\langle \phi_{i\alpha} | V_{xc} | \phi_{j\beta} \rangle$. In the Sankey–Niklewski approximation we just perform a Taylor expansion around an average density $\bar{\rho}_{i\alpha, j\beta}$.

$$\langle \phi_{i\alpha} | E_{xc} | \phi_{i\alpha} \rangle \simeq E_{xc}(\bar{\rho}_{i\alpha, i\alpha}) + \frac{dE_{xc}}{d\rho}(\bar{\rho}_{i\alpha, i\alpha})(\langle \phi_{i\alpha} | \rho | \phi_{i\alpha} \rangle - \bar{\rho}_{i\alpha, i\alpha}) \quad (2.29)$$

$$\langle \phi_{i\alpha} | V_{xc} | \phi_{j\beta} \rangle \simeq V_{xc}(\bar{\rho}_{i\alpha, j\beta})S_{i\alpha, j\beta} + \frac{dV_{xc}}{d\rho}(\bar{\rho}_{i\alpha, j\beta})(\langle \phi_{i\alpha} | \rho | \phi_{j\beta} \rangle - \bar{\rho}_{i\alpha, j\beta}S_{i\alpha, j\beta}) \quad (2.30)$$

In this approximation, the average density is defined as:

$$\bar{\rho}_{i\alpha, j\beta} = \frac{\langle \phi_{i\alpha} | \rho | \phi_{j\beta} \rangle}{\langle \phi_{i\alpha} | \phi_{j\beta} \rangle} = \frac{\rho_{i\alpha, j\beta}}{S_{i\alpha, j\beta}} \quad (2.31)$$

Choosing $\bar{\rho}_{i\alpha, j\beta}$ this way, the second term of the Taylor expansion (that depends on $d^2 E_{xc}/d\rho^2$) is identically zero, and the third term is minimized. Physically it means that the effective density is calculated using *importance sampling*, because the density is weighted more where the bond charge is high.

However this average density lacks for some deficiencies. First of all, it is not defined when the overlap is zero. Moreover, there is no reason why $\rho_{i\alpha, j\beta}$ and $S_{i\alpha, j\beta}$ need to have the same sign, giving unphysical $\bar{\rho}_{i\alpha, j\beta} < 0$. New methods, that correct these deficiencies (that are fatal for transition metals) are needed. We will describe them in the next paragraphs.

Horsfield

An attempt to improve the deficiencies of SN approximation was made by Horsfield [42]. It calculate exchange and correlation using a multi center expansion of density (an idea that will be used in McWEDA also). Different expansions will be made in $\langle \phi_{i\alpha} | V_{xc} | \phi_{j\beta} \rangle$ depending whether $i = j$ or not.

$$\langle \phi_{i\alpha} | V_{xc}[\rho] | \phi_{i\beta} \rangle \simeq \langle \phi_{i\alpha} | V_{xc}[\rho_i] | \phi_{i\beta} \rangle + \sum_{j \neq i} \langle \phi_{i\alpha} | V_{xc}[\rho_i + \rho_j] - V_{xc}[\rho_i] | \phi_{i\beta} \rangle \quad (\text{on-site term}) \quad (2.32)$$

$$\begin{aligned}
\langle \phi_{i\alpha} | V_{xc}[\rho] | \phi_{j\beta} \rangle &\simeq \langle \phi_{i\alpha} | V_{xc}[\rho_i + \rho_j] | \phi_{j\beta} \rangle \\
&+ \sum_{k \neq i, j} \langle \phi_{i\alpha} | V_{xc}[\rho_i + \rho_j + \rho_k] - V_{xc}[\rho_i + \rho_j] | \phi_{j\beta} \rangle \quad (\text{off-site term: } i \neq j)
\end{aligned} \tag{2.33}$$

These integrals can be stored in data tables, just like in the SN approach. Although this approximation is good in many cases, the on-site terms ($i = j$) are not accurate enough for some systems (such as transition metals) and an additional term must be included:

$$\langle \phi_{i\alpha} | \left(V_{xc}[\rho] - V_{xc}[\rho_i] - \sum_{j \neq i} V_{xc}[\rho_i + \rho_j] - V_{xc}[\rho_i] \right) | \phi_{i\beta} \rangle \tag{2.34}$$

Unfortunately these integrals cannot be stored in data tables. Moreover, most of the computational time is spent in calculation of exchange-correlation terms, reducing the efficiency.

McWEDA

A more sophisticated way to improve the SN approximation is the Multi-center Weighted Exchange-correlation Density Approximation (McWEDA), developed by Jelínek and coworkers [43]. This method has been used for all the systems studied in this thesis.

First of all, a new average density is used, using the weighting functions $w_{i\alpha}$ associated with the wavefunctions $\phi_{i\alpha}$ defined this way:

$$\begin{aligned}
\phi_{nlm} &= R_{nl}(r) \Upsilon_l^m(\Omega) \\
w_{nl} &= |R_{nl}(r)| \Upsilon_0^0(\Omega)
\end{aligned} \tag{2.35}$$

so the average density is now:

$$\bar{\rho}_{i\alpha, j\beta} = \frac{\langle w_{i\alpha} | \rho | w_{j\beta} \rangle}{\langle w_{i\alpha} | w_{j\beta} \rangle} \tag{2.36}$$

that does not have the deficiencies of definition (2.31).

We can define a Generalized SN (GSN) approximation where this new $\bar{\rho}_{i\alpha, j\beta}$ is used in the same scheme. However we can go beyond GSN approximation, using the one center matrix element $\langle \phi_{i\alpha} | E_{xc}[\rho_i] | \phi_{j\beta} \rangle$ ($\langle \phi_{i\alpha} | V_{xc}[\rho_i] | \phi_{j\beta} \rangle$) where $\rho_i = \sum_{\alpha} n_{i\alpha}^i |\phi_{i\alpha}(\mathbf{r} - \mathbf{R}_i)|^2$. This element will be the most important term in the total exchange-correlation matrix elements so we can write the total exchange-correlation potential as $\langle \phi_{i\alpha} | V_{xc}[\rho_i] | \phi_{j\beta} \rangle$ plus a correction.

$$\langle \phi_{i\alpha} | E_{xc}[\rho] | \phi_{i\beta} \rangle = \langle \phi_{i\alpha} | E_{xc}[\rho_i] | \phi_{i\beta} \rangle + (\langle \phi_{i\alpha} | E_{xc}[\rho] | \phi_{i\beta} \rangle - \langle \phi_{i\alpha} | E_{xc}[\rho_i] | \phi_{i\beta} \rangle) \quad (2.37)$$

$$\langle \phi_{i\alpha} | V_{xc}[\rho] | \phi_{j\beta} \rangle = \langle \phi_{i\alpha} | V_{xc}[\rho_i] | \phi_{j\beta} \rangle + (\langle \phi_{i\alpha} | V_{xc}[\rho] | \phi_{j\beta} \rangle - \langle \phi_{i\alpha} | V_{xc}[\rho_i] | \phi_{j\beta} \rangle) \quad \text{if } i = j \quad (2.38)$$

$$\begin{aligned} \langle \phi_{i\alpha} | V_{xc}[\rho] | \phi_{j\beta} \rangle &= \langle \phi_{i\alpha} | V_{xc}[\rho_i + \rho_j] | \phi_{j\beta} \rangle \\ &+ (\langle \phi_{i\alpha} | V_{xc}[\rho] | \phi_{j\beta} \rangle - \langle \phi_{i\alpha} | V_{xc}[\rho_i + \rho_j] | \phi_{j\beta} \rangle) \quad \text{if } i \neq j \end{aligned} \quad (2.39)$$

From now on we will consider only the potential term (the same ideas hold for the energy one). We will explain now the $i = j$ case (on-site term). $\langle \phi_{i\alpha} | V_{xc}[\rho_i] | \phi_{i\beta} \rangle$ is a one-center integral and can be very easily calculated and tabulated. The correction part (the term between parentheses) is calculated using the GSN approximation (due to this term is a correction of the main one, the GSN correction should be good enough). So the on-site term is written in McWEDA approximation as:

$$\begin{aligned} \langle \phi_{i\alpha} | V_{xc}[\rho] | \phi_{i\beta} \rangle &= \langle \phi_{i\alpha} | V_{xc}[\rho_i] | \phi_{i\beta} \rangle + V_{xc}(\bar{\rho}_{i\alpha, i\beta}) S_{i\alpha, i\beta} + V'_{xc}(\bar{\rho}_{i\alpha, i\beta}) (\langle \phi_{i\alpha} | \rho | \phi_{i\beta} \rangle \\ &- \bar{\rho}_{i\alpha, i\beta} S_{i\alpha, i\beta}) - V_{xc}(\bar{\rho}_{i\alpha, i\beta}^i) S_{i\alpha, i\beta} - V'_{xc}(\bar{\rho}_{i\alpha, i\beta}^i) (\langle \phi_{i\alpha} | \rho_i | \phi_{i\beta} \rangle \\ &- \bar{\rho}_{i\alpha, i\beta}^i S_{i\alpha, i\beta}) \end{aligned} \quad (2.40)$$

where $\bar{\rho}_{i\alpha, i\beta}^i = \langle w_{i\alpha} | \rho_i | w_{j\beta} \rangle / \langle w_{i\alpha} | w_{j\beta} \rangle$. In the off-site case ($i \neq j$) the evaluation of correction part is also done in the GSN approximation so:

$$\begin{aligned} \langle \phi_{i\alpha} | V_{xc}[\rho] | \phi_{j\beta} \rangle &= \langle \phi_{i\alpha} | V_{xc}[\rho_i + \rho_j] | \phi_{j\beta} \rangle + V_{xc}(\bar{\rho}_{i\alpha, j\beta}) S_{i\alpha, j\beta} \\ &+ V'_{xc}(\bar{\rho}_{i\alpha, j\beta}) (\langle \phi_{i\alpha} | \rho | \phi_{j\beta} \rangle - \bar{\rho}_{i\alpha, j\beta} S_{i\alpha, j\beta}) - V_{xc}(\bar{\rho}_{i\alpha, j\beta}^{ij}) S_{i\alpha, j\beta} \\ &- V'_{xc}(\bar{\rho}_{i\alpha, j\beta}^{ij}) (\langle \phi_{i\alpha} | \rho_i + \rho_j | \phi_{j\beta} \rangle - \bar{\rho}_{i\alpha, j\beta}^{ij} S_{i\alpha, j\beta}) \end{aligned} \quad (2.41)$$

where $\bar{\rho}_{i\alpha, j\beta}^{ij} = \langle w_{i\alpha} | \rho_i + \rho_j | w_{j\beta} \rangle / \langle w_{i\alpha} | w_{j\beta} \rangle$. Recently McWEDA approximation has been improved [44], introducing the effect of charge transfer in $\langle \phi_{i\alpha} | V_{xc}[\rho_i] | \phi_{i\beta} \rangle$ and $\langle \phi_{i\alpha} | V_{xc}[\rho_i + \rho_j] | \phi_{j\beta} \rangle$, where ρ_i and ρ_j in practice were considered the neutral density (that makes the atom electrically neutral) instead of the self-consistent ones. A Taylor expansion is performed around the neutral density ρ_i^0 and ρ_j^0 , and we obtain:

$$\begin{aligned} \langle \phi_{i\alpha} | V_{xc}[\rho_i] | \phi_{i\beta} \rangle &\simeq \langle \phi_{i\alpha} | V_{xc}[\rho_i^0] | \phi_{i\beta} \rangle + \frac{dV_{xc}}{d\rho}[\rho_i^0] (\phi_{i\alpha} | \rho_i - \rho_i^0 | \phi_{i\beta} \rangle) \\ \langle \phi_{i\alpha} | V_{xc}[\rho_i + \rho_j] | \phi_{j\beta} \rangle &\simeq \langle \phi_{i\alpha} | V_{xc}[\rho_i^0 + \rho_j^0] | \phi_{j\beta} \rangle + \frac{dV_{xc}}{d\rho}[\rho_i^0 + \rho_j^0] \\ &\langle \phi_{i\alpha} | \rho_i - \rho_i^0 + \rho_j - \rho_j^0 | \phi_{j\beta} \rangle \end{aligned} \quad (2.42)$$

This has corrected some deficiencies in the energy using extended basis sets, but work on this direction is still in progress. In this thesis there is also some progress in extending McWEDA to the local spin density approximation (LSDA), see Appendix C for details.

2.4.4 Molecular Dynamics and Structure Relaxation

FIREBALL can calculate the energy and the atomic forces acting on our system, so it can be employed as a MD code. Moreover, because of the storage of integrals in data tables make the code very fast, MD simulations can be performed in a reasonable amount of time.

The forces can be calculated as the derivative of the total energy given by the Harris functional:

$$\begin{aligned} \mathbf{F}_i = & -\frac{\partial E_{tot}}{\partial \mathbf{R}_i} = -\frac{\partial}{\partial \mathbf{R}_i} \left(2 \sum_i^{occ} \varepsilon_i \right) - \frac{\partial}{\partial \mathbf{R}_i} \left(\frac{1}{2} \sum_{j,k} \frac{Z_j Z_k e^2}{|\mathbf{R}_j - \mathbf{R}_k|} - \frac{1}{2} \int d^3 \mathbf{r} d^3 \mathbf{r}' \frac{\rho_{in}(\mathbf{r}) \rho_{in}(\mathbf{r}')}{|\mathbf{r} - \mathbf{r}'|} \right) \\ & - \frac{\partial}{\partial \mathbf{R}_i} (E^{xc}[\rho_{in}(\mathbf{r})]) - \int d^3 \mathbf{r} \rho_{in}(\mathbf{r}) V_{xc}[\rho_{in}(\mathbf{r})] = -\frac{\partial E_{BS}}{\partial \mathbf{R}_i} - \frac{\partial (E_{ion-ion} - E_{ee})}{\partial \mathbf{R}_i} - \frac{\partial (\delta U_{xc})}{\partial \mathbf{R}_i} \end{aligned} \quad (2.43)$$

A variation of the Hellman-Feynman theorem [45–47] is used to compute the band structure force. This way, the derivatives with respect to the atomic positions of the matrix elements $\frac{\partial}{\partial \mathbf{R}_i} \langle i\alpha | H | j\beta \rangle$ can be easily calculated using the tabulated interactions and taking the derivative of the interpolation polynomials.

Using forces, not only we can do MD, but also we can relax the systems and find the minimum energy positions of the atoms. There are two main ways of calculating them in FIREBALL: dynamical quenching and conjugate gradients.

Dynamical Quenching

This is a pure MD method for relaxing atomic positions of our system. It is based on energy conservation. When the nuclei are in a minimum of potential energy they have a maximum of kinetic energy. So, if we calculate the kinetic energy of the system we can use it to know when we are in a potential energy minimum.

The mechanism of dynamical quenching is the following one: we have some initial guess of the atomic positions of our system. Then we do MD, taking care of the kinetic energy of the nuclei. Usually it increases (that means that the atomic positions are moving towards a potential energy minimum), but when we find a MD step where the kinetic energy is smaller than the previous one; then potential energy has increased, that means that we have passed through a potential energy minimum. If we don't do anything, the system will go by, or at best, it will begin to oscillate

around the energy minimum. In order to avoid that, a *quenching* is done, that means that all atomic positions are frozen. In the following MD step, we allow the atoms to move, and the kinetic energy begin to increase again, when it begins to decrease, we freeze the atoms again, and then allow to move again, and then freeze, and so on. When the forces (and the difference of potential energy between one step and the previous one) are lower than a tolerance value, we consider that the system is relaxed.

There is a more sophisticated variant of dynamical quenching. It consist on comparing the sign of the components of the velocity of each atom ($v_{i,x}$, $v_{i,y}$, $v_{i,z}$) and the analog components of the forces ($F_{i,x}$, $F_{i,y}$, $F_{i,z}$). If they are different, the component of this atom is frozen (that means that the velocity component is set to zero). By this way, we gain specificity. Instead of frozen all atoms at a time, we can freeze only the velocity atom components that are moving each atom away from the energy minimum.

Conjugate Gradients

This method is not so based on physical arguments, but in functional analysis of several variables. We should consider the energy E as a function of several variables (that can be treated as a vector \mathbf{X}) $E = E(\mathbf{X})$. In our case, the variables will be the atomic positions ($\mathbf{X} = \{\mathbf{R}_\alpha\}$). If we want to reach a minimum, we want to go through the fastest direction (i. e. the direction where the function varies more quickly). This direction is given by the gradient. If the initial positions of the system are given by $\mathbf{X} = \mathbf{X}_1$ then:

$$\mathbf{g}_1 = - \left(\frac{\partial E}{\partial \mathbf{X}} \right)_{\mathbf{X}=\mathbf{X}_1} = \{\mathbf{F}_\alpha\} \quad (2.44)$$

So, the gradient can be calculated using the forces given by FIREBALL. The subindex 1 means that is the first iteration. Now that we know the direction we want to move, we want to find the minimum along this direction. The equation of the line along this direction is:

$$\mathbf{X}_2 = \mathbf{X}_1 + b_1 \mathbf{g}_1 \quad (2.45)$$

Calculating the energy for several values of \mathbf{X}_2 (b_1) we can interpolate the minimum position.

Now that we have \mathbf{X}_2 , we can calculate the gradient \mathbf{g}_2 and find the minimum of $\mathbf{X}_3 = \mathbf{X}_2 + b_2 \mathbf{g}_2$ and get \mathbf{X}_3 , \mathbf{g}_3 and continue until we get the minimum of our system.

The problem of this method is that each line is orthogonal to the line of the previous step, so we will need a lot of steps to find the minimum. We can use *conjugate* gradients. In this case the new direction is not orthogonal to the previous one, but a direction given by a linear combination of the old and new gradient. This way there will not be sudden changes of direction, and each step will have some

‘memory’ of the previous steps. A more in depth discussion of conjugate gradients can be found on [48, 49].

This technique has the advantage of being really fast to relax the system. However, it has two handicaps. The first one is that, by construction, it will find the *local* minimum of our system closer to the original atomic positions, even if a more deeper minimum (or even the absolute one) is also close to the original atomic positions. However, the dynamical quenching explores better the phase space of the system and is able to find deeper minima.

The other problem is that due to the inherent approximations in FIREBALL, the minimum of the forces and of the energy sometimes does not coincide (but the difference is very small for the systems studied in this work). So sometimes, the gradient of the energy does not point to the energy minimum, and the program can go crazy because internal checks of the code. That is the reason why, we have used dynamical quenching in this thesis.

2.5 LCAO-OO Method

The Linear Combination of Atomic Orbitals - Orbital Occupancies (LCAO-OO) method is a variation of DFT based on second quantization Hubbard-like hamiltonians (see appendix A, B and [50]) that relies on the orbital occupancies $n_{i\sigma}$ instead of the charge density [51–53]. It is extensively analyzed in [52], including the proof of Hohenberg–Kohn theorem in terms of orbital occupancies. It combines the simplicity of DFT-like techniques with the power of a second quantized hamiltonian. By this way, sophisticated exchange-correlation functionals, or many-body calculations can be made in a intuitive way.

Equation 2.2 can be written in second quantization and atomic units as:

$$\hat{H} = \sum_{i\sigma} (\varepsilon_{i\sigma} + V_{ii}^{psp}) \hat{n}_{i\sigma} + \sum_{i,j \neq i,\sigma} (t_{ij} + V_{ij}^{psp}) \hat{c}_{i\sigma}^\dagger \hat{c}_{j\sigma} + \sum_{ijkl,\sigma\sigma'} O_{lk}^{ij} \hat{c}_{i\sigma}^\dagger \hat{c}_{j\sigma'}^\dagger \hat{c}_{k\sigma'} \hat{c}_{l\sigma} \quad (2.46)$$

where V_{ij}^{psp} is the pseudopotential of the core electrons and the nuclei and:

$$\begin{aligned} \varepsilon_i &= \int d^3\mathbf{r} \phi_i^*(\mathbf{r}) \left(-\frac{1}{2} \nabla^2 + \sum_{\alpha} \frac{Z_{\alpha}}{|\mathbf{R}_{\alpha} - \mathbf{r}|} \right) \phi_i(\mathbf{r}) \\ t_{ij} &= \int d^3\mathbf{r} \phi_i^*(\mathbf{r}) \left(-\frac{1}{2} \nabla^2 + \sum_{\alpha} \frac{Z_{\alpha}}{|\mathbf{R}_{\alpha} - \mathbf{r}|} \right) \phi_j(\mathbf{r}) \\ O_{lk}^{ij} &= \int d^3\mathbf{r} d^3\mathbf{r}' \phi_i^*(\mathbf{r}) \phi_j^*(\mathbf{r}') \frac{1}{|\mathbf{r} - \mathbf{r}'|} \phi_k(\mathbf{r}') \phi_l(\mathbf{r}) \end{aligned} \quad (2.47)$$

This is the complete many-body hamiltonian of the system. The first two parts correspond to one-electron terms while the last one contains the many-body terms of

the system. We can rewrite the hamiltonian in a more physically meaningful manner, and retain only important terms. The hamiltonian is written now as:

$$\begin{aligned}
\hat{H} = & \sum_{i\alpha\sigma} (\varepsilon_{i\alpha\sigma} + V_{i\alpha,i\alpha}^{psp}) \hat{n}_{i\alpha\sigma} + \sum_{\substack{i\alpha\sigma,i\beta \\ i\alpha \neq i\beta}} (t_{i\alpha,j\beta} + V_{i\alpha,j\beta}^{psp}) \hat{c}_{i\alpha\sigma}^\dagger \hat{c}_{j\beta\sigma} + \\
& + \frac{1}{2} \sum_{\substack{i\alpha\sigma,i\beta\sigma' \\ i\alpha\sigma \neq i\beta\sigma'}} U_{i\alpha,i\beta} \hat{n}_{i\alpha\sigma} \hat{n}_{i\beta\sigma'} - \frac{1}{2} \sum_{\substack{i\alpha\sigma,i\beta \\ i\alpha \neq i\beta}} U_{i\alpha,i\beta}^x \hat{n}_{i\alpha\sigma} \hat{n}_{i\beta\sigma} + \\
& + \frac{1}{2} \sum_{\substack{i\alpha\sigma,j\beta\sigma' \\ i \neq j}} J_{i\alpha,j\beta} \hat{n}_{i\alpha\sigma} \hat{n}_{j\beta\sigma'} - \frac{1}{2} \sum_{\substack{i\alpha\sigma,j\beta \\ i \neq j}} J_{i\alpha,j\beta}^x \hat{n}_{i\alpha\sigma} \hat{n}_{j\beta\sigma} \\
& + \sum_{\substack{i\alpha\sigma,j\beta,k\gamma\sigma' \\ i\alpha \neq j\beta \\ k\gamma\sigma' \neq i\alpha\sigma,j\beta\sigma}} h_{k\gamma,i\alpha j\beta} \hat{n}_{k\gamma\sigma'} \hat{c}_{i\alpha\sigma}^\dagger \hat{c}_{j\beta\sigma} - \sum_{\substack{i\alpha\sigma,j\beta,k\gamma \\ i\alpha \neq j\beta \\ k\gamma \neq i\alpha,j\beta}} h_{k\gamma,i\alpha j\beta}^x \hat{n}_{k\gamma\sigma} \hat{c}_{i\alpha\sigma}^\dagger \hat{c}_{j\beta\sigma} \\
& + \frac{1}{2} \sum_{\substack{i\alpha\sigma,j\beta\sigma \\ k\gamma\sigma'l\delta\sigma' \\ \text{all different}}} O_{l\gamma,k\delta}^{i\alpha,j\beta} \hat{c}_{i\alpha\sigma}^\dagger \hat{c}_{j\beta\sigma'}^\dagger \hat{c}_{k\gamma\sigma'} \hat{c}_{l\delta\sigma}
\end{aligned} \tag{2.48}$$

where the Latin indexes run in all the atoms of the system, and the Greek ones in the orbitals of each atom, and

$$\begin{aligned}
U_{i\alpha,i\beta} &= \int d^3\mathbf{r} d^3\mathbf{r}' |\phi_{i\alpha}(\mathbf{r})|^2 \frac{1}{|\mathbf{r}-\mathbf{r}'|} |\phi_{i\beta}(\mathbf{r}')|^2 \\
U_{i\alpha,i\beta}^x &= \int d^3\mathbf{r} d^3\mathbf{r}' \phi_{i\alpha}^*(\mathbf{r}) \phi_{i\beta}^*(\mathbf{r}') \frac{1}{|\mathbf{r}-\mathbf{r}'|} \phi_{i\alpha}(\mathbf{r}') \phi_{i\beta}(\mathbf{r}) \\
J_{i\alpha,j\beta} &= \int d^3\mathbf{r} d^3\mathbf{r}' |\phi_{i\alpha}(\mathbf{r})|^2 \frac{1}{|\mathbf{r}-\mathbf{r}'|} |\phi_{j\beta}(\mathbf{r}')|^2 \\
J_{i\alpha,j\beta}^x &= \int d^3\mathbf{r} d^3\mathbf{r}' \phi_{i\alpha}^*(\mathbf{r}) \phi_{j\beta}^*(\mathbf{r}') \frac{1}{|\mathbf{r}-\mathbf{r}'|} \phi_{i\alpha}(\mathbf{r}') \phi_{j\beta}(\mathbf{r}) \\
h_{k\gamma,i\alpha j\beta} &= \int d^3\mathbf{r} d^3\mathbf{r}' |\phi_{k\gamma}(\mathbf{r})|^2 \frac{1}{|\mathbf{r}-\mathbf{r}'|} \phi_{i\alpha}^*(\mathbf{r}') \phi_{j\beta}(\mathbf{r}') \\
h_{k\gamma,i\alpha j\beta}^x &= \int d^3\mathbf{r} d^3\mathbf{r}' \phi_{k\gamma}^*(\mathbf{r}) \phi_{i\alpha}^*(\mathbf{r}') \frac{1}{|\mathbf{r}-\mathbf{r}'|} \phi_{j\beta}(\mathbf{r}') \phi_{k\gamma}(\mathbf{r})
\end{aligned} \tag{2.49}$$

Despite of the formidable form of this hamiltonian, we can give an easy physical interpretation to all of this terms, taking into account the form of the integrals in (2.49). $J_{i\alpha,j\beta}$ ($U_{i\alpha,i\beta}$) is just the electrostatic interaction of the charge cloud in orbital α of atom i with the cloud in orbital β of atom j (i). Note that $U_{i\alpha,i\alpha}$ is the interaction of two electrons in the same orbital with spin up and down (that is usually not well considered in DFT). The term $h_{k\gamma,i\alpha j\beta}$ takes into account how the hopping between $i\alpha$ and $j\beta$ varies due to the interaction with an electron placed in $k\gamma$. Finally, the last

$O_{l\gamma,k\delta}^{i\alpha,j\beta}$ term takes into account the effect on the hopping between $i\alpha\sigma$ and $l\delta\sigma$ due to a transition of an electron going from $k\gamma\sigma'$ to $j\beta\sigma'$

For further discussion we are going to ignore terms of order greater than two ($h_{k\gamma,i\alpha j\beta}^{(x)}$, $O_{l\gamma,k\delta}^{i\alpha,j\beta}$) and the exchange terms ($U_{i\alpha,i\beta}^x$, $J_{i\alpha,j\beta}^x$), since they are not critical neither for theoretical nor for numerical reasons. This way we will be able to see the main physics of this model avoiding large formulas that obscure what we are really doing. For calculations taking into account all the terms see [52, 54].

2.5.1 Local Density LCAO-OO

We can make a local density (LD) approach to our LCAO-OO hamiltonian. We only need to write the energy of the system in terms of the occupation numbers $n_{i\alpha\sigma}$: $E = E[\{n_{i\alpha\sigma}\}]$. We can split this functional in one-electron and many body terms $E = E[\{n_{i\alpha\sigma}\}] = E^{OE}[\{n_{i\alpha\sigma}\}] + E^{MB}[\{n_{i\alpha\sigma}\}]$. Then, using a variation of the Kohn–Sham theorem [51, 52, 55] we can introduce the following effective hamiltonian.

$$\hat{H}^{eff} = \sum_{i\alpha\sigma} (\varepsilon_{i\alpha\sigma} + V_{i\alpha,i\alpha}^{psp} + V_{i\alpha\sigma}^{MB}) \hat{n}_{i\alpha\sigma} + \sum_{i\alpha,j\beta \neq i\alpha\sigma} (t_{i\alpha,j\beta} + V_{i\alpha,j\beta}^{psp}) \hat{c}_{i\alpha\sigma}^\dagger \hat{c}_{j\beta\sigma} \quad (2.50)$$

where

$$V_{i\alpha\sigma}^{MB} = \frac{\partial E^{MB}[\{n_{i\alpha\sigma}\}]}{\partial n_{i\alpha\sigma}} \quad (2.51)$$

Hartree and Exchange Functionals

The problem now is to find a many-body energy functional that depends on orbital occupancies $E^{MB}[\{n_{i\alpha\sigma}\}]$ instead of charge density. The case of the Hartree term can be easily derived just noting that the charge density can be written in function of occupation numbers $\rho(\mathbf{r}) = \sum_{i\alpha\sigma,j\beta\sigma} n_{i\alpha\sigma,j\beta\sigma} \phi_{i\alpha}^*(\mathbf{r}) \phi_{j\beta}(\mathbf{r})$, where $n_{i\alpha\sigma,j\beta\sigma} = \langle \hat{c}_{i\alpha\sigma}^\dagger \hat{c}_{j\beta\sigma} \rangle$, and that the Hartree energy is given by:

$$E_H = \frac{1}{2} \int d^3\mathbf{r} d^3\mathbf{r}' \frac{\rho(\mathbf{r})\rho(\mathbf{r}')}{|\mathbf{r} - \mathbf{r}'|} \quad (2.52)$$

Introducing the density in terms of the occupation numbers we get:

$$\begin{aligned}
E_H &= \frac{1}{2} \sum_{\substack{i\alpha\sigma, j\beta \\ k\gamma\sigma', l\delta\sigma'}} O_{k\gamma, l\delta}^{i\alpha, j\beta} n_{i\alpha\sigma, j\beta\sigma} n_{k\gamma\sigma', l\delta\sigma'} \simeq \frac{1}{2} \sum_{\substack{i\alpha\sigma, i\beta\sigma' \\ i\alpha\sigma \neq i\beta\sigma'}} U_{i\alpha, i\beta} n_{i\alpha\sigma} n_{i\beta\sigma'} \\
&+ \frac{1}{2} \sum_{\substack{i\alpha\sigma, j\beta, \sigma' \\ i \neq j}} J_{i\alpha, j\beta} n_{i\alpha\sigma} n_{j\beta\sigma'} \quad (2.53)
\end{aligned}$$

and the exchange energy can be written as²

$$\begin{aligned}
E_X &= -\frac{1}{2} \sum_{\substack{i\alpha\sigma, j\beta \\ k\gamma\sigma, l\delta}} O_{k\gamma, l\delta}^{i\alpha, j\beta} n_{i\alpha\sigma, l\delta\sigma} n_{k\gamma\sigma, j\beta\sigma} \simeq -\frac{1}{2} \sum_{\substack{i\alpha\sigma, i\beta \\ \alpha \neq \beta}} U_{i\alpha, i\beta} n_{i\alpha\sigma, i\beta\sigma} n_{i\beta\sigma, i\alpha\sigma} \\
&- \frac{1}{2} \sum_{\substack{i\alpha\sigma, j\beta \\ i \neq j}} J_{i\alpha, j\beta} n_{i\alpha\sigma, j\beta\sigma} n_{j\beta\sigma, i\alpha\sigma} \quad (2.54)
\end{aligned}$$

we need to note here that this is the *exact* exchange (considering $U_{i\alpha, i\beta}^x = J_{i\alpha, j\beta}^x = h_{k\gamma, i\alpha j\beta}^x = h_{k\gamma, i\alpha j\beta}^x = 0$), not the LD exchange approximation (the functional (2.54) does not depend on $\{n_{i\alpha\sigma}\}$ but on $\{n_{i\alpha\sigma, j\beta\sigma}\}$). In order to get a LD-like exchange approximation we use the following sum rule:

$$\begin{aligned}
\sum_{j\beta} n_{i\alpha\sigma, j\beta\sigma} n_{j\beta\sigma, i\alpha\sigma} &= n_{i\alpha\sigma} \\
\sum_{j\beta \neq i\alpha} n_{i\alpha\sigma, j\beta\sigma} n_{j\beta\sigma, i\alpha\sigma} &= n_{i\alpha\sigma} (1 - n_{i\alpha\sigma}) \quad (2.55)
\end{aligned}$$

Using the sum rule (2.55) we can write the exchange energy as:

$$E_X[\{n_{i\alpha\sigma}\}] = -\frac{1}{2} \sum_{i\alpha\sigma} J_{i\alpha\sigma}^{eff} n_{i\alpha\sigma} (1 - n_{i\alpha\sigma}) \quad (2.56)$$

where the effective interaction $J_{i\alpha\sigma}^{eff}$ can be calculated as:

$$J_{i\alpha\sigma}^{eff} = \frac{\sum_{j\beta} J_{i\alpha, j\beta} |n_{i\alpha\sigma, j\beta\sigma}|^2 + \sum_{\beta \neq \alpha} U_{i\alpha, i\beta} |n_{i\alpha\sigma, i\beta\sigma}|^2}{\sum_{j\beta} |n_{i\alpha\sigma, j\beta\sigma}|^2 + \sum_{\beta \neq \alpha} |n_{i\alpha\sigma, i\beta\sigma}|^2} \quad (2.57)$$

The physical meaning of this equation is very simple: is just the interaction between the electron density at site i $n_{i\alpha\sigma}$, and its exchange hole $(1 - n_{i\alpha\sigma})$ (see the discussion about quasiparticles in Sect. 2.3.1 for the physical origin of this hole).

This form of the exchange energy depends explicitly on the occupation numbers, and can be used as an LD exchange energy. Later in this text (see Sect. 2.7.3) we

² See, for example, [56], Sect. 4.7.

discuss how to use this result to create local orbital hybrid functionals within the FIREBALL code.

Correlation Functional

We can assume correlation effects modify the exchange hole in such a way that it is not localized outside the orbital $i\alpha\sigma$, but a fraction $f_{i\alpha\sigma}$ ($0 < f_{i\alpha\sigma} < 1$) of the hole is transferred back to the site $i\alpha\sigma$. This $f_{i\alpha\sigma}$ is related to the fact that Hartree-Fock approximation (exact exchange and no correlation) does not take into account the screening of the potential (see Sect. 2.3.1). Correlation energy can thus be written as:

$$E_C = -\frac{1}{2} \sum_{i\alpha\sigma} f_{i\alpha\sigma} (U_{i\alpha,i\alpha} - J_{i\alpha\sigma}^{eff}) n_{i\alpha\sigma} (1 - n_{i\alpha\sigma}) \quad (2.58)$$

so the exchange-correlation functional reads as:

$$E_{XC}[\{n_{i\alpha\sigma}\}] = -\frac{1}{2} \sum_{i\alpha\sigma} f_{i\alpha\sigma} U_{i\alpha,i\alpha} n_{i\alpha\sigma} (1 - n_{i\alpha\sigma}) - \sum_{i\alpha\sigma} (1 - f_{i\alpha\sigma}) J_{i\alpha\sigma}^{eff} n_{i\alpha\sigma} (1 - n_{i\alpha\sigma}) \quad (2.59)$$

We have now all the terms of the many-body functional, and can write the effective hamiltonian (2.50) as:

$$\hat{H}^{eff} = \sum_{i\alpha\sigma} (\varepsilon_{i\alpha\sigma} + V_{i\alpha,i\alpha}^{psp} + V_{i\alpha\sigma}^H + V_{i\alpha\sigma}^{xc}) \hat{n}_{i\alpha\sigma} + \sum_{\substack{i\alpha,j\beta \\ \sigma}} (t_{i\alpha,j\beta} + V_{i\alpha,j\beta}^{psp}) \hat{c}_{i\alpha\sigma}^\dagger \hat{c}_{j\beta\sigma} \quad (2.60)$$

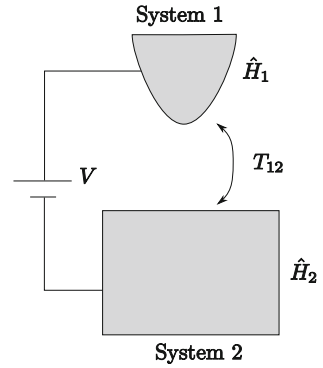
where

$$\begin{aligned} V_{i\alpha\sigma}^H &= \frac{\partial E_H[\{n_{i\alpha\sigma}\}]}{\partial n_{i\alpha\sigma}} \\ V_{i\alpha\sigma}^{XC} &= \frac{\partial E_{XC}[\{n_{i\alpha\sigma}\}]}{\partial n_{i\alpha\sigma}} \end{aligned} \quad (2.61)$$

and the ground state energy:

$$\begin{aligned} E &= \sum_n^{occupied} \varepsilon_n + E_H[\{n_{i\alpha\sigma}\}] + E_{xc}[\{n_{i\alpha\sigma}\}] - \sum_{i\alpha\sigma} (V_{i\alpha\sigma}^H + V_{i\alpha\sigma}^{xc}) \hat{n}_{i\alpha\sigma} \\ &= \sum_n^{occupied} \varepsilon_n - E_H[\{n_{i\alpha\sigma}\}] + E_{xc}[\{n_{i\alpha\sigma}\}] - \sum_{i\alpha\sigma} V_{i\alpha\sigma}^{xc} \hat{n}_{i\alpha\sigma} \end{aligned} \quad (2.62)$$

Fig. 2.3 Scheme of a system partitioned in order to calculate the electrical conductance from 1 to 2



2.6 Calculation of Transport Properties

In this thesis we have analyzed the transport properties of molecular electronic devices at the nanoscale (see Sect. 4.3). A brief introduction to the theory used to calculate these properties will be given in this section.

2.6.1 Current Equation

From a theoretical point of view, let's start with a system that can be divided in two interacting subsystems like the one shown in Fig. 2.3 (this can be the case of an STM, where the tip and sample are the respective subsystems). The Hamiltonian can be written in second quantization as:

$$\hat{H} = \hat{H}_1 + \hat{H}_2 + \hat{H}_{1,2} \quad (2.63)$$

where

$$\begin{aligned} \hat{H}_1 &= \sum_{ij} \varepsilon_i \hat{n}_i + t_{ij} (\hat{c}_i^\dagger \hat{c}_j + \hat{c}_j^\dagger \hat{c}_i) \\ \hat{H}_2 &= \sum_{\alpha\beta} \varepsilon_\alpha \hat{n}_\alpha + t_{\alpha\beta} (\hat{c}_\alpha^\dagger \hat{c}_\beta + \hat{c}_\beta^\dagger \hat{c}_\alpha) \\ \hat{H}_{1,2} &= \sum_{i\alpha} t_{i\alpha} (\hat{c}_i^\dagger \hat{c}_\alpha + \hat{c}_j^\dagger \hat{c}_\alpha) \end{aligned} \quad (2.64)$$

(Latin indexes run over the orbitals in system 1 and Greek ones over orbitals in system 2).

Now consider that we apply an external potential V to one of the electrodes. Now an irreversible current will flow from one system to the other. In order to calculate the

current through the system we will need non-equilibrium techniques. We are going to use Keldysh formalism, that is explained in appendix Sect. A.2.4, to get the current through the system. The interaction hamiltonian $\widehat{H}_{1,2}$ will be treated as a perturbation of $\widehat{H}_0 = \widehat{H}_1 + \widehat{H}_2$ + external potential. One may think that is more “physical” to consider the perturbation as the external potential, but calculations from this point of view will be more complex, and no current will flow neither there is not external potential nor interaction between subsystems.

When we add the perturbation $\widehat{H}_{1,2}$, we can calculate the current that appears using the Keldysh formalism. First of all, we are going to deduce the form of the current operator \widehat{J} in second quantization. A good guess is that it will be proportional to a product of an operator that creates one electron in subsystem 2 and annihilates it on subsystem 1, that is $\widehat{J}_{\alpha i} \propto \widehat{c}_\alpha^\dagger \widehat{c}_i$. We need to consider inverse current from subsystem 2 to 1, so the form of the current operator in second quantization will be:

$$\widehat{J}_{\alpha i} = \lim_{\tau \rightarrow 0} A_{\alpha i} \widehat{c}_\alpha^\dagger(t + \tau) \widehat{c}_i(t) - A_{i\alpha} \widehat{c}_i^\dagger(t + \tau) \widehat{c}_\alpha(t) \quad (2.65)$$

In order to know the value of $A_{i\alpha}$ we will use the continuity equation:

$$\frac{\partial \widehat{\rho}_{ii}}{\partial t} = \sum_{\alpha} \widehat{J}_{\alpha i}; \quad \text{where} \quad \widehat{\rho}_{ii} = \widehat{c}_i^\dagger(t) \widehat{c}_i(t) = \lim_{\tau \rightarrow 0} \widehat{c}_i^\dagger(t + \tau) \widehat{c}_i(t) \quad (2.66)$$

on the other hand, making use of the equation of motion of the operator $\widehat{\rho}_{ii}$ (Eq. A.10) we can find that:

$$\frac{\partial \widehat{\rho}_{ii}}{\partial t} = -i/\hbar [\widehat{\rho}_{ii}, \widehat{H}] = \lim_{\tau \rightarrow 0} \sum_{\alpha} -i/\hbar (t_{\alpha i} \widehat{c}_\alpha^\dagger(t + \tau) \widehat{c}_i(t) - t_{i\alpha} \widehat{c}_i^\dagger(t + \tau) \widehat{c}_\alpha(t)) \quad (2.67)$$

So comparing equations (2.65) and (2.67), we deduce that $A_{\alpha i} = -it_{\alpha i}/\hbar$. Now, in order to know the value of the current from system 1 to system 2 at the ground (non-equilibrium) perturbed state $|\Psi_{0,H}\rangle$ we need to calculate the following sandwich:

$$\begin{aligned} I(t) &= e \sum_{i\alpha} \langle \Psi_{0,H} | \widehat{J}_{\alpha i} | \Psi_{0,H} \rangle \\ &= e \lim_{\tau \rightarrow 0} \sum_{i\alpha} -i/\hbar (t_{\alpha i} \langle \Psi_{0,H} | \widehat{c}_\alpha^\dagger(t + \tau) \widehat{c}_i(t) | \Psi_{0,H} \rangle - t_{i\alpha} \langle \Psi_{0,H} | \widehat{c}_i^\dagger(t + \tau) \widehat{c}_\alpha(t) | \Psi_{0,H} \rangle) \\ &= e \lim_{\tau \rightarrow 0} \sum_{i\alpha} t_{\alpha i} G^{+-}(i, t + \tau, \alpha, t) - t_{i\alpha} G^{+-}(\alpha, t + \tau, i, t) \\ &= e \lim_{\tau \rightarrow 0} \text{Tr}[\mathbb{T}_{21} \mathbb{G}_{12}^{+-}(t + \tau, t) - \mathbb{G}_{21}^{+-}(t + \tau, t) \mathbb{T}_{12}] \end{aligned} \quad (2.68)$$

where we have used the matrix form of the Green-Keldysh function (see Appendix A.2.4).

2.6.2 Stationary Current

Usually we are interested in the stationary regime. In that case, G^{+-} only depends on time difference τ so we can work with the Fourier transform:

$$\lim_{\tau \rightarrow 0} G^{+-}(i, \alpha, \tau) = \frac{1}{h} \lim_{\tau \rightarrow 0} \int_{-\infty}^{\infty} dE G^{+-}(i, \alpha, E) e^{iE\tau/\hbar} = \frac{1}{h} \int_{-\infty}^{\infty} G^{+-}(i, \alpha, E) dE \quad (2.69)$$

If we rewrite (2.68) in the energy space, and we consider that there is no spin dependence on the hamiltonian we can just add a factor 2 and we get [57]:

$$I = \frac{2e}{h} \int_{-\infty}^{\infty} dE \text{Tr}[\mathbb{T}_{21} \mathbb{G}_{12}^{+-}(E) - \mathbb{G}_{21}^{+-}(E) \mathbb{T}_{12}] \quad (2.70)$$

In our case, we are interested in rewrite (2.70) as a function of the unperturbed green functions of the subsystems ($G_{1,2}^0$). Using Dyson equation (A.48) it can be done easily getting [58, 59]:

$$I = \frac{4\pi e^2}{h} \int_{-\infty}^{\infty} dE \text{Tr}[\rho_{22}(E) \mathbb{D}'_{22}(E) \mathbb{T}_{21} \rho_{11}(E - eV) \mathbb{D}^a_{11}(E - eV) \mathbb{T}_{12}] (f_1(E - eV) - f_2(E)) \quad (2.71)$$

where

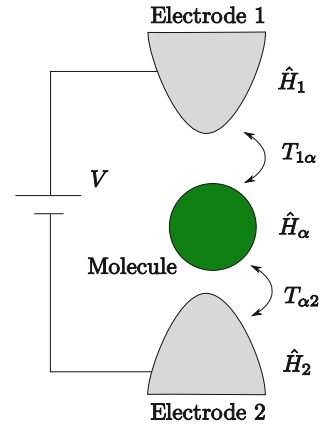
$$\begin{aligned} \rho_{22}(E) &= -\frac{1}{\pi} \text{Im}[\mathbb{G}_{22}^{0,r}(E)], \quad \rho_{11}(E - eV) = -\frac{1}{\pi} \text{Im}[\mathbb{G}_{11}^{0,r}(E - eV)] \\ \mathbb{D}^a_{11}(E - eV) &= [\mathbb{I} - \mathbb{T}_{12} \mathbb{G}_{22}^{0,a}(E) \mathbb{T}_{21} \mathbb{G}_{11}^{0,a}(E - eV)]^{-1} \\ \mathbb{D}'_{22}(E) &= [\mathbb{I} - \mathbb{T}_{21} \mathbb{G}_{11}^{0,r}(E - eV) \mathbb{T}_{12} \mathbb{G}_{22}^{0,r}(E)]^{-1} \\ f_1(E - eV) &= 1 / \left(\exp\left(\frac{E - eV}{k_B T}\right) + 1 \right), \quad f_2(E) = 1 / \left(\exp\left(\frac{E}{k_B T}\right) + 1 \right) \end{aligned} \quad (2.72)$$

We remember here that the voltage was included in the unperturbed subsystems; as it is shown explicitly in (2.71).

The denominators $\mathbb{D}'_{22}(E)$ and $\mathbb{D}^a_{11}(E - eV)$ can be seen as renormalizers of the hopping matrices: $\mathbb{T}'_{12} = \mathbb{D}^a_{11}(E - eV) \mathbb{T}_{12}$, and they take into account the backscattering that tends to saturate the current. This interpretation is clear if we make the series expansion of the denominator:

$$\mathbb{T}'_{12} = \mathbb{D}^a_{11} \mathbb{T}_{12} = \mathbb{T}_{12} + \mathbb{T}_{12} \mathbb{G}_{22}^a \mathbb{T}_{21} \mathbb{G}_{11}^a \mathbb{T}_{12} + \dots \quad (2.73)$$

Fig. 2.4 Scheme of a system divided in three parts in order to calculate the electrical conductance from 1 to 2 (Color figure online)



However, in this work we are interested on differential conductance $g = dI/dV$, in particular when $V \rightarrow 0$. We will consider the electronic temperature as zero (that is a good approximation in metals at room temperature). Using (2.71) we get for that particular case.

$$g = \left(\frac{dI}{dV} \right)_{V \rightarrow 0} = \frac{4\pi e^2}{\hbar} \text{Tr}[\rho_{22}(E_F) \mathbb{T}'_{21} \rho_{11}(E_F) \mathbb{T}'_{12}] \quad (2.74)$$

This conductance can be interpreted as a coherent sum of conductance channels. The analogy with Landauer formalism, based on conductance channels [60] is clear if we write (2.74) in the form

$$g = \frac{4\pi e^2}{\hbar} \text{Tr}[\mathbb{t} \mathbb{t}^\dagger] \quad (2.75)$$

where $\mathbb{t} = 2\pi \rho_{11}^{1/2}(E_F) \mathbb{T}'_{12} \rho_{22}^{1/2}(E_F)$ is the transmission matrix of the system. In order to know the character of different channel and the contribution of orbitals to that channel we can just diagonalize $\mathbb{t} \mathbb{t}^\dagger$.

2.6.3 Conductance with Two Electrodes

However, for some systems (like a C_{60} molecule between two gold tips, studied in Sect. 4.3), it is more natural to divide the system in three subsystems instead of only two. This option, that was not available in the standard conductance module of FIREBALL has been implemented during this thesis. In Fig. 2.4 we can see the division of such that system.

In that case we can use previous results, if we consider the system $(\alpha + 2)$ as the previous system 2. In order to do that, we need first to calculate ρ and \mathbb{G} of the $(\alpha + 2)$ system. The density of states (DOS) is [20]:

$$\rho_{\alpha\alpha}^0 = \mathbb{G}_{\alpha\alpha}^{r,0} \mathbb{T}_{\alpha 2} \rho_{22}^0 \mathbb{T}_{2\alpha} \mathbb{G}_{\alpha\alpha}^{a,0} \quad (2.76)$$

with (2.76) and (2.74) and taking into account that $\mathbb{T}'_{12} = [\mathbb{I} - \mathbb{T}_{12} \mathbb{G}_{22}^{0,a} \mathbb{T}_{21} \mathbb{G}_{11}^{0,a}]^{-1} \times \mathbb{T}_{12} = \mathbb{T}_{12} [\mathbb{I} - \mathbb{G}_{22}^{0,a} \mathbb{T}_{21} \mathbb{G}_{11}^{0,a} \mathbb{T}_{12}]^{-1}$ we get:

$$g = \frac{4\pi e^2}{\hbar} \text{Tr}[\mathbb{T}_{\alpha 1} \rho_{11}^0 \mathbb{T}_{1\alpha} [\mathbb{I} - \mathbb{G}_{\alpha\alpha}^{r,0} \mathbb{T}_{\alpha 1} \mathbb{G}_{11}^{r,0} \mathbb{T}_{1\alpha}]^{-1} \rho_{\alpha\alpha}^0 [\mathbb{I} - \mathbb{T}_{\alpha 1} \mathbb{G}_{11}^{a,0} \mathbb{T}_{1\alpha} \mathbb{G}_{\alpha\alpha}^{a,0}]^{-1}] \quad (2.77)$$

and realizing that

$$\mathbb{G}_{\alpha\alpha}^r = [\mathbb{I} - \mathbb{G}_{\alpha\alpha}^{r,0} \mathbb{T}_{\alpha 1} \mathbb{G}_{11}^{r,0} \mathbb{T}_{1\alpha}]^{-1} \mathbb{G}_{\alpha\alpha}^{r,0} = [(\mathbb{G}_{\alpha\alpha}^{r,0})^{-1} - \mathbb{T}_{\alpha 1} \mathbb{G}_{11}^{r,0} \mathbb{T}_{1\alpha}]^{-1} \quad (2.78)$$

we can rewrite (2.77) as:

$$g = \frac{4\pi e^2}{\hbar} \text{Tr}[\mathbb{T}_{\alpha 1} \rho_{11}^0 \mathbb{T}_{1\alpha} \mathbb{G}_{\alpha\alpha}^r \mathbb{T}_{\alpha 2} \rho_{22}^0 \mathbb{T}_{2\alpha} \mathbb{G}_{\alpha\alpha}^a] \quad (2.79)$$

Let's see the physics of this equation. First of all, if we define $\Sigma_{\alpha\alpha}^{(i)} = \mathbb{T}_{\alpha i} \rho_{ii}^0 \mathbb{T}_{i\alpha}$ we get:

$$g = \frac{4\pi e^2}{\hbar} \text{Tr}[\Sigma_{\alpha\alpha}^{(1)} \mathbb{G}_{\alpha\alpha}^r \Sigma_{\alpha\alpha}^{(2)} \mathbb{G}_{\alpha\alpha}^a] \quad (2.80)$$

that is just the Fisher-Lee equation for the electrical conductance [61]. We can also define a effective hopping $\mathbb{T}'_{12} = \mathbb{T}_{1\alpha} \mathbb{G}_{\alpha\alpha}^r \mathbb{T}_{\alpha 2}$, and introduce it in (2.79). Using the cyclic property of the trace we recover (2.74). Finally, we can connect this with the Landauer formalism [60] defining:

$$\mathfrak{t} = 2\pi \rho_{11}^{1/2} \mathbb{T}'_{12} \rho_{22}^{1/2} = 2\pi \rho_{11}^{1/2} \mathbb{T}_{1\alpha} \mathbb{G}_{\alpha\alpha}^r \mathbb{T}_{\alpha 2} \rho_{22}^{1/2} \quad (2.81)$$

We have checked that the conductance does not depend too much on the division of the system (in two or three) as it should be, because the physical conductance should not depend on how we calculate it.

2.7 Corrections of DFT Deficiencies

Although DFT in its LDA and GGA approximation is usually reliable enough for most applications, its well known failures make its application meaningless for some systems unless we correct these problems. Here we have focused in metal/organic

interfaces; so the significant deficiencies of DFT-LDA (and GGA) we have to overcome are the absence of Van der Waals (vdW) interaction in these functionals and the underestimation of the gap (the last one is a failure of DFT itself, because it is only a ground state theory). In this section we are going to describe the techniques developed in this thesis to deal with these deficiencies.

2.7.1 Weak Chemical and Van der Waals Interaction

Here we adapt the discussion about long-range forces in [62] (Copyright 2011 American Institute of Physics).

Weakly interacting systems, such as some metal/organic interfaces like benzene/Au(111) and TTF/Au(111), cannot be characterized accurately in a standard DFT formalism. The reason is that the vdW interaction is nonlocal and long-range, while exchange-correlation functionals in standard DFT methods are (semi)local and short range, with a typical exponential decay (as stated in Sect. 2.3.2). Due to the importance of this interaction (not only for interfaces but also for carbon nanotubes or biological systems, for instance), a lot of effort has been directed in recent years to develop a practical DFT approach that properly takes into account vdW interactions for these systems (see, e.g. references [63–68]).

In order to accurately determine the vdW interaction between two subsystems (the metal and the adsorbed molecules, in our thesis) we have used here an extension of the LCAO- S^2 +vdW formalism, previously developed for noble gases and graphitic materials [69–71]. We consider that the exchange and correlation is correctly taken into account within each subsystem (metal and organic molecule) but the LDA-like exchange and correlation between subsystems is not well considered, so we take it away, and introduce later with a better approximation. That means, in a first step we consider:

$$V_{xc}[\rho_M + \rho_O] = V_{xc}[\rho_M] + V_{xc}[\rho_O] \quad (2.82)$$

where ρ_M and ρ_O are the electron density of the metal and organic molecule respectively. So we define an electron density for each subsystem and approximate the LDA exchange-correlation energy as the sum of the exchange-correlation energies for the different subsystems. This can be done easily within McWEDA scheme.

After that we introduce the exchange correlation between subsystems in a way that takes into account the dispersive forces. In order to reproduce Van der Waals energy we have used the following simple but correct atom-atom form:

$$E_{vdW}(R) = -f_D(R)C_6/R^6 \quad (2.83)$$

where R is the distance between atoms, and the factor $f_D(R)$ eliminates the vdW contribution for short distances [65, 66, 72]. We are going to use two different damping factors common in literature. The first one has the form $f_D(R) = 1 - \exp(-\alpha(R/R_c)^8)$ [65], where R_c is the sum of covalent radii and $\alpha = 7.5 \times 10^{-4}$ is

Table 2.1 LDA and exact gaps for organic molecules studied in this thesis and some inorganic semiconductors

Gap/molecule	Benzene	C ₆₀	TTF	PTCDA	Si	Ge
LDA gap	4.7	1.6	2.6	1.6	0.55	0
Exact	10.39	4.95	6.3	4.7	1.17	0.74

chosen to reproduce the c lattice constant of graphite. The second one has the form $f_D(R) = 1/(1 + \exp(-d(R/R_{vdW}) - 1))$ [66] where $d = 20$ and R_{vdW} is the sum of Van der Waals radii of the elements under consideration [66]. A similar approach although with different radii can be found in [72]. The choice of the damping factor $f_D(R)$ changes less than 0.2 \AA the value of the adsorption distance of molecules [62, 73]. However the adsorption energy is clearly affected (changes of around 100% are found). But as we are interested in electronic structure properties in this thesis (where only distance between both subsystems is important) and as we have used simple basis for our calculations (so adsorption energies are not very reliable), we consider that this method has a good balance between accuracy and computational cost for our needs.

2.7.2 Underestimation of the Gap

The obtention of an accurate semiconductor gap is critical to understand the metal/organic interfaces as will be shown in Chap. 3. As stated before, DFT is unable to give a correct gap, even if we know the exact exchange-correlation functional, because it is a ground state theory. However, in systems where electrons are not strongly correlated, the quasiparticle image is still valid and we can consider that the distance between the eigenvalue of the highest occupied molecular orbital (HOMO) and the eigenvalue of the lowest unoccupied molecular orbital (LUMO) are a first approximation for the real transport gap.

Unfortunately, this approximation is not good even for systems with low correlation. In Table 2.1 we can see the difference between the LDA gaps and the experimental ones. In molecules, the transport gap is considered as the difference between ionization (IE) and affinity (A) energies $E_g^t = IE - A$ for the experimental case and as $E_g = \varepsilon_{LUMO} - \varepsilon_{HOMO}$ for LDA.

Table 2.1 shows that the difference between LDA and experimental gap can be more than 100% (and even predict that some well known semiconductors are metals). The main reason for this underestimation is the fact that this naive approximation does not take into account the SIC, due to the interaction of the new electron (hole) in the LUMO (HOMO) and the pre-existing charge (Fig. 2.5). In the next subsection we present some corrections developed during this thesis. They rely on a parameter (β in hybrid functionals, U in scissor operator) that cannot be calculated in a straightforward manner. Moreover, in metal/organic interfaces there is an additional effect that

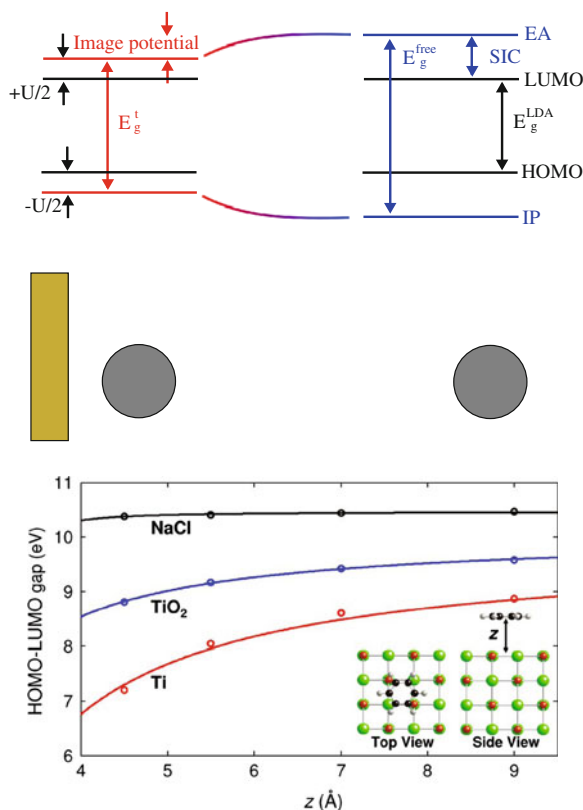


Fig. 2.5 *Up* Scheme of the different effects that determine the actual gap of an organic molecule over a surface. The LDA gap gives an underestimated and surface distance independent gap. At large distances, SIC opens the gap and gives the measured gas phase gap. However, when the molecule approaches to a metallic surface, the effect of the image potential tends to reduce the organic gap. *Down* Dependence of the benzene gap with distance when it is approaching different surfaces. Reprinted from [74] Copyright (2009) by the American Physical Society (Color figure online)

does not appear in bulk semiconductors or gas phase molecules: the image potential. This can be understood classically considering that the introduction of a charge in a molecule over a metal (creating an ion) will have, as a response, an image charge inside the metal in order to get a constant potential in the metal surface, disturbing the molecular spectra (Fig. 2.5). In Chaps. 3 and 4, we will show an easy but reliable way to calculate the gap taking into account these effects, and then getting a value for these unknown parameters (β and U).

2.7.3 Hybrid HF-LDA Functional

In this thesis we have developed and introduced in FIREBALL an hybrid HF-LDA functional (see Sect. 5.6 and [75] for a practical use of it) based on the LCAO-OO approach. Hybrid functionals have been mentioned at the end of Sect. 2.3.2, but here we present a large discussion.

Standard hybrid hamiltonians are based on the adiabatic connection [76, 77]. The derivation of these kind of functionals is based on “turning on” adiabatically the electron-electron interaction. Let’s consider the following many-electron hamiltonian:

$$\widehat{H}_\lambda = \widehat{T} + \widehat{V}_{ext,\lambda} + \lambda \widehat{V}_{ee} \quad (2.84)$$

where $0 \leq \lambda \leq 1$ and $\widehat{V}_{ext,\lambda}$ is an external potential that depends on λ . When $\lambda = 1$ we obtain the physical system, so $\widehat{V}_{ext,1} = \widehat{V}_{ion}$. For every $0 \leq \lambda < 1$, \widehat{H}_λ gives the exact ground state electronic density of the physical system (but not the exact physical wave function). If we denote $|\psi_\lambda\rangle$ as the normalized antisymmetric wavefunction that minimizes the expectation value of $\widehat{T} + \lambda \widehat{V}_{ee}$, the exchange-correlation energy of the physical system is given by:

$$E_{xc}[\rho(\mathbf{r})] = \int_0^1 E_{xc,\lambda}[\rho(\mathbf{r})] d\lambda \text{ where } E_{xc,\lambda}[\rho(\mathbf{r})] = \langle \psi_\lambda | \widehat{V}_{ee} | \psi_\lambda \rangle - E_H[\rho(\mathbf{r})] \quad (2.85)$$

Becke [78] considered that integral (2.85) can be calculated using trapezoidal rule, and he took the following energies for the edge points: The HF exact exchange energy when $\lambda = 0$ and the LDA exchange correlation energy when $\lambda = 1$. So in a first approximation:

$$E_{XC} \simeq \frac{1}{2} E_X^{exact} + \frac{1}{2} E_{XC}^{LDA} \quad (2.86)$$

Better results can be obtained if we consider other values of the fraction of HF exchange and LDA exchange-correlation. By the mean value theorem, there exists a value β that makes the following equation *exact*:

$$E_{XC} = \beta E_X^{exact} + (1 - \beta) E_{XC}^{\lambda=1} \quad (2.87)$$

Our approach, although leads to very similar results is based on a different assumption. In the LCAO-OO method, the local density-like $E_X^{LD}[\{n_{i\alpha\sigma}\}]$ and exact-like $E_X^{HF}[\{n_{i\alpha\sigma}, j\beta\sigma}\}]$ form of the exchange functional are the same, as long as $J_{i\alpha\sigma}^{eff}$ have been calculated using the formula (2.57), so $E_{XC} = \beta E_X^{HF} + (1 - \beta) E_{XC}^{LD}$ is exact for all β . But this is no longer true for the functional derivatives (i.e. potentials), so the exchange potential $V_X = \beta V_X^{HF} + (1 - \beta) V_X^{LD}$ does depend on the value of β . In appendix B is pointed out that the size of the gap depends critically on the exchange potential, so the value of β can be used to determine it.

In our case β has been tuned to obtain $E_g = E_g^{LDA} + U$ where U is calculated following the ideas of Sect. 4.2.1. The exchange-correlation potential is derived using Eqs. (2.54), (2.56) and (2.61). We obtain:

$$\begin{aligned} (V_X^{LD-OO})_{i\alpha\sigma, j\beta\sigma} &= -J_{i\alpha\sigma}^{eff} \left(\frac{1}{2} - n_{i\alpha\sigma} \right) \delta_{i\alpha, j\beta} \\ (V_X^{HF-OO})_{i\alpha\sigma, j\beta\sigma} &= -U_{i\alpha, i\beta} n_{i\alpha\sigma, i\beta\sigma} \delta_{i, j} - J_{i\alpha, j\beta} n_{i\alpha\sigma, j\beta\sigma} \end{aligned} \quad (2.88)$$

Implementation in FIREBALL

The FIREBALL method does not calculate exchange and correlation using LCAO-OO but using McWEDA, that is an approximation to the LDA exchange and correlation. So in order to take the LDA exchange away we have just subtracted to V_{XC}^{McWEDA} the V_X^{LD-OO} part (Eq. 2.88). Then we add V_X^{HF-OO} , so the exchange-correlation matrix elements are:

$$(V_{XC}^{hybrid})_{i\alpha\sigma, j\beta\sigma} = (V_{XC}^{McWEDA})_{i\alpha\sigma, j\beta\sigma} - \beta (V_X^{LD-OO})_{i\alpha\sigma, j\beta\sigma} + \beta (V_X^{HF-OO})_{i\alpha\sigma, j\beta\sigma} \quad (2.89)$$

The values of $U_{i\alpha, i\beta}$ and $J_{i\alpha, j\beta}$ have been calculated using the program *gcluster* [52].

Molecule Interacting with a Metal

The Hartree-Fock approximation does not usually work properly on metals, so in the case of a molecule interacting with a metal, the former will be treated via hybrid functional, while the latter via standard DFT (that means that the matrix elements $V_{i\alpha, j\beta}^{XC}$, where i or j (or both) are index of metallic atoms, will be calculated with standard McWEDA LDA approximation).

It is necessary to take into account that, for a molecule interacting with a surface, the sum rule (2.55) is no longer true, because only a fraction α of the exchange-correlation hole is inside the molecule, so the sum rule needs to be written now as:

$$\sum_{\substack{j\beta; i \neq j \\ i, j \in \text{molecule}}} n_{i\alpha\sigma, j\beta\sigma} n_{j\beta\sigma, i\alpha\sigma} = \alpha_{i\alpha\sigma} n_{i\alpha\sigma} (1 - n_{i\alpha\sigma}) \quad (2.90)$$

So E_X^{LD-OO} and V_X^{LD-OO} reads now as:

$$\begin{aligned}
E_X^{LD-OO}[\{n_{i\alpha\sigma}\}] &= -\frac{1}{2} \sum_{i\alpha\sigma} J_{i\alpha\sigma}^{eff} \alpha_{i\alpha\sigma} n_{i\alpha\sigma} (1 - n_{i\alpha\sigma}) \\
(V_X^{LD-OO})_{i\alpha\sigma, j\beta\sigma} &= -\alpha_{i\alpha\sigma} J_{i\alpha\sigma}^{eff} \left(\frac{1}{2} - n_{i\alpha\sigma}\right) \delta_{i\alpha, j\beta}
\end{aligned} \tag{2.91}$$

The V_X^{HF-OO} part remains unchanged (we didn't use the sum rule (2.55) to deduce it).

As we will see in Chap. 5 the value of α is very high in the case of aromatic compounds adsorbed on metals. For pentacene/Au(111) this value is greater than 0.9, while in first tests in benzene/Au(111) $\alpha \sim 0.7-0.9$. These values depends on the σ or π character of the orbitals (the π orbitals have a lower α due to its greater interaction with the metal surface).

2.7.4 Koopmans' Shift

In this section we present another method to correct the underestimation to the LDA gap. This method relies on Koopmans' theorem [79] and estimates the SIC error.

The actual transport energy gap (E_g^t) is the difference between the ionization (IE) and affinity (A) energies:

$$\begin{aligned}
IE &= E[N - 1] - E[N] \\
A &= E[N] - E[N + 1] \\
E_g^t &= IE - A = E[N + 1] + E[N - 1] - 2E[N]
\end{aligned} \tag{2.92}$$

If we consider $-\varepsilon_{HOMO}$ (the energy of the HOMO) as IE and $-\varepsilon_{LUMO}$ (the energy of the LUMO) as A following the spirit of Koopmans' theorem [79], we obtain the underestimated DFT gap. In order to correct it we have to take into account somehow the SIC. Here we consider that this electron (hole) is described by the Kohn–Sham LUMO (HOMO) eigen-wavefunction, neglecting the electron relaxation effects. This self-interaction is introduced as a correction for the LUMO (HOMO) eigen-energy δA (δIE).

In the LCAO-OO scheme, the orbital occupancies of the $N + 1$ ($N - 1$) system can be computed from the N occupancies, neglecting electron relaxation, as:

$$\begin{aligned}
n_{i\alpha\sigma}^{N+1} &= n_{i\alpha\sigma}^N + \delta n'_{i\alpha\sigma}; n_{i\alpha\sigma}^{N-1} = n_{i\alpha\sigma}^N - \delta n_{i\alpha\sigma} \quad \text{where} \\
\delta n'_{i\alpha\sigma} &= |\langle \phi_{i\alpha} | LUMO_N \rangle|^2; \delta n_{i\alpha\sigma} = |\langle \phi_{i\alpha} | HOMO_N \rangle|^2
\end{aligned} \tag{2.93}$$

For the sake of simplicity we are going to focus on the change of electron affinity due to the extra electron, and consider its spin is upwards. It is just [80]:

$$\begin{aligned}
A = E[N] - E[N + 1] &= \varepsilon_{N+1}^{o.e.} + \frac{1}{2} \sum_{\substack{\alpha, \beta \\ \alpha \neq \beta}} U_{i\alpha, i\beta} (n_{i\alpha\uparrow}^N + \delta n'_{i\alpha\uparrow}) (n_{i\beta\uparrow}^N + \delta n'_{i\beta\uparrow}) + \\
&+ \frac{1}{2} \sum_{\alpha, \beta} U_{i\alpha, i\beta} (n_{i\alpha\uparrow}^N + \delta n'_{i\alpha\uparrow}) n_{i\beta\downarrow}^N + \frac{1}{2} \sum_{\substack{\alpha, j\beta \\ i \neq j}} J_{i\alpha, j\beta} (n_{i\alpha\uparrow}^N + \delta n'_{i\alpha\uparrow}) (n_{j\beta\uparrow}^N + \delta n'_{j\beta\uparrow}) + \\
&+ \frac{1}{2} \sum_{\substack{\alpha, j\beta \\ i \neq j}} J_{i\alpha, j\beta} (n_{i\alpha\uparrow}^N + \delta n'_{i\alpha\uparrow}) n_{j\beta\downarrow}^N - \frac{1}{2} \sum_{i\alpha} J_{i\alpha\uparrow}^{eff} (n_{i\alpha\uparrow}^N + \delta n'_{i\alpha\uparrow}) (1 - n_{i\alpha\uparrow}^N - \delta n'_{i\alpha\uparrow}) \\
&- \frac{1}{2} \sum_{i\alpha\uparrow} f_{i\alpha\uparrow} (U_{i\alpha, i\alpha} - J_{i\alpha\uparrow}^{eff}) (n_{i\alpha\uparrow}^N + \delta n'_{i\alpha\uparrow}) (1 - n_{i\alpha\uparrow}^N - \delta n'_{i\alpha\uparrow}) \\
&- \left[-\frac{1}{2} \sum_{\substack{\alpha, \beta\sigma \\ i\alpha\uparrow \neq i\beta\sigma}} U_{i\alpha, i\beta} n_{i\alpha\uparrow}^N n_{i\beta\sigma}^N + \frac{1}{2} \sum_{\substack{\alpha, \beta \\ i \neq j}} J_{i\alpha, j\beta} n_{i\alpha\uparrow}^N n_{j\beta\sigma}^N \right. \\
&\left. + \frac{1}{2} \sum_{i\alpha} J_{i\alpha\uparrow}^{eff} n_{i\alpha\uparrow}^N (1 - n_{i\alpha\uparrow}^N) + \frac{1}{2} \sum_{i\alpha} f_{i\alpha\uparrow} (U_{i\alpha, i\alpha} - J_{i\alpha\uparrow}^{eff}) n_{i\alpha\uparrow}^N (1 - n_{i\alpha\uparrow}^N) \right]
\end{aligned} \tag{2.94}$$

we can group terms that, that are linear in $\delta n'_{i\alpha\uparrow}$, and quadratic in $\delta n'_{i\alpha\uparrow}$. With some math we obtain:

$$A = E[N] - E[N + 1] = \varepsilon_{N+1}^{o.e.} + \frac{\partial(E_H + E_X)}{\partial n_{i\alpha\uparrow}} \delta n'_{i\alpha\uparrow} + \delta A[O(\delta n_{i\alpha\uparrow}^{\prime 2})] \tag{2.95}$$

It is obvious that the terms linear in $\delta n'_{i\alpha\uparrow}$ are already taken into account on ε_{LUMO}^{DFT} . So the first non-vanishing correction terms are of second order in $\delta n_{i\alpha\uparrow}$. These values for the ionization ($IE = -\varepsilon_{HOMO} + \delta IE$) and affinity ($A = -\varepsilon_{LUMO} + \delta A$) can be written as [80]:

$$\begin{aligned}
\delta IE &= \frac{1}{2} \sum_{i \neq j} J_{i\alpha, j\beta} \delta n_{i\alpha\uparrow} \delta n_{j\beta\uparrow} + \frac{1}{2} \sum_{\alpha \neq \beta} U_{i\alpha, i\beta} \delta n_{i\alpha\uparrow} \delta n_{i\beta\uparrow} \\
&+ \frac{1}{2} \sum_{i\alpha} J_{i\alpha}^{eff} \delta n_{i\alpha\uparrow}^2 + \frac{1}{2} \sum_{i\alpha} f_{i\alpha} (U_{i\alpha, i\alpha} - J_{i\alpha}^{eff}) \delta n_{i\alpha\uparrow}^2 \\
\delta A &= -\frac{1}{2} \sum_{i \neq j} J_{i\alpha, j\beta} \delta n'_{i\alpha\uparrow} \delta n'_{j\beta\uparrow} - \frac{1}{2} \sum_{\alpha \neq \beta} U_{i\alpha, i\beta} \delta n'_{i\alpha\uparrow} \delta n'_{i\beta\uparrow} \\
&- \frac{1}{2} \sum_{i\alpha} J_{i\alpha}^{eff} \delta n_{i\alpha\uparrow}^{\prime 2} - \frac{1}{2} \sum_{i\alpha} f_{i\alpha} (U_{i\alpha, i\alpha} - J_{i\alpha}^{eff}) \delta n_{i\alpha\uparrow}^{\prime 2}
\end{aligned} \tag{2.96}$$

It has been found that this approximation gives good results [80, 81] for the gaps of a variety of π -conjugated organic molecules, in particular, the results are better for larger molecules, due to electron relaxation effects become less important.

This Koopmans' shift can be used not only for the HOMO and LUMO but for all the molecular levels, we only need to change in (2.93) $\delta n_{i\alpha\sigma} = |\langle \phi_{i\alpha} | HOMO_N \rangle|^2$ by $\delta n_{i\alpha\sigma} = |\langle \phi_{i\alpha} | LEVEL_N \rangle|^2$ where $|LEVEL_N\rangle$ is the eigen-wavefunction of the level we want to correct.

So the Koopmans' shift is a good way to improve the underestimation of DFT gap. In particular we can combine it with the scissor operator (see next section) in order to get an improved hamiltonian to calculate, among other things, transport or density of states.

2.7.5 Scissor Operator

We have shown how the Koopmans' shift can deal with the underestimation of the DFT gap, including self energy terms. In Sects. 3.6 and 4.2.1 we will see a method to estimate the gap of our molecules interacting with a metal surface. In this thesis, in order to obtain this corrected HOMO-LUMO gap in our hamiltonian (and play with the relative alignment between organic molecules and metals, as in Chap. 5) we have used the scissor operator. If $|\mu_i\rangle$ ($|v_i\rangle$) are the empty (occupied) molecular orbitals of the isolated, but deformed, molecule (with the actual geometry of the molecule on the surface) then the scissor operator read as:

$$\hat{O}^{scissor} = \sum_{\mu_i} (\varepsilon + \Delta) |\mu_i\rangle \langle \mu_i| + \sum_{v_i} (\varepsilon - \Delta) |v_i\rangle \langle v_i| \quad (2.97)$$

where Δ acts on a different way on the occupied (empty) molecular states, and therefore changes the value of the energy gap, and ε move all molecular orbitals in the same direction. This scissor operator allow us not only to include SIC in the gas phase molecule, but also to tune the gap and the relative alignment between metal and molecular levels in the case of a molecule interacting with a surface.

The case of a molecule over a surface deserves some comments. Although $|\mu_i\rangle$ ($|v_i\rangle$) are defined for the isolated molecule and we shouldn't use them when it is interacting with the metal, we obtain that this approximation works very well (see Chaps. 4 and 5) as long as the deformed molecule geometry (instead of the gas phase one) is used.

We can rewrite it in the fireball atomic basis, in order to introduce it in our hamiltonian. Equation (2.97) reads then:

$$\begin{aligned}
O_{ij}^{scissor} &= \sum_k \Delta_k \langle i | \Psi_k \rangle \langle \Psi_k | j \rangle = \sum_k \Delta_k \langle i | \left(\sum_l c_{kl} | l \rangle \right) \left(\sum_m c_{km}^* \langle m | \right) | j \rangle \\
&= \sum_{k,l,m} \Delta_k c_{kl} c_{km}^* \langle i | l \rangle \langle m | j \rangle \\
O_{ij}^{scissor} &= \sum_{k,l,m} \Delta_k c_{kl} c_{km}^* S_{il} S_{mj} \tag{2.98}
\end{aligned}$$

where $\Delta_k = \varepsilon - \Delta$ for $k \in$ occupied levels and $\Delta_k = \varepsilon + \Delta$ for $k \in$ empty levels and Ψ_k are the eigenvectors of the energy eigenvalues.

2.8 Other Methods for Correcting the Gap

As we have said, the underestimation of the DFT gap is the most important problem for the systems that we are studying on this thesis. In the previous section, we explained the methods used here to deal with this failure. For the sake of completeness, a couple of state-of-the-art methods will be shown. Moreover, they can be inspiring later for some approximations

2.8.1 GW Method

GW Form of Selfenergy

The GW method relies on many-body green functions and self-energy formalism (Sect. A.2). It provides a way to calculate the self-energy in a reasonably amount of time with good accuracy. The deduction of the form of the selfenergy can be found on [82]. The form in time space and energy space is just.

$$\begin{aligned}
\Sigma^{GW}(\mathbf{r}, \mathbf{r}', \tau) &= i\hbar G_0(\mathbf{r}, \mathbf{r}', \tau) W(\mathbf{r}, \mathbf{r}', \tau) \\
\Sigma^{GW}(\mathbf{r}, \mathbf{r}', \omega) &= \frac{i\hbar}{2\pi} \int_{-\infty}^{\infty} d\omega' G_0(\mathbf{r}, \mathbf{r}', \omega + \omega') W(\mathbf{r}, \mathbf{r}', \omega') e^{i\omega'\tau} \tag{2.99}
\end{aligned}$$

where $W(\mathbf{r}, \mathbf{r}', \omega)$ is the screened coulomb interaction, in (2.20). The reason for the name of the method is now clear. It is important to say that this is an improvement with respect to the HF form of the self-energy $\Sigma^{HF}(\mathbf{r}, \mathbf{r}') = i\hbar G_0(\mathbf{r}, \mathbf{r}', 0^-) V_{coulomb}(\mathbf{r}, \mathbf{r}')$, because the screened potential $W(\mathbf{r}, \mathbf{r}', \omega)$ is considerably smaller than the coulomb potential. Besides it introduces dynamic effects since it is energy dependent. To sum up GW selfenergy takes into account exchange and a part of the correlation trough the screening potential.

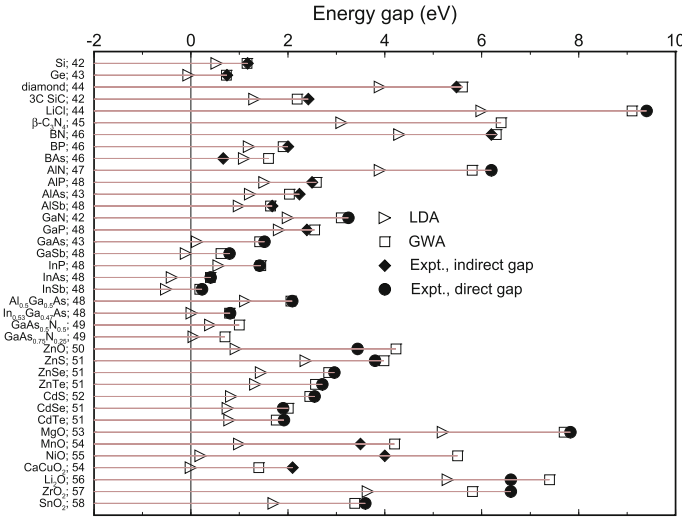


Fig. 2.6 Comparison of characteristic direct and indirect LDA, GW and experimental gap for a big variety of semiconductors. The numbers after the chemical symbols are the references for those values in [83]. Reprinted from [83], Copyright (2000) with permission from Elsevier (Color figure online)

Practical Implementation

It can be demonstrated [83] that the quasiparticles energy in the GW approximation can be calculated using formula:

$$\begin{aligned} \varepsilon_i^{GW} &= \varepsilon_i^{KS} + \frac{1}{Z_i} \langle \phi_i^{KS} | \Sigma^{GW}(\omega_i^{KS}) - V_{xc} | \phi_i^{KS} \rangle \quad \text{where} \\ Z_i &= 1 - \langle \phi_i^{KS} | \frac{1}{\hbar} \frac{\partial \Sigma^{GW}(\omega_i^{KS})}{\partial \omega} | \phi_i^{KS} \rangle \end{aligned} \quad (2.100)$$

where we have assumed that the self-energy correction to the Kohn–Sham potential $\Sigma^{GW}(\mathbf{r}, \mathbf{r}', \omega) - V_{XC}(\mathbf{r})\delta(\mathbf{r} - \mathbf{r}')$ is small and we can use first-order perturbation theory. Moreover, we have considered that $\omega_i^{GW} - \omega_i^{KS} = \varepsilon_i^{GW}/\hbar - \varepsilon_i^{KS}/\hbar$ is small so we can perform a Taylor expansion around ω_i^{KS} . This approximation means that we don't need to compute explicitly the temporal dependence of Σ^{GW} .

So in practice, we first have to know the dielectric function $\varepsilon^{-1}(\mathbf{r}, \mathbf{r}'', \omega)$. We can calculate it using polarization matrix and random phase approximation (RPA) [84, 85], that is accurate but very expensive computationally, or calculate is using plasmon models [83, 86, 87]. Moreover, the exchange and correlation parts of Σ^{GW} are separated (the screened potential W is rewritten as $W = V_{coulomb} + (W - V_{coulomb})$), because the exchange part can be calculated analytically.

As can be seen in Fig. 2.6, GW approximation leads to really good results if we compare gap energies calculated using this method with the experimental results, or, at least it gives better results than LDA. The main problem of this method is that it is much more costly computationally than DFT, even if approximations for the dielectric function are used.

2.8.2 LDA+U Method

The origin of this method is to try to improve standard LDA functional for band systems where coulomb repulsion on localized orbitals introduces an important source of correlation, such as transition metal oxides, where we have delocalized electrons in s and p bands (where LDA works pretty well) and electrons localized in metal d bands, where the electron-electron repulsion U is important.

The LDA+U method is introduced as a functional that treats delocalized electrons correlation in a LDA fashion, and localized ones in a Hubbard-like way. If we take the standard Hubbard hamiltonian (A.8), the underlying idea of LDA+U is simple.

$$\hat{H} = \underbrace{\sum_i \varepsilon_0 \hat{n}_{i\sigma} - \sum_i t(\hat{c}_{i+1\sigma}^\dagger \hat{c}_{i\sigma} + \hat{c}_{i\sigma}^\dagger \hat{c}_{i+1\sigma})}_{\text{delocalized, one electron}} + \underbrace{\sum_i U \hat{n}_{i\uparrow} \hat{n}_{i\downarrow}}_{\text{localized, correlation}}$$

$$E[\rho(\mathbf{r})] = E^{LDA}[\rho(\mathbf{r})] + E^U[\{n_{i\alpha\sigma, i\beta\sigma}\}] \quad (2.101)$$

Note that E^U is a functional of the occupation numbers instead of density. This is because this is the natural language in a Hubbard-like approach to localized electrons. We also need to include a double counting term that takes out the electron correlation already taken into account in LDA.

We are going to summarize here the basic formulas of the method. For a complete description of the method see references [88, 89]. Consider a transition metal with d orbitals where we have imposed spherical symmetry, then the simplest E^U repulsive term one can write is $E^U = \frac{1}{2} U^{eff} \sum_{m \neq m'} n_m n_{m'}$, where m, m' are the magnetic numbers of the d electrons, U^{eff} is calculated as in (2.49), but using the screened coulomb potential W (2.20) instead of the unscreened one. The double counting term E^{dc} , that takes out the interaction taken into account in LDA can be written as $E^{dc} = \frac{1}{2} U^{eff} N(N-1)/2$ (where $N = \sum_i n_i$). So this simplified LDA+U functional can be written as:

$$E = E^{LDA} + E^U - E^{dc} = E^{LDA} + \frac{1}{2} U^{eff} \sum_{m \neq m'} n_m n_{m'} - \frac{1}{2} U^{eff} N(N-1)/2 \quad (2.102)$$

The atomic energies are now (using Janak's theorem [90]):

$$\varepsilon_m^{LDA+U} = \frac{\partial E}{\partial n_m} = \varepsilon_m^{LDA} + U^{eff} \left(\frac{1}{2} - n_m \right) \quad (2.103)$$

This means that the LDA eigenvalues are shifted by $-U^{eff}/2$ if the level is filled ($n_m = 1$) and by $+U^{eff}/2$ if the level is empty ($n_m = 0$).

This method is closely related to our LCAO-OO approach. First of all, a more complete description of the method includes not only Hartree-like corrections but also exchange-like ones, as well as non-diagonal occupations $n_{m,m'}$ [89]. The simplified model explained here correspond to the particular case of [89] where $n_{m,m'}^\sigma = n_m^\sigma \delta_{m,m'}$, $U = \langle m, m' | V_{ee} | m, m' \rangle$ and the other $\langle m, m'' | V_{ee} | m', m''' \rangle$ terms are zero. Moreover, the matrix elements involved in E^U calculation in [89] are nothing but the ones in (2.49), and the form of the functional can be derived using a mean-field approximation of the LCAO-OO Hamiltonian (2.50) (approximating all the operators $\hat{n}_{i\alpha\sigma}$ by its mean values $n_{i\alpha\sigma}$).

A point of caution with the LCAO-OO method analogy has to be taken. In this case the electron-electron potential V_{ee} is not the bare one but the screened one (so $f_{i\alpha\sigma}$ is not needed anymore to take into account correlation). This converts LDA+U in a post-HF theory. This screened potential relates the LDA+U method with the GW one. The relationship between this method and GW and HF ones is extensively studied in [91].

In Sect. 3.6 the ideas of Cococcioni et al. [92] are used to extend this method from metal transition oxides to organic molecules over metal surfaces.

References

1. I. Levine, *Quantum Chemistry*, (Prentice Hall, New Jersey, 2001)
2. K. Ohno, K. Esfarjani, M.C. Holthausen, *Computational Materials Science*, (Springer, Berlin, 1999)
3. W. Koch, M.C. Holthausen, *A Chemist's Guide to Density Functional Theory*, (Wiley-Vch, Weinheim, 2000)
4. L. Pauling, E.B. Wilson, *Introduction to Quatum Mechanics*, (McGraw-Hill, New York, 1935)
5. C. Cohen-Tannoudji, B. Diu, F. Laloë, *Quantum Mechanics*, vol. 2, 2nd edn. (Wiley, New York, 1977)
6. A. Szabo, N.S. Ostlund, *Modern Quantum Chemistry*, (Dover Publications, New York, 1996)
7. C. Møller, M.S. Plesset, Note on an approximation treatment for many-electron systems. *Phys. Rev.* **46**(7), 618 (1934)
8. J. Phillips, Energy-band interpolation scheme based on a pseudopotential. *Phys. Rev.* **112**, 685 (1958)
9. M. Cohen, V. Heine, The fitting of pseudopotentials to experimental data and their subsequent application. *Solid state phys.* **24**, 37 (1970)
10. J. Joannopoulos, T. Starkloff, M. Kastner, Theory of pressure dependence of the density of states and reflectivity of Selenium. *Phys. Rev. Lett.* **38**(12), 660 (1977)
11. A. Redondo, W.A. Goddard, T.C. McGill, Ab initio effective potentials for silicon. *Phys. Rev. B* **15**, 5038 (1977)
12. D. Hamann, M. Schlüter, C. Chiang, Norm-conserving pseudopotentials. *Phys. Rev. Lett.* **43**(20), 1494 (1979)

13. A. Zunger, M. Cohen, First principles nonlocal-pseudopotential approach in the density-functional formalism. II. Application to electronic and structural properties of solids. *Phys. Rev. B* **20**, 4082 (1979)
14. L. Kleinman, D. Bylander, Efficacious form for model pseudopotentials. *Phys. Rev. Lett.* **48**(20), 1425 (1982)
15. E. Shirley, D. Allan, R. Martin, J. Joannopoulos, Extended norm-conserving pseudopotentials. *Phys. Rev. B* **40**, 3652 (1989)
16. D. Vanderbilt, Soft self-consistent pseudopotentials in a generalized eigenvalue formalism. *Phys. Rev. B* **41**, 7892 (1990)
17. K. Laasonen, R. Car, C. Lee, D. Vanderbilt, Implementation of ultrasoft pseudopotentials in ab initio molecular dynamics. *Phys. Rev. B* **43**, 6796 (1991)
18. P. Hohenberg, W. Kohn, Inhomogeneous electron gas. *Phys. Rev.* **136**(3B), B864 (1964)
19. W. Kohn, L. Sham, Self-consistent equations including exchange and correlation effects. *Phys. Rev.* **140**(4A), A1133 (1965)
20. F.J. García-Vidal, F. Flores, S.G. Davison, Propagator theory of quantum-wire transmission. *Prog. Surf. Sci.* **74**(1–8), 177 (2003)
21. A.L. Fetter, J. D. Walecka, *Quantum Theory of Many-Particle Systems*, (Dover Publications, New York, 2003)
22. H. Bruus, K. Flensberg. *Many-Body Quantum Theory in Condensed Matter Physics: An Introduction*, (Oxford University Press, New York, 2004)
23. J.P. Perdew, A. Zunger, Self-interaction correction to density-functional approximations for many-electron systems. *Phys. Rev. B* **23**(10), 5048 (1981)
24. D. Ceperley, B. Alder, Ground state of the electron gas by a stochastic method. *Phys. Rev. Lett.* **45**(7), 566 (1980)
25. A.D. Becke, Density-functional exchange-energy approximation with correct asymptotic behavior. *Phys. Rev. A* **38**(6), 3098 (1988)
26. C. Lee, W. Yang, R.G. Parr, Development of the Colle-Salvetti correlation-energy formula into a functional of the electron density. *Phys. Rev. B* **37**(2), 785 (1988)
27. J.P. Perdew, K. Burke, M. Ernzerhof, Generalized gradient approximation made simple. *Phys. Rev. Lett.* **77**(18), 3865 (1996)
28. J. P. Perdew, S. Kurth, A. Zupan, P. Blaha, Accurate density functional with correct formal properties: A step beyond the Generalized Gradient Approximation. *Phys. Rev. Lett.* **82**(12), 2544
29. S. Kümmel, L. Kronik, Orbital-dependent density functionals: theory and applications. *Rev. Mod. Phys.* **80**(1), 3 (2008)
30. O. Sankey, D. Niklewski, Ab initio multicenter tight-binding model for molecular-dynamics simulations and other applications in covalent systems. *Phys. Rev. B* **40**(6), 3979 (1989)
31. A. Demkov, J. Ortega, O. Sankey, M. Grumbach, Electronic structure approach for complex silicas. *Phys. Rev. B* **52**(3), 1618 (1995)
32. J. Harris, Simplified method for calculating the energy of weakly interacting fragments. *Phys. Rev. B* **31**(4), 1770 (1985)
33. W. Foulkes, R. Haydock, Tight-binding models and density-functional theory. *Phys. Rev. B* **39**(17), 12520 (1989)
34. J. Lewis, K. Glaesemann, G. Voth, J. Fritsch, A. Demkov, J. Ortega, O. Sankey, Further developments in the local-orbital density-functional-theory tight-binding method. *Phys. Rev. B* **64**(19), 195103 (2001)
35. J.P. Lewis, P. Jelínek, J. Ortega, A.A. Demkov, D.G. Trabada, B. Haycock, H. Wang, G. Adams, J.K. Tomfohr, E. Abad, H. Wang, D.A. Drabold, Advances and applications in the FIREBALLab initio tight-binding molecular-dynamics formalism. *physica status solidi b*, **248**(9), 1989 (2011)
36. J. Ortega, First-principles methods for tight-binding molecular dynamics. *Comput. Mater. Sci.* **12**(3), 192 (1998)
37. B. Pieczyrak, C. González, P. Jelínek, R. Pérez, J. Ortega, F. Flores, Mechanical and electrical properties of stretched clean and H-contaminated Pd-nanowires. *Nanotechnology* **19**(33), 335711 (2008)

38. M. Basanta, Y. Dappe, P. Jelínek, J. Ortega, Optimized atomic-like orbitals for first-principles tight-binding molecular dynamics. *Comput. Mater. Sci.* **39**(4), 759 (2007)
39. D.A. Papaconstantopoulos, *Handbook of the Band Structure of Elemental Solids*, (Plenum Press, New York, 1986)
40. P. Löwdin, On the non-orthogonality problem connected with the use of atomic wave functions in the theory of molecules and crystals. *J. Chem. Phys.* **18**, 365 (1950)
41. B. Carlson, J. Keller, Orthogonalization procedures and the localization of wannier functions. *Phys. Rev.* **105**(1), 102 (1957)
42. A. Horsfield, Efficient ab initio tight binding. *Phys. Rev. B* **56**(11), 6594 (1997)
43. P. Jelínek, H. Wang, J. Lewis, O. Sankey, J. Ortega, Multicenter approach to the exchange-correlation interactions in ab initio tight-binding methods. *Phys. Rev. B* **71**(23), 235101 (2005)
44. D. González. Efectos dinámicos en la superficie β -SiC(100), Ph.D. thesis, Universidad Autonoma de Madrid, 2009
45. H. Hellmann, *Einführung in die Quantumchemie*, (Franz Deutsche, Leipzig, 1937)
46. R. Feynman, Forces in molecules. *Phys. Rev.* **56**(4), 340 (1939)
47. B.M. Deb, The force concept in chemistry. *Rev. Mod. Phys.* **45**(1), 22 (1973)
48. P.E. Gill, W. Murray, M.H. Wright, *Practical Optimization* (Academic Press, London, 1981)
49. C. González, Métodos DFT y STM de primeros principios para el estudio de superficies semiconductoras con adsorbatos: pasivación, nanohilos y transiciones de fase, Ph.D. thesis, Universidad Autónoma de Madrid, 2005
50. P. Fulde, *Electron Correlations in Molecules and Solids*, 3rd edn. (Springer, Berlin, 2003)
51. F.J. García-Vidal, J. Merino, R. Pérez, R. Rincón, J. Ortega, F. Flores, Density-functional approach to LCAO methods. *Phys. Rev. B* **50**, 10537 (1994)
52. P. Pou, Energía de canje y correlación como función de los números de ocupación orbitales: cálculos de energías totales y cuasiparticulas, Ph.D. thesis, Universidad Autónoma de Madrid, 2001
53. P. Pou, R. Pérez, F. Flores, A. Yeyati, A. Martín-Rodero, J. Blanco, F. García-Vidal, J. Ortega, Local-density approach and quasiparticle levels for generalized Hubbard Hamiltonians. *Phys. Rev. B* **62**(7), 4309 (2000)
54. H. Vázquez, Energy level alignment at organic semiconductor interfaces, Ph.D. thesis, Universidad Autónoma de Madrid, 2006
55. K. Schönhammer, O. Gunnarsson, R. Noack, Density-functional theory on a lattice: comparison with exact numerical results for a model with strongly correlated electrons. *Phys. Rev. B* **52**(4), 2504 (1995)
56. R.D. Mattuck. *A Guide to Feynman Diagrams in the Many-Body Problem*, Dover Publications, New York, 1992
57. C. Caroli, R. Combescot, P. Nozieres, D. Saint-James, A direct calculation of the tunnelling current: IV. Electron-phonon interaction effects. *J. Phys. C: Solid State Phys.* **4**, 916 (1972)
58. A. Martín-Rodero, F. Flores, N. March, Tight-binding theory of tunneling current with chemisorbed species. *Phys. Rev. B* **38**(14), 10047 (1988)
59. N. Mingo, L. Jurczyszyn, F.J. Garcia-Vidal, R. Saiz-Pardo, P. de Andres, F. Flores, S. Wu, W. More, Theory of the scanning tunneling microscope: Xe on Ni and Al. *Phys. Rev. B* **54**(3), 2225 (1996)
60. R. Landauer, Electrical resistance of disordered one-dimensional lattices. *Philos. Mag.* **21**, 863 (1970)
61. D. Fisher, P. Lee, Relation between conductivity and transmission matrix. *Phys. Rev. B* **23**(12), 6851 (1981)
62. E. Abad, Y.J. Dappe, J.I. Martínez, F. Flores, J. Ortega, C6H6/Au(111): interface dipoles, band alignment, charging energy, and van der Waals interaction. *J. Chem. Phys.* **134**(4), 044701 (2011)
63. J. Ángyán, I. Gerber, A. Savin, J. Toulouse, Van der Waals forces in density functional theory: perturbational long-range electron-interaction corrections. *Phys. Rev. A* **72**(1), 12510 (2005)
64. D.C. Langreth, M. Dion, H. Rydberg, E. Schröder, P. Hyldgaard, B.I. Lundqvist, Van der Waals density functional theory with applications. *Int. J. Quantum Chem.* **101**(5), 599 (2005)

65. F. Ortman, F. Bechstedt, W. Schmidt, Semiempirical van der Waals correction to the density functional description of solids and molecular structures. *Phys. Rev. B* **73**(20), 205101 (2006)
66. S. Grimme, Semiempirical GGA-type density functional constructed with a long-range dispersion correction. *J. Comput. Chem.* **27**(15), 1787 (2006)
67. K. Pernal, R. Podeszwa, K. Patkowski, K. Szalewicz, Dispersionless density functional theory. *Phys. Rev. Lett.* **103**(26), 263201 (2009)
68. N. Marom, A. Tkatchenko, M. Scheffler, L. Kronik, Describing both dispersion interactions and electronic structure using density functional theory: the case of Metal-Phthalocyanine dimers. *J. Chem. Theory Comput.* **6**(1), 81 (2010)
69. M.A. Basanta, Y.J. Dappe, J. Ortega, F. Flores, Van der Waals forces in the local-orbital density functional theory. *Europhys. Lett.* **70**(3), 355 (2005)
70. Y. Dappe, M. Basanta, F. Flores, J. Ortega, Weak chemical interaction and van der Waals forces between graphene layers: a combined density functional and intermolecular perturbation theory approach. *Phys. Rev. B* **74**(20), 205434 (2006)
71. Y. Dappe, J. Ortega, F. Flores, Intermolecular interaction in density functional theory: application to carbon nanotubes and fullerenes. *Phys. Rev. B* **79**(16), 165409 (2009)
72. A. Tkatchenko, M. Scheffler, Accurate molecular van der Waals interactions from ground-state electron density and free-atom reference data. *Phys. Rev. Lett.* **102**(7), 073005 (2009)
73. E. Abad, J. Ortega, F. Flores, Metal/organic barrier formation for a C₆₀/Au interface: from the molecular to the monolayer limit. *Phys. Status Solidi A*. 209, 636 (2012)
74. J.M. Garcia-Lastra, C. Rostgaard, A. Rubio, K.S. Thygesen, Polarization-induced renormalization of molecular levels at metallic and semiconducting surfaces. *Phys. Rev. B* **80**(24), 245427 (2009)
75. B. Pieczyrak, E. Abad, F. Flores, J. Ortega, Charging energy and barrier height of pentacene on Au(111): a local-orbital hybrid-functional density functional theory approach. *J. Chem. Phys.* **135**(8), 084702 (2011)
76. J. Harris, R. Jones, The surface energy of a bounded electron gas. *J. Phys. F: Met. Phys.* **4**, 1170 (1974)
77. J. Harris, Adiabatic-connection approach to Kohn-Sham theory. *Phys. Rev. A* **29**(4), 1648 (1984)
78. A.D. Becke, A new mixing of Hartree-Fock and local density-functional theories. *J. Chem. Phys.* **98**(2), 1372 (1993)
79. T. Koopmans, Ordering of wave functions and eigenenergies to the individual electrons of an atom. *Physica* **1**, 104 (1933)
80. H. Vázquez, P. Jelínek, M. Brandbyge, A.P. Jauho, F. Flores, Corrections to the density-functional theory electronic spectrum: copper phthalocyanine. *Appl. Phys. A* **95**(1), 257 (2008)
81. R. Oszwaldowski, H. Vázquez, P. Pou, J. Ortega, R. Pérez, F. Flores, Exchange correlation energy in the orbital occupancy method: electronic structure of organic molecules. *J. Phys. Condens. Matter* **15**(38), S2665 (2003)
82. L. Hedin. New method for calculating the one-particle Green's function with application to the electron-gas problem. *Phys. Rev.* **139**(3A), A796 (1965)
83. W. Aulbur, L. Jönsson, J. Wilkins, Quasiparticle calculations in solids. *Solid State Phys.* **54**, 1 (1999)
84. D. Pines, D. Bohm, A collective description of electron interactions: II. Collective vs individual particle aspects of the interactions. *Phys. Rev.* **85**(2), 338 (1952)
85. D. Pines, in *Elementary Excitations in Solids*, (New York, W.A. Benjamin, 1961)
86. W. von der Linden, P. Horsch, Precise quasiparticle energies and Hartree-Fock bands of semiconductors and insulators. *Phys. Rev. B* **37**(14), 8351 (1988)
87. G. Engel, B. Farid, Generalized plasmon-pole model and plasmon band structures of crystals. *Phys. Rev. B* **47**(23), 15931 (1993)
88. V.I. Anisimov, J. Zaanen, O.K. Andersen, Band theory and Mott insulators: Hubbard U instead of Stoner I. *Phys. Rev. B* **44**(3), 943 (1991)

89. A.I. Liechtenstein, V.I. Anisimov, J. Zaanen, Density-functional theory and strong interactions: orbital ordering in Mott-Hubbard insulators. *Phys. Rev. B* **52**(8), R5467 (1995)
90. J. Janak, Proof that $\partial E/\partial n = \varepsilon$ in density-functional theory. *Phys. Rev. B* **18**(12), 7165 (1978)
91. V. Anisimov, F. Aryasetiawan, A. Liechtenstein, First-principles calculations of the electronic structure and spectra of strongly correlated systems: the LDA+ U method. *J. Phys. Condens. Matter* **9**, 767 (1997)
92. M. Cococcioni, S. de Gironcoli, Linear response approach to the calculation of the effective interaction parameters in the LDA+U method. *Phys. Rev. B* **71**(3), 035105 (2005)

Chapter 3

Further Developments in IDIS Model

3.1 Introduction

All electronic circuits that rely on the use of semiconductors (the vast majority in the last 50 years) need to deal with a physical challenging system: metal/semiconductor interfaces. Its technological importance led to an extensive research and nowadays, the properties of interfaces between metal and inorganic semiconductors are well understood (band bending, interface states, Bardeen model, IDIS model...). A small review of inorganic interfaces will be given in Sect. 3.2.

In the last decade, organic semiconductors have received a lot of attention both from pure research and industry. As shown in Sect. 1.3, electronic gadgets based on organic semiconductors have already appeared in the market. On the other side, a lot of research papers, reviews and books have been written about this topic [1–5].

The challenge of organic semiconductors is because of their different nature from their inorganic counterparts (the former are molecular solids while the latter are covalent/partial ionic solids). Inorganic semiconductor theoretical tools does not work properly for them (Fig. 3.1).

To get a good performance in semiconductor electronic devices (both in organic and inorganic) the so called electron injection barrier (see Fig. 3.2) must be as small as possible. This means that level alignment at the interface is very important. This alignment appeared simple, but in fact is a complex problem. It has been found to be much more complex than it was thought. The naive Schottky–Mott rule has been widely disproved [2, 6, 7] since some effects that invalidate this rule appear at interfaces: chemical reactions, creation of interface states [7–9], metal-organic charge transfer leading to an interface dipole, orientation of intrinsic molecular dipoles [10, 11], induced Pauli exclusion (pillow) dipoles [12–15], etc. These effects will be briefly introduced in Sect. 3.3.

After the introduction of metal/organic and inorganic semiconductor interfaces, we will present in Sect. 3.4 an extensive description of the IDIS model for metal organic interfaces [4, 15–18]. Then, we will focus on two metal organic interfaces with very different screening: $C_{60}/Au(111)$ and $C_6H_6/Au(111)$. We will show how

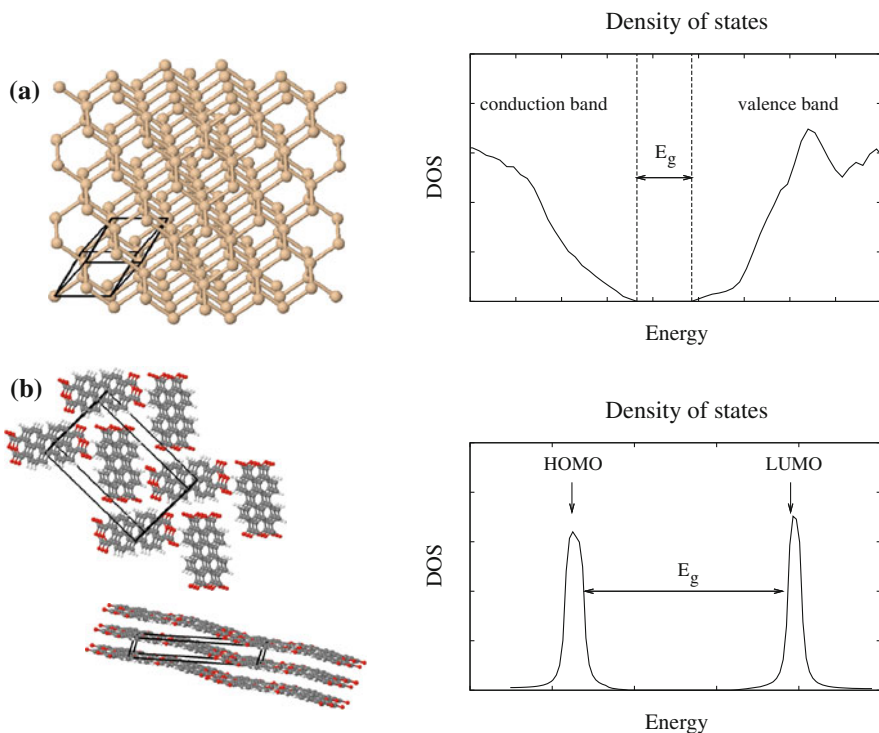
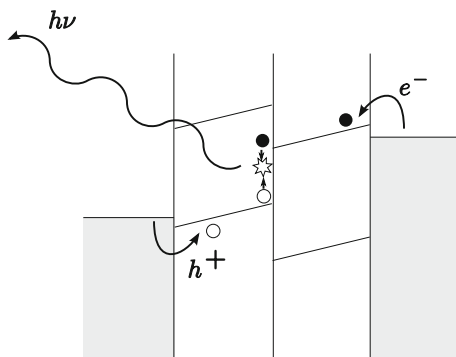


Fig. 3.1 (Color online) **a** Geometry (unit cell is highlighted) and density of states of silicon as an example of a prototypical inorganic semiconductor. **b** Geometry (*upper* and *side* view, unit cell is highlighted) and density of states of PTCDA as an example of a prototypical organic semiconductor

the deficiencies of standard DFT-LDA lead to quantitative disagreement with experimental evidence. A method for correcting this will be highlighted at the end of the chapter.

Fig. 3.2 Schematic view of an (organic) light emitting diode. In order to get a good performance, the electron and hole injection barriers have to be as small as possible. The band alignment at interfaces is critical for this reason



3.2 Brief Introduction to Metal/Inorganic Semiconductor Interfaces

The series of physical changes that take place when a metal/inorganic semiconductor (M/IS) interface is created have been one of the main topics of surface physics, due to its great interest both for science and industry [21]. The first studies of this interfaces come back from late nineteenth century [19].

As stated before, the most important quantity at the interface is the barrier height Φ_b . It is the minimum energy needed for an electron on the metal to penetrate in the conduction band of the semiconductor (or for a hole to penetrate in the valence band, see Figs. 3.2 and 3.3).

3.2.1 Schottky–Mott Limit

Before the statement of the Schottky–Mott rule, it is necessary to say a few words about the concept of work function. It is the energy necessary for an electron at the Fermi Level to reach vacuum at rest. It has two contributions, the bulk contribution (due to the periodic potential inside the solid) and the surface contribution (because of the presence of dipole layer due to the asymmetric electron distribution at the surface [20], as shown in Fig. 3.4).

The work function is well defined in metals, where Fermi Level lies within conduction band, and is uniquely determined. However, semiconductor work function seems ill defined because the Fermi Level can be located at any value within the gap, but it must be remembered that the work function is a statistical concept: the weighted average of the energies necessary to remove an electron from the valence and conduction bands, respectively [21].

Now, consider a metal and a semiconductor with different work functions (usual case). When they are connected electrically, both Fermi levels have to be the same. That implies a charge transfer from the semiconductor to the metal (or the other way around). A net charge will appear in both systems (equal but of opposite sign). This charge will be placed at the surface in the case of a metal (it is a good conductor) but in the case of the semiconductor, since the charge carriers density is orders of magnitude lower, it will be in an extensive zone, of the order of nanometers, called the depletion area. This is the origin of band bending. Also an electric field appears at the region between metal and semiconductors whose value is $\mathcal{E} = V/\delta$. When the distance between both materials goes to zero (i.e. the contact is formed), that potential tends to zero in order to keep \mathcal{E} finite, so the barrier height is:

$$\Phi_b = \Phi_M - \chi_S \quad (3.1)$$

(see Fig. 3.3). This equation is the naive Schottky–Mott rule [22]. It consider implicitly three important assumptions: that the surface contributions to Φ_M and χ_S remain

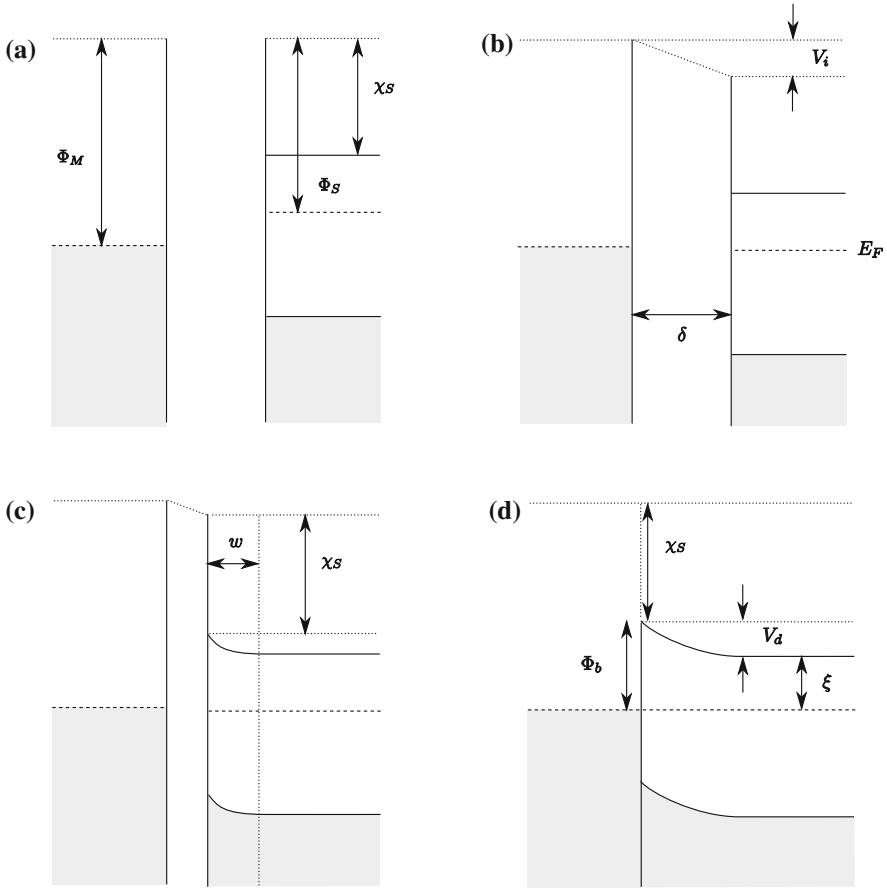


Fig. 3.3 Different stages on the formation of a Schottky M/IS barrier. **a** Isolated materials. **b** Connection of both systems. A potential V_i is established between both. **c** As both materials approach, band bending in the depletion region appears. **d** When the contact is established the barrier height is $\Phi_b = \Phi_M - \chi_S$, as stated in Eq. 3.1

unchanged when both materials are brought into contact, that there are no surface states at the semiconductor and perfect contact between the metal and the semiconductor is established. However, it implies a dipole at the surface, contrary to what sometimes is stated. Since Schottky–Mott rule does not work in practice, it is clear that one or more of the assumptions is wrong.

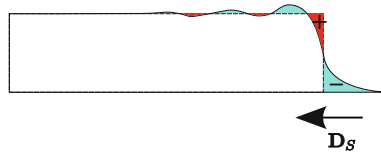
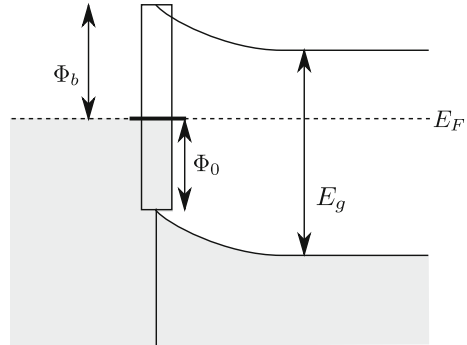


Fig. 3.4 (Color online) Scheme of the charge distribution around a surface in a jellium model. The uncompensated charges creates a dipole pointing to the surface that enlarge the work function (i.e. make it more negative)

Fig. 3.5 Schematic view of the filling of surface states on Bardeen limit



3.2.2 Bardeen Limit

This model can be consider as the opposite limit of the Schottky–Mott model. It was stated by Bardeen [23], based on the fact that the barrier height, Φ_b , is not too much sensitive to the metal work function, Φ_M .

Suppose that there is a continuous distribution of surface states within the gap at the interface filled up to Φ_0 (see Fig. 3.5), if the density of surface states is high enough $\Phi_0 \simeq E_F$, and the barrier height will be given by:

$$\Phi_b = E_g - \Phi_0 \tag{3.2}$$

In this case the barrier height is insensitive of the metal work function.

3.2.3 Intermediate Case

Real M/IS interfaces are between both Schottky–Mott and Bardeen limits. We are going to consider here the Bardeen model when surface states DOS is not very high. Figure 3.6 shows an schematic view of the interface under study (usually, between metal and semiconductor an insulator layer is placed, instead of vacuum, but this does not change the conclusions of the model).

There are three sources of charge in that system, Q_m , the charge on the metal, that is on the surface, Q_d is the charge in the depletion region, that induces band

where

$$S = \frac{1}{1 + eD_s\delta/\epsilon_0} \quad (3.7)$$

is the screening parameter and measures the strength of the pinning at the interface, and is a key parameter of the IDIS model of MO interfaces. Equation (3.6) was first derived by Cowley and Sze [24]. It can be observed that Φ_b tends to the Schottky–Mott limit when $D_s \rightarrow 0$ (no interface states) and to the Bardeen limit when $D_s \rightarrow \infty$ (high density of surface states). Also note that Schottky–Mott and Bardeen limit corresponds to values of $S = 1$ and $S = 0$ respectively.

We have to note that here, as in the Schottky–Mott rule, we have assumed that the surface contributions to Φ_M and χ_S remain unchanged when both materials are brought into contact.

3.2.4 Origin of Interface States

In all these models, the role of interface states is very important for the energy level alignment, so here we will say a few words about them.

Induced Density of Interface States (IDIS)

Heine [25] was the first one to notice that intrinsic semiconductor surface states within the gap resonate with metallic Bloch waves when M/IS interface is formed, leading to resonant gap surface states that is the source of the gap states that appears in Bardeen model and intermediate case by Cowley and Sze. These states are metal conduction band wavefunctions on the metallic side of the interface and penetrate into the semiconductor with an attenuation length of the order of a few angstroms. Based on that assumption, other groups tried to characterize this induced density of interface states [26, 27]

Although the ideas of Heine turned out to be correct, Tejedor and Flores [28] were the ones that obtained quantitative values from theoretical calculations of semiconductors from highly covalent (Si) to the highly ionic limit (ZnS), and Cohen and Louie [29–31] obtained DFT values for those interfaces.

However, as pointed out by Tejedor and Flores [28]; the states induced in the bottom (top) of the gap are accompanied with a reduction of the DOS in the valence (conduction) bands. Since no new states can be created when the interface is formed, we can conclude that the semiconductor (and not the metal) DOS is rearranged at interface formation, so interface states come from valence and conduction semiconductor bands.

Unified Defect Model

This model was proposed by Spicer et al. [32]. They consider that interface states, instead of coming from metal wavefunctions that decay into the semiconductor come from defects in semiconductor surface. Defects, such as vacancies, steps or anti-site defects (change of cation on anion sites, in III–V or II–VI semiconductors) lead to localized states that can lie in the semiconductor band gap. This is validated by experiments, that have shown that intimate metal-semiconductor interfaces are not perfect, and chemical reactions and interdiffusion are common occurrences [21].

However, for high metallic coverages, the screening of these defects implies that the density of defects needed for pinning the Fermi level should be very high. Nowadays, it is considered that the unified defect model explains the Fermi level pinning in low metallic coverage interfaces (~ 1 ML, where very small DOS is induced in the semiconductor due to metal interaction), and the IDIS model in higher coverages.

3.3 Brief Introduction to Metal/Organic Interfaces

As stated before, organic semiconductors are very different from inorganic ones. Due to such small interactions between molecules (compared with the strong covalent interactions in inorganic semiconductors), it was initially thought that Schottky–Mott rule was valid for these semiconductors, since weak vdW interaction between metal and molecules could be excepted, which is unable to induce DOS in the organic gap. However, it has been shown that this rule is disproved for most metal/organic interfaces [2, 6, 7]: a dipole layer appears at the interface. However, although in *M/IS* interfaces the junction effect is extended over the depletion area, in organic semiconductors this effect is reduced mainly to the first organic layer (see Fig. 3.7 and [33]).

It is worth commenting that this disapproval of the Schottky–Mott rule has been found even for organic insulators (where the HOMO–LUMO gap is very wide). We can expect here very small chemical interaction; however studies of a 9 eV gap long-chain alkane $n\text{-C}_{44}\text{H}_{90}$ (TTC) on various interfaces have shown work function changes between -0.3 and -0.7 eV [34, 35].

Several effects have been proposed as the origin of this dipole, and some of them can be acting at the same time (Fig. 3.9). This is a brief summary of these effects.

3.3.1 Charge Transfer and Chemical Reactions

Some molecules that form organic semiconductors are chemisorbed on metals (i.e. strong chemical interaction and bond formation is established between surface metallic atoms and molecules). This effect is restricted to the first organic layer, so it is enough to study a monolayer of molecules on metals.

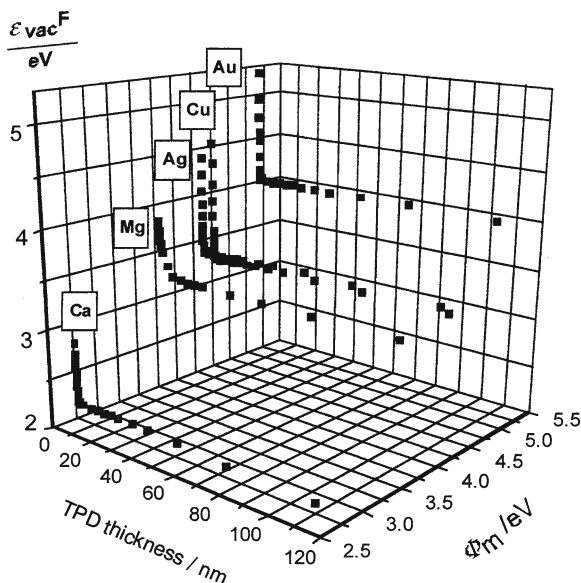


Fig. 3.7 Change of the energy of the vacuum level relative to the Fermi level of the metal substrate (ϵ_{vac}^F , analogous to $\Phi_M - V$ in inorganic semiconductors (see Fig. 3.6b) at the deposition of TPD on five metals of various work functions Φ_M . The two abscissas correspond to the TPD film thickness and the work function of the metal substrate, while the ordinate denotes ϵ_{vac}^F . It can be seen clearly how the potential drop relies in the first layer of organic molecules, and there is no depletion region, as in M/IS interfaces. Reprinted from [33] Copyright (2001) from Elsevier

Table 3.1 Abbreviations and actual names of the organic molecules mentioned in this thesis (the chemical structure is in Fig. 3.8)

Abbreviation	Name
TPD	N,N'-diphenyl-N,N'-(3-methylphenyl)-1,1'-biphenyl-4,4'-diamine
Alq ₃	tris(8-hydroxyquinolino)aluminium
DP-NTCI	N,N'-diphenyl-1,4,5,8-naphthyltetracarboxylimide
TTC	tetratetracontane
α -NPD	N,N'-diphenyl-N,N'-bis(1-naphthyl)-1,1'-biphenyl-4,4'-diamine
PTCDA	3,4:9,10-Perylenetetracarboxylic dianhydride
TTF	tetrathiofulvalene
TCNQ	tetracyanoquinodimethane
PFO	poly(9,9-dioctylfluorene)
P3HT	poly(3-hexylthiophene)

Work function change has been reported for a lot of chemisorbed molecules on metals. Two electrostatic effects contribute to that: First of all, charge transfer between metal and molecule, that creates a dipole layer between both systems, leading to a work function change (the work function is smaller, in absolute value, when

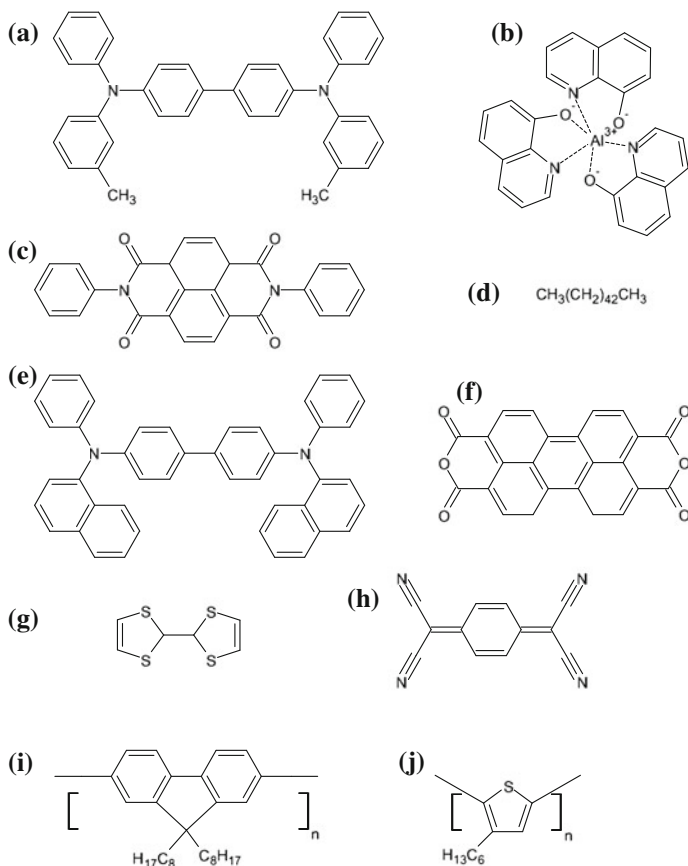


Fig. 3.8 Chemical structures of the compounds mentioned in Table 3.1. **a** TPD, **b** Alq₃, **c** DP-NTCI, **d** TTC, **e** α-NPD, **f** PTCDA, **g** TTF, **h** TCNQ, **i** PFO, **j** P3HT

charge transfer is from chemisorbed molecule to metal and greater in the opposite case). The other effect is charge redistribution due to bond formation.

Charge transfer from the metal to the molecule has been reported on TCNQ/Au, DP-NTCI/Al [8] and PTCDA/Mg,In,Sn [7]. And from the molecule to the metal, TPD/Au [8] and α-NPD/Au [7] are good examples. An example of possible charge rearrangement by bond formation is the case of Alq₃/Al system, where a mid-gap state, due to strong chemical interaction at the interface has been reported [9].

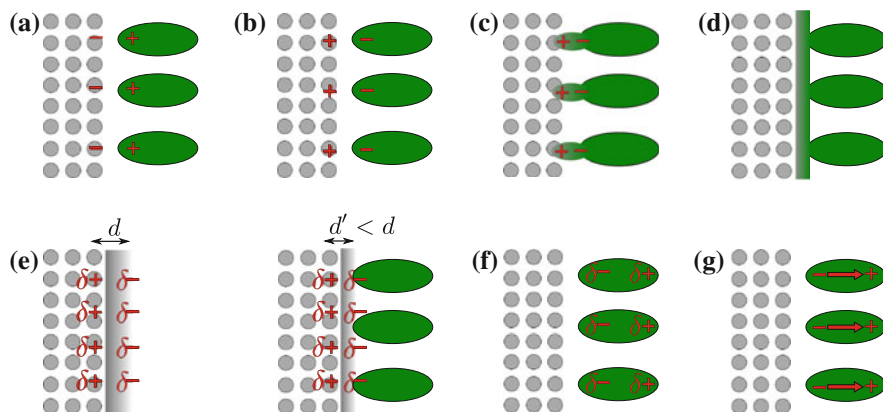


Fig. 3.9 Possible origins of the formation of dipole on M/O interfaces. *Chemical effects* **a, b** dipole formation due to a net charge transfer from the molecule (metal) to the metal (molecule); **c** charge rearrangement due to bond formation. **d** Formation of an interface state. *Physical effects* **e** “Pillow” effect due to Pauli exclusion principle between metal and organic electrons. **f** Redistribution of the electron cloud due to image effect. **g** Permanent dipole

3.3.2 Image Effect and Surface Charge Rearrangement: “Pillow” Dipole

These effects are present always in organic deposition on metals, but are more important in physisorption with no charge transfer of non-polar molecules, due to it is the unique effect that leads to work function change.

The image effect is closely related to the origin of Van der Waals forces. When we have a non-polar molecule (or a noble gas atom); although it does not have an intrinsic dipole, at a certain moment, a net dipole on the molecule can appear because of quantum fluctuations. The metal react to this dipole creating an image dipole. The interaction of these dipoles gives rise to Van der Waals forces.

However, this interaction of the net dipole with the screening charge can give rise to a net displacement of the electron distribution in the adsorbate and create a potential drop at the interface. This effect has been studied (at the DFT–LDA level) in a Xe/jellium system [36, 37], showing that its contribution to the dipole at the interface is not negligible.

Other source of dipole is the “pillow” dipole (sometimes called “cushion” dipole, push-back dipole or exchange dipole). It is due to a pure quantum mechanical effect (as the image effect dipole): the Pauli exclusion principle.

When a molecule is placed on a metallic surface, wave functions of both the metal and the molecular atoms overlap. When we orthogonalize both wave functions, the electron metal tails are pushed back into the metal. This charge rearrangement reduce the surface dipole (as can be deduced from Figs. 3.4 and 3.9). This reduction of the surface dipole means that work function will be reduced whenever a molecule is

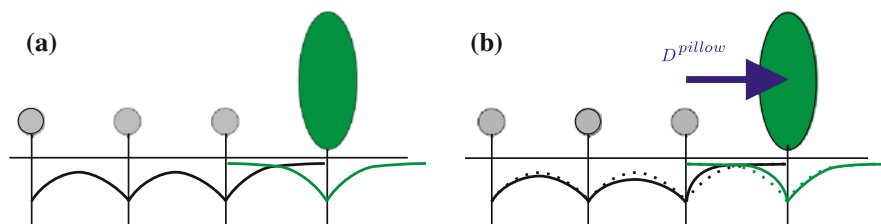


Fig. 3.10 **a** Image of overlap between metal and organic wave functions when both systems are brought together. **b** After orthogonalization, a charge rearrangement appears that creates a net dipole D^{pillow} that lower the metal work function

placed on a metal surface, no matter if the molecule is an electron donor or acceptor, so in the case of an electron acceptor the “pillow” dipole and the charge transfer dipole compete with each other. This effect should be more important in cases where the surface contribution to work function dipole is more important (i.e. transition metals), as has been shown experimentally [38].

3.3.3 Intrinsic Molecular Dipole

Some molecules have a net dipole (for example, Alq_3 , benzene-thiol). When they are adsorbed on a metallic surface, sometimes they have a non negligible component on the direction perpendicular to the surface. This dipole orientation gives rise to a potential drop at the interface (see Fig. 3.9) [10, 11].

3.3.4 Effects on Real Devices

In the case of production of real devices, a few things has to be taken into account that can change the energy level alignment [3]. A few words of these effects will be given.

The first one is the effect of air exposure of the interfaces. The oxygen present in the atmosphere can penetrate into the interface and oxidize the metal surface, changing the work function of the metal and the energy level alignment [6]. This tend to reduce the dipole at the interface, probably due to reduction of the interaction between the metal and the organic molecule due to the surface oxidation or contamination (Fig. 3.11) [33].

Other effect is the order of deposition. In most of the experimental works on MO interfaces, the organic layer is deposited over the metal surfaces, but in real devices is necessary also to deposit metal atoms over organic surfaces. It has been shown that the order of deposition can be important because metal atoms tend to penetrate

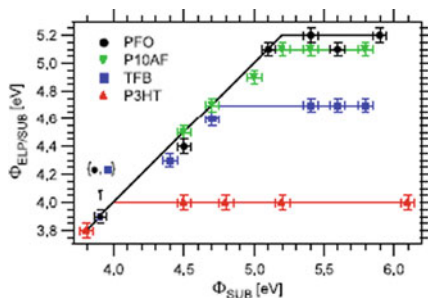
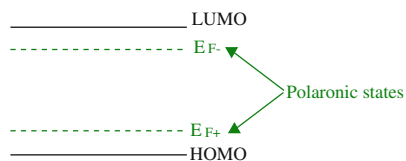


Fig. 3.12 *Left* HOMO and LUMO levels, as well as the polaronic states E_{P+} and E_{P-} , of an electroluminescent polymer. *Right* Dependence of work function of polymer coated substrate $\Phi_{EPL/SUB}$ with the work function of bare substrate, Φ_{SUB} , for four materials studied in [41], namely P3HT, TFB, P10AF and PFO. Reprinted with permission from [41] Copyright IOP publishing 2007

As we will see later, this is complementary to the IDIS model, with a screening parameter $S = 1$ between E_{P+} and E_{P-} and $S = 0$ at E_{P+} , E_{P-} levels.

3.4 IDIS Model for Metal/Organic Semiconductor Interfaces

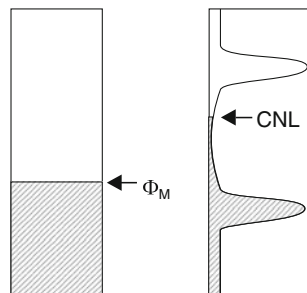
The IDIS model, originally created for metal/inorganic semiconductor interfaces [28, 46], was extended for metal/organic ones in the thesis of Hector Vázquez [16–18]. It has been extended to include pillow dipole and intrinsic molecular dipoles [15] in the Unified-IDIS model. In this section we are going to carefully explain the ideas it is based on.

Before that, we will say some words about our notation. First of all, we will use atomic units ($\hbar = e = 1/4\pi\epsilon_0 = 1$) in all formulas. Second, we are going to avoid the usage of terms like work functions of the interface and “clean” work functions, that is common in literature and can be sometimes confusing. Instead, here we use the following terms: initial Fermi level (that will be designated by Φ_M), that is the metal Fermi level before the contact is established, and coincides (apart from a minus sign) with the “clean” metal work function, as long as the origin of energies is placed at the vacuum level; and the final Fermi level of the interface (designated by E_F) that is the Fermi level of the interacting metal and organic system.

3.4.1 Interface States and the Charge Neutrality Level

The main idea of this model is that the physical/chemical interaction between the first layers of the organic material and the last layers of the metal, induces a non-negligible DOS at the semiconducting gap. This DOS can appear because of the formation of

Fig. 3.13 Metal/organic interface before charge transfer. HOMO and LUMO peaks have been broadened due to interaction between with the metallic surface. The molecular DOS is filled up to CNL



hybrid metal/organic states at the gap due to strong chemical interaction between both materials at the interface (connecting with the ideas at [12, 47]); or due to the broadening of HOMO and LUMO levels due to interaction with the metal. Zangwill [48] and Newns [49] provide a way to estimate this broadening [16], although in this thesis it has been computed from first principles. This induced DOS allow us to define the main parameter of this model, the Charge Neutrality Level (CNL).

The CNL can be seen as a kind of effective Fermi level of the organic molecule. It can be calculated as the integral of the DOS projected on the *interacting* organic molecule up to charge neutrality conditions. As explained above, due to the interaction with the metal substrate, the peak-like DOS of the molecule is transformed in a continuum DOS, allowing us to integrate it (as shown in Fig. 3.13).

$$N = \int_{-\infty}^{\text{CNL}} \rho_{\text{interacting}}(E) dE \quad (3.8)$$

The CNL can be seen as some kind of effective electronegativity of the molecule in the sense that the relative position of the metal work function (Φ_M) with respect to the organic CNL determines the direction of charge transfer (neglecting the effect of pillow dipole and intrinsic molecular dipole). If $\text{CNL} > \Phi_M$ then the electrons will flow from the organic layer to the metal, on the contrary, when $\text{CNL} < \Phi_M$ electron transfer from the metal to the molecule will take place.

It needs to be taken into account that although intuitively the CNL should be at the middle of the HOMO and LUMO levels [12, 50], this is not true. Usually the DOS is higher around the HOMO than around the LUMO [17, 51–53]. This is obvious for the C_{60} since the HOMO is five times degenerated while the LUMO is three times, (without including spin). This pushes the CNL upwards in the gap, but is also true (although less intuitive) for molecules like benzene, PTCDA and TTF (where the HOMO degeneration is not greater than the LUMO one).

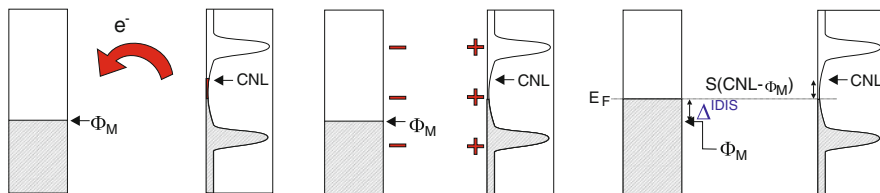


Fig. 3.14 (Color online) Metal/organic interface when charge transfer is allowed. It creates a dipole at the interface that tends to align the metal work-function with the charge neutrality level

3.4.2 Level Alignment and Screening Parameter

Now that we have the induced interface states characterized, and the position of CNL and Φ_M ; let us allow charge transfer between the metal and organic material. As said before, the direction of charge transfer depends on the relative position of CNL with respect to Φ_M . These charge transfer creates a dipole as shown in Fig. 3.14. This dipole induces a potential drop at the interface, as can be seen using pure classical electrostatic arguments.² The effect of this dipole is to move the final Fermi level and tends to pin it to the CNL (Fig. 3.14). This pinning of the Fermi level to the CNL has been observed experimentally in PTCDA [7] and is also strong in C₆₀ [54] and DP-NTCI [55]. The potential drop that changes the interface Fermi level from Φ_M to E_F can be related with the electrostatic dipole through the formula:

$$\Delta = \frac{4\pi D}{A} \quad (3.9)$$

where D is the electrostatic dipole, Δ the potential drop at the interface and A is the surface area that belongs to each molecule (i.e. $A = \text{total area covered}/\text{total number of molecules}$).

This pinning of the Fermi level is governed by the screening parameter, S , that has appeared in the study of M/IS interfaces between the Schottky–Mott and Bardeen limits [Eq. (3.7)], and its meaning is just the same. If we consider that the CNL is always fixed with respect to the vacuum, and the level movement due to the dipole is only on metallic levels, the screening parameter can be written as:

$$S = \frac{\text{CNL} - E_F}{\text{CNL} - \Phi_M} \quad (3.10)$$

or equivalently:

$$(\text{CNL} - E_F) = S(\text{CNL} - \Phi_M) \quad (3.11)$$

² See for example J. D. Jackson *Classical Electrodynamics* (3rd Ed.), Sect. 1.6

So the S parameter can be seen as the value that controls the reduction of the $(\text{CNL} - \Phi_M)$ distance to $(\text{CNL} - E_F)$. So the lower the S parameter is, the greater the pinning of the final Fermi level to the CNL. This implies a higher screening. Note that, as we consider CNL a fixed level, we can also consider S as:

$$S = \frac{\delta E_F}{\delta \Phi_M} \quad (3.12)$$

That is, S control the changes in E_F when we change the metal work function.

Now we can write the potential due to charge transfer (from now on it will be called IDIS potential Δ^{IDIS}) as a function of IDIS parameters:

$$\Delta^{IDIS} = E_F - \Phi_M = (1 - S)(\text{CNL} - \Phi_M) \quad (3.13)$$

3.4.3 Pillow Dipole

In previous section, charge transfer as the unique source of interface dipole has been considered. However there are more sources, although smaller than the charge transfer dipole, and not important for self-consistently results of the calculations, that have to be considered as a second order effect. They are the pillow dipole and the surface dipole.

The first one was explained in Sect. 3.3.2. As said there this effect raises the metal work function. It can be taken into account in our model if we define an effective metal work-function:

$$\tilde{\Phi}_M = \Phi_M + \Delta_0^P \quad \left(\Delta_0^P = \frac{4\pi D^{pillow}}{A} \right) \quad (3.14)$$

And the equivalence of (3.11) is:

$$(\text{CNL} - E_F) = S(\text{CNL} - \tilde{\Phi}_M) = S(\text{CNL} - \Phi_M) - S\Delta_0^P \quad (3.15)$$

And the total potential at the interface:

$$\Delta^{total} = E_F - \Phi_M = E_F - \tilde{\Phi}_M + \Delta_0^P = (1 - S)(\text{CNL} - \tilde{\Phi}_M) + \Delta_0^P \quad (3.16)$$

This can be seen in two different ways. From one side, you can argue that the net potential is the sum of the pillow potential (the second term) and the potential due to the charge transfer (the first term), that can be considered as some kind of pseudo-IDIS potential for the effective work function $\tilde{\Phi}_M$. On the other hand it can be seen as:

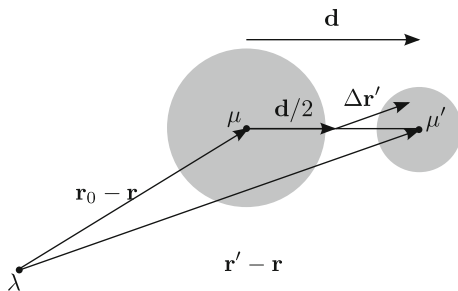


Fig. 3.15 Metal (*left*) and organic (*right*) orbitals separated by a distance d . The probe electronic density λ is considered a point charge, eliminating the integration over \mathbf{r} , and we expand the distance $|\mathbf{r} - \mathbf{r}'|$, placing the origin of integration in \mathbf{r}' at the midpoint between orbitals μ and μ' , as discussed in the text

$$\Delta^{total} = (1 - S)(\text{CNL} - \Phi_M - \Delta_0^P) + \Delta_0^P = (1 - S)(\text{CNL} - \Phi_M) + S\Delta_0^P = \Delta^{IDIS} + \Delta^P \quad (3.17)$$

In this case, the total potential is the sum of the IDIS potential due to charge transfer neglecting the pillow effect plus a screened pillow potential $\Delta^P = S\Delta_0^P$.

In FIREBALL, the “pillow” dipole is not explicitly included. When we calculate Hartree potential, we use a density of the form (2.25). As we said in Sect. 2.4.2, this is an approximation, and, since the Hartree potential is calculated using fireball (non-orthogonal) orbitals, the effect of orthogonalization of both organic and metal orbitals are not correctly taken into account. One can ask if we can trust in charge selfconsistency if this effect is not taken into account, but as we will see later in this thesis this dipole is a small second order correction, so we should not be worried about this. On the other hand, this allow us to separate contributions of the pure charge transfer and “pillow” part from the interface potential.

In order to calculate numerically the pillow dipole, we are going to follow the ideas of Vázquez and coworkers [15]. Consider the “probe orbital” ϕ_λ , that is located far away from a couple of metal ϕ_μ and organic $\phi_{\mu'}$ orbitals. We consider that in both subsystems (metallic and organic) orbitals are orthogonal, but there is an overlap between orbitals of both subsystems. We want to know how the intersite coulomb interaction $J_{\lambda,\mu}$ [see Eq. (2.49)] changes when metal and organic orbitals overlap. First of all the value of $J_{\lambda,\mu}$ when no overlap is taken into account is:

$$J_{\lambda,\mu} = \int d^3\mathbf{r} d^3\mathbf{r}' \phi_\lambda^2(\mathbf{r}) \frac{1}{|\mathbf{r} - \mathbf{r}'|} \phi_\mu^2(\mathbf{r}') \quad (3.18)$$

where orbitals are considered to be real, as fireball orbitals are real.

Now we are going to orthogonalize the orbitals. Following the Löwdin scheme $\varphi_\mu = (S^{-1/2})_{\mu,i} \phi_i$. Since $S_{\mu,\mu'}$ is small we can expand it up to second order in S :

$$\varphi_\mu \simeq \phi_\mu - \frac{1}{2} \sum_{\mu'} S_{\mu,\mu'} \phi_{\mu'} + \frac{3}{8} \sum_{\mu',\nu} S_{\mu,\mu'} S_{\mu',\nu} \phi_\nu \quad (3.19)$$

where μ, ν runs over metallic orbitals and μ' over organic ones. We can introduce this expansion in (3.18) and, after that, expand $|\mathbf{r} - \mathbf{r}'|$ around $|\mathbf{r} - \mathbf{r}_0|$ (see Fig. 3.15). Taking into account that potential created in λ is $J_{\lambda, \mu} n_{\mu\sigma}$ we conclude that the overlaps between orbitals give rise to a dipole D^{pillow} . The value of this dipole is:

$$D_{\mu\mu'\sigma} = (n_{\mu\sigma} + n_{\mu'\sigma})S_{\mu, \mu'} \int d^3\mathbf{r}' \Delta\mathbf{r}' \phi_{\mu}(\mathbf{r}') \phi_{\mu'}(\mathbf{r}') + (n_{\mu'\sigma} - n_{\mu\sigma})S_{\mu, \mu'}^2 \frac{\mathbf{d}}{4} \quad (3.20)$$

where $D_{\mu\mu'\sigma}$ can be seen as a ‘‘bond’’ dipole between the metal orbital $\phi_{\mu}(\mathbf{r})$ and the organic orbital $\phi_{\mu'}(\mathbf{r})$ (see Fig. 3.15), \mathbf{d} is the distance between both atoms and $\Delta\mathbf{r}' = \mathbf{r}' - \mathbf{r}_0$ connects the integration variable \mathbf{r}' with the midpoint between organic and metal atom \mathbf{r}_0 (reference [15] has the detailed mathematical calculations).

This result would be correct if no effect of selfconsistency was included in the occupations $\{n_{\mu\sigma}\}$. However, this is not true, because, as stated in Sect. 2.4.2, the occupations in FIREBALL are obtained by projecting the wavefunction in the *orthonormal* Löwdin orbitals $n_{\mu} = \sum_n^{occ.} |\langle \psi_n | \varphi_{\mu} \rangle|^2$. This makes that the second term in (3.20) is already included in our calculations. So we only need to consider the following off-diagonal contribution.

$$D_{\mu\mu'\sigma} = (n_{\mu\sigma} + n_{\mu'\sigma})S_{\mu, \mu'} \int d^3\mathbf{r}' \Delta\mathbf{r}' \phi_{\mu}(\mathbf{r}') \phi_{\mu'}(\mathbf{r}') \quad (3.21)$$

Finally the total dipole is calculated as $D^{pillow} = \sum_{\mu, \mu', \sigma} D_{\mu\mu'\sigma}$. The interface potential is $\Delta_0^P = 4\pi D^{pillow} / A$.

3.4.4 Intrinsic Molecular Dipole

This case can be treated just like the previous case, considering that this dipole create a potential drop Δ_0^M that can be added to Φ_M (it should be subtracted from the organic part, but this is indifferent, due to we care only on relative alignment of levels of both interfaces). Like the previous case it can be seen in two different ways:

$$\begin{aligned} \Delta^{total} &= E_F - \Phi_M = E_F - \tilde{\Phi}_M + \Delta_0^M = (1 - S)(\text{CNL} - \tilde{\Phi}_M) + \Delta_0^M \\ \Delta^{total} &= (1 - S)(\text{CNL} - \Phi_M) + S\Delta_0^M = \Delta^{IDIS} + \Delta^M \end{aligned} \quad (3.22)$$

3.4.5 Surface Dipole

The ‘‘surface dipole’’ is the other source of dipole at the interface that is not considered by our FIREBALL code. It is a part of the IDIS dipole that needs to be added explicitly.

The form of the input density in (2.25), the form of the output charges (2.26), together with the fact that we are using Harris functional, neglects off-diagonal dipole terms (as said in 2.4.2). They are of the form.

$$\mathbf{D}^{off-diag} = \sum_{i\alpha, j\beta} \mathbf{D}_{i\alpha, j\beta} = \sum_{i\alpha, j\beta} n_{i\alpha, j\beta} \int d^3\mathbf{r} \phi_{i\alpha}^*(\mathbf{r}) \phi_{j\beta}(\mathbf{r}) \mathbf{r} \quad (3.23)$$

where $n_{i\alpha\sigma, j\beta\sigma} = \langle \hat{c}_{i\alpha\sigma}^\dagger \hat{c}_{j\beta\sigma} \rangle$ as defined in Sect. 2.5.1. Due to surface symmetry, only $D_z^{off-diag} \neq 0$. Although the effect of this dipole is small (the change in Δ^{IDIS} is less than 0.1 eV) it is important due to it varies linearly with charge transfer (due to it is part of the IDIS dipole) and need to be taken into account when calculating U (see Sect. 4.2.2). In our calculations we only have taken into account the most important contribution $i = j$ (i.e. the intraatomic dipole).

3.5 Mind the Gap: C₆₀/Au(111) and Benzene/Au(111) Interfaces

In this section we are going to apply the ideas of the IDIS model to analyze the electronic structure of two interfaces: C₆₀/Au(111) and benzene/Au(111). They were chosen because significant difference of screening should appear between them. We start studying these interfaces within the LDA approximation. At the end of this section, we will show how calculations change when a realistic gap, obtained from experimental values, is used. The results have been published in *Applied Physics A* [53] (Copyright 2009, Springer) and *Journal of Vacuum Science and Technology B* [56] (Copyright 2009, AVS), and here we present some excerpts from them. Other authors have studied these systems theoretically. In the case of C₆₀, a complete study of geometry, energy and dipole formation at the interface has been made by Wang and coworkers [57] (they also studied the C₆₀/Cu(111) interface in [58]). Sau and coworkers [59] have focused on the calculation of the transport energy gap using Janak's theorem and a simple energy functional for non-integer number of electrons. Later in this thesis, we have also taken care of the transport gap: our results will be presented in Chap. 5. Regarding the benzene/Au(111) interface, Bagus and coworkers [14] have used the constrained space orbital variation method, while Morikawa and coworkers [60] have followed a DFT-GGA approach.

3.5.1 Geometry

The relaxed geometry of these interfaces has been calculated with the FIREBALL code (Sect. 2.4). For the C₆₀/Au(111) interface, we use the experimental $2\sqrt{3} \times 2\sqrt{3}R30^\circ$ structure that a monolayer of C₆₀ takes when deposited on the Au(111) surface [61] (see Fig. 3.16). For the sake of simplicity, we have used, for benzene/Au(111),

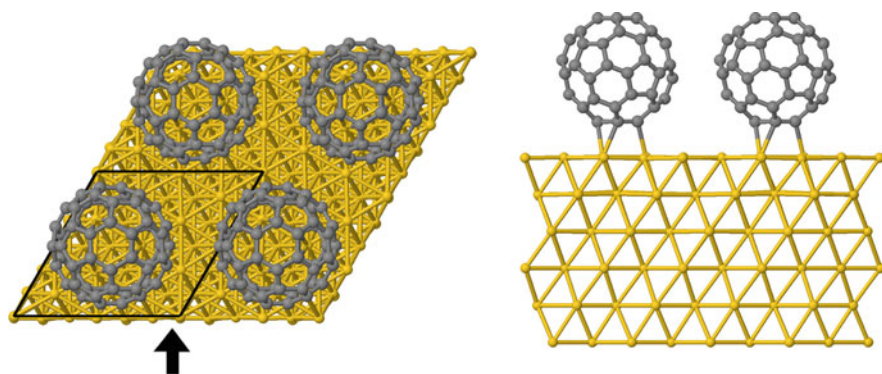


Fig. 3.16 (Color online) $C_{60}/Au(111)-2\sqrt{3} \times 2\sqrt{3}$ structure used in our calculations (unit cell is highlighted). *Upper* and *side view*. For clarity reason, in the *side view* we only represent the first molecular row. Reprinted from [53] (Copyright 2009, Springer). This and other images of atomic geometries have been created with Jmol [62]

a 5×5 periodicity, with 4 molecules per unit cell (Fig. 3.17); in this geometry, the adsorbate hexagonal lattice is the same and the distance between molecules is similar to the one found experimentally in the $\sqrt{52} \times \sqrt{52}$ structure [63] (7.3 Å versus experimental value of 6.95 Å), so that the main difference is that our coverage is slightly smaller ($\sim 10\%$) than the experimental monolayer. Regarding the Au surface, we have used in both cases a film of six layers. Since vdW interaction is very important in the benzene/Au interface, we cannot trust in molecule/metal distances provided by LDA calculations, so it has been deduced indirectly from the available experimental information. In particular, Koch et al. [64] have found for pentacene/Cu(111) a molecule surface distance of 2.34 Å; on the other hand, Duhm et al. [65] have found that for PTCDA/Au(111) the molecule/metal distance is 0.61 Å larger than the one for PTCDA/Cu(111). Since the benzene/Au distance should be similar to the pentacene/Au distance, these results suggest that a reasonable benzene/Au(111) distance is 2.95 Å, extrapolations for C_{60} gives a MO distance of 2.25 Å.

In order to calculate the electronic structure we have used Au double basis set of numerical atomic orbitals (NAOs) for Au $sp^3d^5s^*d^{*5}$, with the following cutoff radii (in a.u.): $s = 6$, $s^* = 6$, $p = 7$ and $d = 5$, $d^* = 5$; optimized $s = 4.5$, $p = 4.5$ (C); and $s = 4.1$ (H) [66]. These basis gives the following bond distances: C–C nearest neighbors distance in benzene of 1.40 Å (to be compared with the experimental value of 1.392 Å [67]) and C–C distance of 1.40 and 1.47 of C_{60} (to be compared with 1.39 and 1.44 obtained in DFT in a plane wave basis [57] and experimental values 1.40, 1.45 Å [68]), and a bulk gold lattice parameter of 4.16 Å (versus an experimental value of 4.07 Å [69]). Some deficiencies appear because we are not using a converged basis set; mainly, the molecular and metal levels are not correctly aligned at the experimental value (the experimental Au work function is 5.1 eV, and the C_{60} and benzene midgaps are 5.4 and 4.05 eV below the vacuum

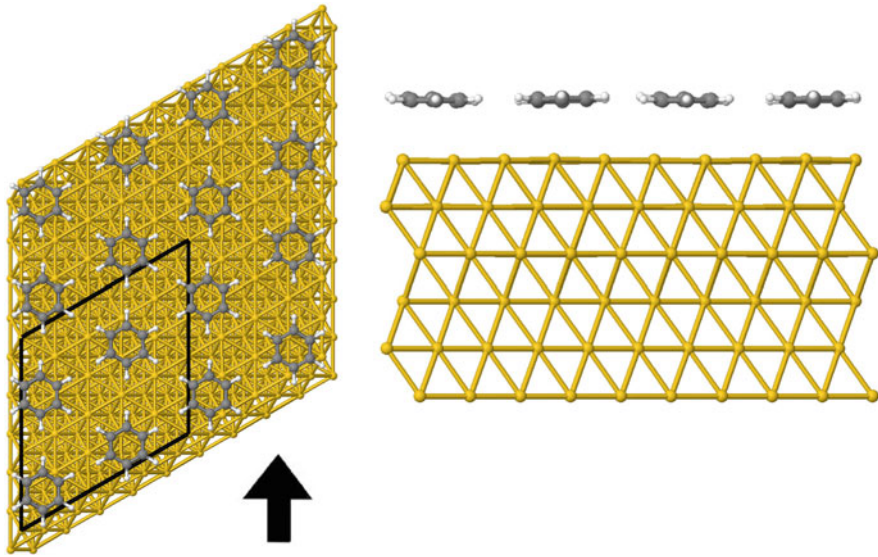


Fig. 3.17 (Color online) Model structure used for the benzene/Au(111)-interface (unit cell is highlighted). *Upper* and *side* view. Reprinted from [53] (Copyright 2009, Springer)

level respectively. Moreover, our HOMO–LUMO gap is 2.2 eV in C_{60} and 6.2 eV in benzene (instead of the plane wave converged values of 1.6 eV [59] and 4.7 eV [60] respectively). In order to have these levels correctly aligned and the correct LDA gap, we use the scissor operator (shown in Sect. 2.7.5) that allow us to shift by ε the molecular levels, and close the gap 2Δ where Δ is a (negative) quantity that closes the gap to the converged LDA gap. This way, direct comparison with plane wave DFT results is possible [57] It has been considered that the C_{60} mid gap coincides initially with the metal work function [61], while in benzene the mid gap is around 0.4 eV above Φ_M [14, 70]; in both cases, the initial HOMO-level is located with respect to the metal work function by correcting its experimental position at the interface by the measured interface potential). This has been achieved using the scissor operator.

3.5.2 Interface Potential with LDA Gap Calculations

IDIS Potential

Figure 3.18 shows our calculated DOS for the C_{60} /Au(111) interface, projected onto the atomic orbitals of C_{60} . It has been calculated using the one electron Green function of our hamiltonian, together with Eq. (A.24). In order to avoid numerical instabilities we have chosen a finite η of 0.01 eV in order to calculate the Green function [see (A.21)] In this figure we show the HOMO and LUMO levels, yielding

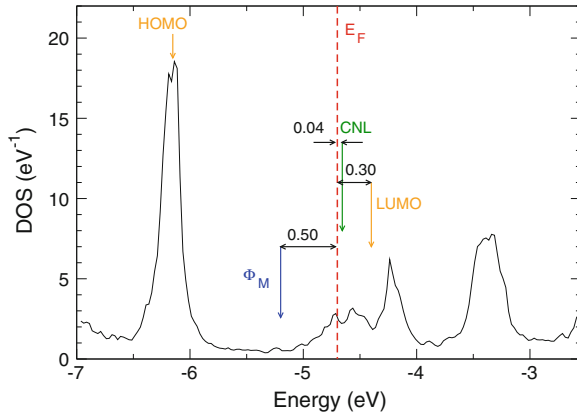


Fig. 3.18 (Color online) DOS per spin projected onto the C_{60} molecule for the $C_{60}/Au(111)$ interface. HOMO, LUMO, CNL, Φ_M and E_F are explicitly shown

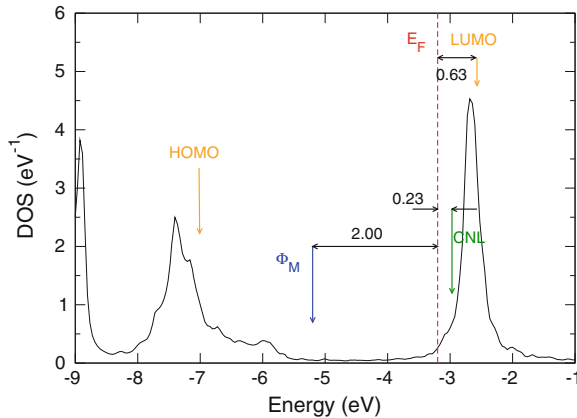


Fig. 3.19 (Color online) Averaged DOS per spin projected onto the benzene molecule for the benzene/ $Au(111)$ interface. HOMO, LUMO, CNL, Φ_M and E_F are explicitly shown

an energy gap of 1.8 eV; the initial Fermi level, Φ_M , which is located at the midgap; the final interface Fermi level, which is 0.50 eV above Φ_M , because of the induced interface potential $\Delta^{IDIS} = 0.50$ eV; and the CNL, which is calculated using (3.8). This CNL for C_{60} is found to be located 0.3 eV below the LUMO-level.

As the IDIS-potential, Δ^{IDIS} , is related to the screening parameter, S , by the Eq. (3.10) we deduce that $S = 0.08$, which represents a case with a rather large screening (consistent with the experimental results [54]).

In Fig. 3.19, we present our results for benzene/ $Au(111)$; the molecule DOS is an average upon the four molecules of the unit cell. The energy gap is 4.5 eV, and the initial Fermi level, Φ_M , is located 0.4 eV below the midgap [14, 70]. In our calculations, the CNL is located 0.4 eV below the LUMO level, and the interface

Fermi level is 2.0 eV above Φ_M . Notice that the HOMO level is much more broadened by the metal than the LUMO. From Eq. (3.10), we obtain the following screening parameter for benzene/Au(111), $S = 0.10$, which represents an interface with smaller screening than $C_{60}/Au(111)$ but still important.

Total Dipole

The Pauli repulsion, not included in the previous calculations, is going to be described by the ‘‘pillow’’ potential, Δ_0^P , as mentioned in Sect. 3.4.3. We have obtained the following values for these interfaces:

$$\Delta_0^P(C_{60}/Au(111)) = 3.3 \text{ eV} \text{ and } \Delta_0^P(\text{benzene}/Au(111)) = 1.0 \text{ eV}.$$

Using these values and the results given above we get the following total potentials:

$$\Delta^T(C_{60}/Au(111)) = S\Delta_0^P + \Delta^{IDIS} = 0.26 \text{ eV} + 0.50 \text{ eV} = 0.76 \text{ eV}.$$

$\Delta^T(\text{benzene}/Au(111)) = S\Delta_0^P + \Delta^{IDIS} = 0.1 \text{ eV} + 2.0 \text{ eV} = 2.1 \text{ eV}$. which should be compared with the experimental evidence. In the case of the $C_{60}/Au(111)$, $\Delta^T(C_{60}/Au(111) \text{ experimental}) = 0.6 \text{ eV}$ [61] in good agreement with our theoretical analysis; for benzene/Au(111), $\Delta^T(\text{benzene}/Au(111) \text{ experimental}) = 1.1 \text{ eV}$ [14]. So our calculations give an overestimated value of the interface dipole.

We should comment that it is very satisfactory that the case $C_{60}/Au(111)$ presents such good agreement: for this interface the LDA gap approximation is not such bad. The benzene/Au(111) is different: first of all, the molecule/metal distance we have used in our calculations was an educated guess. We have explored how the total potential changes with the benzene/metal distance. For instance, for 3.25 Å (the distance we obtain with an accurate *ab-initio* calculation, see 5.3), our results yield, $S = 0.29$, the CNL at the same position (a very robust level), and $\Delta^P = 0.4 \text{ eV}$, so that $\Delta^T = 1.50 \text{ eV (IDIS)} + 0.12 \text{ eV (pillow)} = 1.62 \text{ eV}$, closer to the experimental evidence [14], but still too large. The main point here is the great underestimation of the actual gap, that accurate calculations indicate that it is between 7.0–7.7 eV [52, 71] (that means, an underestimation of more than 3 eV), that reduces the potential Δ^t around 50%.

3.5.3 $C_{60}/Au(111)$ Interface with a Larger Gap

As it has been previously addressed, the HOMO–LUMO gap obtained in LDA is a poor approximation to the actual one, since it is systematically underestimated.

A deep look at the literature confirm us this fact. Direct measurement of the transport gap in C_{60} by STS made by Lu et al. [72] (see Fig. 3.20) show us that the actual gap is $2.7 \pm 0.3 \text{ eV}$, in agreement with theoretical calculations [59]. We

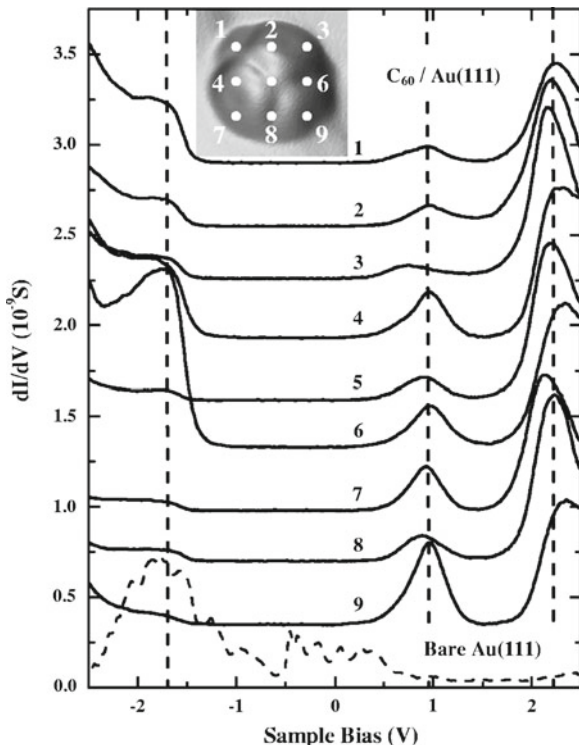


Fig. 3.20 dI/dV spectra of a single C_{60} molecule on $Au(111)$ at $T = 7$ K. Spectra 1–9 were taken at indicated spots on the inset image and are shifted vertically for clarity. Tunneling parameters were $V = 2.0$ V, $I = 1.0$ nA before taking the spectra. The *dashed spectrum* was obtained from the bare $Au(111)$ surface. (Image scale is $\sim 20 \times 20$ Å). Reprinted from [72] Copyright (2004) by the American Physical Society

have repeated the calculations of the DOS and IDIS potential for a gap $E_g = 2.5$ eV (using the scissor operator to tune it). The C_{60} -metal distance is taken to be 2.5 Å [57] and the work function is located 0.15 eV above the midgap.

Figure 3.21 shows our calculated DOS for the $C_{60}/Au(111)$ interface, projected onto the atomic orbitals of the organic molecule. In this figure we show the HOMO and LUMO levels, the initial (Φ_M) and the final Fermi levels (E_F). The IDIS potential (the difference between Φ_M and E_F) is $\Delta^{IDIS} = 0.61$ eV; and the organic CNL is located 0.45 eV from the LUMO-level so that, $CNL - E_F = 0.04$ eV.

The screening parameter S can be obtained changing fictitiously the initial Fermi level and calculating the corresponding change in the interface Fermi energy using (3.12), which is found to be 0.07 , very similar to the case obtained using Eq. (3.10). Regarding the “pillow” potential, it yields $\Delta_0^P = 1.9$ eV; so we get $\Delta^P = S\Delta_0^P = 0.14$ eV and $\Delta^T = 0.75$ eV. Note that these values are a different from the values obtained for the LDA gap.

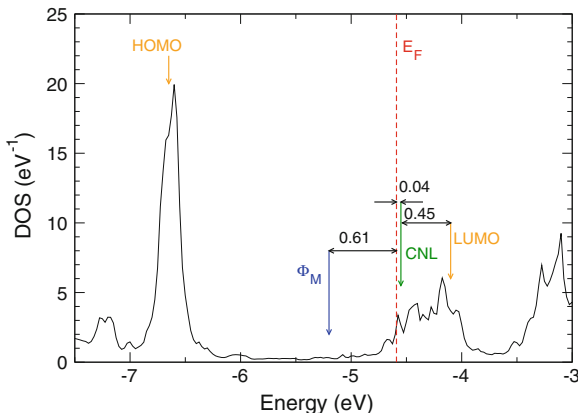


Fig. 3.21 (Color online) DOS per spin projected onto the C_{60} molecule for the $C_{60}/Au(111)$ interface with a gap of 2.5 eV. HOMO, LUMO, CNL, Φ_M and E_F are explicitly shown

3.5.4 Discussion

Despite our results are in reasonable agreement with experiments (at least for C_{60}), some details of the calculation can be improved. There is a list of some of them.

1. First of all, in previous section we showed that the correct value of the gap is critical to have a realistic interface potential. If we compare results for a C_{60} molecule with a gap of 1.8 and 2.5 (only 0.7 eV increment) we see that the IDIS potential changes from 0.50 to 0.61 (despite the $C_{60}/metal$ distance is larger), and the LUMO–CNL distance also increases from 0.25 to 0.45 eV. As we will see in Sect. 5.3, for the benzene case, the difference is dramatic. The potential reduces from 1.50 to 0.85 eV, and the LUMO–CNL distance is increased from 0.40 to 1.25 eV, showing that a LDA calculation in this case does not give correct quantitative results.
2. We have used an extended gold basis set in order to obtain a realistic pillow dipole. However, it is in the frontier of the valid basis for the FIREBALL method, the form of the output charge (2.26) relies on the assumption that the overlap is small enough to use the approximation ($\varphi_{i\alpha}^{Löwdin} = \varphi_{i\alpha}^{fireball}$) in the Hartree potential. This is the reason why the basis is not suitable for geometry calculations, due to forces are more sensitive to this fact. However, electronic structure calculations with more simple sp^3d^5 basis of cut-off radii (in a.u.) $s = 4.5$, $p = 4.9$, $d = 4.3$, show us that the difference in the total dipole is around 10%, within the error bar of our calculations and we can be sure that FIREBALL approximations work well for a basis set of this size. However, the screening parameter is greater, due to a smaller interaction between the metal and the molecule (because metal orbitals have smaller cutoff radius).

3. Calculation of the screening parameter S using (3.10) although gives good results, can be calculated more accurately using the definition in (3.12), as done in 3.5.3
4. Reliable distances have been obtained extrapolating other experimental or theoretical results. A fully ab-initio calculation of the distance is desirable.

The most important of this list is the first one. All along this thesis we will try to correct the deficiencies explained here.

3.6 The Gap Problem

Although in the previous section we have addressed the importance of a reliable gap for the C₆₀/Au(111) interface, we still do not have a systematic way to obtain realistic values for it without using techniques really expensive computationally. In this section we are going to point out the main ideas we have followed in order to correct it. In next chapter we will apply these ideas in the framework of the IDIS model in order to obtain in practice a realistic gap.

We can see the underestimation of the LDA gap using two complementary points of view. The first one is more physical, and has been introduced in the thesis in Sect. 2.7.2, the other one is based on mathematical properties of the energy functional in DFT. As explained in Sect. 2.7.4, in LDA, selfinteraction correction, due to interaction of an extra electron with the others, is not taken into account and the ionization potential and electron affinity are under and overestimated respectively. This allow us to write the gap in terms of the charging energy U^0 that arises from Coulomb repulsion between two electrons in the molecule.

$$E_g^t = E_g^{LDA} + U^0 \quad (3.24)$$

In this case we have not only SIC, but also image potential: our molecules are deposited over a metal, so the charging energy of the molecule is reduced (because of the interaction of the image charge, that weakens the interaction of the “real” charge). This can be taken into account by substituting U^0 by an effective image charge $U < U^0$.

Mathematically, the underestimation of the LDA gap is related with the derivative discontinuities in non-integer DFT. The exact value of the ground state energy should be piecewise linear with respect to the number of electrons [73], however, in standard local approximations it is not the case. So the derivative discontinuity Δ_{xc} defined as:

$$E_g^t = E_g^{KS,LDA} + \left\{ \left(\frac{\partial E_{xc}}{\partial N} \right)_{N=N+0^+} - \left(\frac{\partial E_{xc}}{\partial N} \right)_{N=N-0^+} \right\} = E_g^{KS,LDA} + \Delta_{xc} \quad (3.25)$$

is zero in LDA [74]. Sau et al., within the spirit of the LDA+U method, suggested the following correction to the LDA functional.

$$E[N + \delta n] \simeq E^{LDA}[N + \delta n] + \frac{U_{\pm}}{2} |\delta n| (1 - |\delta n|) \quad (3.26)$$

where δn is the fractional charge of the system ($0 < \delta n < 1$) and U_+ for $\delta n > 0$ and U_- for $\delta n < 0$ (that are closely related to the charging energy U). The quadratic term corrects the piecewise linearity of LDA, and allow us to obtain for integer values $E[N + 0, 1] \simeq E^{LDA}[N + 0, 1]$. If we apply Janak's theorem to this functional for the HOMO and LUMO levels of a molecule we get:

$$\begin{aligned} \left(\frac{\partial E}{\partial(\delta n)} \right)_{\delta n < 0} &\simeq \varepsilon_{HOMO}^{LDA} - \frac{U_{HOMO}}{2} \\ \left(\frac{\partial E}{\partial(\delta n)} \right)_{\delta n > 0} &\simeq \varepsilon_{LUMO}^{LDA} + \frac{U_{LUMO}}{2} \end{aligned} \quad (3.27)$$

We can relate $U_{HOMO,LUMO}$ (equivalent to $U_{-,+}$ respectively) with the charging energy U as $U = 1/2(U_{HOMO} + U_{LUMO})$. Note that these results are equivalent to the Eq. (2.103) obtained at Sect. 2.8.2, but for the molecular levels instead of the atomic ones.

Taking the second derivative $\frac{\partial^2 E}{\partial(\delta n)^2}$ when $\delta n \rightarrow 0$, and realizing that it is zero (since the total energy is piecewise linear with respect to the occupancy) we get:

$$U_i = \frac{\partial \varepsilon_i^{LDA}}{\partial(\delta n)} \quad (3.28)$$

for $i = \text{HOMO, LUMO}$ and $\delta n < 0, > 0$ respectively.

If we find an easy way to calculate the change on the molecular spectra due to the molecule charging, we will get U using this equation and we will be able to correct the LDA gap. As we will see in the next chapter this is straightforward within the IDIS model.

References

1. W.R. Salaneck, S. Stafstrom, J.L. Bredas, *Conjugated Polymer Surfaces and Interfaces: Electronic and Chemical Structure of Interfaces for Polymer Light Emitting Diodes*. (Cambridge University Press, Cambridge, 1996)
2. H. Ishii, K. Sugiyama, E. Ito, K. Seki, Energy level alignment and interfacial electronic structures at organic/metal and organic/organic interfaces. *Adv. Mater.* **11**(8), 605 (1999)
3. W.R. Salaneck, K. Seki, A. Kahn, J.J. Pirauex (eds.), *Conjugated Polymer and Molecular Interfaces* (Dekker, New York, 2002)
4. F. Flores, J. Ortega, H. Vázquez, Modelling energy level alignment at organic interfaces and density functional theory. *Phys. Chem. Chem. Phys.* **11**(39), 8658 (2009)
5. P. Samori, F. Cacialli (ed.), *Functional Supramolecular Architectures: For Organic Electronics and Nanotechnology* (Wiley-Vch, Weinheim, 2010)

6. S. Narioka, H. Ishii, D. Yoshimura, M. Sei, Y. Ouchi, K. Seki, S. Hasegawa, T. Miyazaki, Y. Harima, K. Yamashita, The electronic structure and energy level alignment of porphyrin/metal interfaces studied by ultraviolet photoelectron spectroscopy. *Appl. Phys. Lett.* **67**(13), 1899 (1995)
7. I.G. Hill, A. Rajagopal, A. Kahn, Y. Hu, Molecular level alignment at organic semiconductor-metal interfaces. *Appl. Phys. Lett.* **73**(5), 662 (1998)
8. H. Ishii, K. Sugiyama, D. Yoshimura, E. Ito, Y. Ouchi, K. Seki, Energy-level alignment at model interfaces of organic electroluminescent devices studied by UV photoemission: trend in the deviation from the traditional way of estimating the interfacial electronic structures. *IEEE J. Sel. Top. Quantum Electron.* **4**(1), 24 (1998)
9. D. Yoshimura, T. Yokoyama, E. Ito, H. Ishii, Y. Ouchi, S. Hasegawa, K. Seki, Electronic structures of Alq₃/LiF/Al interfaces studied by UV photoemission. *Synth. Met.* **1102**, 1145 (1999)
10. M. Knupfer, G. Paasch, Origin of the interface dipole at interfaces between undoped organic semiconductors and metals. *J. Vac. Sci. Technol. A* **23**(4), 1072 (2005)
11. S. Yanagisawa, Y. Morikawa, Theoretical investigation of the electronic structure of the Alq₃/Mg interface. *J. Phys. Condens. Matter* **21**(6), 64247 (2009)
12. X. Crispin, V. Geskin, A. Crispin, J. Cornil, R. Lazzaroni, W.R. Salaneck, J.-L. Brédas, Characterization of the interface dipole at organic/metal interfaces. *J. Am. Chem. Soc.* **124**(27), 8131 (2002)
13. P. Bagus, V. Staemmler, C. Wöll, Exchangelike effects for closed-shell adsorbates: interface dipole and work function. *Phys. Rev. Lett.* **89**(9), 96104 (2002)
14. G. Witte, S. Lukas, P.S. Bagus, C. Wöll, Vacuum level alignment at organic/metal junctions: "Cushion" effect and the interface dipole. *Appl. Phys. Lett.* **87**(26), 263502 (2005)
15. H. Vázquez, Y.J. Dappe, J. Ortega, F. Flores, Energy level alignment at metal/organic semiconductor interfaces: "pillow" effect, induced density of interface states, and charge neutrality level. *J. Chem. Phys.* **126**(14), 144703 (2007)
16. H. Vázquez, Energy level alignment at organic semiconductor interfaces. Ph.D. thesis, Universidad Autónoma de Madrid, 2006
17. H. Vázquez, R. Oszwaldowski, P. Pou, J. Ortega, R. Pérez, F. Flores, A. Kahn, Dipole formation at metal/PTCDA interfaces: role of the charge neutrality level. *Europhys. Lett.* **65**(6), 802 (2004)
18. H. Vázquez, F. Flores, R. Oszwaldowski, J. Ortega, R. Pérez, A. Kahn, Barrier formation at metal-organic interfaces: dipole formation and the charge neutrality level. *Appl. Surf. Sci.* **234**(1–4), 107 (2004)
19. A. Schuster, On unilateral conductivity. *Philos. Mag.* **48**(4), 251 (1874)
20. M.C. Desjonquères, D. Spanjaard, *Concepts in Surface Physics*. (Springer, Berlin, 1996)
21. E.H. Rhoderick, R.H. Williams, *Metal-Semiconductor Contacts*. (Oxford University Press, Oxford, 1988)
22. N.F. Mott, Note on the contact between a metal and an insulator or semi-conductor. *Math. Proc. Camb. Philos. Soc.* **34**(4), 568 (1938)
23. J. Bardeen, Surface states and rectification at a metal semi-conductor contact. *Phys. Rev.* **71**(10), 717 (1947)
24. A.M. Cowley, S.M. Sze, Surface states and barrier height of metal-semiconductor systems. *J. Appl. Phys.* **36**(10), 3212 (1965)
25. V. Heine, Theory of surface states. *Phys. Rev.* **138**(6A), A1689 (1965)
26. J. Phillips, Elementary excitations at metal-semiconductor interfaces. *Phys. Rev. B* **1**(2), 593 (1970)
27. E. Louis, F. Yndurain, F. Flores, Metal-semiconductor junction for (110) surfaces of zinc-blende compounds. *Phys. Rev. B* **13**(10), 4408 (1976)
28. C. Tejedor, F. Flores, E. Louis, The metal-semiconductor interface: Si (111) and zincblende (110) junctions. *J. Phys. C Solid State Phys.* **10**, 2163 (1977)
29. S. Louie, M. Cohen, Electronic structure of a metal-semiconductor interface. *Phys. Rev. B* **13**(6), 2461 (1976)

30. S. Louie, J. Chelikowsky, M. Cohen, Ionicity and the theory of Schottky barriers. *Phys. Rev. B* **15**(4), 2154 (1977)
31. J. Ihm, S. Louie, M. Cohen, Electronic structure of Ge and diamond Schottky barriers. *Phys. Rev. B* **18**(8), 4172 (1978)
32. W.E. Spicer, P.W. Chye, P.R. Skeath, C.Y. Su, I. Lindau, New and unified model for Schottky barrier and III-V insulator interface states formation. *J. Vac. Sci. Technol.* **16**(5), 1422 (1979)
33. K. Seki, N. Hayashi, H. Oji, E. Ito, Y. Ouchi, H. Ishii, Electronic structure of organic/metal interfaces. *Thin Solid Films* **393**(1–2), 298 (2001)
34. E. Ito, H. Oji, H. Ishii, K. Oichi, Y. Ouchi, K. Seki, Interfacial electronic structure of long-chain alkane/metal systems studied by UV-photoelectron and metastable atom electron spectroscopies. *Chem. Phys. Lett.* **287**(1–2), 137 (1998)
35. M. Yamamoto, Y. Sakurai, Y. Hosoi, H. Ishii, K. Kajikawa, Y. Ouchi, K. Seki, Structures of a long-chain n-alkane, n-C₄₄H₉₀, on a Au(111) surface: an infrared reflection absorption spectroscopic study. *J. Phys. Chem.* **104**, 7363 (2000)
36. N. Lang, Interaction between closed-shell systems and metal surfaces. *Phys. Rev. Lett.* **46**(13), 842 (1981)
37. N. Lang, A. Williams, Theory of local-work-function determination by photoemission from rare-gas adsorbates. *Phys. Rev. B* **25**(4), 2940 (1982)
38. Y. Chen, J. Cunningham, C. Flynn, Dependence of rare-gas-adsorbate dipole moment on substrate work function. *Phys. Rev. B* **30**(12), 7317 (1984)
39. Y. Hirose, A. Kahn, V. Aristov, P. Soukiassian, V. Bulovic, S. Forrest, Chemistry and electronic properties of metal-organic semiconductor interfaces: Al, Ti, In, Sn, Ag, and Au on PTCDA. *Phys. Rev. B* **54**(19), 13748 (1996)
40. H. Oji, E. Ito, M. Furuta, H. Ishii, Y. Ouchi, K. Seki, Metal-on-p-sexiphenyl films studied by electron spectroscopies. *Synth. Met.* **121**, 1721 (2001)
41. M. Fahlman, A. Crispin, X. Crispin, S.K.M. Henze, M.P.D. Jong, W. Osikowicz, C. Tengstedt, W.R. Salaneck, Electronic structure of hybrid interfaces for polymer-based electronics. *J. Phys. Condens. Matter* **19**(18), 183202 (2007)
42. P.S. Davids, A. Saxena, D.L. Smith, Nondegenerate continuum model for polymer light-emitting diodes. *J. Appl. Phys.* **78**(6), 4244 (1995)
43. P. Davids, A. Saxena, D. Smith, Bipolaron lattice formation at metal-polymer interfaces. *Phys. Rev. B* **53**(8), 4823 (1996)
44. I. Campbell, T. Hagler, D. Smith, J. Ferraris, Direct measurement of conjugated polymer electronic excitation energies using metal/polymer/metal structures. *Phys. Rev. Lett.* **76**(11), 1900 (1996)
45. W. Osikowicz, M.P. de Jong, S. Braun, C. Tengstedt, M. Fahlman, W.R. Salaneck, Energetics at Au top and bottom contacts on conjugated polymers. *Appl. Phys. Lett.* **88**(19), 193504 (2006)
46. F. Flores, C. Tejedor, Energy barriers and interface states at heterojunctions. *J. Phys. C Solid State Phys.* **12**, 731 (1979)
47. I.G. Hill, J. Schwartz, A. Kahn, Metal-dependent charge transfer and chemical interaction at interfaces between 3,4,9,10-perylenetetracarboxylic bisimidazole and gold, silver and magnesium. *Org. Electron.* **1**(1), 5 (2000)
48. A. Zangwill, *Physics at Surfaces*. (Cambridge University Press, Cambridge, 1988)
49. D. Newns, Self-consistent model of hydrogen chemisorption. *Phys. Rev.* **178**(3), 1123 (1969)
50. X. Crispin, Interface dipole at organic/metal interfaces and organic solar cells. *Sol. Energy Mater. Sol. Cells* **83**(2–3), 147 (2004)
51. E. Abad, J. Ortega, F. Flores, Metal/organic barrier formation for a C₆₀/Au interface: from the molecular to the monolayer limit. *Phys. Status Solidi. A* **209**, 636 (2012)
52. E. Abad, Y.J. Dappe, J.I. Martínez, F. Flores, J. Ortega, C₆H₆/Au(111): interface dipoles, band alignment, charging energy, and van der Waals interaction. *J. Chem. Phys.* **134**(4), 044701 (2011)
53. E. Abad, J. Ortega, Y.J. Dappe, F. Flores, Dipoles and band alignment for benzene/Au(111) and C₆₀/Au(111) interfaces. *Appl. Phys. A* **95**(1), 119 (2009)

54. J.O. Bockris, B.E. Conway, E. Yeager (eds.), *Comprehensive Treatise of Electrochemistry*, vol. 1. (Plenum Press, New York, 1980)
55. M. Fujihira, Photoinduced electron transfer and energy transfer in Langmuir–Blodgett films. *Adv. Chem. Ser.* **240**, 373 (1994)
56. E. Abad, J. Ortega, F. Flores, Density functional theory calculations and the induced density of interface states model for noble metals/C₆₀ interfaces. *J. Vac. Sci. Technol. B* **27**(4), 2008 (2009)
57. L.-L. Wang, H.-P. Cheng, Density functional study of the adsorption of a C₆₀ monolayer on Ag(111) and Au(111) surfaces. *Phys. Rev. B* **69**(16), 165417 (2004)
58. L.-L. Wang, H.-P. Cheng, Rotation, translation, charge transfer, and electronic structure of C₆₀ on Cu(111) surface. *Phys. Rev. B* **69**(4), 45404 (2004)
59. J. Sau, J. Neaton, H. Choi, S. Louie, M. Cohen, Electronic energy levels of weakly coupled nanostructures: C₆₀-metal interfaces. *Phys. Rev. Lett.* **101**(2), 26804 (2008)
60. K. Toyoda, Y. Nakano, I. Hamada, K. Lee, S. Yanagisawa, Y. Morikawa, First-principles study of benzene on noble metal surfaces: adsorption states and vacuum level shifts. *Surf. Sci.* **603**(18), 2912 (2009)
61. C.-T. Tzeng, W.-S. Lo, J.-Y. Yuh, R.-Y. Chu, K.-D. Tsuei, Photoemission, near-edge X-ray-absorption spectroscopy, and low-energy electron-diffraction study of C₆₀ on Au(111) surfaces. *Phys. Rev. B* **61**(3), 2263 (2000)
62. Jmol: an open-source Java viewer for chemical structures in 3D. <http://www.jmol.org/>
63. P. Han, B.A. Mantooth, E.C.H. Sykes, Z.J. Donhauser, P.S. Weiss, Benzene on Au[111] at 4 K: monolayer growth and tip-induced molecular cascades. *J. Am. Chem. Soc.* **126**(34), 10787 (2004)
64. N. Koch, A. Gerlach, S. Duhm, H. Glowatzki, G. Heimel, A. Vollmer, Y. Sakamoto, T. Suzuki, J. Zegenhagen, J.P. Rabe, F. Schreiber, Adsorption-induced intramolecular dipole: correlating molecular conformation and interface electronic structure. *J. Am. Chem. Soc.* **130**(23), 7300 (2008)
65. S. Duhm, A. Gerlach, I. Salzmann, B. Bröker, R. Johnson, F. Schreiber, N. Koch, PTCDA on Au(111), Ag(111) and Cu(111): correlation of interface charge transfer to bonding distance. *Org. Electron.* **9**(1), 111 (2008)
66. M. Basanta, Y. Dappe, P. Jelínek, J. Ortega, Optimized atomic-like orbitals for first-principles tight-binding molecular dynamics. *Comput. Mater. Sci.* **39**(4), 759 (2007)
67. J. Pliva, J. Johns, L. Goodman, Infrared bands of isotopic benzenes: ν_{13} and ν_{14} of 13C6D6. *J. Mol. Spectrosc.* **148**(2), 427 (1991)
68. C.S. Yannoni, P.P. Bernier, D.S. Bethune, G. Meijer, J.R. Salem, NMR determination of the bond lengths in C₆₀. *J. Am. Chem. Soc.* **113**(8), 3190 (1991)
69. A. Maeland, T. Flanagan, Lattice spacings of gold-palladium alloys. *Can. J. Phys.* **42**(11), 2364 (1964)
70. F. Ample, C. Joachim, A semi-empirical study of polyacene molecules adsorbed on a Cu(110) surface. *Surf. Sci.* **600**(16), 3243 (2006)
71. J.M. Garcia-Lastra, C. Rostgaard, A. Rubio, K.S. Thygesen, Polarization-induced renormalization of molecular levels at metallic and semiconducting surfaces. *Phys. Rev. B* **80**(24), 245427 (2009)
72. X. Lu, M. Grobis, K. Khoo, S. Louie, M. Crommie, Charge transfer and screening in individual C₆₀ molecules on metal substrates: A scanning tunneling spectroscopy and theoretical study. *Phys. Rev. B* **70**(11), 115418 (2004)
73. J.P. Perdew, M. Levy, J.L. Balduz, Density-functional theory for fractional particle number: derivative discontinuities of the energy. *Phys. Rev. Lett.* **49**(23), 1691 (1982)
74. P. Mori-Sánchez, A. Cohen, W. Yang, Localization and delocalization errors in density functional theory and implications for band-gap prediction. *Phys. Rev. Lett.* **100**(14), 146401 (2008)

Chapter 4

The IDIS Model at the Molecular Limit

4.1 Introduction

In the previous chapter we have shown that the IDIS model is a simple yet accurate model for predicting and studying energy level alignment at metal-organic interfaces, that appear in new organic electronic devices like OLEDs. However there are other systems where metal-organic interaction takes place, but are not an infinite metal-organic interface. This is the case of molecular electronics devices (where an organic molecule is attached to two metallic electrodes) [1–5], or individual molecules deposited over surfaces at extremely low coverage [6]. It should be desirable to extend our model to those kind of systems.

This extension is only valid if the physical interactions governing these systems have the same physical origin than in MO interfaces. This means that the induced interface states can occur *locally*, that is, there can be non extended states inside the organic gap. This is true if we consider them as states coming mainly from hybridization of metallic and organic states (an effect that can take place at the molecular limit). We will show that the lack of extended surface states does not affect our model.

When going from monolayer to molecular limit, a word of caution should be said. At molecular limit, the change on work function (the potential drop at the surface, considering it as a macroscopic quantity) is different than the potential that the molecule suffers due to MO interaction. Figure 4.1 shows schematically the difference between both. In the case of the IDIS model, the IDIS potential is the potential that a molecule suffers. The “macroscopic” work function is just the value given by formula (3.9) where the dipole is the total one (charge transfer + pillow + surface + intrinsic). The difference between both is clearly seen at extremely low coverage. The change of the macroscopic work function of the surface is negligible (we only have a few molecules over the metal surface); however, the molecule does suffer a potential drop due to the local dipole that appears between the metal and the molecule. In order to distinguish both quantities, from now on, we are going to consider Δ the change in macroscopic work function and V the local potential drop

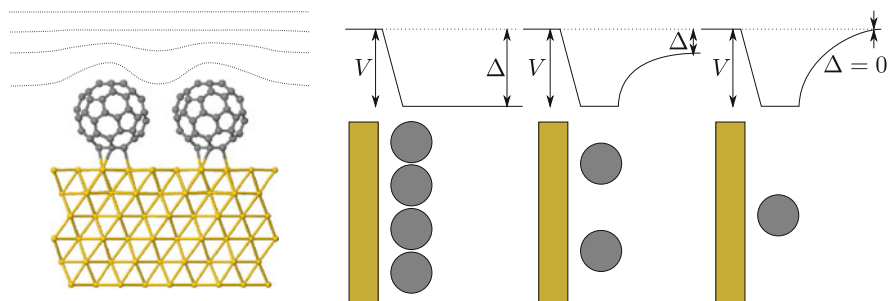


Fig. 4.1 *Left* Scheme of the difference between the rise in metal work function and the potential that the molecule suffers. The former is the measurement of the potential far away from the surface (when it is essentially flat, and makes sense talk about work function rise), while the latter is the potential that the molecule sees, that is not flat and can be very different from the former. At high coverages, potential curves tend to flatten very quickly and both quantities are essentially the same. *Right* Dependence on the average potential over a plane for different coverages. At high coverages, the potential does not depend on distance to the surface, and the origin of V is the interface dipole layer. For lower coverages, $V > \Delta$ and there is a distance dependence of the potential. At the limit of low coverages $\Delta = 0$ (since there is no dipole layer over the *whole* surface)

at the molecule. At high coverages, as the cases studied in previous chapter, both quantities are almost the same ($\Delta \simeq V$).

In the next section we are going to focus on a C_{60} molecule over Au(111) surface (where experimental results are available) and show that the IDIS model remains valid even if only one molecule is involved. In Sect. 5.2 we will see that this case can be considered as a limit of the IDIS model for low coverages. These results are an extended version of the work published in *Physica Status Solidi A* [16] (Copyright 2012 by WILEY-VCH Verlag).

4.2 C_{60} Molecule Over a Au(111) Surface

The adsorption of a C_{60} molecule over a Au(111) surface has been simulated with a 8×8 Au cluster with no periodicity and 4 layers. The cluster size has been checked to be high enough to avoid border effects. All C_{60} atoms and surface atoms (apart from the boundary gold atoms, and the last layer) have been allowed to relax. The adsorption distance has found to be 2.4 \AA (a complete discussion about the role of vdW interaction in this interface will be given in Sect. 5.2.1). In this case, we have used both for the geometric relaxation and for the electronic structure calculations an Au sp^3d^5 basis with the following cut-off radii (in a.u.): $s = 4.5$, $p = 4.9$, $d = 4.3$, that gives a lattice parameter of 4.12 \AA (compared with experimental value of 4.07 \AA [7]). The reason for this choice is to improve the accuracy/speed ratio of our calculations (not so important here, but critical for comparison with other results in Sect. 5.2.3). We have checked that our results are independent of basis choice

Fig. 4.2 Geometry of the 8×8 cluster without periodicity used for simulating a single molecule adsorbed over a gold surface (*upper* and *side* view)

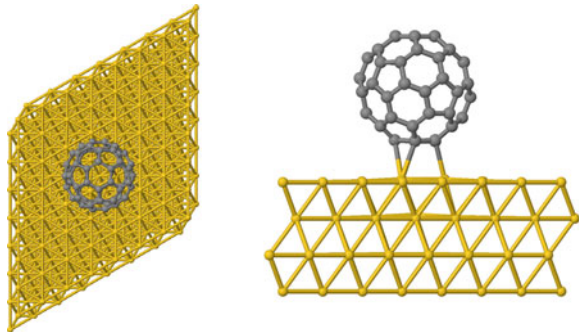
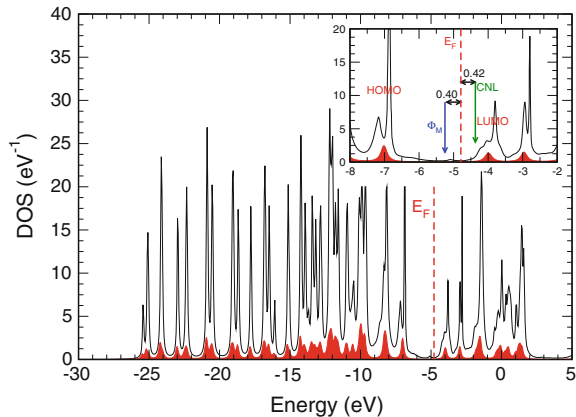


Fig. 4.3 DOS projected on the C₆₀ orbitals for the case of an isolated C₆₀ over a Au(111) surface. Molecular levels of the isolated (but deformed) molecule are indicated by red lines. *Right inset* enlarged image for the area around the Fermi level, showing HOMO, LUMO and CNL of the molecule, Φ_M and the Fermi level (E_F) of the system



changing the Au, C basis (see Sect. 5.3.5). The C basis set is the same as in previous calculations in Sect. 3.5. Regarding the gap, we have calculated an accurate value taking into account SIC and image potential, using the ideas presented in 4.2.1, obtaining $E_g^t = 3.1$ eV. This will be carefully explained in next section. Geometry has been shown in Fig. 4.2 and DOS in Fig. 4.3.

In this case, although the same formulas as in 3.5.2, (A.20) and (A.21), are used in order to calculate the DOS, a $\eta = 0.1$ eV for Au orbitals is introduced in order to correctly mimic the continuous DOS of the surface; and a $\eta = 0.001$ for C orbitals in order to get the peak-like DOS of the molecules. That is:

$$G_{jj}^{-1}(E) = H_{jj} - E + i\eta_j \begin{cases} \eta_j = 0.1 & \text{if } j \in \text{Au} \\ \eta_j = 0.001 & \text{if } j \in \text{C} \end{cases} \quad (4.1)$$

by this way, we obtain a more realistic DOS, and we avoid artifacts that appear when we take a η too high.

We are tempted to interpret the DOS in terms of the IDIS model, placing the CNL, Φ_M and IDIS potential (V^{IDIS} , remember the difference between V and

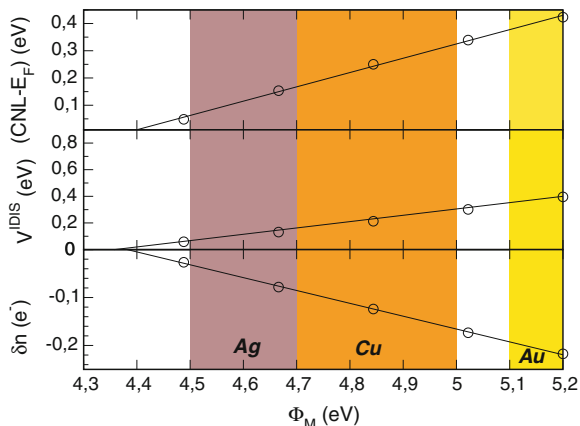


Fig. 4.4 Values of $CNL-E_F V^{IDIS}$ and δn versus the initial Fermi level for the C_{60} molecule over Au surface. Linear behavior support our assumption that the IDIS model is valid at the molecular limit

Δ), and calculating the screening parameter, obtaining $S = 0.53$. However, is this interpretation valid? We can check the validity of the IDIS model calculating S using not only Eq. (3.10) but also (3.12). If the movement of the Fermi level with respect to the work function behaves linearly, and the value of S coincides with the one calculated previously, the suitability of the IDIS model to describe this kind of metal/organic contact will be strongly validated.

Figure 4.4 shows perfect linearity, and the slope value is $S = 0.53$ too. So, IDIS model for low coverages can be considered valid. In Sect. 5.2 we will see a few more facts that strength the validity of the IDIS model at the molecular limit).

4.2.1 IDIS Based Calculation of Charging Energy

In Sect. 3.6 we presented the formula:

$$U_i = \frac{\partial \varepsilon_i^{LDA}}{\partial (\Delta n)} \quad (4.2)$$

obtained by Sau and coworkers [8] based on a LDA + U correction of the linearity of energy functional in DFT for non-integer numbers. It allows to calculate the charging energy if we calculate the movement of the HOMO and LUMO levels when we add or subtract some charge δn to the molecule. How can we do it when the molecule is not isolated but placed over a surface?

The answer is very simple if we think on the IDIS model. In this model naturally occurs an addition or subtraction of charge δn to the molecule (due to the charge

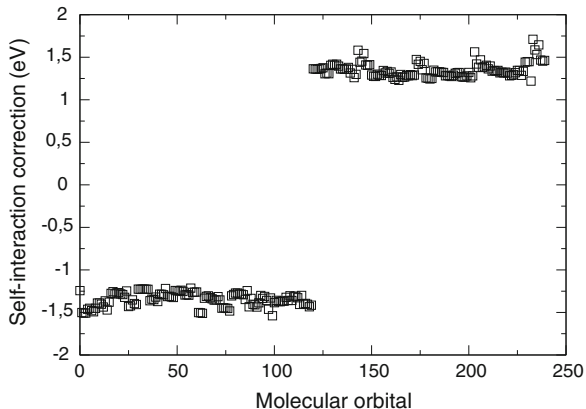


Fig. 4.5 Value of SIC using Koopmans' theorem, see Eq. (2.96), to the DFT level of isolated C₆₀ as a function to the molecular level. It can be seen that all values are around ± 1.4 eV

transfer). On the other hand, there is also a natural movement of the HOMO and LUMO levels (the potential drop due to the IDIS dipole), so in our case we can define:

$$U = \frac{\delta V^{IDIS}}{\delta n} \quad (4.3)$$

So using only IDIS parameters we can deal with the underestimation of the LDA gap and give a good approximation to the exact one without expensive methods like GW (that for long molecules such as PTCDA/Au(111) with 208 atoms or low coverage interfaces, such as C₆₀/Au(111) $5\sqrt{3} \times 5\sqrt{3}R30^\circ$, with 360 atoms) would be completely prohibitive.

Some words of caution need to be addressed here. First of all, in actual geometries there is no charge transfer from/to the HOMO/LUMO, but to the interface states that are around the CNL. That means that we are neither calculating U^{HOMO} , nor U^{LUMO} but a mixture of both. However, these charging energies should be very similar. Calculations of Koopmans' correction, using (2.96) show that this correction (that is actually the charging energy U^0) for free molecule in C₆₀ and benzene is more or less the same for all levels (other molecules, such as PTCDA were calculated in [9, 10]). That means that although we are taking interface states, that are mainly a mixture of HOMO and LUMO levels, we will obtain good results.

4.2.2 Practical Implementation

The formula can be written in a more practical way. If we consider that the density of states is more or less constant between the Fermi level and the CNL, that is what

actually happens (see Fig. 4.3); we can consider that $\delta n = \tilde{D}(\text{CNL} - E_F)$; where \tilde{D} is the average DOS. With this and (3.11) and (3.13) we obtain:

$$S = \frac{1}{1 + U\tilde{D}} \quad (4.4)$$

In this equation, $U\tilde{D}$ plays the same role that the term $4\pi e^2 d\tilde{D}/A$ does in the elementary theory of Schottky barriers (d is the effective distance between the positive and negative charge transferred between the metal and the molecule, and A the area per molecule). So, with the screening parameter and the average DOS at the Fermi Level we can obtain easily the charging energy. This formula is better for practical use in systems with small S and large broadening of the HOMO/LUMO levels because we can calculate S and \tilde{D} more exactly than V^{IDIS} . Note that S and \tilde{D} should change with the size of the gap: the larger the gap, the smaller the DOS at the Fermi Level (HOMO and LUMO broadened levels are farther to the Fermi level), and the larger the value of S (the screening is lower because the insulator character is higher). In our calculations, we have opened the gap with the scissor operator (Eq. 2.97) and recalculated S , \tilde{D} and U until we get a selfconsistent U .

Up to now we did not care about the metal “ U ” since it should be zero. However, the surface has been simulated using a cluster (so it is not longer a true metal but a very narrow gap semiconductor; so a small spurious “ U^{metal} ” will appear. In the 8×8 cluster, $U^{metal} \sim 0.2$ eV. This has to be taken into account. For example “ $V_{metal}^{IDIS} = U^{metal} \delta n$ ” is around 0.04 eV, so in order to calculate S or U this small spurious contribution has to be neglected (otherwise S will be 0.49, too small and $U = 1.8$ too high).

We have considered this by calculating $(\text{CNL} - E_F)$ for different initial Fermi levels, let’s say Φ_M and $\Phi_M + \Delta$. By virtue of Eq. (3.12) the screening parameter should be:

$$\begin{aligned} S &= \frac{(\text{CNL} - E_F)_{\Phi_M + \Delta} - (\text{CNL} - E_F)_{\Phi_M}}{(\Phi_M + \Delta) - \Phi_M} \\ &= \frac{(\text{CNL} - E_F)_{\Phi_M + \Delta} - (\text{CNL} - E_F)_{\Phi_M}}{\Delta} \end{aligned} \quad (4.5)$$

but as $U^{metal} \neq 0$ there is an spurious “IDIS potential” in the metal $V_{metal}^{IDIS} = \delta n U^{metal}$ that has to be subtracted. The corrected screening parameter S is then calculated via:

$$S = \frac{(\text{CNL} - E_F)_{\Phi_M + \Delta} - (\text{CNL} - E_F)_{\Phi_M}}{\Delta - V_{metal}^{IDIS}} \quad (4.6)$$

Last but not least, the surface potential (mentioned in Sect. 3.4.5) tends to reduce the gap, and this effect is not taken into account in our fireball code. So we need to calculate it using formula (3.23) and see how it changes with charge transfer. The actual value of U is $U = U^{fireball} - |U^{off-diag}|$ where $U^{off-diag}$ is:

$$U^{off-diag} = \frac{\delta V^{off-diag}}{\delta n} \quad (4.7)$$

When all this considerations are taken into account, we get for the isolated C₆₀ molecule over a gold “surface” (actually a cluster, as stated before) a value of 1.5 eV.

The discussion of the calculation of U for a finite coverage will be given in Sect. 5.2.

4.2.3 Calculation of Pillow and Surface Potential at Low Coverages

In previous sections we have seen that the interaction of a C₆₀ molecule with a gold surface can be understood in terms of the IDIS model, obtaining an IDIS potential $V^{IDIS} = (1 - S)(CNL - \Phi_M)$. However, to obtain a good picture of the interface not only the IDIS potential but also the pillow and the surface ones need to be calculated. There is no problem in calculating \mathbf{D}^{pillow} and $\mathbf{D}^{off-diag}$ but, what is the potential drop induced in the molecule due to these dipoles? In order to calculate that, we will guide us by the behavior of the IDIS potential. The difference on the pillow and surface potential ($\Delta^{P,off-diag}$) for high coverages and molecular limit can be calculated by taking into account that $\frac{1/S-1}{D}$ is the induced potential drop at the interface by one electron transferred from the molecule to the surface (see Eq. 3.7). So the difference between potential drops for high coverages and the molecular limit, is, in a first approximation:

$$\frac{V_{mol}^{P,off-diag}}{\Delta_{ML}^{P,off-diag}} = \frac{(1/S_{mol} - 1)D_{ML}}{(1/S_{ML} - 1)D_{mol}} \quad (4.8)$$

(D is the DOS at the Fermi Level). Applying this to the pillow potential we have obtained V_0^P 0.07 eV for the isolated molecule. The surface potential acts on the opposite way (tends to reduce $\Phi_M - E_F$) and is 0.03 eV for the molecule. Although these values are very small, $V_{mol}^{off-diag}$ play a significant role in calculating the actual gap of the system (see previous subsection).

4.2.4 C₆₀/Au(111) Gap Calculation: Summary and Conclusions

We are going to give a brief review of the contents of this section and how we have applied it to our system.

1. First of all we take the isolated molecule over the surface and calculate S correcting the effect of U^{metal} , and \tilde{D} as $\tilde{D} = \delta n / (CNL - E_F)$.
2. With S and \tilde{D} we obtain U using (4.4).

3. We use the scissor operator to open the gap from E_g^{LDA} to $E_g^t = E_g^{LDA} + U$. After that we recalculate S , \tilde{D} and U
4. We repeat steps 2 and 3 several times until we get an selfconsistent gap (*i. e.* we have a gap $E_g^t = E_g^{LDA} + U_1$ and with formula (4.4) we obtain $U_2 = U_1$)
5. We calculate the surface-potential $V^{off-diag}$ and $U^{off-diag}$ via Eqs. (3.23), (4.7) and (4.8). The final U is $U = U^{fireball} - |U^{off-diag}|$.

If we compare our predicted gap (3.1 eV) with other theoretical and experimental results, we get good agreement. Lu *et al.* [6] found an experimental value of 2.7 eV using STS (see Fig. 3.20); and Sau *et al.* [8] calculated a gap of 2.5 eV obtained using a similar approach as the one exposed here combined with a GW-like self-energy.

The advantage of this method is the much lower computational cost, as compared with standard approaches based on GW or other beyond-HF techniques. It has some details (the spurious V_{metal}^{IDIS} , the fact that we are not calculating $U^{off-diag}$) but we obtain reasonably good gaps (slightly overestimated). We need to say that, as we will see in Sect. 5.6, the use of an hybrid potential reduces the obtained gap due to exchange hole delocalization.

4.3 Application of the IDIS Model at the Molecular Level: C₆₀ Between Two Tips

In this section we are going to apply our IDIS model to a C₆₀ molecule between two gold tips. This section is adapted from the article published in *Organic Electronics* (Copyright 2010 by Elsevier). This work has been made with help and advice from César González [11].

Some work has also been addressed to understand the quantum dot formed by an isolated C₆₀-molecule located between two metallic tips [12–14], but in these references many-body corrections have been neglected. In our case we combine a DFT calculation at the LDA level of the geometry during the approach the two tips to the C₆₀ molecule, with an electronic structure analysis in terms of the IDIS model. Also, an study of the charging energy of the molecule U and its changes during the tips-C₆₀ approach have been done, applying the ideas presented in Sect. 4.2.1.

4.3.1 Mechanical Study

In our DFT simulations, the Au-tips consist of pyramidal-shape clusters of 46 Au atoms in a (111) geometry, with 3, 6, 10 and 27 atoms in the first, second, third and last layer respectively [15] (see Fig. 4.6). The basis set used is the same as in previous calculations of Sect. 4.2. The contact formation is analyzed by approaching each Au-tip in steps of 0.1 Å; after each step the atoms are relaxed to their corresponding minimum energy positions, except the atoms in the last Au-layer of both tips, which

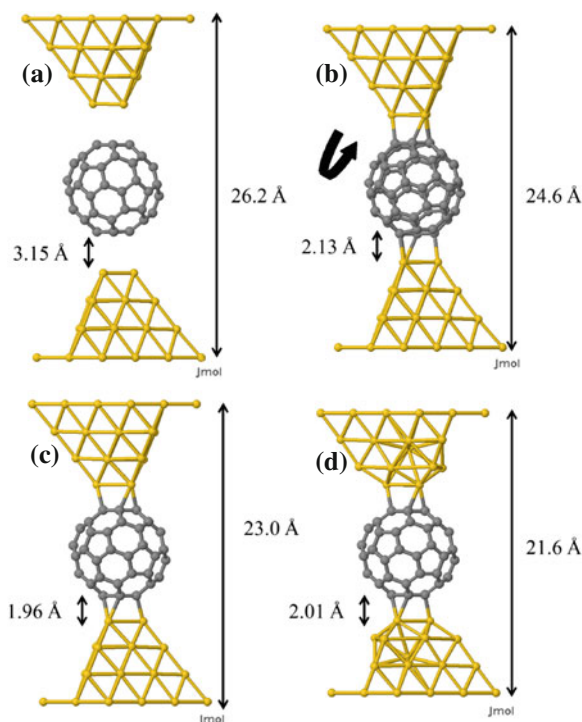
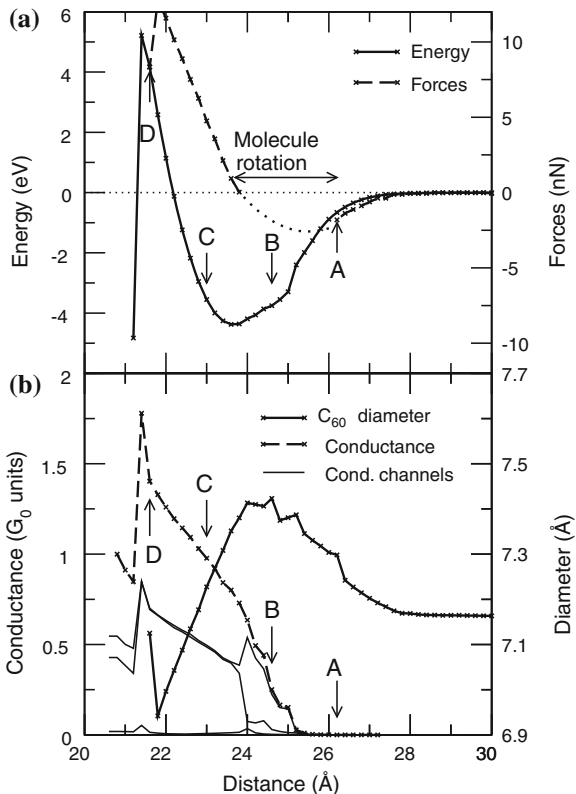


Fig. 4.6 Geometry of the tip/C₆₀/tip system for different values of the distance d between the fixed Au-layers. The arrow in case (b) suggests how the molecule rotates. Reprinted from [11]. Copyright (2010) from Elsevier

are fixed. We have also calculated electrical conductance of the system at each step of the deformation process using the Keldysh–Green’s function formalism explained in Sect. 2.6, for a molecule between two electrodes, together with the first-principles hamiltonian obtained after the relaxation.

Figure 4.6 shows the calculated geometry of the tip/C₆₀/tip contact as a function of the distance, d , measured between the fixed Au-layers of both tips. Initially (Fig. 4.6a), C₆₀ is attracted by the tips, its diameter increasing along the tip-tip direction (see Fig. 4.7b). The buckyball suffers, however, a slight rotation (Fig. 4.6b) in the attractive region between distances $d = 23.7$ and 26.4 Å where the molecule jumps between different minima in such a way that the force cannot be calculated as the derivative of the energy (in Fig. 4.7a this is represented by a dashed line for the force which is only a guide to the eye, calculated smoothing the energy curve). When the force is ~ 0 , the C₆₀ returns to its original orientation, and after that, the molecule starts to be compressed (Fig. 4.6c), shortening its diameter along the tip-tip direction. Eventually, the tips starts to break (Fig. 4.6d). Notice also that the maximum attractive energy for one interface is 2.2 eV, and that the maximum attractive force is (probably) in the order of 3.8 nN; as expected, this force is around twice the one calculated for

Fig. 4.7 **a** Energy, forces and **b** conductance at the Fermi level and the diameter of C_{60} along the contact direction, for the system shown in Fig. 4.6 as a function of the distance d

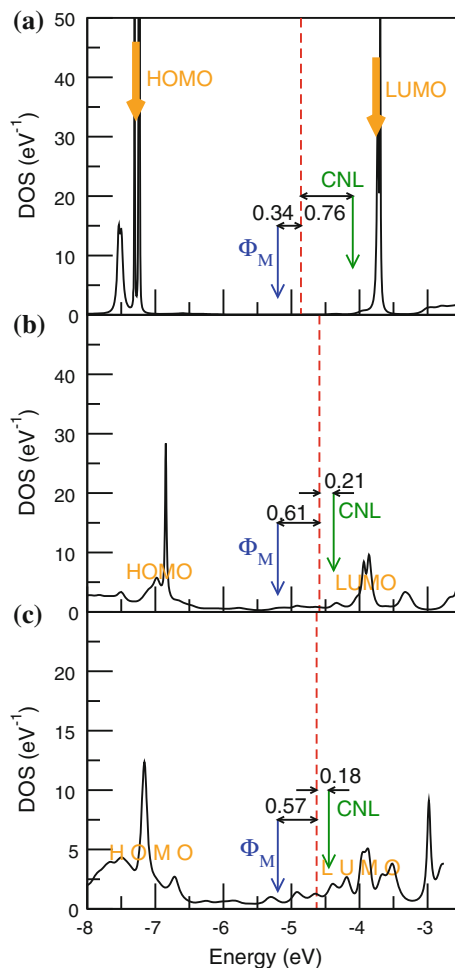


a tip/nanotube contact of the same diameter [15]. Van der Waals forces are found to be small (see discussion in [16] and Sect. 5.2.1).

The conductance at the Fermi level of the tip/ C_{60} /tip contact (Fig. 4.7b) shows a maximum of $1.8G_0$ in the compressive region, while it is $\sim 0.8G_0$ for the equilibrium position. For long distances, $d > 25.7 \text{ \AA}$, 3 channels contribute equally to the conductance, as corresponds to the three orbitals of the LUMO level while, due to the symmetry breaking of that level, only two channels contribute at short distances. At intermediate distances only one channel dominates the conductance due to the rotation of the molecule.

We should comment here that the conductance has been calculated with the corrected hamiltonian (with the scissor operator) so the molecular gap is the realistic one: calculations without this correction lead to a maximum value of $2G_0$ (the difference ratio is larger when the distance between tips increase).

Fig. 4.8 (a–c) DOS (per spin) as a function of energy for geometries (a–c) in Fig. 4.6. Each case shows: HOMO, LUMO and CNL levels, as well as the initial (Φ_M) and final (E_F) Fermi levels



4.3.2 Electronic Analysis: Unified IDIS Model and Self-Interaction Correction

Figure 4.8 shows the density of states projected on the C₆₀ orbitals for the cases a, b and c of Fig. 4.6. For each case, the HOMO and LUMO levels, the molecule CNL, the initial (Φ_M) and final (E_F) Fermi levels are shown. As in the case of a single C₆₀ molecule adsorbed on a gold surface, the tip/C₆₀/tip contact reacts creating a mean potential, V^t , between the tips and the molecule that tries to align the organic CNL and the metal work-function. In case a, since the “pillow” dipole is negligible, that potential is created only by the charge transfer between the two materials that is, $V^t = V^{IDIS}$.

In Fig. 4.8a, $CNL - \Phi_M = 1.1$ eV and $V^{IDIS} = 0.34$ eV, so that $S = 0.7$. As in other cases, we have checked that the screening parameter is the same using Eqs. (3.10) and (3.12). We have calculated the transport energy gap by means of the method exposed in Sect. 4.2.1, using Eq. (4.4). In this case $U = 2.0$ eV, so the transport energy gap has been fitted to 3.6 eV by means of the scissor operator presented on 2.7.5. Moreover, using this scissor operator, the Au work function has been placed 0.3 eV above the midgap.

Note that this gap differs from the gap of 3.1 eV found for a molecule over a metal surface. This means that the gap of the molecule depends on the geometric details of the structure; the gap over a metal surface is different than the gap between two metal tips.

In cases b and c the distance ($CNL - \Phi_M$) = 0.82 (b), 0.75 (c) eV has been reduced to ($CNL - E_F$) = 0.21 (b) and 0.18 (c) eV, so the IDIS potential is 0.61 (b) and 0.57 (c) eV and the screening parameter $S = 0.26$ (b) and 0.24 (c), indicating that in these two cases, for small tip-C₆₀ distances the interface screening is much more effective than in case a, saturating around the energy minimum. Moreover our selfconsistent calculations yield the following values of U : 1.6 (b) and 1.3 (c) eV, and the following transport energy gaps: 3.2 eV (b) and 2.9 eV (c), as can be approximately appreciated from the strongly broadened HOMO and LUMO levels of those figures.

Regarding the pillow potential, in these cases it is not so small, so the total potential has pillow contribution too. The corresponding values of V_0^P for cases b and c are 0.45 and 0.96 eV respectively, that are screened to $SV_0^P = V^P = 0.12$ eV (b), 0.23 eV (c). Note that in this last case, the pillow potential is able to change the charge transfer direction (in Sect. 5.2.6 we suggest that this mechanism can be present also in C₆₀/Au(111) monolayer).

Finally, a word of caution about $U^{off-diag}$ should be addressed here. We are now dealing with a tip instead of with a complete surface so the change in U due to the off-diagonal surface potential will be smaller. Since we know that in the whole surface case the change in U is not bigger than 10%, we can expect here that $U^{off-diag} < 0.1$ eV and we did not include it.

4.3.3 Conclusions

We have applied the IDIS model, that was originally applied to metal/semiconductor interfaces (organic and inorganic) to a complete different field: molecular electronics. We have shown that the IDIS model help to interpret the electronic structure of the system, and allow us to calculate a realistic gap where both the SIC and the image potential are taken into account. Note that here, a semi-classical calculation of the image potential¹ is not an easy task. Also is important to note that, the gap of the molecule depends on the tip-molecule distance. Moreover, the Au geometry also influences the gap size. This will be explicitly pointed out in next section but these

¹ As for example in [17], Sect. 5.8.2.

results suggest the same: note that we obtain the same U for a C₆₀/tip distance of $\sim 2 \text{ \AA}$ than for a C₆₀/surface distance of $\sim 2.4 \text{ \AA}$, that suggests that the image potential in the surface case is higher for the same C₆₀/Au distance.

In conclusion, our method allow us to correct the gap in molecular electronic systems (very important, for example, to calculate a realistic conductance of the device) without too much computational cost (our system has 152 atoms; a number of atoms that makes other methods, like GW, prohibitively expensive).

4.4 Barrier Formation for a Tip/C₆₀/Au(111) Configuration

In this section we will study another nanogap organic molecular junction formed by a C₆₀ molecule in-between a Au-tip and a Au(111)-surface. As in the previous case, we first calculate the atomic geometry of the tip/C₆₀/Au(111) nanocontact as a function of the tip-surface distance, but for different molecule adsorption sites. The electronic structure, barrier height formation and charging energy are analyzed using the IDIS model. Our results are shown to be in good agreement with the experimental evidence. This work has been published in *Journal of Physics: Condensed Matter* in collaboration with Dr. José Ignacio Martínez [18]; and this section is an adapted version of it (Copyright 2010 by IOP publishing).

4.4.1 Geometry Calculations

The Au tip is the same as considered in Sect. 4.3 and the surface is simulated using the 8×8 cluster mentioned before. The basis set is the same as the one used from 2 tips/C₆₀ and C₆₀/surface calculations. As in previous sections, all atoms are free to relax apart from the cluster boundaries and the first tip layer.

Figs. 4.9 and 4.10 show the calculated geometries of the tip/C₆₀/Au(111) contact for different tip/metal distances. Figure 4.9 shows three cases (a, b and c) for a long tip/metal distance (26.2 \AA), with the molecule adsorbed on the tip, on the Au surface, or located in the mid-point between the tip and the surface. In our calculations, the adsorption on the tip is the most favorable one with an adsorption energy of around 1.3 eV , while on the surface the molecule is only bound by 0.3 eV , and in case (c) by 1.0 eV . These values for the adsorption energies cannot be expected to be very accurate, because of the minimal basis used in the calculations; moreover, for an accurate calculation of the adsorption energies, one should include vdW energy that have not been analyzed in this paper [15, 16]. However, vdW forces will not change the geometries very much as will be shown in 5.2.1.

Figure 4.10 shows cases (d–f): two of them (d and e) correspond to an intermediate tip/metal distance (25.4 \AA) and the last one (f) to the shortest distance (24.6 \AA). For the intermediate distance, the molecule has been assumed to be adsorbed either on the tip or the surface, the adsorption on the tip being again energetically more favorable,

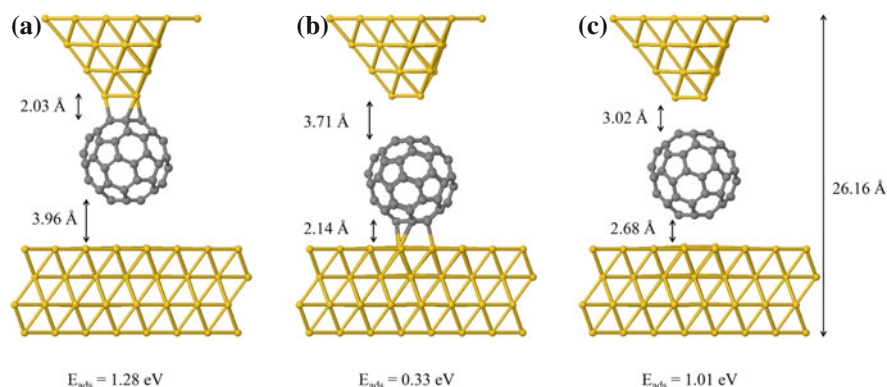


Fig. 4.9 Relaxed geometries, and adsorption energies, for a C_{60} molecule in-between a Au-tip and a Au(111)-surface: configurations (a–c). In these three cases the distance between the Au-tip upper layer and the Au(111) lower layer is 26.16 Å. Reprinted with permission from [18]. Copyright IOP publishing 2010

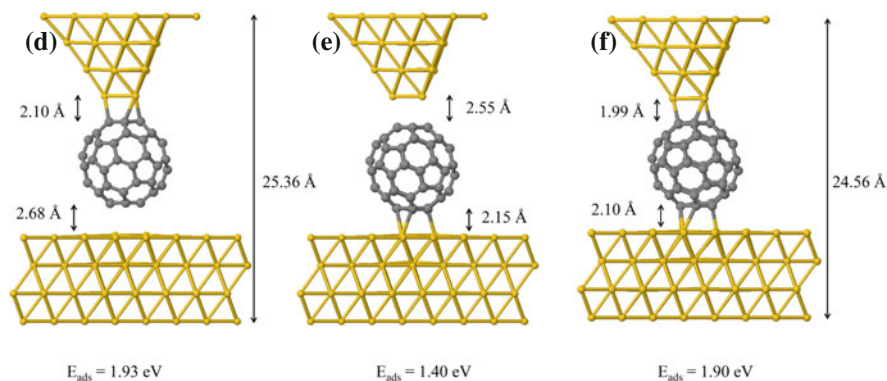


Fig. 4.10 Relaxed geometries, and adsorption energies, for a C_{60} molecule in-between a Au tip and a Au(111) surface: configurations (d–f). In configurations (d, e) the distance between the Au-tip upper layer and the Au(111) lower layer is 25.36 Å while it is 24.56 Å for case (f). Reprinted with permission from [18]. Copyright IOP publishing 2010

while for the shortest distance only one case is possible with the molecule touching simultaneously the tip and the surface. After obtaining the desired geometries, we analyze the barrier height formation and the charging energy for the cases a–f. As in the tip/ C_{60} /tip configuration, the work function is placed 0.3 eV above the gas-phase C_{60} midgap (both for the tip and for the surface).

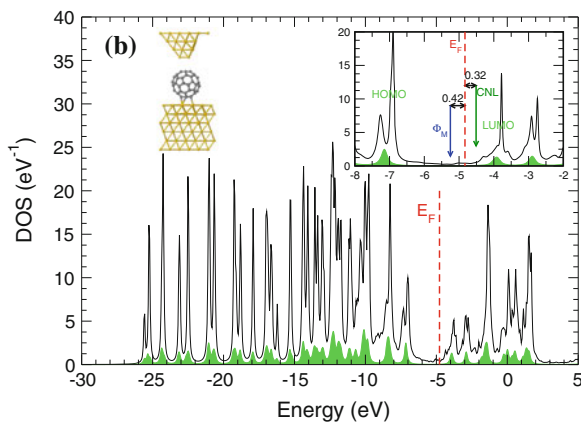


Fig. 4.11 DOS (per spin) projected on the C₆₀ orbitals for the geometry **b** of Fig. 4.9 (*left inset*). Molecular levels of the isolated (but deformed) molecule are indicated by green shaded region. *Right inset*: enlarged image for the area around the Fermi level, showing HOMO, LUMO and CNL of the molecule, Φ_M of non-interacting gold electrodes, and Fermi level (E_F) of the system

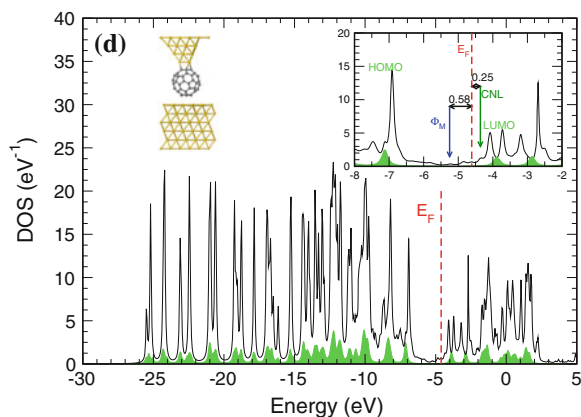


Fig. 4.12 As Fig. 4.11 for the geometry **(d)** of Fig. 4.10 (*left inset*)

4.4.2 Barrier Formation and Charging Energy

Figures 4.11, 4.12 and 4.13 show the DOS projected on the C₆₀ orbitals for the cases b, d and f of Figs. 4.9 and 4.10, for the molecule adsorbed either on the surface or on the tip (DOS of cases a and e are similar to d and b). At this stage we have neglected the “pillow” potential. In a further step (to be discussed later), we have analyzed how this “pillow” potential changes the interface Fermi level and the junction barrier height.

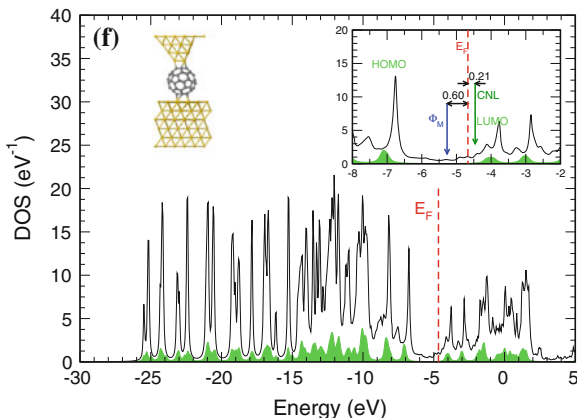


Fig. 4.13 As Fig. 4.11 for the geometry (f) of Fig. 4.10 (left inset)

Table 4.1 Screening parameter, S (dimensionless), difference between the charge neutrality level and the Fermi energy, $CNL - E_F$ (in eV), and U (in eV) for all the configurations analyzed in this study (cases a–f)

Quantity / case	(a)	(b)	(c)	(d)	(e)	(f)
S	0.36	0.43	0.56	0.30	0.33	0.26
$CNL - E_F$ (eV)	0.28	0.32	0.54	0.25	0.26	0.21
U (eV)	1.66	1.47	1.67	1.61	1.46	1.39

The right insets of Figs. 4.11, 4.12 and 4.13 show for each case the DOS around the energy gap, the initial Fermi level, Φ_M (which is taken to be the same for the tip and the surface), the LUMO and HOMO levels, as well as the CNL, and the Fermi energy E_F (dashed lines) as obtained from our DFT-calculations (with the corrected gap $E_g^t = E_g^{LDA} + U$).

As in previous cases, we are going to deal with this system using the IDIS model, that has been proved to be valid at the molecular limit. Table 4.1 shows our results for S and $(CNL - E_F)$, for the different structures of Figs. 4.9 and 4.10. In our calculations, the strongest screening ($S = 0.26$) appears for case f, when the molecule is encapsulated between the tip and the surface. This is expected: in this case the interaction is the highest one. S increases for larger tip-metal distances (smaller screening) and, for the same tip-metal distance, the smallest screening appears with the molecule on the surface (case b versus case a), or in between the tip and the metal (case c versus cases a and b). The values of $CNL - E_F$ follow a similar trend, with $CNL - E_F$ smaller for larger screening (S smaller); in all these calculations, $CNL - \Phi_M$ is around 0.8 eV, except for case c where $CNL - \Phi_M = 0.95$ eV a little larger, probably because of a slight molecule stretching. Notice also that in all the DOS the LUMO level is about 0.6 eV above the CNL.

Table 4.2 α parameter (dimensionless), V_0^{pillow} (in eV), SV_0^{pillow} and $CNL - E_F$ (in eV) for all the configurations analyzed in this study (cases a-f)

Quantity / case	(a)	(b)	(c)	(d)	(e)	(f)
α	0.51	0.27	0.95	0.43	0.51	0.36
V_0^{pillow} (eV)	0.83	0.43	0.05	0.61	0.49	0.94
SV_0^{pillow} (eV)	0.30	0.18	0.03	0.18	0.16	0.25
$CNL - E_F$ (eV)	-0.01	0.14	0.51	0.07	0.09	-0.04

We should stress that, in these calculations, the transport energy gap (the HOMO-LUMO energy difference) has been fitted selfconsistently with theory presented in 4.2.1.

4.4.3 Pillow Potential

Up to this point, we have neglected the ‘‘pillow’’ potential. For a symmetric case, with similar interfaces on both sides of the molecule (like the case of C₆₀ between two symmetrical tips), the analysis of the ‘‘pillow’’ effect is simple, tending to move upwards by the same amount the initial Fermi levels of both tips.

In a non-symmetric junction, the ‘‘pillow’’ potentials of both interfaces, say $V_0^{pillow-tip}$ and $V_0^{pillow-surf}$, tend to shift differently the tip and metal Fermi levels. In a DFT-calculation, we have to move the Fermi levels accordingly and recalculate how the barrier height has changed. Our results can be interpreted in terms of $V_0^{pillow-tip}$ and $V_0^{pillow-surf}$, introducing an ‘‘average’’ pillow potential, V_0^{pillow} , which we define by:

$$V_0^{pillow} = (\alpha V_0^{pillow-tip} + (1 - \alpha) V_0^{pillow-surf}). \quad (4.9)$$

Using this effective pillow potential, we can use the standard Eq. (3.17) to calculate how the pillow effect changes the barrier height, or equivalently, $CNL - E_F$. We stress that the parameter α can only be obtained by means of a first-principles calculation.

In Table 4.2 we include the values of SV_0^{pillow} for the different geometries of Figs. 4.9 and 4.10. $CNL - E_F$ are reduced to the values indicated in Table 4.2 Notice that in our case (b), the LUMO level is located around 0.75 eV above the corrected E_F ; in Lu *et al.* [6] (the experimental realization of this case) $LUMO - E_F$ is about 0.95 ± 0.2 eV in reasonable agreement with our results.

4.4.4 Conclusions

We have presented here DFT calculations of a tip/C₆₀/Au(111) system that simulates the STM/STS measurement of a buckyball molecule on a Au surface. This system

can also be considered as a particular representation of a quantum dot, whereby an organic molecule is encapsulated between two electrodes. We have calculated the absorption geometries and energies of the system, finding that the C₆₀ molecule prefers to attach to the tip rather than to the surface. We have also analyzed in detail the metal/organic barrier formation, the molecule charging energy and the DOS of the molecule at the interface. In particular, using the IDIS model, we have calculated the screening parameter, S , the induced potential V^{IDIS} , the “pillow” potential and the charging energy, U , as a function of the distance between the C₆₀ molecule and the tip and/or surface, and of the absorption site. This charging energy allow us to correctly calculate the molecule transport energy gap and its DOS. Note that for the same distance, the gap is smaller when molecule is attached to the surface than when it is attached to the tip. Our results are shown to be in good agreement with the experimental evidence.

4.5 Conclusions

In the first part of this chapter we have shown that the IDIS model for metal/organic interfaces is valid not only at the monolayer limit but also at the molecular limit.

Moreover, the IDIS model allow us to correct the underestimation of the LDA gap. We consider that the actual transport energy gap is $E_g^t = E_g^{LDA} + U$, where U is the charging energy of our system. We can obtain the charging energy as the change on the molecular levels position due to the change in the molecular charge. In the IDIS model, this change on molecular levels position is because of the IDIS potential V^{IDIS} and the charge change is the charge transfer, so in a first approximation $U = \delta V^{IDIS} / \delta n$.

Finally we show some examples of the use of the IDIS model at the molecular level. The first one, a C₆₀ molecule over a Au(111) surface, illustrates the validity of the IDIS model at this limit and its usefulness to obtain reliable values of the charging energy. In the second one we study two Au tips approaching to a C₆₀ molecule, calculating the relaxed geometry and the change on the IDIS parameters when the C₆₀/tips distance changes. We see, as expected, that the IDIS and pillow potentials increase when we decrease the distance. Also the gap decrease when we decrease the distance, due to the image potential is stronger for shorter distances. In the last one, we present a tip/C₆₀/surface, and calculate the IDIS parameters for different tip/surface distances and for different adsorption sites (the C₆₀ adsorbed on the tip or on the surface). We see that the molecule prefers to be attached at the tip, and that the screening and the molecular gap are higher when it is attached to it.

References

1. B. Xu, N.J. Tao, Measurement of single-molecule resistance by repeated formation of molecular junctions. *Science* **301**(5637), 1221 (2003)
2. N.J. Tao, Electron transport in molecular junctions. *Nat. Nanotechnol.* **1**(3), 173 (2006)

3. M. Kiguchi, O. Tal, S. Wohlthat, F. Pauly, M. Krieger, D. Djukic, J. Cuevas, J. van Ruitenbeek, Highly conductive molecular junctions based on direct binding of benzene to platinum electrodes. *Phys. Rev. Lett.* **101**(4), 46801 (2008)
4. M. Reed, C. Zhou, C. Muller, T. Burgin, J. Tour, Conductance of a molecular junction. *Science* **278**(5336), 252 (1997)
5. M. Ruben, A. Landa, E. Lörtscher, H. Riel, M. Mayor, H. Görls, H.B. Weber, A. Arnold, F. Evers, Charge transport through a cardan-joint molecule. *Small* **4**(12), 2229 (2008)
6. X. Lu, M. Grobis, K. Khoo, S. Louie, M. Crommie, Charge transfer and screening in individual C₆₀ molecules on metal substrates: a scanning tunneling spectroscopy and theoretical study. *Phys. Rev. B.* **70**(11)115418 (2004)
7. A. Maeland, T. Flanagan, Lattice spacings of gold-palladium alloys. *Can. J. Phys.* **42**(11), 2364 (1964)
8. J. Sau, J. Neaton, H. Choi, S. Louie, M. Cohen, Electronic energy levels of weakly coupled nanostructures: C₆₀-metal interfaces. *Phys. Rev. Lett.* **101**(2), 26804 (2008)
9. H. Vázquez, Energy level alignment at organic semiconductor interfaces. Ph.D. thesis, Universidad Autónoma de Madrid, 2006
10. F. Flores, J. Ortega, H. Vázquez, Modelling energy level alignment at organic interfaces and density functional theory. *Phys. Chem. Chem. Phys.* **11**(39), 8658 (2009)
11. E. Abad, C. González, J. Ortega, F. Flores, Charging energy, self-interaction correction and transport energy gap for a nanogap organic molecular junction. *Org. Electron.* **11**(2), 332 (2010)
12. J. Palacios, Coulomb blockade in electron transport through a C₆₀ molecule from first principles. *Phys. Rev. B.* **72**(12), 125424 (2005)
13. J. Palacios, A. Pérez-Jiménez, E. Louis, J. Vergés, Fullerene-based molecular nanobridges: a first-principles study. *Phys. Rev. B.* **64**(11), 115411 (2001)
14. N. Sergeev, A.A. Demkov, H. Guo, Inelastic resonant tunneling in C₆₀ molecular junctions. *Phys. Rev. B.* **75**, 233418 (2007)
15. C. González, J. Ortega, F. Flores, D. Martínez-Martín, J. Gómez-Herrero, Initial Stages of the contact between a metallic tip and carbon nanotubes. *Phys. Rev. Lett.* **102**(10), 106801 (2009)
16. E. Abad, J. Ortega, F. Flores, Metal/organic barrier formation for a C₆₀/Au interface: from the molecular to the monolayer limit. *Phys. Status Sol A* **209**, 636 (2012)
17. M. C. Desjonquères, D. Spanjaard, *Concepts in Surface Physics*. Springer-Berlin (1996)
18. E. Abad, J.I. Martínez, J. Ortega, F. Flores, Barrier formation and charging energy for a variable nanogap organic molecular junction: a tip/C₆₀/Au(111) configuration. *J. Phys. Condens. Matter* **22**(30), 304007 (2010)

Chapter 5

Results for Various Interfaces: C₆₀, Benzene, TTF, TCNQ and Pentacene over Au(111)

5.1 Introduction

In the previous chapter, we have extended the IDIS model to the molecular limit: we have shown how, applying the ideas exposed in Sect. 3.6 to the IDIS model we can correct the underestimation of the LDA gap and get a realistic value for an organic molecule over a metal surface, where both the SIC and the image potential contribute to the size of the gap. We have also employed all these ideas for two systems of technological and scientific interest: a C₆₀ molecule between two gold tips (as an example of the application of this method to molecular electronics) and a tip/C₆₀/surface (as a typical STM-like configuration).

Now we want to extend these ideas and correct the molecular gap in MO interfaces in order to obtain realistic values for the electron and hole injection barriers. Moreover, the correction of the LDA hamiltonian will allow us to obtain realistic STM images (like the TTF over gold surface one in Sect. 5.4).

In the following section we will revisit the C₆₀/Au(111) interface for various coverages, and show the variation of the IDIS parameters when going from the monolayer to the molecular limit, strongly supporting the validity of this model for all coverages. Then, these findings will be applied to other interfaces: benzene, TTF, TCNQ and pentacene over Au(111).

5.2 C₆₀/Au(111) Interface at Various Coverages

The C₆₀/Au(111) interface has been studied both at the monolayer limit (with a LDA gap) in Sect. 3.5.2 and at the molecular limit in Sect. 4.2. Now we are going to recalculate the monolayer with the gap obtained in Sect. 4.2. We will study not only the $2\sqrt{3} \times 2\sqrt{3}R30^\circ$ monolayer, but also lower coverages. This will allow us to see how the IDIS parameters (screening parameter and IDIS potential) behaves when we change the interface coverage, and compare the molecular case with the limit of low

coverages. This section is an adapted and extended version of the article published in *Physica Status Solidi A* [1] (Copyright 2012 WILEY-VCH Verlag).

5.2.1 Geometry

Regarding the C_{60} /Au geometry we are going to consider the effect of vdW interactions that were neglected in the systems of Chap. 4. Definitely it plays an important role in adsorption energy calculations: the C_{60} molecule is very big, and the interaction energy from the carbon atoms located far away the gold surface is not accurately obtained in standard LDA. However, the forces that govern the C_{60} /Au distance are not supposed to be too much affected by the inclusion of vdW forces (the Au–C covalent distance is 2.1 Å, and the adsorption distance is 2.4 Å). In order to measure the effect of the vdW forces we have calculated the relaxed geometries and the C_{60} /Au distance using both the standard LDA approach and the weak chemical interaction (WCI) energy described in Sect. 2.7.1.

Figure 5.1 shows our results for the adsorption energy of a C_{60} ML on Au(111): the black line represents our DFT-LDA energy, while the blue line corresponds to the WCI result. These two curves can be considered as two limiting cases for the short-range C_{60} –Au interaction (basically the interaction of Au and the six nearest C atoms of C_{60}): the WCI corresponds to weakly interacting systems, and the LDA to covalently bonded systems. In order to obtain the total adsorption energy we must add the long-range vdW interactions to this short-range energy. The C_{60} –Au vdW interaction [calculated via Eq. (2.83)] is the result of many distant C–Au atom–atom interactions (the damping function $f_D(R)$ eliminates the contributions for C–Au atom pairs at closer distances). The purple and red curves in Fig. 5.1 show the energies calculated adding the vdW energy to both short-range curves. The C_6 coefficients for the C–Au pair of atoms have been calculated using London theory as a guide to extrapolate the coefficient as calculated for the C–C interaction on graphitic materials [2]. This approximation for the C_6 coefficient has already been used successfully in other systems [3] where a value $C_6 = 36 \text{ eV} \cdot \text{Å}^6$ is obtained. The damping factor is chosen as $f_D(R) = 1/(1 + \exp(-d(R/R_{vdW}) - 1))$ and $R_{vdW}(\text{Au–C}) = 4.1 \text{ Å}$ and $R_{vdW}(\text{C–C}) = 3.8 \text{ Å}$ following the ideas of [4]. The minimum energy for the LDA + vdW result (purple curve) is located at a distance z (between the upper Au-layer and lower C-atoms of C_{60}) of $\sim 2.3 \text{ Å}$, and at $\sim 2.6 \text{ Å}$ for the WCI + vdW one (red curve). The adsorption energy is 2.2 eV and 1.9 eV, respectively; for comparison, the experimental value is 1.87 eV [5]. This good agreement is probably fortuitous because of the minimal basis set used in our calculations; in particular, our LDA-adsorption energy is around 0.8 eV smaller than the one calculated using a LDA plane-wave converged basis [6], while a LDA-approach yields adsorption energies typically a few tenths of eVs larger than a GGA-calculation. Moreover, taking $R_{vdW}(\text{Au–C}) = 3.3 \text{ Å}$ and $R_{vdW}(\text{Au–C}) = 2.9 \text{ Å}$ [7] in the long range vdW damping factor yields $z \sim 2.2 \text{ Å}$ (LDA + vdW) and $\sim 2.4 \text{ Å}$ (WCI + vdW), with adsorption energies of 2.9 and 2.5 eV, respectively. Notice that the adsorption energies change significantly

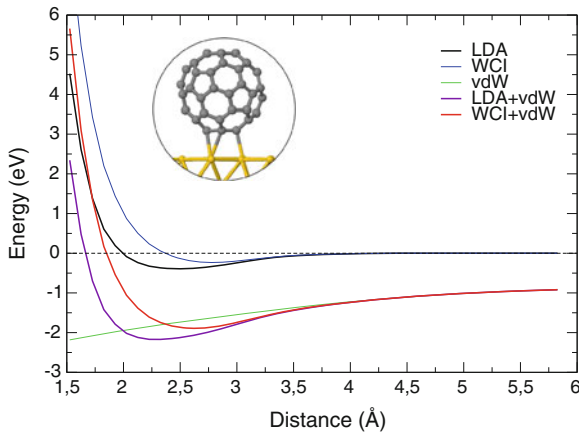


Fig. 5.1 Adsorption energy for a C₆₀ monolayer on Au(111) as a function of the distance between both subsystems, for several approximations. *Black line* standard LDA-FIREBALL. *Blue line* WCI-FIREBALL calculation. *Green line* vdW correction. *Purple line* LDA Fireball + vdW correction (good approximation at small distances). *Red line* WCI + vdW correction (good approximation at large distances) (Color figure online)

when changing the value of R_{vdW} , while the equilibrium distance is much less affected. This suggests that the actual C₆₀–Au(111) equilibrium distance should be in between the z values obtained in the LDA + vdW and WCI + vdW calculations. We conclude that 2.4 Å (the initial LDA guess) is a good guess to the distance between C₆₀ and Au(111).

The C₆₀–C₆₀ interaction is a constant that we calculate from reference [8], including the damping factor $f_D(R)$ (with $R_{vdW}(C-C) = 2.9$ Å [7] or 3.8 Å [4], and $d = 20$).

5.2.2 The $2\sqrt{3} \times 2\sqrt{3}R30^\circ$ Monolayer

Figure 5.2 shows the molecular local DOS for the $2\sqrt{3} \times 2\sqrt{3}R30^\circ$ geometry and the location of Φ_M , E_F , CNL and the HOMO and LUMO levels. The basis set is the same as Sect. 4.2 and the gap is also 3.1 eV, since C₆₀–C₆₀ interaction (the difference between both cases) does not change the gap size. Notice that the few peaks below the HOMO level are in good agreement with the ones observed in angle-resolved valence-band photoemission spectroscopy for a monolayer of C₆₀ on Au(111) [5].

It is important to notice that the quantity (CNL – Φ_M) is the same for the molecular and monolayer limit (0.8 eV). However (CNL – E_F) is different, because S changes ($S = 0.19$). It is significantly smaller than in the case of the single molecule on the surface. This is related to the interaction between C₆₀ molecules, that enhances screening. Another point of view is that, as CNL and Φ_M are “fixed” parameters, and as CNL – E_F increases, charge transfer increases (since charge transfer $\delta n =$

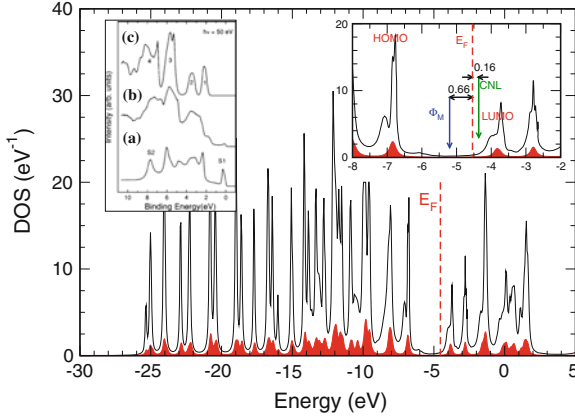


Fig. 5.2 DOS projected on the C_{60} orbitals for the case of the $2\sqrt{3} \times 2\sqrt{3}R30^\circ$ $C_{60}/Au(111)$ monolayer. Molecular levels of the isolated (but deformed) molecule are indicated by *red lines*. *Right inset* enlarged image for the area around the Fermi level, showing HOMO, LUMO and CNL of the molecule, Φ_M and the Fermi level (E_F) of the system. *Left inset* Experimental angle-resolved valence-band photoemission spectra from **a** Au(111), **b** annealed 1 ML of C_{60} on Au(111) and **c** 3 ML of C_{60} on Au(111), from [5] (Copyright 2000 by the American Physical Society). Features 1 and 2 stand for HOMO and HOMO-1, respectively, for the 3 ML film

$\tilde{D}(CNL-E_F)$), that means that for molecular case, where we don't have depolarizing effect (whose origin is parallel dipole-dipole interaction), dipoles are higher, that implies greater charge transfer, and bigger $CNL-E_F$ distance, so S is greater, by virtue of Eq. (3.10). Then, IDIS potential also decreases. Moreover, if we compare this S with the one obtained in Sect. 3.5.3 we realize that it is bigger. It can be explained by three differences between both calculations. The first one is that the gap is higher in this case (3.1 compared with 2.5), the second one is the use of a different basis (in Sect. 3.5.3 the gold basis was an extended $sp^3d^5s^*d^{*5}$ one), and finally, the way of calculating DOS is different: instead of using a global $\eta = 0.01$, we use different η for the molecule and the surface Eq. (4.1) and the CNL position slightly changes.

5.2.3 IDIS Parameters for Various Coverages

In $C_{60}/Au(111)$ we have calculated not only the IDIS parameters for a monolayer, but also for other lower coverages. In this section we are going to study the $m\sqrt{3} \times m\sqrt{3}R30^\circ$ interfaces for $m = 3, 4, 5$ (for the sake of comparison we include $m = 2$ case, studied above). We want to see how the IDIS parameters change when we change the coverage. We can expect that S will increase monotonically, and the IDIS potential decreases, linking the monolayer and molecular cases.

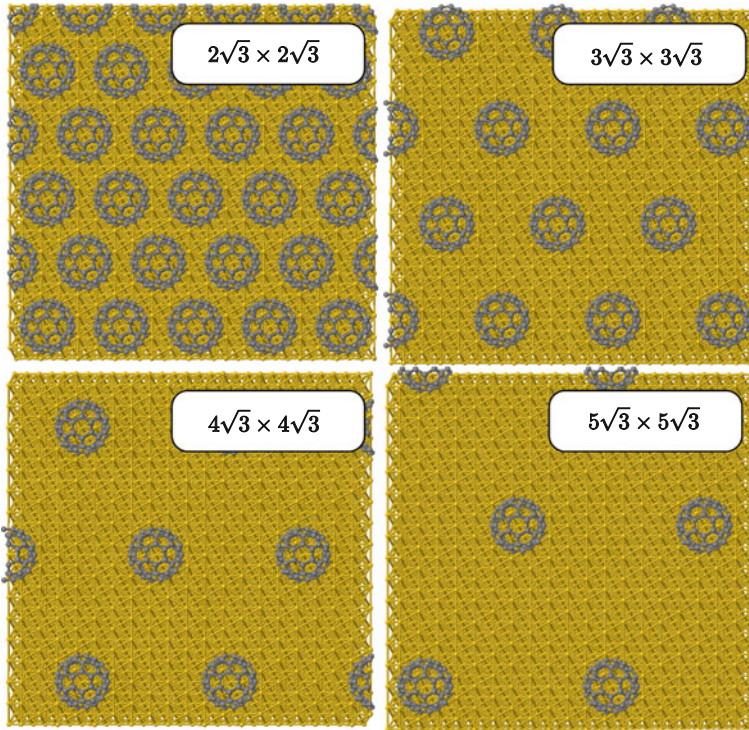


Fig. 5.3 Geometry of different coverages used in this work (Color figure online)

In Fig. 5.4 we show the DOS projected on C₆₀ around Fermi level for this coverages. As we expect, the value of CNL- E_F increases monotonically with decreasing coverage. The same occurs with S (increases as coverage decreases, that means, the screening is lower) that has values of 0.19, 0.23, 0.29 and 0.31 for $m = 2, 3, 4, 5$. In Fig. 5.5 we can see the tendency of S with C₆₀-C₆₀ distance (i.e. with coverage). It is worth to mention that, the CNL position is practically the same, 0.8 eV, above the initial metal Fermi level (-5.2 eV), in all coverages, with an error bar of ± 0.02 eV.

From Fig. 5.5 we can expect a $S = 0.39$ for the limit of extremely low coverage (that means, an isolated molecule). Direct calculations gave us $S = 0.53$, not too far. Moreover, a look insight in our prediction model (explained in Sect. 5.2.4) show that a better extrapolation gives $S = 0.50$, much similar to the computed $S = 0.53$, that enhances the idea that the molecular MO interaction can be seen as a limit for low coverages of the IDIS model.

As we did on the molecular limit, we have calculated S using Eq. (3.12) to check that the change of CNL- E_F with respect to CNL- Φ_M is linear and compares well with calculations using Eq. (3.10). Figure 5.6 shows perfect linearity, and the slope values are the same as obtained in the other way. Moreover, in all cases CNL = E_F at approximately $-\Phi_M = 4.4$ eV (that is, shifting the initial Fermi level 0.8 eV with

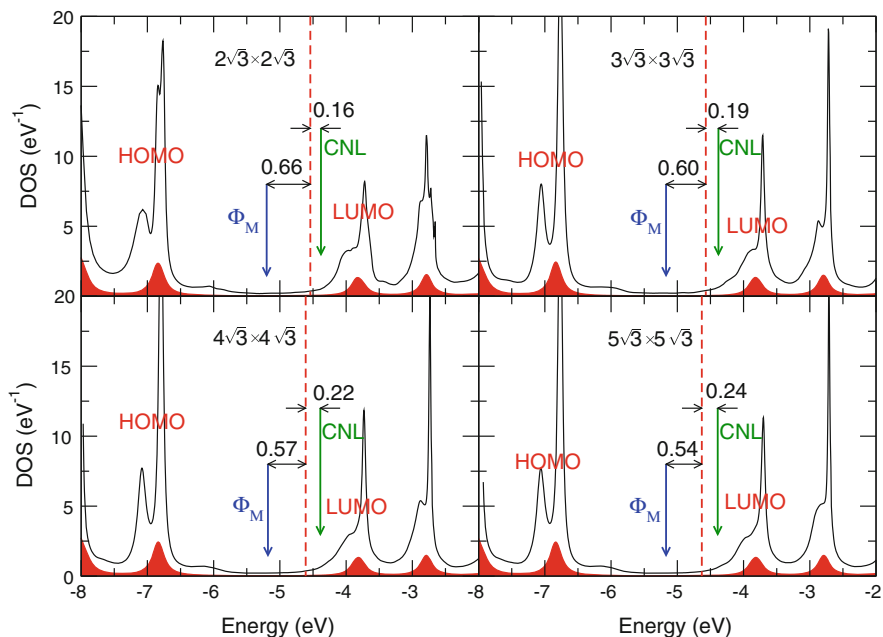


Fig. 5.4 DOS projected on the C_{60} near Fermi level (E_F) for the $m\sqrt{3} \times m\sqrt{3}R30^\circ$ coverages ($m = 2, 3, 4, 5$) discussed in the text. HOMO, LUMO, Fermi Level, CNL and Φ_M are shown. Molecular levels of the isolated (but deformed) molecule are indicated by red shaded region

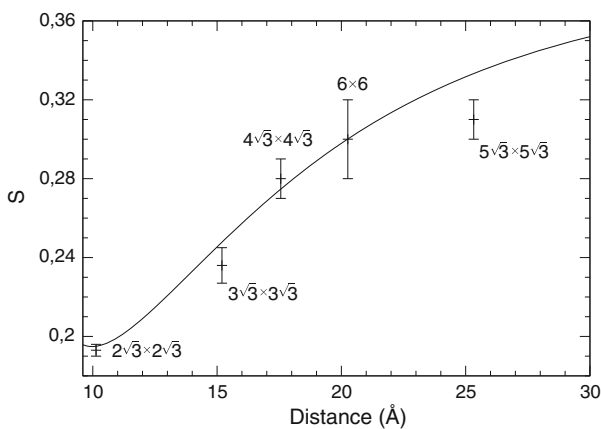


Fig. 5.5 Screening parameter versus distance between centers of nearest C_{60} for different coverages. The *straight line* corresponds to a theoretical fitting (see Sect. 5.2.4 and Fig. 5.8). S for a 6×6 interface has also been calculated to obtain a better fitting

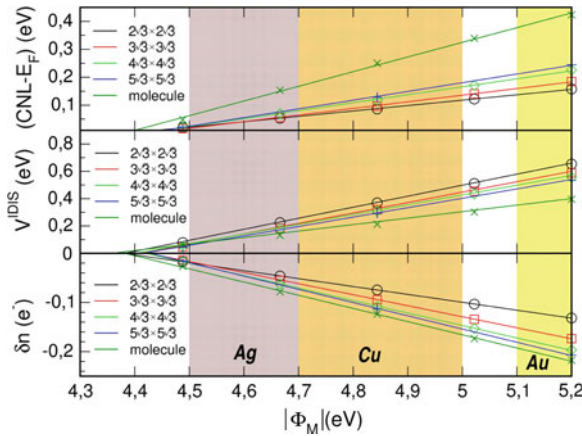


Fig. 5.6 Values of $(\text{CNL}-E_F)$, V^{IDIS} and δn versus the initial Fermi level, for the different interfaces analyzed. The values of $\text{CNL}-E_F$ and V^{IDIS} have an error bar of ± 0.03 eV; for δn the error bar is ± 0.003

respect to the gold one). This agrees very good with the $\text{CNL}-\Phi_M$ distance of 0.8 eV that appears in Fig. 5.4. This shows the validity of the IDIS models for all coverages, including the molecular limit.

5.2.4 Charging Energy for High Coverages

When we want to calculate the charging energy in a periodic system we need to be cautious. In the case of a layer of molecules, the formula Eq. (4.3) does not give the real charging energy of the molecule, but an effective one (U^{eff}) that cannot be used to correct the gap. The physical meaning of U^{eff} is how the HOMO and LUMO levels change due to charge transfer from the Au to the C₆₀ monolayer. The difference is that, while the correct U of a molecule on a periodic system should be calculated by transferring charge from (to) the metal to (from) *one* molecule, what we have when we use Eq. (4.3) is that the transfer of charge is from (to) the metal to (from) the *whole layer*. That means that other effects, like dipole-dipole interaction between different molecules, are included (although they shouldn't). Somehow, in a OO (Hubbard) language $U^{eff} = U + \sum_i J_i$ where J_i is the coulomb interaction between different molecules. An scheme is shown in Fig. 5.7. The value of U^{eff} for different $m\sqrt{3} \times m\sqrt{3}R30^\circ$ structures with $m = 2, 3, 4$ and 5 is $U^{eff} = 4.8, 3.3, 2.7$ and 2.35 eV, ($U^{off-diag}$ is not taken into account). After the introduction of this effect they are reduced to $U^{eff} = 4.4, 3.0, 2.4$ and 2.1 eV.

We can also calculate U^{eff} as a function of C₆₀-C₆₀ distance. We expect $U^{eff} = U + C/d^3$ (due to J_i is mainly a dipole-dipole interaction), or $U^{eff} = U + A/d^3 + B/d^4$ if we want to include more multipole terms. In Fig. 5.8 we represent this dependence of U^{eff} .

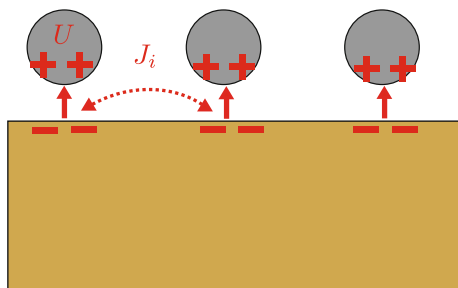


Fig. 5.7 Scheme of the difference between U , the change in molecular levels due to the charge transfer from *one* molecule (the one in the *left side*), and U^{eff} . The latter includes change in molecular levels due to the interaction with the dipole formed in adjacent molecules created by the charge transfer to those molecules (Color figure online)

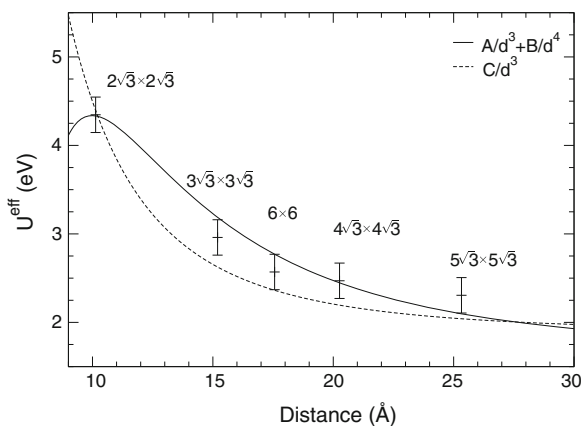


Fig. 5.8 Corrected U^{eff} values versus distance between centers of nearest C_{60} for different coverages. The values have been adjusted to a $A/d^3 + B/d^4$ curve suggested by the multipole electrostatic interaction between molecules; a fitting including only a d^{-3} term has also been shown. A 6×6 geometry has been added in order to get a better fitting of the curve

We have made some internal checks to our model. First of all, we have plotted U^{eff} versus C_{60} – C_{60} distance, and adjust it to a $U^{eff} = U + A/d^3 + B/d^4$ curve, obtaining good agreement (we have checked that the B/d^4 term is more critical if the molecule–metal and molecule–molecule distance is smaller). Comparing the value of charging energy calculated for an isolated molecule over the surface in Sect. 4.2.2 ($U = 1.5$ eV) and the value obtained by U^{eff} versus distance fitting ($U = 1.6$ eV) we check that the calculation of U^{eff} is consistent with our assumptions. In practice, for the other molecules studied in the thesis, we obtain U at the molecular level, since a complete study of U^{eff} at different coverages in order to fit the value of U demands too much time and computational resources.

From this behavior of U^{eff} we can predict also the value of the screening parameter for different coverages. As stated before, we can calculate it from Eq. (4.3) so:

$$U^{eff} = \frac{\delta V^{IDIS}}{\delta n} \Rightarrow S = \frac{1}{1 + U^{eff} \bar{D}} \quad (5.1)$$

and, as shown in Fig. 5.8, $U^{eff} \simeq U + A/d^3 + B/d^4$. Using $U = 1.6 \text{ eV}$, $A = 1.1 \times 10^4 \text{ eV} \cdot \text{\AA}^3$, $B = -8.1 \times 10^4 \text{ eV} \cdot \text{\AA}^4$, obtained by least square fitting, we obtain the curve predicted by this model, shown in Fig. 5.5, also with actual values. We can see that the fitting is quite good.

However, the molecular limit is underestimated. Direct calculation gives $S = 0.53$ while curve prediction is $S = 0.39$. Both results can reconcile if we realize that \bar{D} is more than 30% lower in the isolated molecule (probably because we only use Γ point for this calculation). If we take this into account we obtain a value of $S = 0.50$, much closer to the direct calculation.

To sum up, the IDIS model is valid at all big and small coverages limits. Moreover, our calculation of the behavior U^{eff} and its relationship with U agrees with some simple physical arguments.

5.2.5 Extrapolation to the C₆₀/Ag(111) and C₆₀/Cu(111) Interfaces

We can extrapolate the results of this work to C₆₀/Ag(111) and C₆₀/Cu(111) interfaces. Taking into account that $\Phi_M(\text{Ag}) = 4.46 \text{ eV}$ and $\Phi_M(\text{Cu}) = 4.9 \text{ eV}$, Fig. 5.6 suggests that $\Delta^{IDIS}(\text{Ag}) = 0.03 \text{ eV}$ and $\Delta^{IDIS}(\text{Cu}) = 0.23 \text{ eV}$, far from the experimental values -0.13 eV for Ag [6] and 0.10 eV for Cu [9]. Moreover, if we include the pillow potential, the calculated potentials deviate even more from experiments.

In order to get a good extrapolation, once again, we have to mind the gap. In Ag and Cu, the metal, molecule distance is smaller (0.1 \AA smaller for Ag [6] and 0.5 \AA for Cu [10]) We can estimate the gap semiclassically taking into account that the image plane position increases for Ag and Cu (see [11]). This give us a gap around 2.5 eV for Ag and 1.9 eV for Cu.

The change in the gap implies a change in S . If we assume that S change with the energy gap as $S = 1/[1 + (a/E_g)^2]$, we get that for Ag $S = 0.13$ and for Cu $S = 0.08$. Regarding the pillow potential, with values calculated along this thesis we can assume an exponential dependence $e^{-\alpha d}$ where d is the metal/molecule distance and $\alpha \simeq 3.4 \text{ \AA}^{-1}$. This gives an estimation of $\Delta_0^P = 0.60 \text{ eV}$ for Ag and $\Delta_0^P = 2.15 \text{ eV}$ for Cu.

All these values yield the following results:

Ag/C₆₀

For this interface, $(\text{CNL} - \Phi_M) = -0.14 \text{ eV}$ and $\Delta^{IDIS} = -0.12 \text{ eV}$ (0.15 eV smaller than estimation based on Fig. 5.6), so that this potential brings the Fermi

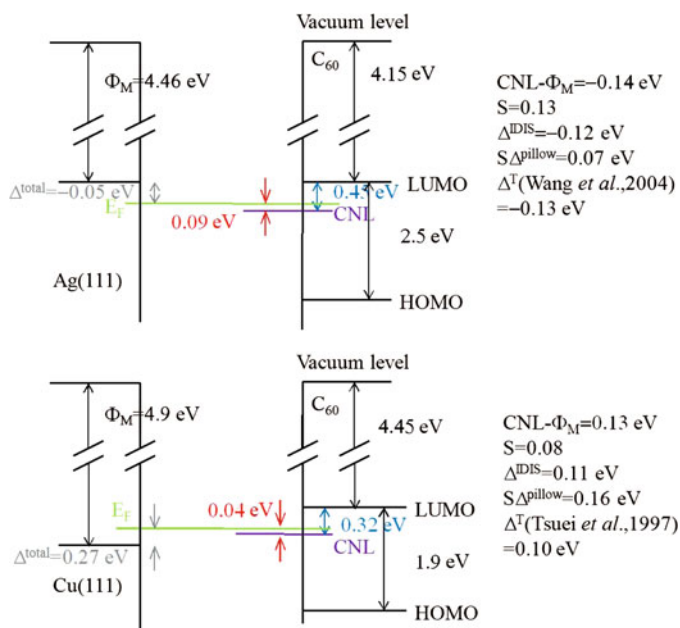


Fig. 5.9 Schematic view of the different parameters in the $C_{60}/\text{Ag(111)}$ and $C_{60}/\text{Cu(111)}$ interfaces (Color figure online)

level to 0.02 eV above the CNL. On the other hand: $\Delta^P = 0.07 \text{ eV}$. Combining these two dipoles we find that E_F is 0.09 eV above the CNL, and the total dipole is $-0.12 \text{ eV} + 0.07 \text{ eV} = -0.05 \text{ eV}$, in good agreement with other independent DFT-calculations [6].

Notice the change in the dipole sign, which is mainly the result of having the initial metal work-function 0.14 eV above the CNL. This is due to the small metal workfunction of Ag (4.46 eV) and to the reduction of C_{60} energy gap.

Cu/ C_{60}

In this case, $(\text{CNL}-\Phi_M) = +0.13 \text{ eV}$ and $(1-S)(\text{CNL}-\Phi_M) = 0.11 \text{ eV}$. Moreover, $\Delta^P = 0.16 \text{ eV}$; then, the total potential is $+0.27 \text{ eV}$ (closer to the experimental evidence, 0.08 eV [9]), than the previous value: $0.23 + 0.16 = 0.39 \text{ eV}$ and the interface Fermi level is 0.04 eV above the CNL (see Fig. 5.9). Notice that in this case, the combination of the metal workfunction (4.9 eV) and the molecule energy gap (1.9 eV) yields a metal workfunction very close to the organic CNL. In this case the pillow contribution is *larger* than the IDIS one.

5.2.6 Conclusions

In this section we have studied the C₆₀/Au(111) metal/organic interface formation for different coverages: $m\sqrt{3} \times m\sqrt{3}R30^\circ$ where $m = 2$ (experimental monolayer), 3, 4, 5, that corresponds to coverages $\theta = 1, 4/9, 1/4$ and $4/25$. We have taken care of the dependence of the IDIS parameters with coverage, including the molecular case, seen as the low coverage limit.

As expected we obtain that the IDIS potential monotonically decreases, and the screening parameter increases when the coverage decreases. Regarding the molecular gap, we have used $E_g = 3.1$ eV, calculated in Sect. 4.2. We point out that for finite coverage S and U are related through: $S = 1/(1 + U^{eff} \bar{D})$ where U^{eff} accounts not only for molecule charging energy but also for C₆₀-C₆₀ dipolar interaction $U^{eff} = U + \sum_i J_i$. Where $J_i \propto 1/d^3 +$ multipolar terms. The values obtained for U^{eff} (4.4, 3.0, 2.4 and 2.1 eV for $m\sqrt{3} \times m\sqrt{3}R30^\circ$, $m = 2, 3, 4, 5$) can be used to calculate J_i and thus obtain an effective many-body Hamiltonian for the adlayers [12].

Finally, we have extrapolated our results to a C₆₀ monolayer over Ag(111) and Cu(111) surfaces. The prediction for the IDIS potential given by Fig. 5.6 are in disagreement with experimental evidence. The reason for this is the different C₆₀/surface distances for these metals, that change the size of the gap (and the value of S). When we consider this, we obtain results in better agreement with experiments.

We make a final comment about the atomic orbital basis set used in our calculations. The point to stress is that our basis set is not a converged one; this is reflected in two deficiencies of our calculations: one is about the initial alignment of the metal/organic levels (that was pointed out in Sect. 3.5, early in this thesis); the second one is related to our calculated energy gap which is a little too large (2.1 eV instead of 1.6 eV). Both have been corrected using the scissor operator. We have still explored the corrections introduced in our calculations by a more extended basis set, by using for C a basis set of sp^3d^5 atomic orbitals with cutoff radii: 4.0 (s), 4.5 (p), 5.4 (d) (in atomic units). Obviously, using this basis set, the molecular levels are significantly shifted, but the scissor operator allow us to fit the molecular energy gap and its energy position to the experimental values. These corrections finally make our new calculation of the interface potential and the value of U reasonably insensitive to the details of the new basis set (larger V^{IDIS} when larger cutoff radii are employed); however, our pillow potentials are increased in the new basis set by about 20%, so that $S eV_0^P$ takes now the values: 0.08 eV for the molecule, 0.10 eV for the $m = 2$ adlayer case, and 0.08 eV for $m = 3, 4$ and 5. Results with the extended $sp^3d^5s^*d^{*5}$ basis set for Au used in Sect. 3.5 suggest that the pillow potential can increase up to 0.2 for the monolayer case, and 0.16 for the isolated molecule. Notice that for the full monolayer case ($m = 2$), this potential can reverse the sign of $(CNL - E_F)$, changing the direction in which charge is flowing between C₆₀ and Au. This, however does not affect to our main conclusions: here we have consider the point of view suggested by Eq. (3.17), and the IDIS potential sign does not depend on the final charge transfer direction when the pillow potential is taken into account. If we would have considered the point of view of Eq. (3.16), the term $(1 - S)(CNL - \tilde{\Phi}_M)$ had

changed its sign with charge transfer direction, but at the end we will have get the same result for V' (since in this case, the total potential remains positive due to the large positive value of the bare pillow part).

5.3 Benzene/Au(111) Revisited: Realistic Gap and Benzene/Au Distance

We have improved the previous calculations of the benzene/Au(111) interface, correcting the main deficiencies discussed in Sect. 3.5.4. First of all, using the WCI + vdW technique we have obtained a realistic first principles benzene/Au distance. Then, the *ab initio* gap has been calculated at the molecular limit. After that, the gap is applied to the full monolayer, and the IDIS potential and the screening parameter are calculated. We have used the sp^3d^5 basis for Au (as in previous section) and the C, H basis are the same as in first benzene/Au calculations in Sect. 3.5. This interface can be considered as a typical interface with small screening (opposite to the $C_{60}/Au(111)$ case). These results have been published in *Journal of Chemical Physics* [13], in collaboration with Dr. Yannick Dappe and Dr. José Ignacio Martínez. This section is an adapted and extended version of this article (Copyright 2011 American Institute of Physics).

5.3.1 Interaction Energy and Van der Waals Forces

We have calculated both the standard LDA and WCI energy versus distance curves. Due to the Au–C covalent distance is 2.1 Å and the LDA adsorption one is around 3.0 Å we can expect that the LDA does not work properly at this distance. So we are going to add to the WCI (that has no exchange–correlation interaction between metal and molecule) the vdW interaction.

We have used the standard Eq. (2.83) for the vdW interaction, with $C_6 = 36\text{eV} \cdot \text{Å}^6$ for the Au–C interaction and no Au–H interaction has been included (the C_6 coefficient is much lower than the Au–C one). The factor $f_D(R)$ eliminates the vdW contribution for short distances [2, 7]. We are going to use two different damping factors in order to check the reliability of our results. The first one has the form $f_D(R) = 1 - \exp(-\alpha(R/R_c)^8)$ Following references [2, 3], we take $\alpha = 7.5 \times 10^{-4}$, and $R_c = 2.3 \text{Å}$. The second one has the form $f_D(R) = 1/(1 + \exp(-d(R/R_{vdW}) - 1))$ [7] where $d = 20$ and R_{vdW} is the sum of vdW radii of the elements under consideration, that is around 3.3 Å [7]. The last one was also employed in $C_{60}/Au(111)$.

The results of these calculations for a benzene monolayer on Au(111) are presented in Fig. 5.10. We have plotted the benzene/Au(111) interaction energy versus the benzene–surface distance for standard LDA (black curve, FB-LDA) and WCI calculations (blue curve, WCI). The FIREBALL LDA calculation gives a binding energy of around 0.20 eV, too small. In a second step, we have added to the WCI energy the

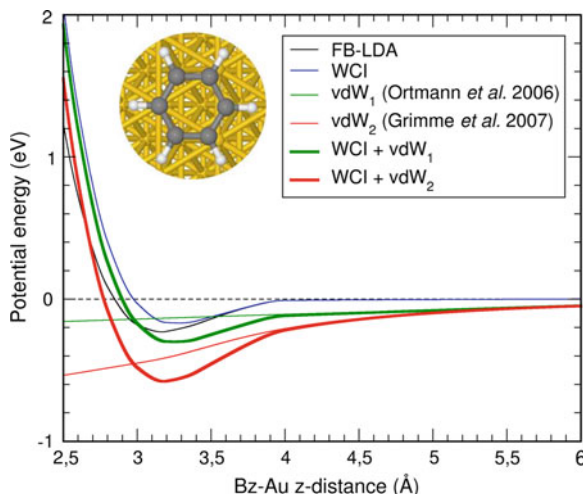


Fig. 5.10 Energy versus distance for the benzene/Au(111) interaction. *Black line* standard LDA-FIREBALL calculation. *Thin blue line* WCI-FIREBALL calculation. *Thin green and red lines* two different parameterizations of the vdW interaction (vdW₁ [2] and vdW₂ [7]). *Thick green and red lines* total benzene–Au interaction (WCI + vdW₁, WCI + vdW₂). Reprinted from [13] Copyright 2011 American Institute of Physics (Color figure online)

vdW interaction (the thin green and red curves) with Ortmann et al. [2] and Grimme [7] parameterizations for the damping factor $f_D(R)$, obtaining the thick green and red lines: the binding energy of the system for both parameterizations. In this way, we obtain an equilibrium distance of around 3.25 Å. The binding energy per molecule for this distance, which depends on the damping factor $f_D(R)$ used, is 0.30 eV using the parameterization by Ortmann et al. [2] and 0.60 eV for the parameterization by Grimme [7]. The second energy is in good agreement with the experimental evidence [14], and the Au/benzene distance is similar to the one found in other calculations [15]. We should point out that, although different parameterizations gives different energy adsorptions, the critical factor for the study of the interface dipole is the benzene/Au distance, which is independent of the choice of $f_D(R)$. Now, considering this equilibrium geometry, we analyze in the next sections the charging energy, the interface dipole potentials and the charge transfer at this interface.

5.3.2 Molecular Limit: U and δU

In order to obtain an accurate gap value of benzene over Au(111), we have calculated the adsorption of a benzene molecule over the 8×8 cluster with 4 layers. The benzene–Au distance is the same as in the monolayer case (see Fig. 5.11).

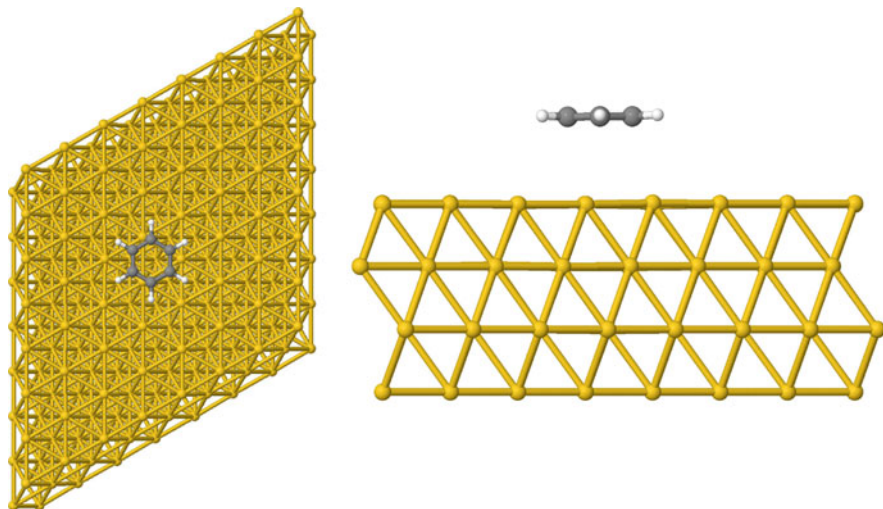


Fig. 5.11 Geometry of the 8×8 cluster without periodicity used to simulate a single molecule adsorbed over a gold surface (*upper and side view*) (Color figure online)

In this case, we get $U = 4.8$ eV. Instead of calculating the transport gap as $E_g^t = E_g^{LDA} + U$, we make here a different approach. First of all, we have calculated in our basis set the transport gap of the gas phase molecule using $E_g^t = E[N + 1] + E[N - 1] - 2E[N]$, that gives a value of 13.2 eV, larger than the experimental 10.3 eV [16, 17]. The theoretical gap overestimation is because of the minimal basis set used. The LDA gap is also overestimated (6.1 as compared to converged plane wave calculations, that yield 4.7 eV [15]). So in the gas phase molecule we get with FIREBALL $U^0 = E_g^t - E_g^{LDA} = 7.1$ eV instead of the value of $U^0 = 5.6$ eV (taking the experimental gap and the plane wave LDA gap). So, instead of adding our $U = 4.8$ eV to our gap of 6.1 eV (that would give $E^t = 10.9$ larger than the gas phase molecule gap), we have considered the reduction δU of the gap between the gas phase molecule and the molecule over the surface. In this case we obtain $\delta U = 2.3$ eV so we get a gap of $E^t = 8.0$ eV. After insertion of $U^{off-diag}$, it is finally reduced to $E^t = 7.7$ eV. This reduction δU is the effect of the image potential on the molecular gap.

It is important to mention that this also happened in C_{60} molecule. Accurate values of the transport gap of the gas phase molecule and the LDA gap are 4.9 and 1.6 eV respectively [18], so $U = 3.3$ eV for the gas phase molecule. However, results of E_g^t for the gas phase molecule and the LDA gap with our basis set give a value of 5.4 and 2.1 eV respectively, so $U = 3.3$ eV for the gas phase molecule (the same as the more accurate one). That is the reason why the calculation of δU was not necessary in C_{60} .

We have checked that the benzene gap calculation is independent of the basis set. For this reason, we have used a sp^3d^5 basis set for C. For this basis, the LDA and the

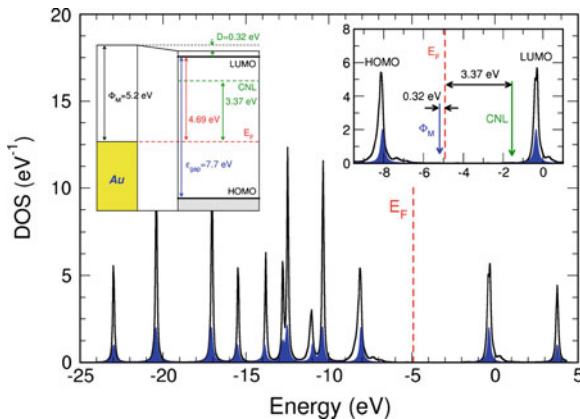


Fig. 5.12 DOS for a single benzene molecule on Au(111); the initial molecular levels are shown by the *blue lines* (with a broadening of $\eta = 0.1$ eV). The *right inset* shows an energy window around the HOMO and LUMO levels indicating the initial work-function, Φ_M , and the CNL. The *left inset* shows an energy diagram of the benzene/Au interface. Reprinted from [13] Copyright 2011 American Institute of Physics (Color figure online)

transport gap are 4.8 and 11.0 eV respectively so $U^0 = 6.2$ eV (closer to the accurate U^0 than the previous basis set). The reduction of the gap δU is 1.8 eV if we don't include $U^{off-diag}$ and 2.6 if we do so. The final gap for this basis is 7.8 eV, 0.1 eV larger, and within the error of our calculations (that are estimated to be around 10 %).

Finally, a full study of electronic structure of a single benzene molecule over a gold surface has been done (see Fig. 5.12). The total induced potential has been found to be $V^{IDIS} = 0.32$, associated with a charge transfer of ~ 0.07 electrons from the molecule to the surface and its corresponding dipole of 1.19 D. This induced interface potential is the one on the molecule due to the charge transfer. As in C_{60} , it is smaller than the monolayer limit (see next section), and also the screening (that is $S = 0.91$ in this case, a case of rather low screening). We have also checked that the screening parameter calculated as Eq. (3.10) and as Eq. (3.12) coincide, showing also that for a benzene molecule the Fermi level, and the IDIS potential, change linearly when we change the initial metal Fermi level, using the scissor operator. However, due to the low DOS within the gap, the calculation of CNL is not accurate enough for obtaining a reliable screening parameter value (let alone U) so in this case we have considered the LUMO level (a level that is well defined in this case, not as in C_{60} : Fig. 5.12 vs. Fig. 4.3) as the reference level, and we have studied variation of LUMO- E_F as a function of the fictitious changes on the initial metal Fermi level (shown in Fig. 4.3).

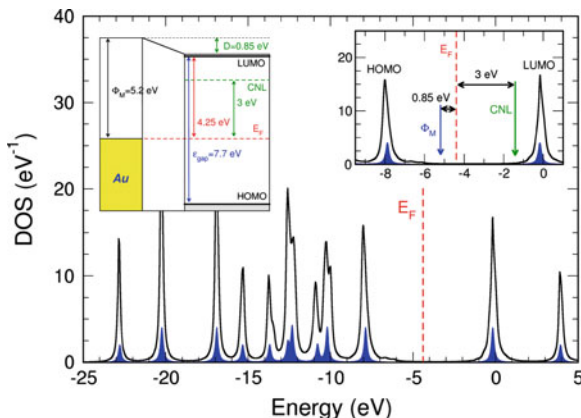


Fig. 5.13 As Fig. 5.12 for a benzene monolayer on Au(111). Reprinted from [13] Copyright 2011 American Institute of Physics (Color figure online)

5.3.3 Benzene Monolayer Interface Dipole

Density of States and IDIS Potential

Figure 5.13 shows our calculated DOS for the monolayer relaxed geometry obtained in previous section. The final Fermi level position in this case is located 0.85 eV above the initial one. For this particular case we find, $S = 0.79$. Figure 5.14 shows also linearity in $LUMO-E_F$ and IDIS potential versus initial Fermi level (as in molecular case) with slopes S and $(1 - S)$ respectively. The gap is 7.7 eV as calculated in previous section.

Figure 5.14 shows also that for a monolayer the interface Fermi level, the interface dipole potential V^{IDIS} and the charge transfer, change linearly with the initial Fermi level. Regarding the charge transfer from the benzene monolayer to the metal surface, it is now ~ 0.06 electrons per molecule (a dipole \mathcal{D} of 0.99 D per molecule). This charge transfer is smaller than in the case of a single benzene molecule on Au(111), reflecting the depolarizing effect due to the other benzene molecules. This charge transfer can be used to obtain an average interface dipole potential of $\Delta = 0.81$ eV, using the relation Eq. (3.9). Notice that Δ is quite close the value $V^{IDIS} = 0.85$ eV, that corresponds to the potential on each benzene molecule. The relation Eq. (3.9) has been used to extrapolate the results of cluster calculations to *e.g.* the monolayer case, assuming that the dipole per molecule \mathcal{D} is the same in both cases (*i.e.* neglecting the depolarizing effect for the monolayer). Using the \mathcal{D} values obtained in our cluster calculation we obtain $\Delta = 0.97$ eV for our 5×5 monolayer, and $\Delta = 1.05$ eV for the $\sqrt{52} \times \sqrt{52}$ experimental monolayer, values that are very different from the induced interface potential $V^{IDIS} = 0.32$ eV obtained for the cluster calculation. Finally, assuming that the dipole per molecule is the same in the 5×5 and $\sqrt{52} \times \sqrt{52}$ structures, yields a dipole potential $\Delta = 0.88$ eV for the $\sqrt{52} \times \sqrt{52}$ case. This

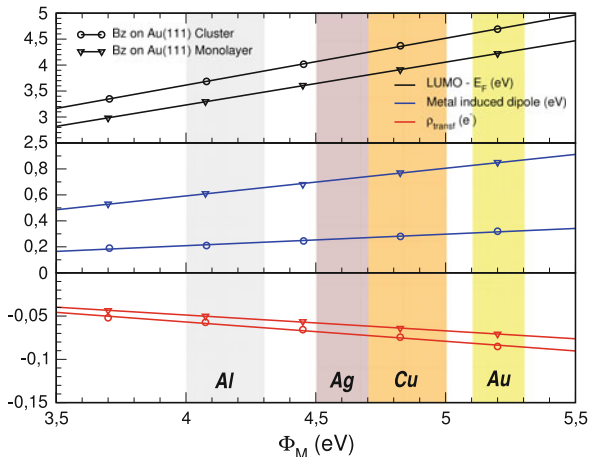


Fig. 5.14 ($LUMO - E_F$) (upper panel), V^{DIS} (center panel) and transfer of charge (lower panel) as a function of the initial metal Fermi level. The fictitious change in the initial metal Fermi level tries to simulate how the interface properties depend on the different metals: this issue is shown in the figure by superimposing the initial metal Fermi levels of Al, Ag, Cu and Au for comparison. Reprinted from [13] Copyright 2011 American Institute of Physics (Color figure online)

reinforces the ideas of Sect. 4.1 that at the monolayer limit $V \simeq \Delta$. The higher difference has been found when using the cluster dipole for calculate the monolayer Δ ; showing the importance of the depolarizing effect (that is a physical phenomena completely unrelated with the difference between V and Δ).

Pillow and “Surface Metal” Dipole Corrections

The pillow potential $\Delta^P = S\Delta_0^P$ is 0.04 eV (very small due to the long absorption distance, that makes this effect a minor correction).

In an opposite way, $E_F - \Phi_M$ is reduced by 0.1 eV due to the off-diagonal surface potential, so the net effect of those potentials is a reduction of the total potential of 0.06 eV (appreciable, but very small). However, as we have seen, the contribution of this effect to the gap size calculation is not such small (it reduces the gap around 0.3 eV, and the gap without taking into account this effect is 8.0 eV, definitely too large). This effect is higher in a more complete sp^3d^5 C basis (the gap is reduced by 0.8 eV).

5.3.4 Extrapolation to Benzene/Ag, Cu Interfaces

We are going to use these results to estimate the energy level alignment in benzene/Ag (Bz/Ag) and benzene/Cu (Bz/Cu) interfaces. If we use Fig. 5.14 in order to

estimate the IDIS potential we obtain the following interface potentials: 0.85 eV for Bz/Au(111); 0.69 eV for Bz/Ag(111) and 0.78 eV for Bz/Cu(111). Morikawa and coworkers [15] have calculated 1.14 eV for Bz/Au(111); 0.76 eV for Bz/Ag(111) and 1.06 eV for Bz/Cu(111). The experimental values [19] are the following: Bz/Au(111)= 1.10 eV; Bz/Ag(111)= 0.70 eV and Bz/Cu(111)= 1.05 eV. Morikawa et al.'s results are in excellent agreement with the experiments but the equilibrium Bz/metal distances (3.1 Å(Au); 3.3 Å(Ag) and 2.9 Å(Cu)) were basically fitted to reproduce these potentials. Our interface potentials show the same trend than the experimental data, with a minimum value for the Ag case and a maximum one for Au, although our absolute values seem to be a little too small: as commented above this can be due to the “pillow” potentials that are underestimated in our calculations, and also to the different molecule–metal distances for Ag and Cu (and its effect on gap size, see Sect. 5.2.5). Comparing the experimental evidence and our theoretical results we can consider that: $V^P(\text{Au})=0.25$ eV; $V^P(\text{Ag})=0.01$ eV and $V^P(\text{Cu})=0.27$ eV, in agreement with the Bz/metal distances found by Morikawa et al.: larger for Ag and smaller for Cu. The benzene/metal distance, and the size of the gap (should be larger in the benzene/Ag than in benzene/Au because of its larger distance to the image plane) can also play a role (as they played in C_{60} /noble metals interface).

5.3.5 Discussion

We have presented fully abinitio corrected DFT calculations for benzene on Au(111) in two limits: an isolated molecule and a full monolayer. A first principles gap of 7.7 eV has been used, calculated in Sect. 5.3.2. A correct value of this energy gap is important in order to analyze the interface potential induced between benzene and Au(111). In particular, this effect partially explains the big differences found between the results presented now and the ones presented in Sect. 3.5, where we assumed the transport energy gap to be much smaller, around 4.8 eV. Moreover, we assumed the metal/benzene distance to be smaller too, 2.95 Å, an effect that tends to decrease S and enhances the amount of charge transfer between the molecule and the metal. In this case, the benzene/Au distance has been computed properly taking into account vdW interactions.

Using these energy gap and distance, we have calculated the case of a benzene-monolayer and have found that the final Fermi level is 0.85 eV above its initial position. This value compares well with the experimental one of 1.1 eV, as given by Bagus and coworkers [19], although part of the discrepancy might come from some overestimation of the energy gap. To check this point, we have also calculated the monolayer case taking an energy gap of 7.0 eV for the benzene molecule. This value still can be considered compatible with our previous calculation for E_g , taking into account the error bar of 10% appearing in the calculations due to numerical uncertainties, related to the small induced DOS at the gap. This value is also suggested by extrapolating the data in [20] and by semiclassical image potential calculations. Figure 5.15 shows for this case our calculated DOS projected onto the molecule and

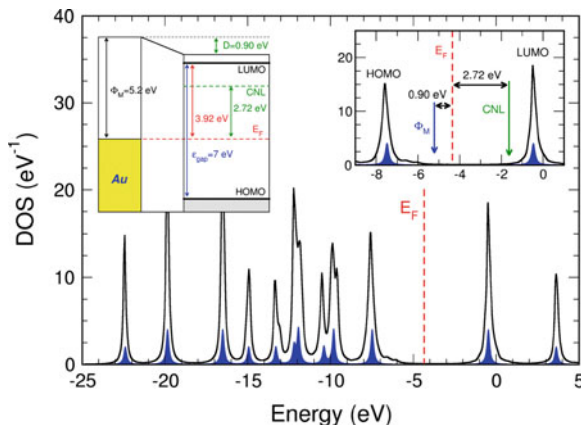


Fig. 5.15 DOS for a benzene monolayer on Au(111), with a molecule transport energy gap of 7.0 eV; the initial molecular levels are shown by the blue lines. The *right inset* shows an energy window around the HOMO and LUMO levels, indicating the initial work-function, Φ_M , and the CNL. The *left inset* shows an energy diagram of the Au/benzene interface. Reprinted from [13] Copyright 2011 American Institute of Physics (Color figure online)

the interface barrier; the point to realize is that with this transport energy gap, the interface potential has slightly increased to 0.9 eV.

It is also important to discuss the issue of the convergence of our calculations with the basis set. We have studied this convergence by analyzing how our results depend on a more extended basis set; in particular, we have used $sp^3d^5s^*d^{*5}$ numerical atomic orbitals for Au, sp^3d^5 for C and ss^* for H. These Au and C basis have been used in Sects. 3.5 and 5.2.2 respectively. If we fit the molecule energy gap and position, our new calculation is reasonably insensitive to the details of the new basis set.

As in the C_{60}/Au interface, an exception is the calculation of the “pillow” potential: using this more extended basis increases this potential to 0.15 eV (similar to the value obtained in Sect. 3.5 with the same basis set). We conclude that the small difference between our calculated interface potential (for a full monolayer), 0.85 eV, and the experimental one, 1.1 eV, is probably due to this underestimation of the “pillow” potential and the confinement of orbitals.

The estimation of the IDIS potential for other noble metals lead to the following values: 0.85 eV for Bz/Au(111); 0.69 eV for Bz/Ag(111) and 0.78 eV for Bz/Cu(111). Independently, Bagus and coworkers [19] using a wave-function-based *ab initio* method and a cluster model have obtained 0.87 eV for Bz/Au(111); 0.77 eV for Bz/Ag(111) and 1.08 eV for Bz/Cu(111), in good agreement with our results. It is worth commenting that, based on a Constrained Space Orbital Variation (CSOV) analysis of these calculations, these authors conclude that the observed interface dipole is largely due to the exchange (or Pauli) repulsion between electrons in the metal and in the organic [19], an observation that seems to be in contradiction with

the findings of our work, that indicate that the main mechanism behind the interface dipole formation is the charge transfer between the metal and the organic. A deeper analysis shows, however, that there is no contradiction between these two points of view. Firstly, notice that in a DFT calculation the different wavefunctions are orthogonalized to each other, including in this way the effect of the Pauli repulsion in the interface barrier formation, an effect that automatically leads to a significant charge transfer at the interface; consequently, our DFT FIREBALL calculation includes the “exchange repulsion” effect discussed by Bagus et al., except for the small contribution analyzed above in the “pillow effect” section. Secondly, notice that in the frozen-orbital step in the COSV analysis, the (Pauli exclusion principle) requirement of orthogonalization of the wavefunctions in the metal and in the molecule already leads to a “major net motion of charge from the adsorbate toward the substrate” [21], which will appear in our analysis as a charge transfer between the two media.

5.3.6 Conclusions

To sum up, we have corrected the DFT calculation of the interface properties of the benzene/Au(111) interface presented in Sect. 3.5, introducing a self-consistent analysis of the molecule charging energy and its transport energy gap. From our calculations we have also analyzed other noble metals by changing fictitiously the initial Fermi level while keeping the Au electronic properties. This allows to mimic other metals with different workfunction, because the value of the initial Fermi level coincides in absolute value with the metal workfunction when the vacuum level is the origin of energies. Our results have been favorably compared with other theoretical and experimental data, lending strong support to our interpretation of the formation of bz/noble metal interfaces as due to the charge transfer between the metal and the molecule, as described in the IDIS-model.

5.4 TTF/Au(111) Interface

Another interesting MO interface is the tetrathiofulvalene (TTF) over Au(111). TTF is a prototypical electron donor, and a potential material for molecular electronics [22, 23]. As in previous sections, we calculate the interface barrier evolution when going from the isolated molecule to the full monolayer case, and calculate the charging energy, and consequently, the molecule energy gap.

As in benzene, vdW forces are important; not only for energy calculations but also to obtain a reliable TTF/Au distance (very important, as we saw in Sect. 3.5.4). Moreover, a reliable description of the TTF geometry at the interface cannot be accurately achieved neither using conventional DFT-calculations nor other techniques involving semiempirically vdW forces. For this reason, we have analyzed the TTF geometry by combining experimental STM-images [24] with a detailed calculation of the

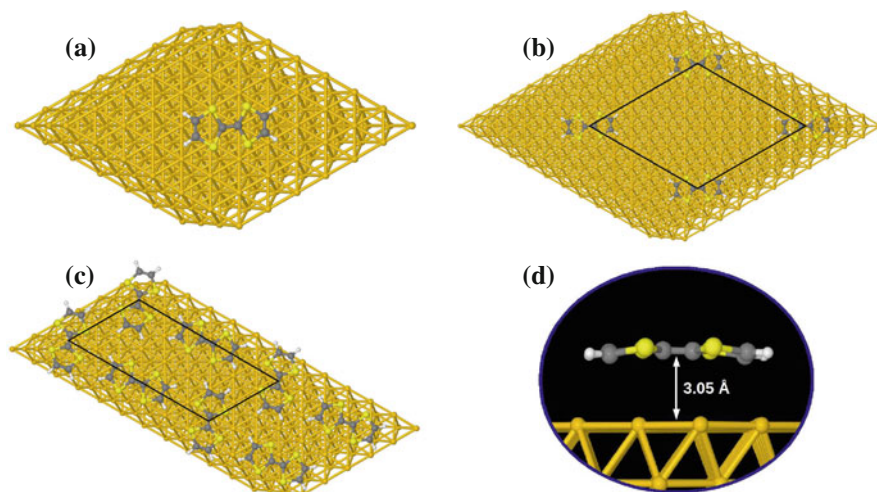


Fig. 5.16 TTF coverages on the Au(111) surface: **a** cluster model; **b** dilute structure ($a = b = 17.56 \text{ \AA}$, $\hat{a}b = 60^\circ$); **c** herringbone structure ($a = 17.56 \text{ \AA}$ and $b = 8.78 \text{ \AA}$, $\hat{a}b = 60^\circ$); and **d** side view of a TTF molecule on the Au(111) surface. For **b** and **c**, the *solid lines* denote the surface unit cells used in the calculations. Reprinted from [25], Copyright 2012 by Elsevier (Color figure online)

tunneling currents using the formalism explained in Sect. 2.6; in this approach we obtain the TTF geometry by fitting the theoretical calculations to the experimental image. Once we obtain the molecule geometry we analyze the molecule DOS, the charge transfer, the interface dipole and other properties related to the TTF/Au interface. This work has been done in close collaboration with Dr. José Ignacio Martínez and Dr. César González. This section is adapted from the paper published in *Organic Electronics* [25] (Copyright 2012 by Elsevier).

5.4.1 Calculation Details

Figure 5.16 shows the systems and geometries we are interested in: an isolated TTF molecule deposited on a 7×7 Au(111) cluster (Fig. 5.16a); and two different TTF coverages on a Au(111) surface. We have considered the 6×6 [22] (Fig. 5.16b) and the herringbone (HB) 6×3 geometries [23] (Fig. 5.16c); this approach will allow us to analyze how the interface properties depend on the layer coverage.

The basis set used in our calculations consist on the sp^3d^5 Au basis used in previous calculations; sp^3d^5 C basis used in C_{60} and benzene to check basis convergence; s H basis used in benzene/Au, and sp^3d^5 for S with cut-off radii $s = 4.2$, $p = 4.7$, $d = 5.5$ (in a. u.). For the TTF molecule this calculational approach yields C–C nearest neighbors distances of 1.40 and 1.47 \AA —to be compared with 1.39 and 1.44 obtained in DFT in a plane wave basis [22], and experimental values of 1.40,

1.45 Å [26]—(no available data for the C–H and S–C experimental bond lengths), and a LDA gap of 3.3 eV, to be compared with 2.6 eV for converged basis set LDA or GGA calculations [22]. It is also worth mentioning that a calculation of the affinity/ionization gap for TTF yields a value of 6.3 eV carried out by the real-space OCTOPUS code [27] (by using an accurate hybrid GGA–PBE0 exchange–correlation functional [28]); using FIREBALL $E_g = E[N + 1] + E[N - 1] - 2E[N]$ is found to be 8.19 eV.

In order to accurately determine the equilibrium distance of TTF adsorbed on a gold surface, we have used here the WCI + vdW method used for C₆₀ and benzene on Au(111) and explained in Sect. 2.7.1. The C₆ parameter in vdW Eq. (2.83) has been taken $C_6 = 36 \text{ eV} \cdot \text{Å}^6$ in for Au–C, $C_6 = 0$ for Au–H (as in previous calculations) and $C_6 = 57 \text{ eV} \cdot \text{Å}^6$ for Au–S. We have used both Ortmann et al. [2] and Grimme [7] parametrization for $f_D(R)$. In both cases, the TTF/Au distance obtained is 3.10 ± 0.05 Å. Using only LDA we obtain a distance of 3.2 Å (larger than the vdW one).

5.4.2 STM Images and TTF Geometry

As mentioned above, we have determined the TTF molecule geometry by analyzing the STM-image and looking for the configuration yielding the best agreement with the available experimental evidence [24]. In our calculations we have assumed to have a W-(100) tip formed by 5 atoms, one of them in the apex, joined to a W crystal. Tunneling currents and STM images are calculated using the ideas of Sect. 2.6 and reference [29].

Figure 5.17 shows our calculated STM-images for three different TTF geometries calculated with different approximations: configurations I, II and III have been obtained using different codes; I: VASP(LDA) [30, 31]; II: DACAPO(GGA) [32] and III: VASP(GGA) [24], respectively. W-tip height from TTF monolayer and surface voltage, V_s , take the typical values of 4.5 Å and -1 V (below the E_F), respectively, in order to mimic experimental STM signal [24]. It is worth to stress that the variation of the W-tip height between 4 and 4.5 Å does not reveal any significant change in the STM signal. These images do not seem to agree with the experimental image shown on the top-right part of the figure. Then we have explored more than 200 different geometries and Fig. 5.17 (bottom-right) shows the one found yielding the best agreement with the experimental image (see top-right image). In this geometry, the molecule is rather flat, being located 3.05 Å from the surface. A side view of the theoretically STM-engineered structure is also shown in Fig. 5.17.

In order to calculate the TTF/Au for various coverages, we deposit the TTF geometry from our previous STM engineering and vdW considerations over different Au(111) surfaces. In the isolated molecule case, a 7×7 cluster arrangement (see Fig. 5.16a) with no periodicity has been used. It has been checked that this cluster size is enough to avoid border effects. The dilute geometry (see Fig. 5.16b) was taken as a low coverage case with 6×6 periodicity. The geometry used in our calculations for the herringbone monolayer case (see Fig. 5.16c) has been constructed in base to

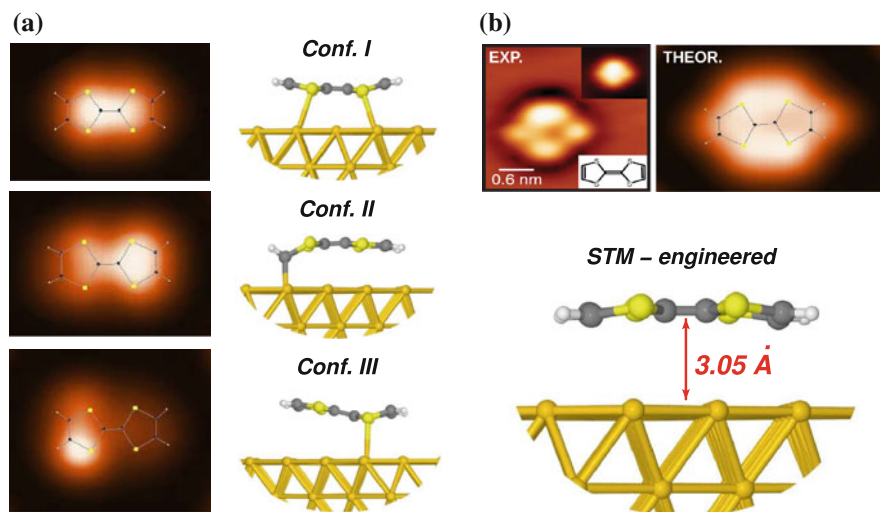


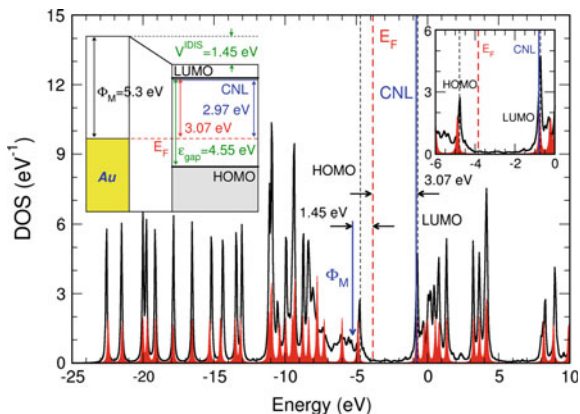
Fig. 5.17 **a** Theoretical STM images of TTF on Au(111) surface for three different configurations (explained in the text); and **b** comparison between experimental [24] and theoretical STM images. A *side view* of the optimized TTF on Au (111) surface is also shown. Reprinted from [25], Copyright 2012 by Elsevier (Color figure online)

a recent STM experiment by HuiJuan and coworkers [23], and it has been modeled as a 6×3 periodicity lattice with two TTF molecules (as obtained in our STM calculations) per unit cell. After that, we have relaxed our system with no significant variations on the final structure with respect to the starting one. All the calculations were performed for slabs of 4 and 6 Au layers where the last 2 and 3 layers were fixed; in particular we found that 4 Au-layers are enough to obtain converged results for the electronic structure. We have used 8 special k-points for the Brillouin zone sampling. The TTF/Au(111) geometries were first relaxed at the LDA level keeping the 2(3) lower Au layers fixed, while the first 2(3) layers were allowed to relax, respectively for the cases with 4(6) slabs considered.

5.4.3 Interface Properties

Once we have obtained the interface geometry, we calculate the interface electronic properties of: (a) the single molecule; and (b) the other TTF-layers, as well as the corresponding charging energy effects.

Fig. 5.18 DOS profile for a single TTF molecule on Au(111) (cluster model); the initial molecular levels are shown by the *red shaded region* (with a broadening of $\eta=0.05$ eV). The metal work-function, and the Fermi, HOMO and LUMO levels are also indicated on the figure. The *left inset* shows an energy diagram for the system. Reprinted from [25], Copyright 2012 by Elsevier (Color figure online)



TTF Molecule on Au(111)

Figure 5.18 shows the electron density of states (DOS) projected on the TTF orbitals for the case of a single molecule adsorbed on Au(111) (Fig. 5.16a). In the same figure we also show the molecule energy levels of the isolated (but deformed) molecule; the energy window around the energy gap is enlarged in the inset. The initial Fermi level, Φ_M , the interface Fermi energy, E_F , the HOMO and LUMO levels, as well as the CNL, are shown.

We have calculated the screening parameter S by changing in our calculations Φ_M fictitiously (see Fig. 5.19), just like in Sects. 4.2 and 5.3.2, obtaining $S = 0.70$. We have calculated also a charge transfer of 0.43 electrons, a surface dipole of 6.3 debyes, and a charging energy $U = 3.2$ eV (if we include the off-diagonal surface dipole we obtain $U = 2.95$ eV). Regarding the pillow potential, we obtain a value of $V_0^P = 0.03$ eV for the isolated molecule that is reduced to 0.02 eV when it is screened to SV_0^P .

Monolayer (HB) and Fraction of Monolayer Cases

Figure 5.21 shows the molecule local DOS for the HB-geometry (the monolayer case). As in previous cases we obtain a higher IDIS potential (i.e. an smaller screening parameter) than in the molecular case. In the case of the HB structure $S = 0.47$. This case is also analyzed in Fig. 5.19. For the 6×6 geometry (see Fig. 5.20) we find an interface behavior similar to the single molecule case, indicating that for this second adlayer the molecule–molecule interaction is very small. Notice also that in our results we find that the TTF–CNL is located around 0.1 eV from the LUMO level of the interacting molecule, namely, 0.8 eV from vacuum, which corresponds (as expected) to a case having a strong donor character.

In Figs. 5.20 and 5.21 we have also shown the IDIS potential, V^{IDIS} , induced in the molecule by the charge transfer; in our calculations, this charge transfer per

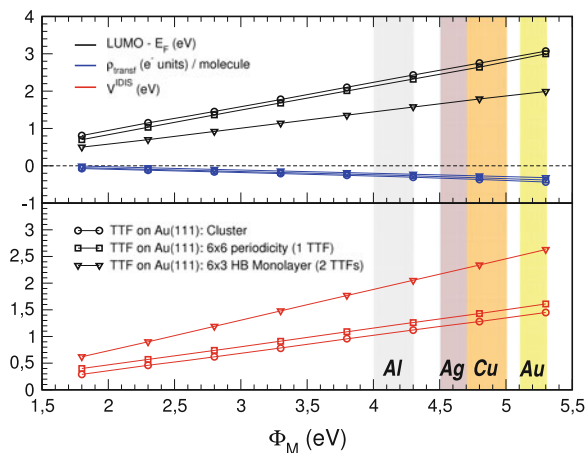


Fig. 5.19 ($LUMO-E_F$) and transfer of charge (*upper panel*), and V^{IDIS} (*lower panel*) as a function of the initial Fermi level (that can be seen as a “fictitious” metal work-function). The fictitious change in the metal work-function tries to simulate how the interface properties depend on the different metals: this issue is shown in the figure by superimposing the clean metal work-functions of Al, Ag, Cu and Au for comparison. Reprinted from [25], Copyright 2012 by Elsevier (Color figure online)

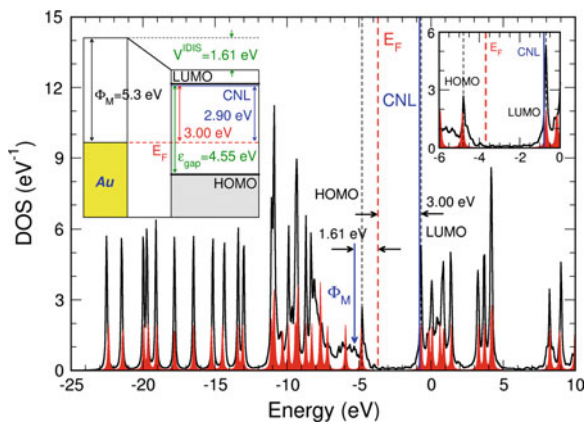


Fig. 5.20 As in Fig. 5.18 for the dilute geometry (see Fig. 5.16). Reprinted from [25], Copyright 2012 by Elsevier (Color figure online)

molecule is 0.37 and 0.31 electrons for the 6×6 -geometry and the HB-structure, respectively, with the corresponding surface dipoles: 5.4 (6×6) and 4.5 (HB) debyes, and $V^{IDIS} = 1.61$ (6×6) and 2.63 (HB) eV. From our calculations we obtain the following value of U^{eff} for the HB-case: $U^{eff} = 6.7$ eV. Regarding the pillow potential, we obtain $V_0^P = 0.1$ eV for the HB monolayer and 0.03 for the 6×6

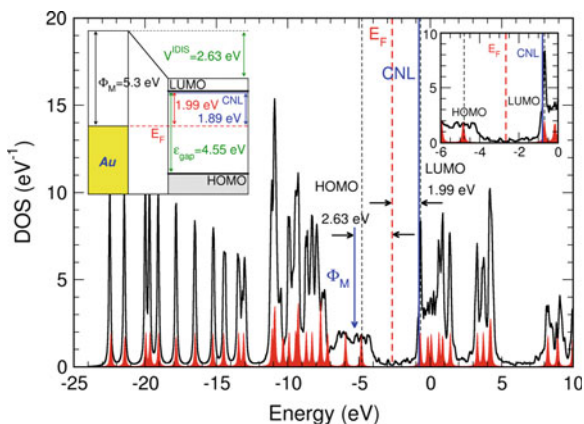


Fig. 5.21 As in Fig. 5.18 for the herringbone geometry (see Fig. 5.16). Reprinted from [25], Copyright 2012 by Elsevier (Color figure online)

structure, that are screened to 0.05 and 0.02 eV via V_0^P . These “pillow” potentials tend to increase slightly the interface dipoles calculated above.

5.4.4 Discussion and Conclusions

Other theoretical calculations for the TTF/Au(111) interface have already been reported by Fernández-Torrente et al. [24] and Hofmann et al. [22]. In Refs. [24] and [22], 6×4 and 6×5 unit cells have been considered, respectively. In both studies a DFT–GGA code has been used, although it has been agreed that probably “the actual equilibrium distance between the organic adsorbate and the metal surface lies in between the two extreme cases provided by GGA and LDA formalisms” [22].

In our approach we took advantage of looking for the best TTF geometry, by comparing the STM images reported by reference [24] with the theoretical ones calculated for more than 200 geometries. The geometry obtained in this way is shown in Fig. 5.17; the calculated STM-image for the best candidate fits considerably well with the experimental one and improves a lot the images calculated for the geometries provided by conventional LDA or GGA calculations. That new geometry is rather flat, parallel to the Au-surface, and located at 3.05 Å from it.

This adsorption distance has been calculated using the WCI + vdW method explained in Sect. 2.7.1. This calculation yields a minimum energy for a distance of 3.05 Å between the molecule and Au. The adsorption energy seems to depend, however, on the approximations introduced in the damping factor for the vdW energy as in benzene and C₆₀, with difference around 100% for Grimme’s and Ortman’s parametrization for $f_D(R)$.

TTF has a strong donor character, which is shown in the present study by the position of the CNL for all the considered system models, located at 0.8 below

the vacuum, and by the electron charge transfer from TTF to Au, which for the isolated molecule is 0.43 electrons, and 0.37 and 0.31 electrons for the 6×6 and HB structures, respectively. Our calculations yield induced dipoles per molecule of 6.3 (isolated cluster), 5.4 (6×6 geometry) and 4.5 (HB structure) debyes. It is interesting to remark that these values do not differ significantly from those found by Fernández-Torrente et al. [24]: 5 debyes for a 6×4 unit cell, and Hofmann et al.: 4.5 debyes for a $5 \times 3\sqrt{3}$ unit cell, showing that the charge transfer mechanism is not altered too much by the molecule geometries.

Regarding the organic energy gap and charging energy, we have obtained $U = 2.9$ eV, and $E_g = 4.4$ eV; notice that the TTF “exact” transport energy gap is 6.3 eV, indicating that image potential effects has reduced this gap by around $\delta U = 1.9$ eV. This value corresponds to an effective distance of 3.8 \AA between the TTF induced charge and its image (notice that the molecule size is around 7 \AA). DFT-GGA calculations [24] yield an energy gap of 2.2 eV, one half of the one obtained self consistently within our formalism; although the HOMO and LUMO level positions (as determined by the transport energy gap) change dramatically the barrier heights for electrons or holes, our calculations indicate, in this particular interface, that the amount of charge transferred from TTF to Au does not seem to vary too much for having either $E_g = 4.4$ or 2.2 eV.

We have obtained, as usual, that our results are rather insensitive to a basis set change. However, as in previous cases, the pillow dipole is substantially increased using a more extended basis. In particular, the “pillow” dipole, SV_0^P , of 0.05 eV found (for the HB structure) with the minimal basis set is increased to 0.30 eV for the extended basis; for the isolated molecule and the 6×6 structure the new value of SV_0^P is set in 0.12 eV. We conclude that in the calculations presented in Figs. 5.18, 5.20 and 5.21, because of the minimum basis set used in the calculations, Fermi level should be shifted towards the CNL by 0.10, 0.10 and 0.25, respectively.

5.5 TCNQ/Au(111) Interface: Molecular Dipole

In previous section we have studied the adsorption of TTF over Au, an electron donor molecule. Now we are going to focus in a prototype electron acceptor, that has attracted a lot of attention: tetracyanoquinodimethane (TCNQ). A strong tendency to bond to transition metal atoms, mainly due to its strong electrophilic character [33], makes the TCNQ a perfect candidate to be used in the formation of charge transfer compounds, as a p-dopant in organic semiconductors [34], and in novel nanoelectronic metal/organic devices. Additionally, an unpaired electron added to TCNQ via metal/organic interaction reveals an interesting magnetic behavior with promising applications in the synthesis of organic magnetic materials [35, 36]. Recently, STM and STS experiments [37] have demonstrated isolated TCNQ molecules absorbed on Au(111) surface to form highly ordered molecular assemblies due to strong tendency of the TCNQ molecules to form $N \cdots H$ intermolecular bonds. This work has been done in close collaboration with Dr. José Ignacio Martínez. This section is an

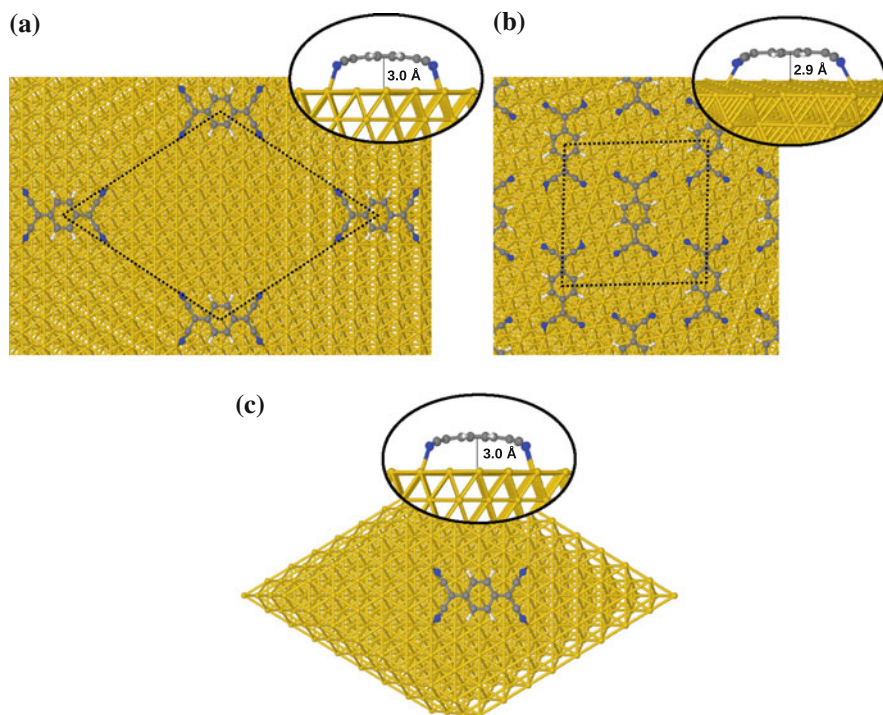


Fig. 5.22 TCNQ/Au(111) systems analyzed: **a** dilute structure ($a = b = 20.49 \text{ \AA}$, $\hat{a}\hat{b} = 60.0^\circ$); **b** self-assembled structure [37] ($a = 16.21 \text{ \AA}$, $b = 15.70 \text{ \AA}$, $\hat{a}\hat{b} = 93.0^\circ$); **c** single molecule on Au(111) (cluster model); for all the three geometries a side view of a TCNQ molecule on the Au(111) surfaces is shown. For **a** and **b** the *dashed lines* denote the surface unit cells used in the calculations. Adapted from *Physica Status Solidi B* [38] Copyright 2011 Wiley-VCH (Color figure online)

adapted version of the article published in *Physica Status Solidi B* (Copyright 2011 WILEY-VCH Verlag) [38].

5.5.1 Calculation Details and Geometry

The adsorption geometry has been calculated using the FIREBALL code with the standard sp^3d^5 Au and s H basis set, the $C sp^3d^5$ basis set used in TTF/Au(111) calculations. For N an sp^3d^5 with the following cutoff radii has been chosen: $s = 3.6$, $p = 4.1$ and $d = 5.2$ (a.u.).

As for TTF, we analyze an isolated molecule over the Au(111) surface, a dilute periodic geometry and a monolayer similar to the self-assembled geometry observed experimentally [37] (see Fig. 5.22). As starting geometries for the dynamical relaxations we have taken TCNQ molecules perfectly flat, for different parallel positions

lying on the Au(111) surface. Case a represents a dilute geometry, using a (7×7) periodic unit cell with 49 metal atoms per layer, and containing one TCNQ molecule per unit cell. The final optimized structure reveals the TCNQ lying bent on the Au surface with the center of the molecule on a surface “hollow” site, the higher atoms located at around 3 \AA , and the lower ones (the edge nitrogens) at around 2.4 \AA above the gold surface. Case b represents the experimental self-assembled geometry [37], where the TCNQ molecules form a close-packed monolayer. In this case, the final geometrical distortions of the molecule are slightly different than in the dilute geometry, with a rather flat profile of the central part of the molecules on the metal (located at 2.9 \AA above the gold), and with the edge N atoms in closer positions with respect to the surface, showing a covalent-like bonding. The unit cell for this case has (5×5) -like periodicity, with 34 metal atoms per layer in the Au substrate, and containing two TCNQ molecules per unit cell. The center of one of the molecules is located on a surface “bridge” site and the other on a “top” site, which make the molecules slightly non-equivalent electronically. Since the N atoms form bonds with the surface, we can neglect vdW forces: the driving adsorption force is the chemical force on the Au–N bond.

Although the distance between neighboring TCNQ molecules in case a is large ($>10 \text{ \AA}$), some depolarization effects may appear due to long-range electrostatic interactions. (In $5\sqrt{3} \times 5\sqrt{3} R30^\circ C_{60}/\text{Au}(111)$ layer this interaction was important, although the distance between molecules was more than 15 \AA). In order to eliminate this effect, we also analyze a single molecule adsorption simulating the interface via a (9×9) cluster with 81 metal atoms per layer (large enough to avoid border effects), with no periodicity and the same final adsorption geometry than case a (see Fig. 5.22c). This configuration allow us to properly calculate U , as in the other interfaces. In all cases, the Au(111) surface is simulated with 4 layers. We have checked that 6 layers yield results very similar to the 4 layers case.

Regarding the LDA gap, for TCNQ with this basis set it has a value of 1.65 eV , to be compared with 2.14 eV for converged LDA basis set or GGA calculations. The transport gap between ionization and affinity levels of the gas-phase TCNQ molecule is around 5.3 eV (see below). As in TTF/Au, we have calculated the exact value of the transport gap calculating ionization and affinity levels using the OCTOPUS simulation package [27] and the GGA–PBE0 hybrid functional [28]. From this calculation we obtain that U for the gas-phase TCNQ is $U = 3.7 \text{ eV}$.

5.5.2 Theoretical STM Images

Theoretical STM calculations have been performed for the TCNQ/Au(111) self-assembled structure (Fig. 5.22b) in order to make a detailed comparison with the experimental evidence [37]. The STM images are obtained using the Green-Keldysh function approach mentioned in Sect. 2.6, as in the TTF/Au interface. We have assumed to have the same W tip as in TTF/Au.

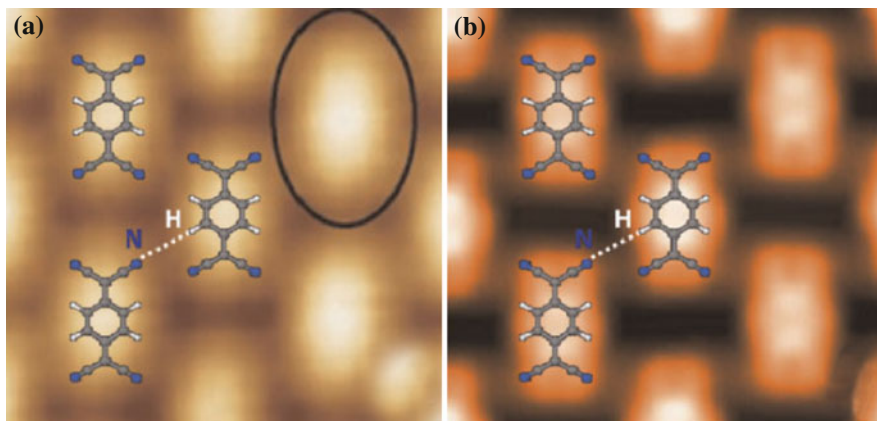


Fig. 5.23 **a** Experimental STM image of the self-organized TCNQ on Au(111) structure [37] (constant tip-height, $V_s = 0.3$ V). Experimental image from Fernandez-Torrente and coworkers [37]; and **b** theoretical STM image for the geometry of Fig. 5.22b (constant tip-height, $V_s = 0.5$ V). Reprinted from Physica Status Solidi B [38] Copyright 2011 Wiley-VCH (Color figure online)

Figure 5.23b shows our calculated STM images for the TCNQ/Au(111) self-assembled structure (Fig. 5.23b). W-tip height from TCNQ monolayer and surface voltage, V_s , take the typical values of 4.5 \AA and 0.5 V (above the Fermi level), in order to mimic experimental STM signal [37]. It is worth to stress that the variation of the W-tip height between 4 and 5 \AA does not reveal any significant change in the STM image. Experimentally it is observed that TCNQ molecules absorbed on Au(111) surface form highly ordered molecular assemblies [37]. As shown in Fig. 5.23, our theoretical STM image for the relaxed structure of Fig. 5.22b is in very good agreement with the experimental STM image for the self-assembled structure. The theoretical STM images also show some $\text{N} \cdots \text{H}$ intermolecular bonding between adjacent molecules; this bonding has been proposed to be responsible for the self-assembling of the TCNQ molecules [37]. Also, due to the slight non-equivalence between TCNQ molecules in the same unit cell of our calculations, small differences can be appreciated for alternating TCNQ molecules. Note that, although at first glance experimental STM images suggest that the organic molecule lies flat on the gold surface, our results with a bent geometry reproduce quite well the experimental STM image. Finally we also mention that theoretical STM images for a flat adsorption geometry (not shown) do not agree so well with experimental evidence.

5.5.3 Electronic Structure and Interface Potential

We analyze in this section the interface barrier formation. Upon adsorption of TCNQ, the relative position of the Fermi level with respect to the molecular levels changes due to the total potential induced on the molecule $V^{tot} = V^{DIS} + V_0^M$. Note

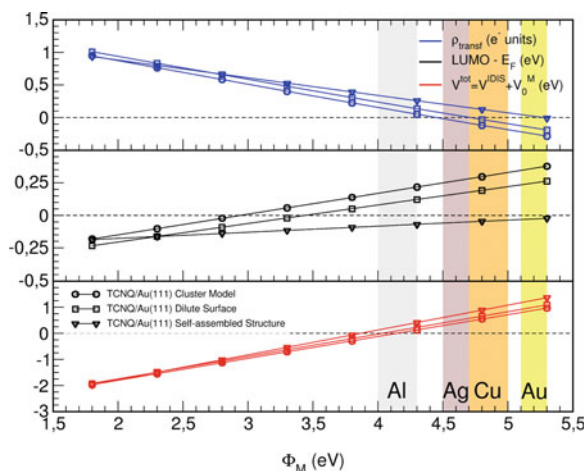


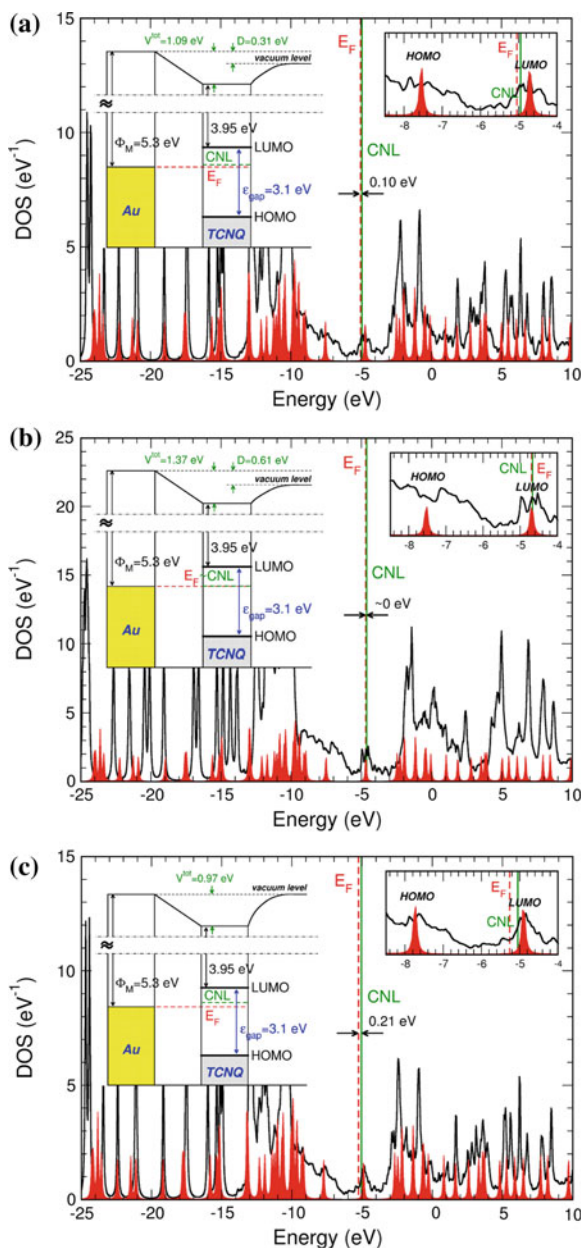
Fig. 5.24 (LUMO- E_F), transfer of charge δn and total potential, $V^I = V^{DIS} + V_0^M$, as a function of the initial Fermi level. The initial Fermi levels of Al, Ag, Cu and Au are shown for comparison. Reprinted from *Physica Status Solidi B* [38] Copyright 2011 Wiley-VCH (Color figure online)

that now we have a new term that adds to the standard IDIS potential. It is the “intrinsic” molecular dipole. It was introduced in Sect. 3.4, but it is the first case where it appears in practice in our thesis. The fact that a symmetric molecule like TCNQ can have an “intrinsic” dipole can be shocking; but as we said previously, the molecule is substantially deformed upon adsorption. The N atoms are closer to the Au surface, and they are negatively charged. On the contrary, the aromatic C ring, that is above the N atoms is positively charged, giving rise to a nonzero dipole along the z direction (that comes purely from charge reorganization in the TCNQ, not from charge transfer with surface), that certainly affects the interface potential. The value of V_0^M can be easily obtained as the total potential just for zero charge transfer. From Fig. 5.24, $V_0^M = 1.37$ eV. Note that in this case $\delta n = 0$ implies $V^{DIS} = 0$ but $V^{tot} = V_0^M \neq 0$ as opposed to the other interfaces of this work where zero charge transfer implied zero potential (if we neglect the pillow potential). The value of V_0^M for the single molecule case and the dilute geometry is 0.20 and 0.53 eV, respectively (see Fig. 5.24).

Note that also, in Fig. 5.24, when $\Phi_M = -5.2$ eV (the initial Fermi level of gold), $\delta n = 0$. This is in good agreement with the experimental evidence [37], where TCNQ is detected to be neutral on the Au(111) surface. Also, a very good linear scaling is observed for all the cases as Φ_M varies.

Figure 5.25c shows the DOS projected onto the molecular orbitals for the case of a single TCNQ on Au(111) (levels of a non-interacting molecule are also shown for comparison). For this case we obtain $S = 0.16$. Notice the visible level broadening associated with the TCNQ/metal interaction. Regarding the charging energy calculation for this molecular case, we obtain that $\delta U = 2.2$ eV and the transport gap is $E_g^I = 3.1$ eV (the effect of the “metal surface” dipole has been taken into

Fig. 5.25 DOS projected on the TCNQ orbitals for the geometries of Fig. 5.22 (case **a** dilute geometry; case **b** monolayer self-assembled structure; and case **c** single molecule on the surface). CNL, HOMO, LUMO and final Fermi (E_F) levels of the system are also shown. Molecular levels of the isolated TCNQ molecule are indicated by a red-shaded profile (y-scaled $\times 1/3$). Right inset enlarged image for the area around E_F . Left inset interface levels scheme for each case, showing V^{tot} . The vacuum level defines the energy zero. Reprinted from Physica Status Solidi B [38] Copyright 2011 Wiley-VCH (Color figure online)



account). The potential induced in the molecule is $V^{tot} = 0.97$ eV. Figure 5.25a shows our calculated DOS for the geometry of Fig. 5.22a; these results are similar to those presented for the single molecule, except for the Fermi level position, which in this case is located 1.09 eV above the initial metal Fermi level. This reflects a larger

surface screening due to the interaction between different molecules: for this particular case we find a value for the screening parameter of $S = 0.14$. The results for the monolayer geometry (Fig. 5.22b) are shown in Fig. 5.25b. The DOS profile for this case is similar to the ones found in previous cases, but in this case the Fermi level coincides with CNL. As previously mentioned, we find a large interface potential of 1.37 eV, and a really small screening parameter of $S = 0.05$. This small value of S reflects the large screening associated with this compact geometry; more tightly packed geometries increase the molecule–molecule interaction, an effect that also increases V^{tot} and the interface surface screening. Notice that in the left insets of Fig. 5.25a and b we have also shown the Helmholtz dipole potential layer Δ using the Eq. (3.9), with values of 0.31 and 0.61 eV for the dilute and monolayer structures, respectively ($\Delta = 0$ for the molecule over Au surface).

Regarding the pillow and “metal-surface” dipole, we find that both effects tend to cancel each other; nevertheless, the “metal-surface” dipole still slightly affects the value of U reducing it 0.2 eV, which reduces the transport energy gap by the same amount to the final value of 3.1 eV.

5.5.4 Conclusions

In summary, we have analyzed the organic-molecule/metal interface TCNQ/Au(111) using the formalism developed in this thesis. We find that the N atoms of the molecule bond to the surface, resulting in a bent geometry for the adsorbed TCNQ molecules, and practically no charge transfer between the metal and the molecules. Our theoretical STM images for the monolayer case are in very good agreement with the experimental STM images for the self-assembled geometry. Finally, we have analyzed the interface barrier formation and energy level alignment in terms of the IDIS model, showing the importance in this case of the “intrinsic” molecular dipole appearing on the TCNQ molecules on the Au(111) surface due to its bent geometry, that in this case leads the main contribution to the interface dipole.

5.6 Pentacene/Au(111) Interface: Hybrid Method in Practice

Finally we are going to consider the pentacene/Au interaction. Pentacene is one of the most widely used organic semiconductors both in research and industry, because of its high field-effect mobility. In this case, the molecular gap has been calculated using the standard scissor technique used in the previous interfaces and the hybrid HF-LDA functional explained in Sect. 2.7.3. As mentioned there, the β parameter, that controls the amount of exact and LDA exchange is chosen in order to obtain $E_g = E_g^{LDA} + U$; where U has been calculated using formula Eq. (4.3), as in previous interfaces. This work has been done in close collaboration with Dr. Barbara Pieczyrak, and has been published in *Journal of Chemical Physics* [39]. This section is an adapted version of that paper (Copyright 2011 American Institute of Physics).

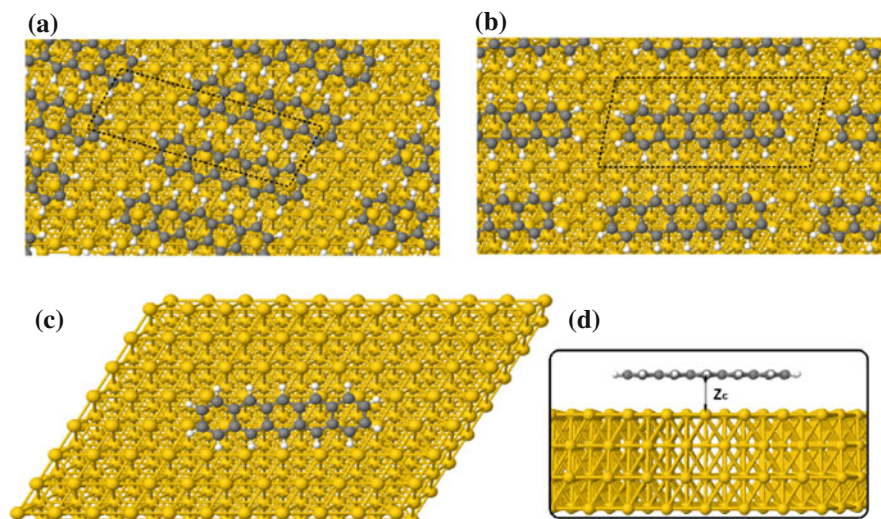


Fig. 5.26 Pentacene on the Au(111) surface: **a** $2 \times \sqrt{39}$ structure; **b** $6 \times \sqrt{7}$ structure; **c** cluster model; and **d** *side view* of a pentacene molecule on the Au(111) surface ($Z_C = 3.2 \text{ \AA}$). For **a** and **b** the *dashed lines* denote the surface unit cells used in the calculations. Reprinted from [39] Copyright 2011 American Institute of Physics (Color figure online)

This interface has also been analyzed theoretically by Toyoda et al. [40]; but at the DFT–GGA (+semiempirical vdW) level of theory. We have reconsidered the interface in order to accurately describe the barrier height formation, with a realistic organic transport energy gap.

5.6.1 Geometry

As in the other cases, we are going to analyze the pentacene/Au(111) barrier height for a single molecule and a full monolayer (see Fig. 5.26); in our calculations, we have assumed to have one of four predominant experimental unit cells: $2 \times \sqrt{39}$ structure (Fig. 5.26a); we use this one because at lower coverages pentacene molecules tend to have larger spacings between the rows of molecules such as in the chosen type [41]. For the sake of comparison with the work of Toyoda et al., we also have taken into account the $6 \times \sqrt{7}$ geometry they used in their research [40] (Fig. 5.26b).

The basis set used in our calculations is the same as in the benzene/Au interface. This yields a range of values between 1.36 and 1.47 Å for the C–C nearest neighbors distance in pentacene, to be compared with the experimental values of 1.35–1.45 Å [42] (in GGA–DFT these distances are 1.38–1.46 Å) [43].

In order to accurately determine the equilibrium distance of pentacene adsorbed on a gold surface, we have used here the WCI + vdW method used for C₆₀ and benzene

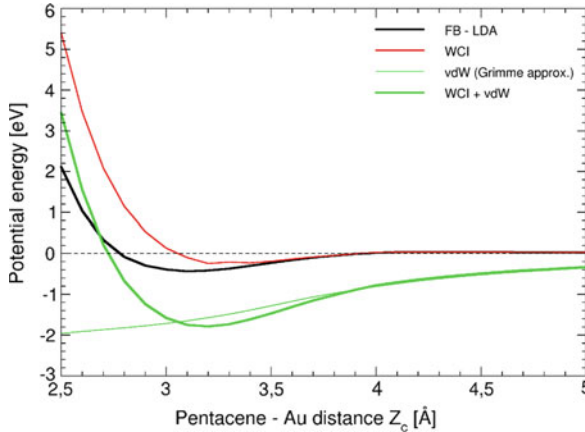


Fig. 5.27 Energy versus distance for the pentacene/Au(111) interaction. *Black line* standard LDA-FIREBALL (FB-LDA) calculation. *Red line* WCI calculated as discussed in the text. *Thin green line* Grimme parametrization of the vdW interaction. *Thick green line* total pentacene–Au interactions (WCI + vdW). Reprinted from [39] Copyright 2011 American Institute of Physics (Color figure online)

on Au(111) and explained in Sect. 2.7.1. The C_6 parameter in vdW Eq. (2.83) has been taken $C_6 = 36 \text{ eV} \cdot \text{Å}^6$ in for Au–C, $C_6 = 0$ for Au–H (as in previous calculations).

Regarding $f_D(R)$ we have used Grimme [7] parametrization obtaining a pentacene/Au distance of 3.2 Å, to be compared with LDA distance (3.1 Å), the WCI (without vdW) distance (3.3 Å) and the distance obtained by Toyoda et al. (3.2 Å), see Fig. 5.27.

5.6.2 Density of States, Interface Dipole and Charging Energy

Hybrid Potential Results

First of all we are going to present calculations for pentacene/Au(111) using the hybrid potential. Figure 5.28 shows our calculated DOS projected on the molecular orbitals for the three cases we have considered: a single molecule (c); the $6 \times \sqrt{7}$ —adlayer (b); and the $2 \times \sqrt{39}$ —monolayer (a) (see Fig. 5.26).

In these figures we also represent the molecular levels of the isolated molecule (in green). The energy gap has been calculated selfconsistently using the standard method explained in Sect. 4.2. This time, however, is the parameter β the one that has been fitted in order to have a selfconsistent gap. The transport gap obtained is $E^t = 3.1 \text{ eV}$, for a value of $\beta = 0.31$. The metal surface dipole effect in the gap (a reduction of 0.2 eV) has already been included.

Notice that this energy gap is a little larger than the peak-to-peak gap obtained from the calculated DOS; in particular, $E^t = 2.65, 2.8$ and 2.9 eV for cases a, b, and c, respectively. The usual levels, HOMO, LUMO, CNL and E_F , are shown. The

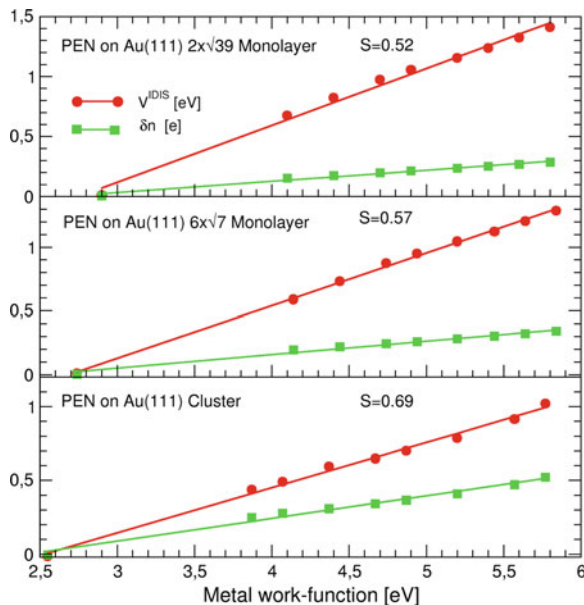


Fig. 5.29 V^{IDIS} and δn -charge transfer from the molecule to the metal (obtained with the hybrid potential) as a function of the initial Fermi Level (that can be seen as the absolute value of the metal work function). This change in the initial Fermi level. Reprinted from [39] Copyright 2011 American Institute of Physics (Color figure online)

CNL is located around ~ 0.2 eV from the LUMO peak (fluctuations around this value are probably related to the precision of our calculations). The IDIS potential takes the values: $V^{IDIS} = 1.15$ eV (a); 1.09 eV (b); and 0.79 eV (c). As in other interfaces, it decreases from the compact monolayer to the single molecule interfaces.

Figure 5.29 shows, for the cases a, b and c, V^{IDIS} and the charge transfer, δn , as a function of the initial Fermi level, that can be seen as a “fictitious” metal work-function, which is introduced by means of the scissor operator with $\Delta = 0$ (see Eq. 2.97). As the cases when we use the scissor operator, V^{IDIS} and δn depend linearly on Φ_M , and $V^{IDIS} \simeq 0$ when $\delta n = 0$. This shows that our IDIS model is valid when using a hybrid functional to correct the gap, and confirms that the general behavior predicted by the IDIS model does not depend on the method used to obtain an accurate value of the gap.

From Fig. 5.29 we find: $S = 0.52$ (a); 0.57 (b) and 0.69 (c), indicating that in the compact structure screening effects are the largest, and in the single molecule the smallest, like in the other interfaces studied previously.

Regarding the “pillow” dipole, we find it negligible in the minimal basis set used in our calculations. We have found, however, that using the more extended basis set ($sp^3d^5s^*d^{*5}$ for Au, sp^3d^5 for C and ss^* for H; used in previous interfaces) yields a bare pillow dipole potential, V_0^P , of 0.5 eV for the $2 \times \sqrt{39}$ monolayer. Screening effects reduce this potential to $V^P = SV_0^P = 0.25$ eV. Regarding the

metal surface dipole correction, we find that in the tight-packed $2 \times \sqrt{39}$ monolayer, $(E_F - \Phi_M)$ is reduced by 0.15 eV, this effect compensating to a large extent the potential, V^P , created by the “pillow” effect. For the single molecule case, we find that this compensation is even better; this metal surface dipole correction reduces, however, U and the transport energy gap by 0.2 eV, as stated before.

LDA with a Scissor Operator

We have also calculated the pentacene/Au(111) interface using the scissor operator to correct the transport gap, in order to compare both approaches and see the difference that this simpler approximation introduces in the band alignment and in the molecule energy gap. Figure 5.30 shows the DOS projected on the molecular orbitals for the same cases shown in Fig. 5.28; notice that the calculated DOS using the scissor operator is very similar to the one obtained with the hybrid potential. There are, however, some relevant differences, because although V^{DIS} is the same in both cases for all geometries, we find an important change in the molecule energy gap: while for the hybrid potential case we find for the isolated molecule $E^t = 3.1$ eV, using the scissor operator yields $E^t = 3.4$ eV, so that the peak-to-peak energy gap is: $E^t = 3.05$ (a), 3.2 (b) and 3.15 eV (c). The important point to realize about these results is that the calculated energy gap for the molecule, using the hybrid potential, is 0.3 eV smaller than the one calculated using the scissor operator.

We believe this difference is due to the delocalization of the intra-molecular exchange hole over the metal: for the isolated molecule, one can think of the SIC (or the charging energy, U_0) as being created by the exchange hole that eliminates the interaction of the molecular charge with itself (see Sect. 2.7.2); the metal–organic interaction delocalizes that hole and reduces, in our Hartree–Fock calculation, the SIC. We have found that, due to this pentacene/Au interaction, around 8% of the molecular exchange hole is delocalized into the metal.

Figure 5.31 shows V^{DIS} and δn as a function of the fictitious metal work-function. The behavior is very similar, but the slopes (i.e. the screening parameter) are different. The values for the screening parameter are $S = 0.52, 0.57, 0.69$ for the geometries a, b, c, respectively.

Regarding the “pillow” dipole and the metal-surface dipole corrections, we find that our results are very similar to the ones calculated using the hybrid potential approach.

5.6.3 Discussion and Conclusions

We have applied the hybrid-DFT calculation for pentacene on Au(111) considering the following cases: a single molecule, a $6 \times \sqrt{7}$ —adlayer and a $2 \times \sqrt{39}$ —monolayer. The hybrid potential is introduced to fix the transport energy gap, E^t , instead of the scissor operator used in previous interfaces. The accurate value of E^t and U ,

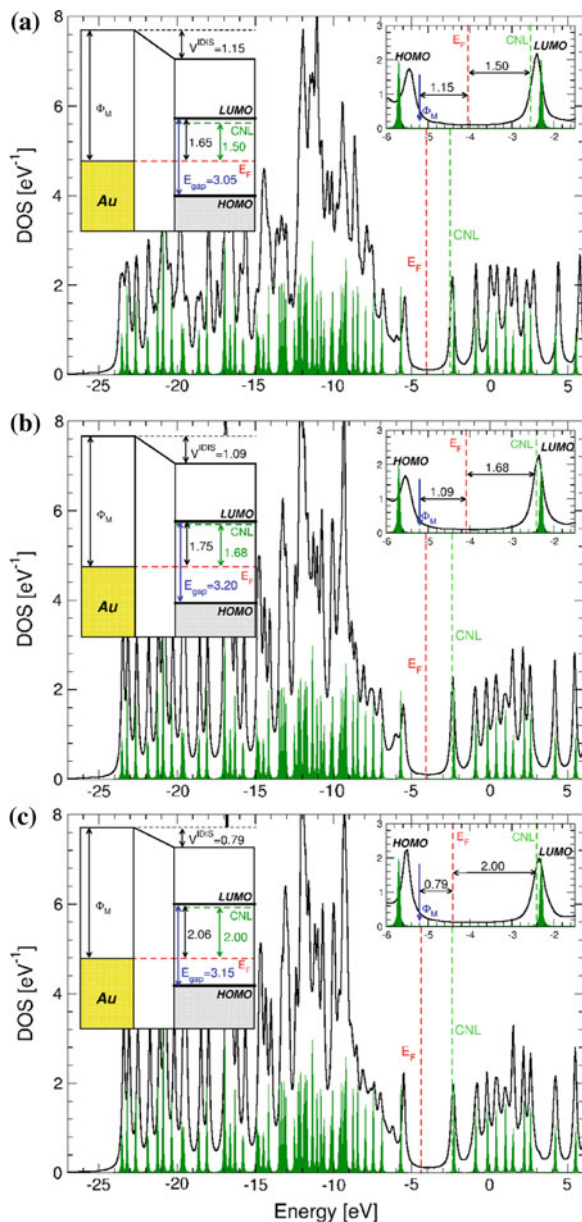


Fig. 5.30 DOS (obtained with the scissor operator) projected on the pentacene orbitals for the geometries of Fig. 5.26 (case **a** $2 \times \sqrt{39}$ structure; case **b** $6 \times \sqrt{7}$ structure; and case **c** cluster model). *CNL* of the molecule, metal work-function and Fermi level of the system are also shown. Molecular levels of the isolated molecule are indicated in green. *Right inset* enlarged image for the area around the HOMO and LUMO levels. *Left inset* interface levels scheme. All values are given in eV. Reprinted from [39] Copyright 2011 American Institute of Physics (Color figure online)

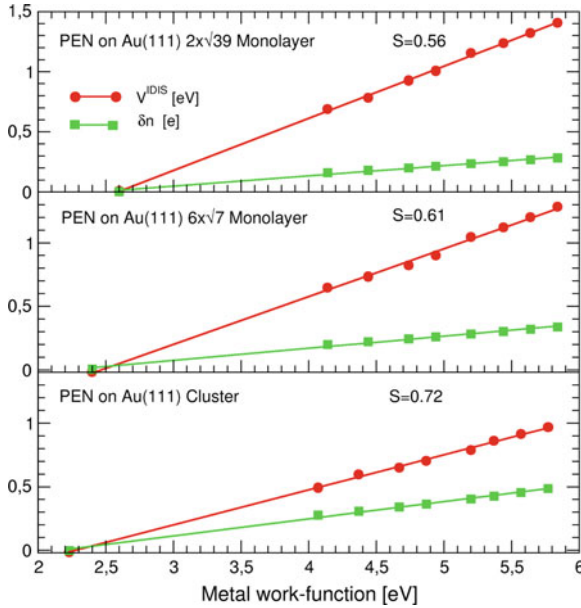


Fig. 5.31 V^{DIS} and δn -charge transfer from the molecule to the metal (obtained with the scissor operator) as a function of the initial Fermi Level (that can be seen as the absolute value of the metal work function). Reprinted from [39] Copyright 2011 American Institute of Physics (Color figure online)

has been obtained as in previous cases using Eq.(4.3). We have also analyzed the pentacene/Au interface using the “scissor” operator. It is interesting to stress that the results of both approaches, the hybrid potential and the “scissor” operator, are similar, showing that the interface barrier height is basically controlled by the charge transfer between the two materials; the only significant difference is found for transport energy gap, E^t , that is around 0.35 eV smaller in the case of the hybrid potential. We interpret that result as due to the delocalization in the metal of the exchange-hole associated with the SIC. [44] The values found for E^t in the $2 \times \sqrt{39}$ structure are 2.65 eV (hybrid potential) and 3.05 eV (scissor operator); these quantities can be compared with the experimental data of Amy et al. [45], who have measured $E^t = 2.88$ eV for a pentacene thickness of 20 \AA , in good agreement with our hybrid-DFT calculations (one can expect E^t to be slightly smaller than 2.88 eV for a pentacene monolayer). [45].

Regarding the metal work-function change due to the pentacene deposition, we have found in our calculations that the $6 \times \sqrt{7}$ and the $2 \times \sqrt{39}$ structures yield very similar results. In both cases, the interface electrostatic dipole $\Delta = 4\pi \frac{d\delta n}{A}$ Eq.(3.9), where d is the effective distance between the charges of the molecule, coincides practically with V^{DIS} : 1.09 and 1.15 eV for the b and a structures, respectively. The experimental evidence [41, 46, 47] indicates that this interface dipole is 0.95 eV, in good agreement with our results. Toyoda and coworkers [40] have

calculated an interface dipole of 1.19 eV for a $6 \times \sqrt{7}$ pentacene/Au(111) structure and a pentacene–Au distance of 3.2 Å; the interface dipole and the metal/organic distance are both in good agreement with our calculations.

As in previous cases, apart from the pillow dipole, our results does not depend significantly on the basis set, provided that the initial molecular levels are correctly aligned and the transport energy gap is set to the accurate value. This is also checked independently by the good agreement found with the calculations of Toyoda et al. [40].

In the case of the ‘pillow’ dipole; that we find to depend largely on the atomic basis set; as discussed in other interfaces: for an extended basis set V_0^P for a full monolayer is 0.25 eV, a value that is largely compensated by the surface dipole correction. This suggests that our calculated change of the metal work-function for the $6 \times \sqrt{7}$ and the $2 \times \sqrt{39}$ structures has an error bar of 0.1 eV.

In conclusion, both our hybrid HF and LDA + scissors results show a good agreement with the experimental data for the transport energy gap and the metal work-function change for a monolayer coverage, and with an independent theoretical calculation. This lends strong support to our interpretation of this metal/organic level alignment as due to the charge transfer between the metal and pentacene, as described in the IDIS-model.

5.7 Conclusions

In this chapter we have employed the ideas presented in previous chapter to obtain a realistic gap and calculate the interface properties of a variety of MO interfaces: C₆₀/Au(111), benzene/Au(111), TTF/Au(111), TCNQ/Au(111) and pentacene/Au(111). We see that obtaining an accurate gap size is usually critical in order to obtain realistic interface dipoles (the paradigmatic case is benzene), although in some cases is not that important (TTF). However, the electron and hole injection barriers depends explicitly on the HOMO/LUMO position so a correction to the Kohn–Sham levels is completely necessary for that case.

We have employed two different methods to address the gap correction: in both we rely on the calculation of the charging energy (U) for an isolated molecule over a metal surface. The formula Eq. (5.1) is not suitable to obtain the charging energy in the case of high coverages, since intermolecular electrostatic dipole-dipole terms are included. After that we open the gap both using a scissor operator or a hybrid HF functional (where Δ or β parameters are chosen to reproduce the gap $E_g^t = E_g^{KS} + U$).

We have also included in the calculations the effect of vdW interactions, in order to calculate a reliable molecule/metal distance. We have seen that they are necessary to get a realistic distance in most of the interfaces (apart from the C₆₀ case). Although our WCI + vdW approach does not give reliable energies, the distances are in good agreement with independent calculations for benzene and pentacene [15, 40].

References

1. E. Abad, J. Ortega, F. Flores, Metal/organic barrier formation for a C_{60} /Au interface: from the molecular to the monolayer limit. *Phys. Status Solidi A* **209**, 636 (2012)
2. F. Ortmann, F. Bechstedt, W. Schmidt, Semiempirical van der Waals correction to the density functional description of solids and molecular structures. *Phys. Rev. B* **73**(20), 205101 (2006)
3. C. González, J. Ortega, F. Flores, D. Martínez-Martín, J. Gómez-Herrero, Initial stages of the contact between a metallic tip and carbon nanotubes. *Phys. Rev. Lett.* **102**(10), 106801 (2009)
4. A. Tkatchenko, M. Scheffler, Accurate molecular van der Waals interactions from ground-state electron density and free-atom reference data. *Phys. Rev. Lett.* **102**(7), 073005 (2009)
5. C.-T. Tzeng, W.-S. Lo, J.-Y. Yuh, R.-Y. Chu, K.-D. Tsuei, Photoemission, near-edge x-ray-absorption spectroscopy, and low-energy electron-diffraction study of C_{60} on Au(111) surfaces. *Phys. Rev. B* **61**(3), 2263 (2000)
6. L.-L. Wang, H.-P. Cheng, Density functional study of the adsorption of a C_{60} monolayer on Ag(111) and Au(111) surfaces. *Phys. Rev. B* **69**(16), 165417 (2004)
7. S. Grimme, Semiempirical GGA-type density functional constructed with a long-range dispersion correction. *J. Comput. Chem.* **27**(15), 1787 (2006)
8. Y. Dappe, J. Ortega, F. Flores, Intermolecular interaction in density functional theory: application to carbon nanotubes and fullerenes. *Phys. Rev. B* **79**(16), 165409 (2009)
9. K.-D. Tsuei, J.-Y. Yuh, C.-T. Tzeng, R.-Y. Chu, S.-C. Chung, K.-L. Tsang, Photoemission and photoabsorption study of C_{60} adsorption on Cu(111) surfaces. *Phys. Rev. B* **56**(23), 15412 (1997)
10. L.-L. Wang, H.-P. Cheng, Rotation, translation, charge transfer, and electronic structure of C_{60} on Cu(111) surface. *Phys. Rev. B* **69**(4), 45404 (2004)
11. M.C. Desjonquères, D. Spanjaard, *Concepts in Surface Physics*. (Springer, Berlin, 1996)
12. P. Pou, R. Pérez, F. Flores, A. Yeyati, A. Martín-Rodero, J. Blanco, F. García-Vidal, J. Ortega, Local-density approach and quasiparticle levels for generalized hubbard hamiltonians. *Phys. Rev. B* **62**(7), 4309 (2000)
13. E. Abad, Y.J. Dappe, J.I. Martínez, F. Flores, J. Ortega, C_6H_6 /Au(111): interface dipoles, band alignment, charging energy, and van der Waals interaction. *J. Chem. Phys.* **134**(4), 044701 (2011)
14. D. Syomin, J. Kim, B.E. Koel, G.B. Ellison, Identification of adsorbed phenyl (C_6H_5) groups on metal surfaces: electron-induced dissociation of benzene on Au(111). *J. Phys. Chem. B* **105**(35), 8387 (2001)
15. K. Toyoda, Y. Nakano, I. Hamada, K. Lee, S. Yanagisawa, Y. Morikawa, First-principles study of benzene on noble metal surfaces: adsorption states and vacuum level shifts. *Surf. Sci.* **603**(18), 2912 (2009)
16. D.R. Lide (ed.), *Handbook of Chemistry and Physics* (Chemical Rubber Company Press, Boca Raton, 1998)
17. I. Nenner, G. Schulz, Temporary negative ions and electron affinities of benzene and N-heterocyclic molecules: pyridine, pyridazine, pyrimidine, pyrazine, and s-triazine. *J. Chem. Phys.* **62**(5), 1747 (1975)
18. J. Sau, J. Neaton, H. Choi, S. Louie, M. Cohen, Electronic energy levels of weakly coupled nanostructures: C_{60} -metal interfaces. *Phys. Rev. Lett.* **101**(2), 26804 (2008)
19. G. Witte, S. Lukas, P.S. Bagus, C. Wöll, Vacuum level alignment at organic/metal junctions: "Cushion" effect and the interface dipole. *Appl. Phys. Lett.* **87**(26), 263502 (2005)
20. J.M. Garcia-Lastra, C. Rostgaard, A. Rubio, K.S. Thygesen, Polarization-induced renormalization of molecular levels at metallic and semiconducting surfaces. *Phys. Rev. B* **80**(24), 245427 (2009)
21. P.S. Bagus, K. Hermann, C. Wöll, The interaction of C_6H_6 and C_6H_{12} with noble metal surfaces: electronic level alignment and the origin of the interface dipole. *J. Chem. Phys.* **123**(18), 184109 (2005)

22. O.T. Hofmann, G.M. Rangger, E. Zojer, Reducing the metal work function beyond pauli push-back: A computational investigation of tetrathiafulvalene and viologen on coinage metal surfaces. *J. Phys. Chem. C* **112**(51), 20357 (2008)
23. H. Yan, S. Li, C. Yan, Q. Chen, L. Wan, Adsorption of TTF, TCNQ and TTF-TCNQ on Au (111): an in situ ECSTM study. *Sci. China Ser. B Chem.* **52**(5), 559 (2009)
24. I. Fernandez-Torrente, S. Monturet, K. Franke, J. Fraxedas, N. Lorente, J. Pascual, Long-range repulsive interaction between molecules on a metal surface induced by charge transfer. *Phys. Rev. Lett.* **99**(17), 176103 (2007)
25. J. Martínez, E. Abad, C. González, J. Ortega, F. Flores, Theoretical characterization of the TTF/Au (111) interface: STM imaging, band alignment and charging energy. *Org. Electron.* **13**, 399 (2012)
26. C.S. Yannoni, P.P. Bernier, D.S. Bethune, G. Meijer, J.R. Salem, NMR determination of the bond lengths in C₆₀. *J. Am. Chem. Soc.* **113**(8), 3190 (1991)
27. M.A.L. Marques, A. Castro, G.F. Bertsch, A. Rubio, Octopus: a first-principles tool for excited electron-ion dynamics. *Comput. Phys. Commun.* **60** 151 (1), (2003)
28. C. Adamo, G.E. Scuseria, V. Barone, Accurate excitation energies from time-dependent density functional theory: assessing the PBE0 model. *J. Chem. Phys.* **111**(7), 2889 (1999)
29. J.M. Blanco, F. Flores, R. Perez, STM-theory: image potential, chemistry and surface relaxation. *Prog. Surf. Sci.* **81**(10–12), 403 (2006)
30. G. Kresse, J. Furthmüller, Efficient iterative schemes for ab-initio total-energy calculations using a plane-wave basis set. *Phys. Rev. B* **54**(16), 11169 (1996)
31. M.C. Payne, T.A. Arias, J.D. Joannopoulos, Iterative minimization techniques for ab initio total-energy calculations: molecular dynamics and conjugate gradients. *Rev. Mod. Phys.* **64**(4), 1045 (1992)
32. B. Hammer, L. Hansen, J. Nørskov, Improved adsorption energetics within density-functional theory using revised perdew-burke-ernzerhof functionals. *Phys. Rev. B* **59**(11), 7413 (1999)
33. W. Kaim, M. Moscherosch, The coordination chemistry of TCNE, TCNQ and related polynitrile π acceptors. *Coord. Chem. Rev.* **129**(1–2), 157 (1994)
34. A. Kahn, N. Koch, W. Gao, Electronic structure and electrical properties of interfaces between metals and π -conjugated molecular films. *J. Polym. Sci. Part B Polym. Phys.* **41**(21), 2529 (2003)
35. J.M. Manriquez, G.T. Yee, R.S. McLean, A.J. Epstein, J.S. Miller, A room-temperature molecular/organic-based magnet. *Science* **252**(5011), 1415 (1991)
36. J.S. Miller, A.J. Epstein, Organic and organometallic molecular magnetic materials—designer magnets. *Angew. Chem. Int. Ed.* **33**(4), 385 (1994)
37. I. Fernandez-Torrente, K. Franke, J. Pascual, Structure and electronic configuration of tetracyanoquinodimethane layers on a Au(111) surface. *Int. J. Mass spectrom.* **277**(1–3), 269 (2008)
38. J.I. Martínez, E. Abad, F. Flores, J. Ortega, Simulating the organic-molecule/metal interface TCNQ/Au(111). *Phys. Status Solidi B* **248**(9), 2044 (2011)
39. B. Pieczyrak, E. Abad, F. Flores, J. Ortega, Charging energy and barrier height of pentacene on Au(111): a local-orbital hybrid-functional density functional theory approach. *J. Chem. Phys.* **135**(8), 084702 (2011)
40. K. Toyoda, I. Hamada, K. Lee, S. Yanagisawa, Y. Morikawa, Density functional theoretical study of pentacene/noble metal interfaces with van der Waals corrections: vacuum level shifts and electronic structures. *J. Chem. Phys.* **132**(13), 134703 (2010)
41. P.G. Schroeder, C.B. France, J.B. Park, B.A. Parkinson, Energy level alignment and two-dimensional structure of pentacene on Au(111) surfaces. *J. Appl. Phys.* **91**(5), 3010 (2002)
42. R.B. Campbell, J.M. Robertson, J. Trotter, The crystal structure of hexacene, and a revision of the crystallographic data for tetracene. *Acta Crystallogr.* **15**, 289 (1962)
43. R.G. Endres, C.Y. Fong, L.H. Yang, G. Witte, C. Wöll, Structural and electronic properties of pentacene molecule and molecular pentacene solid. *Comput. Mater. Sci.* **29**(3), 362 (2004)

44. F. Flores, J. Ortega, H. Vázquez, Modelling energy level alignment at organic interfaces and density functional theory. *Phys. Chem. Chem. Phys.* **11**(39), 8658 (2009)
45. F. Amy, C. Chan, A. Kahn, Polarization at the gold/pentacene interface. *Org. Electron.* **6**(2), 85 (2005)
46. X. Liu, Y. Zhan, S. Braun, F. Li, M. Fahlman, Interfacial electronic properties of pentacene tuned by a molecular monolayer of C₆₀. *Phys. Rev. B* **80**(11), 115401 (2009)
47. N. Koch, Energy levels at interfaces between metals and conjugated organic molecules. *J. Phys. Condens. Matter* **20**(18), 184008 (2008)

Chapter 6

General Conclusions and Future Work

6.1 Conclusions

This thesis has been focused mainly on metal/organic interactions. Layers of organic molecules over metal surfaces (of technological importance in organic electronic devices); and molecules between metal electrodes (like the ones present in molecular electronic devices) have been analyzed using DFT (and introducing the appropriate corrections). For these systems it is very important to have correctly characterized the electron and hole injection barriers, in order to get realistic electrical conductance through these devices.

The study of these interfaces is challenging from a theoretical point of view. First of all, the vacuum level rule is disproved for most of them, indicating that a dipole layer is created. This fact has led to an extensive study, and some effects have been proposed to understand the origin of the dipole layer. These effects were summarized in Sect. 3.3. Special emphasis has been made on the IDIS model in Sect. 3.4. This model explains the origin of the dipole layer on metal/inorganic semiconductor interfaces [1, 2], and metal-organic interfaces [3–5]. Also an extension to include pillow dipole and intrinsic molecular dipoles has been made [6], called Unified-IDIS model. We interpret the results of our *ab initio* DFT calculations in terms of the IDIS model.

However, there is a fundamental problem when we make a theoretical *ab initio* approach to these interfaces. Standard DFT based techniques do not take into account some effects critical to describe these systems. The first one is the long range dispersive (vdW) forces, due to the locality (or semilocality) of the exchange-correlation functionals used. These forces are necessary to obtain reliable molecule-metal adsorption distances and energies. In this work an extension of the ideas of the LCAO- S^2 +vdW formalism, previously developed for noble gases and graphitic materials [7–9] has been applied, correcting the overbinding introduced in LDA. After that we include the vdW forces by introducing the standard correction with the form of Eq. (2.83). The idea of adding a semi-empirical vdW interaction to a “corrected” DFT energy is similar to the one developed by Pernal et al. [10]. We

have checked that this method gives reliable molecule-metal distances as compared with other calculations [11, 12].

The other problem with DFT for these interfaces, is that it does not take into account the SIC and the image potential effects. These effects are critical in order to have a correct description of the gap of the molecule over the metal surface. Ignoring these effects can lead to gaps underestimated by more than 50% and an interface dipole overestimation of the same amount. In order to correctly characterize these effects the scientific community have focused on more accurate *ab initio* methods, like GW or MP2 that have the disadvantage that the computational cost is orders of magnitude larger than standard DFT. This forces to use very small clusters to simulate the surface, and some important effects, like the molecule-molecule interaction will be missing (the importance of this interaction has been showed in Sect. 5.2.3 and [13]).

In this thesis a method for correctly estimate the change on the gap size by the SIC and the image potential effects has been developed. This method obtains gaps that compare well with other theoretical and experimental results (within an error bar of around 10%); and it has the advantage that the correct gap can be calculated using only the IDIS parameters obtained from an standard DFT calculation, as explained in Sect. 4.2.1, so no need of extensive computational resources are needed. Once the correct gap is obtained, it is introduced in the hamiltonian in two different ways: The first one is a scissor operator, whose implementation has been explained in Sect. 2.7.5. The other method is an hybrid DFT-HF method, also developed in this thesis (see Sect. 2.7.3 for details). Both approaches have been shown to give very similar results. The first principles code where these corrections are implemented is the FIREBALL code [14, 15].

In order to strength the importance of these effects to the calculation of the level alignment on MO interfaces, we have compared the results of $C_{60}/Au(111)$ interfaces and benzene/ $Au(111)$ interfaces using standard DFT-LDA techniques (Sect. 3.5) and using accurate molecule-metal distance and gap size (Sects. 5.2 and 5.3). In $C_{60}/Au(111)$ interface we clearly see how the increment of the energy gap from 1.8 to 3.1 also enlarge the interface barrier due to the IDIS dipole. However, the inclusion of vdW energy does not change very much the molecule-metal distance, indicating that the LDA geometry in this case is accurate enough for interface potential calculations. In benzene, both the vdW forces and the correction of the gap underestimation are critical to obtain a reliable interface potential (otherwise errors of more than 100% appear).

However, our method can be applied not only to MO interfaces but also to other kind of MO contact: the molecule-electrode contact that appear in molecular electronic devices. In this thesis, in Sects. 4.2 and 5.2.3, we have also shown how the IDIS model can be applied at the molecular level. This allows us to interpret the interface barriers that appear in molecular devices in terms of the IDIS model, and to obtain reliable values of the organic gap (critical for obtaining a quantitative value of the electrical conductance through the organic molecule). We have applied this to the approach of two gold tips to a C_{60} molecule (Sect. 4.3) and to a C_{60} molecule between a gold tip and a $Au(111)$ surface, with different adsorption sites (Sect. 4.4).

To sum up, in this thesis we have found a practical way to deal with vdW interactions and the underestimation of the LDA gap in MO interfaces, in the framework of DFT, and using the IDIS parameters, allowing realistic calculations with a computational effort of the order of magnitude of standard DFT calculations. We have applied this method to MO interfaces (C_{60} , benzene, TTF, TCNQ, pentacene on Au(111)). In this work, we have shown that the main ideas of the IDIS model remains valid at the molecular level; so we have employed this method in molecular electronic devices (a C_{60} molecule between two gold tips, and between a gold tip and a Au(111) surface).

6.2 Future work

In this work, there are still some details that can be refined. First of all, the “off-diagonal” and “pillow” potentials can be more accurately calculated. There is an new option on the FIREBALL code still under testing process that allow us to solve the Kohn-Sham equations in a real-space grid, introducing naturally the effect of these dipoles. Second, the extreme dependence with the basis set of “pillow” dipole is still not correctly understood, and although the dipole has been shown to be small, it is desirable to have it correctly described.

Regarding the vdW forces, we are working on new efficient methods to obtain a dispersionless exchange and correlation interaction, and its numerical implementation in FIREBALL. Moreover, we are working on more sophisticated calculations of the vdW energy (beyond formula (2.83)), following the ideas of [7, 8].

We also want to extend these ideas to organic/organic interfaces. A semiquantitative approach was developed in Hector Vázquez thesis [3]. However, we want to calculate the interface properties using first principles FIREBALL code, and with a realistic value for the organic gap. Nowadays, our research group is working on typical organic/organic interfaces such as pentacene/ C_{60} and TTF/TCNQ.

Finally, our model allow us to calculate a full variety of metal/organic interfaces of technological interest, that are being calculated or will be calculated in the following months (TTF-TCNQ/Au, C_{60} /Ag, C_{60} /Cu...). This model, combined with a Green-Keldysh calculation of transport properties [16] also allow us to calculate realistic conductances and currents through organic molecules between two electrodes. Some molecules of scientific interest (such as benzene-dithiol) can be calculated with this method.

References

1. C. Tejedor, F. Flores, E. Louis, The metal-semiconductor interface: Si (111) and zincblende (110) junctions. *J. Phys. C Solid State Phys.* **10**, 2163 (1977)

2. F. Flores, C. Tejedor, Energy barriers and interface states at heterojunctions. *J. Phys. C Solid State Phys.* **12**, 731 (1979)
3. H. Vázquez. Energy level alignment at organic semiconductor interfaces. Ph.D. thesis, Universidad Autónoma de Madrid (2006)
4. H. Vázquez, R. Oszwaldowski, P. Pou, J. Ortega, R. Pérez, F. Flores, A. Kahn, Dipole formation at metal/PTCDA interfaces: role of the charge neutrality level. *Europhys. Lett.* **65**(6), 802 (2004)
5. H. Vázquez, F. Flores, R. Oszwaldowski, J. Ortega, R. Pérez, A. Kahn, Barrier formation at metal-organic interfaces: dipole formation and the charge neutrality level. *Appl. Surf. Sci.* **234**(1–4), 107 (2004)
6. H. Vázquez, Y.J. Dappe, J. Ortega, F. Flores, Energy level alignment at metal/organic semiconductor interfaces: “pillow” effect, induced density of interface states, and charge neutrality level. *J. Chem. Phys.* **126**(14), 144703 (2007)
7. M.A. Basanta, Y.J. Dappe, J. Ortega, F. Flores, Van der Waals forces in the local-orbital density functional theory. *Europhys. Lett.* **70**(3), 355 (2005)
8. Y. Dappe, M. Basanta, F. Flores, J. Ortega, Weak chemical interaction and van der Waals forces between graphene layers: a combined density functional and intermolecular perturbation theory approach. *Phys. Rev. B* **74**(20), 205434 (2006)
9. Y. Dappe, J. Ortega, F. Flores, Intermolecular interaction in density functional theory: application to carbon nanotubes and fullerenes. *Phys. Rev. B* **79**(16), 165409 (2009)
10. K. Pernal, R. Podeszwa, K. Patkowski, K. Szalewicz, Dispersionless density functional theory. *Phys. Rev. Lett.* **103**(26), 263201 (2009)
11. K. Toyoda, Y. Nakano, I. Hamada, K. Lee, S. Yanagisawa, Y. Morikawa, First-principles study of benzene on noble metal surfaces: adsorption states and vacuum level shifts. *Surf. Sci.* **603**(18), 2912 (2009)
12. K. Toyoda, I. Hamada, K. Lee, S. Yanagisawa, Y. Morikawa, Density functional theoretical study of pentacene/noble metal interfaces with van der Waals corrections: vacuum level shifts and electronic structures. *J. Chem. Phys.* **132**(13), 134703 (2010)
13. E. Abad, J. Ortega, F. Flores, Metal/organic barrier formation for a C60/Au interface: from the molecular to the monolayer limit. *Phys. Status Solidi A.* **209**, 636 (2012)
14. J. Lewis, K. Glaesemann, G. Voth, J. Fritsch, A. Demkov, J. Ortega, O. Sankey, Further developments in the local-orbital density-functional-theory tight-binding method. *Phys. Rev. B* **64**(19), 195103 (2001)
15. P. Jelínek, H. Wang, J. Lewis, O. Sankey, J. Ortega, Multicenter approach to the exchange-correlation interactions in ab initio tight-binding methods. *Phys. Rev. B* **71**(23), 235101 (2005)
16. F.J. García-Vidal, F. Flores, S.G. Davison, Propagator theory of quantum-wire transmission. *Prog. Surf. Sci.* **74**(1–8), 177 (2003)

Appendix A

Introduction to Second Quantization

A.1 Second Quantization

The so-called first quantization (quantum mechanics based on the idea of wavefunctions), has the advantage of being reasonably intuitive and can take advantage of all the mathematical tools of calculus and partial and ordinary differential equations. However, it lacks of a natural way of introducing symmetrization or antisymmetrization of wavefunctions when we are dealing with many identical particles.

Second quantization offers a natural framework to take this into account, being the appropriate tool for the study of many-body systems. It is inspired in the algebraic resolution of a one dimensional particle in an harmonic potential, and relies on the use of creation and annihilation operators.

A.1.1 Creation and Annihilation Operators

Let's consider $|0\rangle$ as the vacuum state (a quantum state with no particles in it), different from the zero vector. The bosonic (fermionic) creation operator \hat{a}_i^\dagger (\hat{c}_i^\dagger) acts in the vacuum state creating a boson (fermion) in the state i , $|i\rangle$ (the i index can include spin variables). In an analog way the bosonic (fermionic) annihilation operator \hat{a}_i (\hat{c}_i) destroys a boson (fermion) in the state i . That is:

$$\begin{aligned} |i\rangle &= \hat{a}_i^\dagger |0\rangle \text{(for bosons)} |i\rangle = \hat{c}_i^\dagger |0\rangle \text{(for fermions)} \\ |0\rangle &= \hat{a}_i |i\rangle \text{(for bosons)} |0\rangle = \hat{c}_i |i\rangle \text{(for fermions)} \end{aligned} \tag{A.1}$$

The action of the annihilation operator in the vacuum state is the zero vector: $\hat{a}_i |0\rangle = \hat{c}_i |0\rangle = 0$ (they are not the same!). The bosonic (fermionic) creation and annihilation operators are mutually hermitian conjugate, and they have specific commutation (anticommutation) properties:

$$\begin{aligned}
[\hat{a}_i, \hat{a}_j] &= 0 & [\hat{a}_i^\dagger, \hat{a}_j^\dagger] &= 0 & [\hat{a}_i, \hat{a}_j^\dagger] &= \delta_{ij} \\
\{\hat{c}_i, \hat{c}_j\} &= 0 & \{\hat{c}_i^\dagger, \hat{c}_j^\dagger\} &= 0 & \{\hat{c}_i, \hat{c}_j^\dagger\} &= \delta_{ij}
\end{aligned}
\tag{A.2}$$

where the standard commutator (anticommutator) definitions $[A, B] = AB - BA$ ($\{A, B\} = AB + BA$) are used. An important operator is the number operator $\hat{n}_i = \hat{a}_i^\dagger \hat{a}_i$ (the same for fermions). It can be easily proved [1] that this operator gives the number of particles of state i .

If we want to rewrite an operator \hat{a}_i^\dagger in terms of other quantum indexes α , we need only to notice that:

$$\hat{a}_\alpha^\dagger |0\rangle = |\alpha\rangle = \sum_i \langle i|\alpha\rangle |i\rangle = \sum_i \langle i|\alpha\rangle \hat{a}_i^\dagger |0\rangle \Rightarrow \hat{a}_\alpha^\dagger = \sum_i \langle i|\alpha\rangle \hat{a}_i^\dagger
\tag{A.3}$$

and the same for fermions.

From now on we are going to focus on fermionic operators (since electrons are fermions). An important fact deduced from (A.2) is that: $\hat{c}_i^\dagger \hat{c}_i^\dagger = 0$, that means that there cannot be two fermions in the same quantum state i : the Pauli exclusion principle. Note that in second quantization this principle appears naturally, instead of being an *ad-hoc* assumption, showing the strength of this formalism.

Operators in Second Quantization

It is not difficult to rewrite the first quantization operators in second quantization form. Let's consider a one particle operator \hat{O} (like the kinetic energy) that operates in all particles ($\hat{O} = \sum_l \hat{O}(l)$). The result is:

$$\hat{O} = \sum_{ij} \langle i|\hat{O}(1)|j\rangle \hat{c}_i^\dagger \hat{c}_j
\tag{A.4}$$

For a two particle operator $\hat{V} = \sum_{l,j} \hat{V}(l, j)$ (like the electron-electron interaction) we obtain:

$$\begin{aligned}
\hat{V} &= \sum_{ijkl} V_{ijkl} \hat{c}_i^\dagger \hat{c}_j^\dagger \hat{c}_l \hat{c}_k \quad \text{where} \\
V_{ijkl} &= \int d^3\mathbf{r} d^3\mathbf{r}' \psi_i^*(\mathbf{r}) \psi_j^*(\mathbf{r}') \mathbf{V}(\mathbf{r}, \mathbf{r}') \psi_k(\mathbf{r}) \psi_l(\mathbf{r}')
\end{aligned}
\tag{A.5}$$

note the positions of \hat{c}_l and \hat{c}_k in the second quantized form of the operator.¹

¹ A derivation of the one particle and two particle operator formula can be found in [2], Chap. 1

A.1.3 Examples: Tight Binding and Hubbard Hamiltonians

We will show now a practical usage of second quantization formalism. Consider the following one-dimensional tight-binding hamiltonian:

$$\hat{H} = \sum_j \varepsilon_0 \hat{n}_j - \sum_j t(\hat{c}_{j+1}^\dagger \hat{c}_j + \hat{c}_j^\dagger \hat{c}_{j+1}) \quad (\text{A.6})$$

Its physical interpretation is very easy. The first sum gives the energy of an electron in the atomic orbital of site j (we are considering only one orbital per site), and the second term annihilates an electron in site j and move it to the neighbor (or annihilates a neighbor electron and create it in site j), that is, the hopping term. Introducing $\hat{c}_j = \sum_k e^{ikx_j} \hat{c}_k$ (where $x_j = aj$, the position of site j) we get:

$$\begin{aligned} \sum_j \hat{n}_j &= \sum_j \hat{c}_j^\dagger \hat{c}_j = \sum_{j,k,k'} e^{i(k-k')x_j} \hat{c}_k^\dagger \hat{c}_k = \sum_{k,k'} \delta_{k,k'} \hat{c}_k^\dagger \hat{c}_k = \sum_k \hat{c}_k^\dagger \hat{c}_k = \sum_k \hat{n}_k; \\ \sum_j \hat{c}_{j+1}^\dagger \hat{c}_j &= \sum_{j,k,k'} e^{i(k-k')x_j} e^{-ik'(x_{j+1}-x_j)} \hat{c}_k^\dagger \hat{c}_k = \sum_k e^{-ika} \hat{n}_k; \\ \hat{H} &= \sum_k (\varepsilon_0 - t(e^{-ika} + e^{ika})) \hat{n}_k = \sum_k (\varepsilon_0 - 2t \cos(ka)) \hat{n}_k \end{aligned} \quad (\text{A.7})$$

that is, with this variable change we obtain a diagonal hamiltonian, where the eigenvectors are plan waves and eigenenergies $E = \varepsilon_0 - 2t \cos(ka)$ that is the typical band dispersion in tight binding hamiltonian.

But this hamiltonian is one-electron (the electron-electron interaction is not taken into account). A simple hamiltonian that includes electron-electron interaction is the Hubbard hamiltonian.

$$\hat{H} = \sum_{i,\sigma} \varepsilon_0 \hat{n}_{i\sigma} - \sum_{i,\sigma} t(\hat{c}_{i+1\sigma}^\dagger \hat{c}_{i\sigma} + \hat{c}_{i\sigma}^\dagger \hat{c}_{i+1\sigma}) + \sum_i U \hat{n}_{i\uparrow} \hat{n}_{i\downarrow} \quad (\text{A.8})$$

where the explicit spin dependence has been shown. The extra term accounts for the coulomb repulsion of two electrons on the same site. Although this seems a very simple hamiltonian, trying to diagonalize it is far from simple. It has been done only for a certain number of dimensions, and new mathematical tools (like the renormalization group and quantum simulators) are necessary for diagonalizing it (when it is possible). On the other hand, the physics of this model is incredibly rich. The parameters governing this hamiltonian are U/t and the mean occupation $n = 1/2 \langle \sum_\sigma \hat{n}_{i\sigma} \rangle$ (we can get rid of ε_0 with a redefinition of the origin of energies). Ferromagnetism, antiferromagnetism and superconductivity appears depending on the values of U/t and n . More realist hamiltonians include the coulomb interaction between sites $\sum_{ij\sigma\sigma'} J_{ij} \hat{n}_{i\sigma} \hat{n}_{i\sigma'}$. This is the basis of the LCAO-OO hamiltonian shown in [Sect. 2.5](#).

A.1.4 Schrödinger and Heisenberg Pictures

In second quantization is usual to use the Heisenberg picture instead of the Schrödinger one (more usual in first quantization). The main difference between both is that in the Heisenberg picture the temporal evolution of the system lie on the operators, instead of the states of the system ($\widehat{O}_H = \widehat{O}_H(t)$; $|\Psi(t)\rangle_H = |\Psi(0)\rangle_H$). It is easy to change between both pictures using the evolution operator $\widehat{U}(t) = e^{-i\widehat{H}t/\hbar}$:

$$|\Psi(t)\rangle_S = \widehat{U}(t)|\Psi\rangle_H; \quad \widehat{O}_H(t) = \widehat{U}^\dagger(t)\widehat{O}_S\widehat{U}(t) \quad (\text{A.9})$$

And the equation of motion for the operators:

$$i\hbar \frac{d}{dt} \widehat{O}_H(t) = [\widehat{O}_H(t), H] \quad (\text{A.10})$$

A.2 Green Functions

The (causal) Green function of a system is defined (in the Heisenberg picture) as:

$$G_{\sigma,\sigma'}(\mathbf{r}, t, \mathbf{r}', t') = -\frac{i}{\hbar} \langle \Psi_0 | T[\widehat{c}_{\mathbf{r},\sigma}(t)\widehat{c}_{\mathbf{r}',\sigma'}^\dagger(t')] | \Psi_0 \rangle \quad (\text{A.11})$$

where $|\Psi_0\rangle$ is the ground state of the system and T is the time ordering operator, that ensures that the operators are placed in chronological order. That means:

$$G_{\sigma,\sigma'}(\mathbf{r}, t, \mathbf{r}', t') = \begin{cases} -i/\hbar \langle \Psi_0 | \widehat{c}_{\mathbf{r},\sigma}(t)\widehat{c}_{\mathbf{r}',\sigma'}^\dagger(t') | \Psi_0 \rangle & \text{if } t > t' \\ +i/\hbar \langle \Psi_0 | \widehat{c}_{\mathbf{r}',\sigma'}^\dagger(t')\widehat{c}_{\mathbf{r},\sigma}(t) | \Psi_0 \rangle & \text{if } t < t' \end{cases} \quad (\text{A.12})$$

Green functions can be expressed not only in terms of the position \mathbf{r} but also in terms of a general quantum state i . In this case its definition will be:

$$G(i, t, j, t') = -\frac{i}{\hbar} \langle \Psi_0 | T[\widehat{c}_i(t)\widehat{c}_j^\dagger(t')] | \Psi_0 \rangle \quad (\text{A.13})$$

We can define also retarded and advanced Green functions:

$$\begin{aligned} G^r(i, t, j, t') &= -\frac{i}{\hbar} \theta(t - t') \langle \Psi_0 | \{\widehat{c}_i(t)\widehat{c}_j^\dagger(t')\} | \Psi_0 \rangle \\ G^a(i, t, j, t') &= +\frac{i}{\hbar} \theta(t' - t) \langle \Psi_0 | \{\widehat{c}_i(t)\widehat{c}_j^\dagger(t')\} | \Psi_0 \rangle \end{aligned} \quad (\text{A.14})$$

Rewriting the green function $G(i, t, j, t')$ using the quantum states α, β ($G(\alpha, t, \beta, t')$) is easy if we use the formula (A.3). From now on, in order to simplify the notation we are going to work in units where $\hbar = 1$

A.2.1 One Electron Green Functions

In order to understand better the physical meaning of the Green function, we are going to consider that we are dealing with a simple one-electron time-independent hamiltonian. If we take the index j to run over the eigenstates of the Hamiltonian, we can calculate easily the sandwiches of retarded green function (remember we are on the Heisenberg picture). This way we get, for the first part of anticommutator:

$$\langle \Psi_0 | e^{iHt} \hat{c}_j e^{iH(t'-t)} \hat{c}_j^\dagger e^{-iHt'} | \Psi_0 \rangle = e^{iE_0\tau} \langle \Psi_0 | \hat{c}_j e^{iH(t'-t)} \hat{c}_j^\dagger | \Psi_0 \rangle = e^{iE_0\tau} e^{-i(\varepsilon_j + E_0)\tau} = e^{-i\varepsilon_j\tau} \quad (\text{A.15})$$

where $\tau = t - t'$ and we have supposed that level j is occupied (otherwise the sandwich is zero). For the other part of the anticommutator, we get the same result $e^{-i\varepsilon_j\tau}$ if the level j is empty (otherwise is zero), so the retarded green function is:

$$G^r(j, \tau) = -i\theta(\tau)e^{-i\varepsilon_j\tau} \quad (\text{A.16})$$

no matter if state j is occupied or empty. If we make the time Fourier transform:

$$G^r(j, \omega) = \int_{-\infty}^{\infty} d\tau e^{i\omega\tau} (-i\theta(\tau)e^{-i\varepsilon_j\tau}) = \lim_{\eta \rightarrow 0^+} \int_0^{\infty} d\tau (-ie^{i(\omega - \varepsilon_j + i\eta)\tau}) = \lim_{\eta \rightarrow 0^+} \frac{1}{\omega - \varepsilon_j + i\eta} \quad (\text{A.17})$$

where η is a positive infinitesimal quantity necessary for the convergence of the integral. In an analog way, the advanced green function in energy space:

$$G^a(j, \omega) = \lim_{\eta \rightarrow 0^+} \frac{1}{\omega - \varepsilon_j - i\eta} \quad (\text{A.18})$$

or in other basis:

$$G^{r,a}(\alpha, \beta, \omega) = \lim_{\eta \rightarrow 0^+} \sum_j \frac{\langle \alpha | j \rangle \langle j | \beta \rangle}{\omega - \varepsilon_j \pm i\eta} \quad (\text{A.19})$$

The green function can be rewritten as a matrix operator, using this definition

$$G^{r,a}(\alpha, \beta, \omega) = \langle \alpha | \mathbb{G}^{r,a}(\omega) | \beta \rangle; \quad \text{where} \quad \mathbb{G}^{r,a}(\omega) = \sum_j \frac{|j\rangle \langle j|}{\omega - \varepsilon_j \pm i\eta} \quad (\text{A.20})$$

This is known as the spectral representation of the green function. The meaning of Green function, and the connection with Green functions in classical physics can be made just noting that $\mathbb{G}^{r,a}(\omega)$ can be written as:

$$\mathbb{G}^{r,a}(\omega) = [(\omega \pm i\eta)\mathbb{I} - \mathbb{H}]^{-1} \quad (\text{A.21})$$

This is the usual definition of Green functions in classical theory: the “inverse” of a differential operator, (in this case $(\omega \pm i\eta)\mathbb{I} - \mathbb{H}$). This is the reason of the name and definition of this function. Moreover, this definition can be useful for one-electron problems. For instance, in the FIREBALL code, this is the way the green function is defined.

Coming back to formula (A.20), we can use the Green matrix to calculate the local density of states (very important in our MO interfaces). It is defined as:

$$\rho_\alpha(E) = \sum_j |\langle \alpha | j \rangle|^2 \delta(E - \varepsilon_j) \quad (\text{A.22})$$

And introducing in (A.20) the mathematical relation:

$$\lim_{\eta \rightarrow 0^+} \frac{1}{E - \varepsilon_j \pm i\eta} = \mathcal{P} \left[\frac{1}{E - \varepsilon_j} \right] \mp i\pi \delta(E - \varepsilon_j) \quad (\text{A.23})$$

we get the following equality (\mathcal{P} is the Cauchy principal value of the integral):

$$\rho_\alpha(E) = \mp \frac{1}{\pi} \text{Im}[\mathbb{G}_{\alpha\alpha}^{r,a}(E)] \quad (\text{A.24})$$

A.2.2 Many-Body Green Functions

If we are dealing with many-body electron interacting systems, properties of Green functions are not as straightforward as the one-electron ones. However, we can deduce some properties about them (that of course, apply for one-electron green functions too). Let’s consider the energy space representation of Green functions. For the retarded green function, the first part of the anticommutator is:

$$\begin{aligned} \langle \Psi_0 | e^{iHt} \hat{c}_i e^{iH(t-t')} \hat{c}_j^\dagger e^{-iHt'} | \Psi_0 \rangle &= \sum_m e^{iE_0^N \tau} \langle \Psi_0 | \hat{c}_i e^{iH(t-t')} | \Psi_m^{N+1} \rangle \langle \Psi_m^{N+1} | \hat{c}_j^\dagger | \Psi_0 \rangle \\ &= \sum_m e^{-i(E_m^{N+1} - E_0^N) \tau} \langle \Psi_0 | \hat{c}_i | \Psi_m^{N+1} \rangle \langle \Psi_m^{N+1} | \hat{c}_j^\dagger | \Psi_0 \rangle \end{aligned} \quad (\text{A.25})$$

where we have used the property $\mathbb{I} = \sum_m | \Psi_m^{N+1} \rangle \langle \Psi_m^{N+1} |$. This equation is not as simple as (A.15), but some information can be taken from it. If we repeat a similar argument for the second part of the anticommutator we get $\sum_m e^{-i(E_0^N - E_m^{N-1}) \tau} \langle \Psi_0 | \hat{c}_j^\dagger | \Psi_m^{N-1} \rangle \langle \Psi_m^{N-1} | \hat{c}_i | \Psi_0 \rangle$. The temporal dependence of both equations is the same as one-electron green function, so the Fourier transform is analog to (A.17) and we get:

$$G^{r,a}(i,j,\omega) = \sum_m \frac{\langle \Psi_0 | \hat{c}_i | \Psi_m^{N+1} \rangle \langle \Psi_m^{N+1} | \hat{c}_j^\dagger | \Psi_0 \rangle}{\omega - (E_m^{N+1} - E_0^N) \pm i\eta} + \sum_m \frac{\langle \Psi_0 | \hat{c}_j^\dagger | \Psi_m^{N-1} \rangle \langle \Psi_m^{N-1} | \hat{c}_i | \Psi_0 \rangle}{\omega - (E_m^{N-1} - E_0^N) \pm i\eta} \quad (\text{A.26})$$

and the causal Green function is:

$$G^c(i,j,\omega) = \sum_m \frac{\langle \Psi_0 | \hat{c}_i | \Psi_m^{N+1} \rangle \langle \Psi_m^{N+1} | \hat{c}_j^\dagger | \Psi_0 \rangle}{\omega - (E_m^{N+1} - E_0^N) + i\eta} + \sum_m \frac{\langle \Psi_0 | \hat{c}_j^\dagger | \Psi_m^{N-1} \rangle \langle \Psi_m^{N-1} | \hat{c}_i | \Psi_0 \rangle}{\omega - (E_m^{N-1} - E_0^N) - i\eta} \quad (\text{A.27})$$

This is known as Lehmann representation (or spectral representation). We can see that the green function has not only information of our system, but also of the system with $N \pm 1$ electrons. If we consider the thermodynamic limit $N \rightarrow \infty$, then $E_0^{N+1} - E_0^N \rightarrow \mu$ (chemical potential), and $\omega_m^{N\pm 1} = E_m^{N\pm 1} - E_0^{N\pm 1}$ are the excited states of the system with an extra electron (hole). This way the Green functions can be written as:

$$G^{r,a}(i,j,\omega) = \sum_m \frac{\langle \Psi_0 | \hat{c}_i | \Psi_m^{N+1} \rangle \langle \Psi_m^{N+1} | \hat{c}_j^\dagger | \Psi_0 \rangle}{\omega - \mu - \omega_m^{N+1} \pm i\eta} + \sum_m \frac{\langle \Psi_0 | \hat{c}_j^\dagger | \Psi_m^{N-1} \rangle \langle \Psi_m^{N-1} | \hat{c}_i | \Psi_0 \rangle}{\omega - \mu + \omega_m^{N-1} \pm i\eta} \quad (\text{A.28})$$

With this expression, there are some properties about Green Functions that can be deduced easily. First of all, the pole structure: they have poles at quasiparticle energies. Due to $\pm i\eta$, the poles do not lie at real axis, but slightly displaced in complex plane. Also the relationships between the Green matrices:

$$\begin{aligned} \mathbb{G}^a(\omega) &= \mathbb{G}^{r,\dagger}(\omega) \\ \mathbb{G}^c(\omega) &= \begin{cases} \mathbb{G}^r(\omega) & \text{if } \omega > \mu \\ \mathbb{G}^a(\omega) & \text{if } \omega < \mu \end{cases} \end{aligned} \quad (\text{A.29})$$

Another important property of diagonal Green functions, is the Hilbert transform relationship between real and imaginary part of green functions, due to their pole structure

$$\begin{aligned} \text{Re } G_{ii}^{r,a}(\omega) &= \mp \frac{1}{\pi} \mathcal{P} \int_{-\infty}^{\infty} d\omega' \frac{\text{Im } G_{ii}^{r,a}(\omega')}{\omega - \omega'} \\ \text{Re } G_{ii}^c(\omega) &= \mp \frac{1}{\pi} \mathcal{P} \int_{-\infty}^{\infty} d\omega' \frac{\text{Im } G_{ii}^c(\omega') \text{sgn}(\omega' - \mu)}{\omega - \omega'} \end{aligned} \quad (\text{A.30})$$

A.2.3 Equilibrium Perturbation Theory and Interaction Picture

Apart from historical Schrödinger and Heisenberg pictures (defined in A.1.4), there is a third picture of quantum mechanics, very useful in perturbation theory: the interaction picture. Consider that we have a hamiltonian of the form:

$$\widehat{H} = \widehat{H}_0 + \widehat{V} \quad (\text{A.31})$$

where \widehat{H}_0 is a exactly solvable hamiltonian, and \widehat{V} a small perturbation of the hamiltonian (that can depend on t , $\widehat{V} = \widehat{V}(t)$). In this case we can use perturbation theory, in order to have a series expansion whose terms are of the order \widehat{V}^n (see below). The states and operators are defined in interaction picture as:

$$\begin{aligned} |\Psi(t)\rangle_I &= e^{i\widehat{H}_0 t/\hbar} |\Psi(t)\rangle_S = e^{i\widehat{H}_0 t/\hbar} e^{-i\widehat{H} t/\hbar} |\Psi\rangle_H \\ \widehat{O}_I(t) &= e^{i\widehat{H}_0 t/\hbar} \widehat{O}_S e^{-i\widehat{H}_0 t/\hbar} \end{aligned} \quad (\text{A.32})$$

Note that $e^{i\widehat{H}_0 t/\hbar} e^{-i\widehat{H} t/\hbar} \neq e^{-i\widehat{V} t/\hbar}$ due to $[\widehat{H}_0, \widehat{H}] \neq 0$ in general. The equations of motion of the states and operators are on the form:

$$i\hbar \frac{d}{dt} |\Psi(t)\rangle_I = \widehat{V}(t) |\Psi(t)\rangle_I; \quad i\hbar \frac{d}{dt} \widehat{O}_I(t) = [\widehat{O}_I, \widehat{H}_0] \quad (\text{A.33})$$

In the interaction picture the temporal evolution operator is defined as $|\Psi(t)\rangle_I = \widehat{S}(t, t_0) |\Psi(t_0)\rangle_I$, and has the following properties:

$$\begin{aligned} i \frac{d}{dt} \widehat{S}(t, t_0) &= \widehat{V} \widehat{S}(t, t_0) \\ \widehat{S}(t, t_0) &= e^{i\widehat{H}_0 t/\hbar} e^{-i\widehat{H}(t-t_0)/\hbar} e^{-i\widehat{H}_0 t_0/\hbar} \\ |\Psi\rangle_H &= \widehat{S}(0, t) |\Psi(t)\rangle_I; \quad \widehat{O}_H(t) = \widehat{S}(0, t) \widehat{O}_I(t) \widehat{S}(t, 0) \end{aligned} \quad (\text{A.34})$$

As said before, we can perform a series expansion of $\widehat{S}(t, t_0)$ using the first equation in (A.34). If we start with $\widehat{S}(t, t_0) = \mathbb{I}$ and solve iteratively the first equation on (A.34); we get:

$$\begin{aligned} \widehat{S}(t, t_0) &= \mathbb{I} + \sum_{n=1}^{\infty} \frac{(-i)^n}{n!} \int_{t_0}^t dt_1 \dots \int_{t_0}^t dt_n T[\widehat{V}(t_1) \dots \widehat{V}(t_n)] \\ &= T \left[\exp \left(-i \int_{t_0}^t dt_1 \widehat{V}(t_1) \right) \right] \end{aligned} \quad (\text{A.35})$$

where T is the time ordering operator.

Adiabatic hypothesis

Usually, in quantum mechanics, what we want to calculate is the mean value of an observable O in the ground state, that is what can be measured experimentally. It can be calculated (in Heisenberg picture) as:

$$\langle O \rangle(t) = \frac{\langle \Psi_{0,H} | \widehat{O}_H(t) | \Psi_{0,H} \rangle}{\langle \Psi_{0,H} | \Psi_{0,H} \rangle} \quad (\text{A.36})$$

that can be rewritten in interaction picture as:

$$\langle O \rangle(t) = \frac{\langle \Psi_{0,H} | \widehat{S}(0, t) \widehat{O}_I(t) \widehat{S}(t, 0) | \Psi_{0,H} \rangle}{\langle \Psi_{0,H} | \Psi_{0,H} \rangle} \quad (\text{A.37})$$

Now we are going to make use of the *adiabatic hypothesis*. It consist on switching on (and off) the perturbation very slowly, so the perturbation is practically constant (and equal to the actual perturbation) during the time scale of the problem, but this interaction does not exist in $t = -\infty, +\infty$. Mathematically, we introduce a time dependence $\widehat{V}(t) = \widehat{V} e^{-\eta|t|}$, where $\eta \rightarrow 0^+$. With this hypothesis we ensure that the at $t = -\infty$ the ground state is the ground state of the unperturbed hamiltonian (\widehat{H}_0): $|\Psi_{0,H}^0\rangle$. On the other hand, $|\Psi_{0,H}\rangle$, the ground state of the perturbed one is (apart from a phase factor):

$$|\Psi_{0,H}\rangle = \widehat{S}(0, -\infty) |\Psi_{0,H}^0\rangle \quad (\text{A.38})$$

Introducing this back in Eq. (A.37) we get:

$$\langle O \rangle(t) = \frac{\langle \Psi_{0,H}^0 | \widehat{S}(\infty, t) \widehat{O}_I(t) \widehat{S}(t, -\infty) | \Psi_{0,H}^0 \rangle}{\langle \Psi_{0,H}^0 | \widehat{S}(\infty, -\infty) | \Psi_{0,H}^0 \rangle} = \frac{\langle \Psi_{0,H}^0 | T[\widehat{O}_I(t) \widehat{S}(\infty, -\infty)] | \Psi_{0,H}^0 \rangle}{\langle \Psi_{0,H}^0 | \widehat{S}(\infty, -\infty) | \Psi_{0,H}^0 \rangle} \quad (\text{A.39})$$

where, due to temporal symmetry, the ground state at $t = -\infty$ and $t = \infty$ is the same except for a phase factor, that is exactly canceled with the denominator. We can introduce here the explicit value of \widehat{S} (A.35), and what we get is sandwiches of the form $\langle \Psi_{0,H}^0 | T[\widehat{O}_I(t) \widehat{V}(t_1) \dots \widehat{V}(t_n)] | \Psi_{0,H}^0 \rangle$. And if we write $\widehat{O}_I(t)$ and $\widehat{V}(t_1)$ in terms of creation and annihilation operators (using (A.4),(A.5) and remembering that $\widehat{O}_I(t) = e^{i\widehat{H}_0 t} \widehat{O}_S e^{-i\widehat{H}_0 t}$ does not depend on the perturbed hamiltonian), we get sandwiches of the form:

$$\begin{aligned} & \langle \Psi_{0,H}^0 | T[\hat{c}_i(t_1) \hat{c}_i^\dagger(t_2) \dots \hat{c}_i(t_{n-1}) \hat{c}_i^\dagger(t_n)] | \Psi_{0,H}^0 \rangle \\ &= \sum (-1)^\gamma \langle \Psi_{0,H}^0 | T[\hat{c}_i(t_1) \hat{c}_i^\dagger(t_2)] | \Psi_{0,H}^0 \rangle \dots \langle \Psi_{0,H}^0 | T[\hat{c}_i(t_{n-1}) \hat{c}_i^\dagger(t_n)] | \Psi_{0,H}^0 \rangle \end{aligned} \quad (\text{A.40})$$

where the sum is extended to all possible permutations of the operators, and γ is the number of permutations. The previous equation is called Wick theorem and is very important in many-body theory.

It is necessary to note that, due to Wick theorem, we get terms of the form $\langle \Psi_{0,H}^0 | T[\hat{c}_i(t)\hat{c}_j^\dagger(t')] | \Psi_{0,H}^0 \rangle$, that are precisely (apart from a factor) the causal green function of the unperturbed system. Here relies one of the most important uses of Green functions.

Dyson equation

If we take $\widehat{O}_H(t) = \hat{c}_i(t)\hat{c}_j^\dagger(t')$ in (A.37), and realize that $\langle O \rangle(t) = G^c(i, t, j, t')$ we can use the work of previous section to obtain a perturbative expansion of the green function.

$$G(i, t, j, t') = \frac{1}{\langle \Psi_{0,H}^0 | \widehat{S}(\infty, -\infty) | \Psi_{0,H}^0 \rangle} \times \left[G^0(i, t, j, t') + \sum_{n=1}^{\infty} \frac{(-i)^{n+1}}{n!} \int_{-\infty}^{\infty} dt_1 \dots \int_{-\infty}^{\infty} dt_n \langle \Psi_{0,H}^0 | T[\hat{c}_i(t)\widehat{V}(t_1) \dots \widehat{V}(t_n)\hat{c}_j^\dagger(t')] | \Psi_{0,H}^0 \rangle \right] \quad (\text{A.41})$$

Applying Wick theorem to Eq. (A.41) leads to a sum of terms that can be easily understood in terms of Feynman diagrams (see for example [3] for a complete discussion about Feynman diagrams). However we are not interested now about diagrams. Just realize that in that expansion we will have always terms on the form $\langle \Psi_{0,H}^0 | T[\hat{c}_i(t)\hat{c}_j^\dagger(t')] | \Psi_{0,H}^0 \rangle$ (there are other terms, but they are zero, or are canceled by the denominator). It can be proved [2] that expansion can be written in the following form:

$$G(i, t, j, t') = G^0(i, t, j, t') + \sum_{k,l} \int_{-\infty}^{\infty} dt_1 \int_{-\infty}^{\infty} dt_2 G^0(i, t, k, t_1) \Sigma_I(k, t_1, l, t_2) G^0(l, t_2, j, t') \quad (\text{A.42})$$

or in energy space

$$G(i, j, \omega) = G^0(i, j, \omega) + \sum_{k,l} G^0(i, k, \omega) \Sigma_I(k, l, \omega) G^0(l, j, \omega) \quad (\text{A.43})$$

or in matrix notation.

$$\mathbb{G}(\omega) = \mathbb{G}^0(\omega) + \mathbb{G}^0(\omega) \Sigma_I(\omega) \mathbb{G}^0(\omega) \quad (\text{A.44})$$

where Σ_I is the *improper* selfenergy. It can be used to describe the effect of an external potential or the electron-electron interaction. It is necessary to realize the compactness of this equation, if it is compared with (A.41), due to all the effect of the perturbation is included in Σ_I .

In the case of an external potential, the meaning of Σ_I can be easily understood as the bare electron scattering an arbitrary number of times with the potential (the series expansion term of order n of Σ_I contains n scattering events). It can be written in a different form, considering that the self energy contains only one

scattering processes, but with the *dressed* electron instead of the bare one. Mathematically that means:

$$\Sigma_I(\omega)\mathbb{G}^0(\omega) = \Sigma(\omega)\mathbb{G}(\omega) \quad (\text{A.45})$$

where Σ is the *proper* selfenergy (or just selfenergy). So we arrive to the important Dyson equation

$$\mathbb{G}(\omega) = \mathbb{G}^0(\omega) + \mathbb{G}^0(\omega)\Sigma(\omega)\mathbb{G}(\omega) \quad (\text{A.46})$$

We can easily solve the equation for $\mathbb{G}(\omega)$:

$$\mathbb{G}(\omega) = [\omega\mathbb{I} - \mathbb{H}_0 - \Sigma(\omega)]^{-1} \quad (\text{A.47})$$

This equation shows that the effect of selfinteraction is to renormalize dynamically (it depends on ω) the unperturbed hamiltonian.

In the case that the external potential \hat{V} is a one-electron one we get:

$$\mathbb{G}(\omega) = \mathbb{G}^0(\omega) + \mathbb{G}^0(\omega)\mathbb{V}\mathbb{G}(\omega) \quad (\text{A.48})$$

This can be derived without this complex many-body perturbation theory formalism, just taking into account that $\mathbb{G}(\omega) = [\omega\mathbb{I} - \mathbb{H}_0 - \mathbb{V}]^{-1}$ and $\mathbb{G}^0(\omega) = [\omega\mathbb{I} - \mathbb{H}_0]^{-1}$ (Eq. (A.21)).

A.2.4 Non Equilibrium Perturbation Theory and Keldysh Formalism

The formalism developed in previous section can be used for a full variety of different situations as long as processes during adiabatic perturbation switching on and off are *reversible*. The problem is that many processes of physical interest are *irreversible*, so the hypothesis that the ground state at $t = \pm\infty$ only differs in a phase factor is no longer true. A very important irreversible processes that has been investigated during this thesis is the electron transport (current through molecules or STM simulations). In this case, the perturbation generates an electron flow from one electrode to the other that changes irreversibly the system.

Keldysh [4] considered the following argument. If we don't know what the state of the system at $t = +\infty$ will be, let's evolve our system back to $t = -\infty$ again, so:

$$\langle O \rangle(t) = \langle \Psi_{0,H}^0 | \hat{S}(-\infty, t) \hat{O}_I(t) \hat{S}(t, -\infty) | \Psi_{0,H}^0 \rangle \quad (\text{A.49})$$

The denominator is not needed, because we evolve our state back to $t = -\infty$. We can use the property $\hat{S}(-\infty, t) = \hat{S}(-\infty, +\infty)\hat{S}(+\infty, t)$.

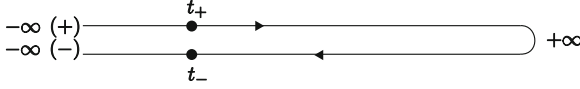


Fig. A.1 Scheme of a system divided in three subsystems in order to calculate the electrical conductance from 1 to 2

$$\begin{aligned} \langle O \rangle(t) &= \langle \Psi_{0,H}^0 | \widehat{S}(-\infty, +\infty) \widehat{S}(+\infty, t) \widehat{O}_I(t) \widehat{S}(t, -\infty) | \Psi_{0,H}^0 \rangle \\ &= \langle \Psi_{0,H}^0 | \widehat{S}(-\infty, +\infty) T[\widehat{O}_I(t) \widehat{S}(+\infty, -\infty)] | \Psi_{0,H}^0 \rangle \end{aligned} \quad (\text{A.50})$$

In order to have a more compact expression the idea of temporal Keldysh contour is introduced (see Fig. A.1). We go from $-\infty$ to $+\infty$ following the “positive” chronological branch (denoted by the subindex +), and then come back to $-\infty$ following the “negative” antichronological branch (denoted by the subindex -), so the contour evolution operator \widehat{S}^c follows $\widehat{S}^c(-\infty_-, -\infty_+) = \widehat{S}(-\infty, +\infty) \widehat{S}(+\infty, -\infty)$, and Eq. (A.50) can be rewritten as:

$$\langle O \rangle(t) = \langle \Psi_{0,H}^0 | T^c[\widehat{O}_I(t) \widehat{S}^c(-\infty_-, -\infty_+)] | \Psi_{0,H}^0 \rangle \quad (\text{A.51})$$

This is the analog to (A.39) for the non-equilibrium case. And, like in (A.39) we can use Wick theorem to rewrite the expression in terms of Green functions. However, now we have to realize that we have four different Green functions, depending on which branch are times t and t' . These are:

$$\begin{aligned} G^{++}(i, t, j, t') &= -i \langle \Psi_0 | T_c[\hat{c}_i(t_+) \hat{c}_j^\dagger(t'_+)] | \Psi_0 \rangle = -i \langle \Psi_0 | T[\hat{c}_i(t) \hat{c}_j^\dagger(t')] | \Psi_0 \rangle \\ G^{--}(i, t, j, t') &= -i \langle \Psi_0 | T_c[\hat{c}_i(t_-) \hat{c}_j^\dagger(t'_-)] | \Psi_0 \rangle = -i \langle \Psi_0 | \bar{T}[\hat{c}_i(t) \hat{c}_j^\dagger(t')] | \Psi_0 \rangle \\ G^{+-}(i, t, j, t') &= -i \langle \Psi_0 | T_c[\hat{c}_i(t_+) \hat{c}_j^\dagger(t'_-)] | \Psi_0 \rangle = -i \langle \Psi_0 | \hat{c}_j^\dagger(t') \hat{c}_i(t) | \Psi_0 \rangle \\ G^{-+}(i, t, j, t') &= -i \langle \Psi_0 | T_c[\hat{c}_i(t_-) \hat{c}_j^\dagger(t'_+)] | \Psi_0 \rangle = -i \langle \Psi_0 | \hat{c}_i(t) \hat{c}_j^\dagger(t') | \Psi_0 \rangle \end{aligned} \quad (\text{A.52})$$

where \bar{T} orders anti-chronologically the operators (in the negative branch). Further details about this formalism and its relationship with conductance calculation can be found in [5, 6].

References

1. R.D. Mattuck, *A Guide to Feynman Diagrams in the Many-Body Problem* (Dover Publications, New York, 1992)
2. A.L. Fetter, J.D. Walecka, *Quantum Theory of Many-Particle Systems* (Dover Publications, New York, 2003)
3. G.D. Mahan, *Many Particle Physics*, 3rd edn. (Springer, New York, 2000)
4. L.V. Keldysh, Diagram technique for nonequilibrium processes. *Sov. Phys.: J. Experim. Theor. Phys.* **20**, 1018 (1965)

5. C. González, Métodos DFT y STM de primeros principios para el estudio de superficies semiconductoras con adsorbatos: pasivación, nanohilos y transiciones de fase. Ph.D. thesis, Universidad Autónoma de Madrid, 2005
6. J.M. Blanco, Estudio teórico del microscopio de efecto túnel con métodos de primeros principios. Ph.D. thesis, Universidad Autónoma de Madrid, 2004

Appendix B

Different Approximations for a Simple Benzene Model: Hybrid Functionals

B.1 Simple Hydrogen and Benzene Toy-Model

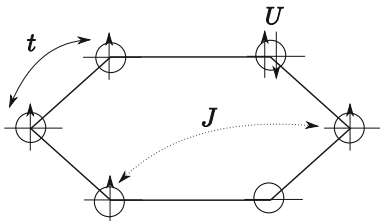
In Sect. 2.7, we presented some methods that allow us to correct the underestimation of the LDA gap. In this section we will apply these approximations to simple Hubbard-like benzene and hydrogen models, where we only consider one electron per site. The simplicity of these models allow us to gain some insight on the physical meaning of the different approximation used in this thesis, and try more sophisticated ones. Moreover, as these hamiltonian are exactly solvable we can compare the validity of the different approximations.

In benzene model we are going to consider only 6 π orbitals (that are the orbitals that contribute to the HOMO and LUMO) and a $S_z^{total} = 0$ configuration. First neighbors interact via a hopping $t = 2.54$ eV. Electrons at the same site experiment a coulomb repulsion characterized by $U = 19.2$ eV (see Sect. 2.5 and A.1.3) that has been calculated using *gcluster* [1] for p_z orbitals; and electrons at different sites experiment a coulomb repulsion J that behaves with distance as $J \propto 1/d$. In our case the proportionality constant is 12.56 eV·Å. Simpler benzene models also have been studied. The mathematical form of the hamiltonian is:

$$\hat{H} = \sum_{i,\sigma} \varepsilon_0 \hat{n}_{i\sigma} - \sum_{i,\sigma} t (\hat{c}_{i+1\sigma}^\dagger \hat{c}_{i\sigma} + \hat{c}_{i\sigma}^\dagger \hat{c}_{i+1\sigma}) + \sum_i U \hat{n}_{i\uparrow} \hat{n}_{i\downarrow} + \frac{1}{2} \sum_{i,j,\sigma,\sigma'} J_{ij} \hat{n}_{i\sigma} \hat{n}_{j\sigma'} \quad (\text{B.1})$$

Using the finite basis set $\{|n_{1,\uparrow}, n_{1,\downarrow}, \dots, n_{6,\uparrow}, n_{6,\downarrow}\}_{n_{i\sigma}=0,1}$ we can write the hamiltonian in a matrix form and diagonalize it. It is not very demanding because of the matrix size is $\binom{6}{3} \times \binom{6}{3} = 400 \times 400$; however, it is interesting to note that this number increases as $n!$ so, for instance, a 8 atom aromatic hydrocarbon matrix size will be $\binom{8}{4} \times \binom{8}{4} = 4900 \times 4900$, or if we want to take into

Fig. B.1 Schematic figure of the idealized benzene that we are considering in our calculations



account all the valence electrons in benzene (including hydrogen s), we will need a $\binom{30}{15} \times \binom{30}{15} = (2.4 \times 10^{16}) \times (2.4 \times 10^{16})$ matrix, that means, that if we want to store it we will need 2 sextillion TB of RAM in single precision (let alone diagonalize it!). That is the reason why we need approximations in any realistic system, and only idealized systems can be analyzed exactly.

The hydrogen toy model is much simpler, because we only have a 4×4 matrix, since we are going to consider only 1 s orbitals for each hydrogen, with a hopping t between orbitals. Intraatomic (U) and interatomic (J) interaction are also included. This model (without the J parameter) was solved analytically in the thesis of Alvaro Martín-Rodero [2]. The hamiltonian is just:

$$\begin{aligned} \hat{H} = \varepsilon_0 \sum_{\sigma} (\hat{n}_{1\sigma} + \hat{n}_{2\sigma}) - t \sum_{\sigma} (\hat{c}_{1\sigma}^{\dagger} \hat{c}_{2\sigma} + \hat{c}_{2\sigma}^{\dagger} \hat{c}_{1\sigma}) \\ + U(\hat{n}_{1\uparrow} \hat{n}_{1\downarrow} + \hat{n}_{2\uparrow} \hat{n}_{2\downarrow}) + J \sum_{\sigma, \sigma'} \hat{n}_{1\sigma} \hat{n}_{2\sigma'} \end{aligned} \quad (\text{B.2})$$

B.2 “DFT” spectra

Let’s begin with the simplest approximation: the DFT-like approach. It is clear that in such a mean-field like model, the ground state will have one electron at each site, so $n_{i\sigma} = 1/2$. In this kind of approach the Hartree, exchange and correlation potential will be (see Sect. 2.5.1).

$$\begin{aligned} (V_H^{LD-OO})_{i\sigma, j\sigma} &= \sum_{\sigma'} U n_{i, \sigma'} + \sum_{\substack{j, \sigma' \\ j \neq i}} J_i n_{i, \sigma'} \\ (V_X^{LD-OO})_{i\sigma, j\sigma} &= -J_i^{eff} \left(\frac{1}{2} - n_{i\sigma'} \right) \delta_{i, j} \\ (V_C^{LD-OO})_{i\sigma, j\sigma} &= -f_{i\sigma} (U - J_i^{eff}) \left(\frac{1}{2} - n_{i\sigma'} \right) \delta_{i, j} \end{aligned} \quad (\text{B.3})$$

Note that, exchange and correlation potentials are just zero (because $n_{i\sigma} = 1/2$), so what we get is that the Hartree and DFT quasiparticle spectra coincide (note that the energies are different: $E^X = -1/2 \sum_{i\sigma} J_i^{eff} n_{i\sigma} (1 - n_{i\sigma}) \neq 0$). The DFT solution is analytical both for the benzene and hydrogen cases.

B.2.1 Hydrogen

In the case of hydrogen the hamiltonian is just a two level system, whose eigenvalues are $\varepsilon = \varepsilon_0 + \frac{U}{2} + J \pm t$, and the gap is $E_g = 2t$.

B.2.2 Benzene

The benzene solution is:

$$\psi_m = \frac{1}{\sqrt{6}} \sum_{j=1}^6 e^{i\varphi_m j} \phi_j \quad \text{where } \varphi_m = m \frac{2\pi}{6} \quad m = 1, \dots, 6 \quad (\text{B.4})$$

$$\begin{aligned} E_m &= \varepsilon_0 + 2t \cos \varphi_m + \frac{U}{2} + 2J_{1,2} + 2J_{1,3} + J_{1,4} \\ &= \begin{cases} \varepsilon_0 \pm 2t + \frac{U}{2} + 2J_{1,2} + 2J_{1,3} + J_{1,4} \\ \varepsilon_0 \pm t + \frac{U}{2} + 2J_{1,2} + 2J_{1,3} + J_{1,4} \end{cases} \end{aligned} \quad (\text{B.5})$$

So the gap in this simple model is just $E_g = 2t = 5.08$ eV. As we have said before, due to the exchange and correlation potentials are zero in this approximation, the DFT solution is the same as the Hartree one.

B.3 Hartree-Fock Versus Exact Results

In this section we will compare the Hartree-Fock solution with the exact one. For the benzene case, several approximations to the hamiltonian presented in B.1 will be introduced in order to gain some insight in the comparison between Hartree-Fock and exact results.

As stated in Sect. 2.7.3 the hamiltonian can be rewritten with a non-diagonal potential of the form (Eq. 2.88):

$$(V_X^{HF-OO})_{i\sigma,j\sigma} = -J_{ij} n_{i\sigma} n_{j\sigma} \quad (\text{B.6})$$

B.3.1 Hydrogen

Exact solution

The hamiltonian eigenvalues of the full 4×4 matrix are (see [8]):

$$\begin{aligned}\varepsilon_4 &= 2\varepsilon_0 + \frac{U+J}{2} + \frac{1}{2}\gamma \\ \varepsilon_3 &= 2\varepsilon_0 + U \\ \varepsilon_2 &= 2\varepsilon_0 + J \\ \varepsilon_1 &= 2\varepsilon_0 + \frac{U+J}{2} - \frac{1}{2}\gamma\end{aligned}\tag{B.7}$$

where $\gamma = \sqrt{(U-J)^2 + 16t^2}$. However, the gap is *not* $E_g = \varepsilon_2 - \varepsilon_1 = \frac{J-U}{2} + \frac{1}{2}\gamma$, because we need to calculate the ground state of the system with ± 1 electrons. When we do so we get:

$$\begin{aligned}\text{For } N-1 & \begin{cases} \varepsilon_2 = \varepsilon_0 + t \\ \varepsilon_1 = \varepsilon_0 - t \end{cases} \\ \text{For } N+1 & \begin{cases} \varepsilon_2 = 3\varepsilon_0 + U + 2J + t \\ \varepsilon_1 = 3\varepsilon_0 + U + 2J - t \end{cases}\end{aligned}\tag{B.8}$$

The actual transport energy gap $E_g = E[N+1] + E[N-1] - 2E[N] = J + \gamma - 2t$. Note that $\gamma > 4t$ so this gap is *always* greater than the DFT gap, no matter the value of J is. The same holds for benzene, as we will see.

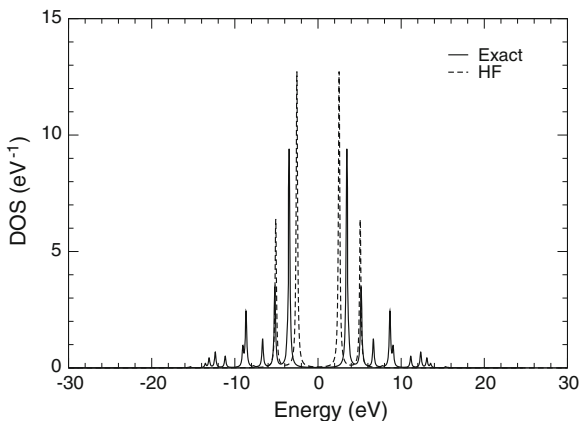
Hartree-Fock approximation

For hydrogen we get that $n_{1,2} = \sum_{n \in occ.} c_1^n c_2^n = 1/2$ and $(V_X^{HF-OO})_{1,2} = -J/2$, and the Hartree-Fock hamiltonian is just the DFT one with an effective hopping $-t \rightarrow -t - J/2$ that gives the following spectra:

$$\begin{aligned}\varepsilon_2 &= \varepsilon_0 + \frac{U}{2} + \frac{3J}{2} + t \\ \varepsilon_1 &= \varepsilon_0 + \frac{U}{2} + \frac{J}{2} - t\end{aligned}\tag{B.9}$$

The gap in this case is $E_g = 2t + J$ that is greater than the DFT gap $E_g^{DFT} = 2t$. However, it is still smaller than the exact gap $E_g^{exact} = \gamma - 2t + J$ (remember that $\gamma = \sqrt{(U-J)^2 + 16t^2} > 4t$), so the gap is underestimated. Note that, when $U = J$ the Hartree-Fock and the exact gap coincide. This is because the correlation depends on $U - J$ (see Eq. 2.58, and the form of self-energy in (B.11)). In benzene we also obtain this result.

Fig. B.2 DOS of the exact hamiltonian of the benzene molecule (with $J = 0$) and of the HF approximation for the same parameter values. The origin of energies has been chosen to be the mid-gap to see the electron-hole symmetry of the problem



B.3.2 Benzene: $J = 0$ Case

For the sake of simplicity first we are going to consider a benzene hamiltonian where $J = 0$ and the effect of J is taken into account in U^{eff} , that has the value $U^{eff} = U - J^{eff} = 10.73$ eV. The Hartree-Fock and the DFT hamiltonian coincide (since $J = 0$) and we get the following Hartree-Fock spectra:

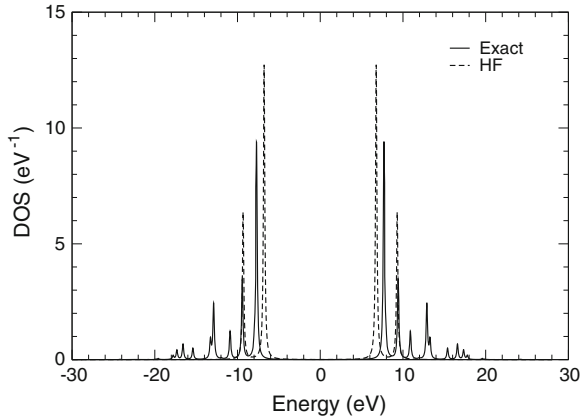
$$\begin{aligned} \varepsilon_0 \pm 2t + \frac{U^{eff}}{2} \\ \varepsilon_0 \pm t + \frac{U^{eff}}{2} \end{aligned} \quad (\text{B.10})$$

The exact gap for this case is 7.12 eV, larger than the DFT (HF) one (5.08 eV). However, the difference between the DFT and the exact gap is smaller, compared with cases where $J \neq 0$. In Fig. B.2 we show the DOS for both the HF and the exact hamiltonian. The DOS for the HF case has been calculated using the one-electron green function formulas (A.21) and (A.24), and the exact DOS has been calculated with the spectral representation of the many-body green function (A.26). It can be seen that the exact spectra contains much more features than the approximate ones due to many-body interactions. This also makes the weight of the HOMO and LUMO peaks smaller.

B.3.3 Benzene: All J Equal, But $J \neq 0$

Although this is not very physical, this system is simpler than the realistic case where $J \propto 1/d$, because $J_{i,j} = J^{eff}$ for all i, j . It allow us to compare its results directly with the more sophisticated approach including second order self-energy where $U^{eff} = U - J$.

Fig. B.3 DOS of the exact hamiltonian of the benzene molecule (with the same coulomb interaction J) and of the HF approximation for the same set of parameters



In the case of the benzene molecule, we obtain the values $n_{1,2} = 1/3$, $n_{1,3} = 0$, and $n_{1,4} = -1/6$ that can be calculated using the eigenfunctions of (B.4). Note that, although the HF hamiltonian is not the same as the DFT one (it has the non-diagonal elements $(V_X^{HF-OO})_{ij} = -Jn_{i,j}$) the eigenfunctions remain the same, due to the symmetry of the hamiltonian. The value for all J is 8.47 eV, obtained through Eq. (2.57). The obtained gap is 13.55 eV, not far from the Hartree-Fock gap calculated using all J different (see next section). On the other hand, the exact gap, calculated with this set of parameters is 15.40, so Hartree-Fock give us an underestimation of 1.85 eV, instead of the usual Hartree-Fock overestimation [3].

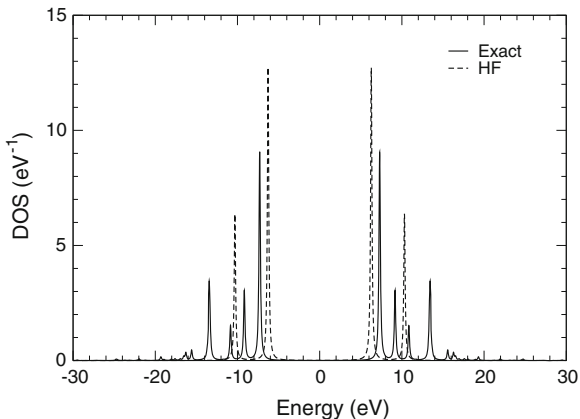
As in hydrogen, we analyze the special case $J = U$, that makes $U^{eff} = U - J = 0$, and the second order selfenergy is zero. In this particular case, as in hydrogen, the Hartree-Fock approximation gives the *exact* solution of the system. Both gives the same DOS, with a gap of 24.28 eV.

B.3.4 Benzene: All J Different

This is the most physical case. The exact gap that we get is 14.59 eV, larger than the previous case. Note that this gap is far from the 10.38 eV experimental gap. This is due to the extremely minimal basis set used. In Fig. B.4 there is a figure of the DOS for the exact case.

In this case the HF gap is 12.55 eV, again smaller than the exact case, but much closer to the exact gap than the DFT functional. In the next section we will go beyond the Hartree-Fock approximation and try to get better results by including self-energy terms.

Fig. B.4 DOS of the exact hamiltonian of the benzene molecule (with all J different) and of the HF approximation for the same set of parameters



B.4 Beyond Hartree-Fock: Including Self Energy Terms

As stated in [2], a relatively simple Feynman diagram expansion of self energy, up to second order gives us the following formula:

$$\begin{aligned} \Sigma_{ij}^{(2)}(\omega) = & (U_{ij}^{eff})^2 \int_{-\infty}^{E_F} dE_2 \int_{E_F}^{\infty} dE_3 \int_{E_F}^{\infty} dE_4 \frac{\rho_{ij,-\sigma}^{(0)}(E_2)\rho_{ij,-\sigma}^{(0)}(E_3)\rho_{ij,+\sigma}^{(0)}(E_4)}{\omega + E_2 - E_3 - E_4 + i\eta} \\ & + (U_{ij}^{eff})^2 \int_{E_F}^{\infty} dE_2 \int_{-\infty}^{E_F} dE_3 \int_{-\infty}^{E_F} dE_4 \frac{\rho_{ij,-\sigma}^{(0)}(E_2)\rho_{ij,-\sigma}^{(0)}(E_3)\rho_{ij,+\sigma}^{(0)}(E_4)}{\omega + E_2 - E_3 - E_4 + i\eta} \end{aligned} \tag{B.11}$$

where $\rho_{ij,-\sigma}^{(0)}$ is the local, non-diagonal density of states for DFT and $U_{ij}^{eff} = U - J_{ij}$. Despite of the complicated structure of the selfenergy, all integrals are analytical (both for benzene and hydrogen) because the non-diagonal density of states consist on a sum of delta functions. By this way we can write an effective hamiltonian (in the matrix form):

$$\mathbb{H}^{eff}(\omega) = \mathbb{H}^{HF} + \Sigma^{(2)}(\omega) \Rightarrow \mathbb{G}^{(2)} = \mathbb{G}(\omega) = [\omega\mathbb{I} - \mathbb{H}^{eff}]^{-1} \tag{B.12}$$

B.4.1 Hydrogen

For the hydrogen, there is an analytical solution at this level. Using (B.11) and $\rho_{11}(\omega) = \rho_{22}(\omega) = 1/2\delta(\omega - \varepsilon_0 - U/2 - J + t) + 1/2\delta(\omega - \varepsilon_0 - U/2 - J - t)$, $\rho_{12}(\omega) = \rho_{21}(\omega) = 1/2\delta(\omega - \varepsilon_0 - U/2 - J + t) - 1/2\delta(\omega - \varepsilon_0 - U/2 - J - t)$ we obtain that:

$$\begin{aligned}\Sigma_{11}(\omega) = \Sigma_{22}(\omega) &= \frac{(U - J)^2}{8} \left[\frac{1}{\omega - \varepsilon_0 - U/2 - J - 3t} + \frac{1}{\omega - \varepsilon_0 - U/2 - J + 3t} \right] \\ &= \frac{(U - J)^2}{4} \frac{\omega - \varepsilon_0 - U/2 - J}{(\omega - \varepsilon_0 - U/2 - J)^2 - 9t^2}\end{aligned}\tag{B.13}$$

and for the non-diagonal self-energy:

$$\begin{aligned}\Sigma_{12}(\omega) = \Sigma_{21}(\omega) &= \frac{(U - J)^2}{8} \left[\frac{1}{\omega - \varepsilon_0 - U/2 - J - 3t} - \frac{1}{\omega - \varepsilon_0 - U/2 - J + 3t} \right] \\ &= \frac{3(U - J)^2}{4} \frac{t}{(\omega - \varepsilon_0 - U/2 - J)^2 - 9t^2}\end{aligned}\tag{B.14}$$

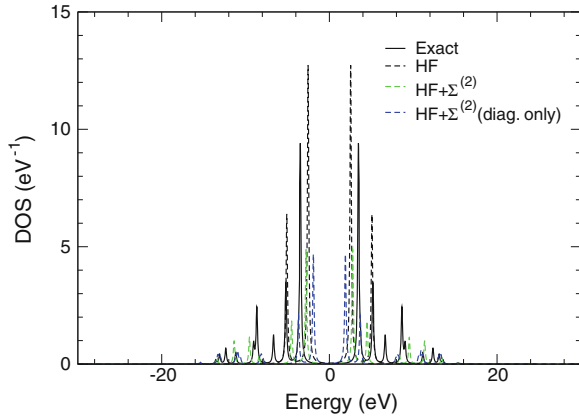
Now we can construct the green function using (B.12) and calculate its poles; they are the peaks at the density of states, and consequently, the quasiparticle spectra. These values are:

$$\omega_i = \varepsilon_0 + \frac{U}{2} + J \pm \left(t - \frac{J}{4} \right) \pm \frac{1}{2} \sqrt{(U - J)^2 + \left(4t + \frac{J}{2} \right)^2}\tag{B.15}$$

The gap at this level is $E_g = J/2 + \sqrt{(U - J)^2 + (4t + J/2)^2} - 2t$ (for $J < 4t$). Note that apart from the cases $J = 0$, or $U - J = 0$ and $J < 4t$ second order Σ is not able to get the exact gap; however it is a better approximation than HF alone (it can be shown that the difference between the exact gap and the approximate gap is always greater in HF than at this level). However for systems with big J ($J > 4t$), the gap is $E_g = 2t - J/2 + \sqrt{(U - J)^2 + (4t + J/2)^2}$, that is *smaller* than the HF gap, so the value of the gap is worst in this case including the second order self-energy than if we do not include it.

So, in strongly correlated systems (with large J), the second order selfenergy is not able to improve the HF gap (actually it worsens it).

Fig. B.5 DOS of the exact hamiltonian of the benzene molecule (with $J = 0$), the HF hamiltonian and the beyond-HF case. *Black line:* Exact results; *red line:* HF results; *green line:* HF with second order self-energy; *blue line:* HF with only diagonal self-energy



B.4.2 Benzene

For the benzene, we are going to analyze the three different approximations made in last section. First the case with $U = U^{eff}$ and $J = 0$, then the case where all $J_{i,j} = J^{eff}$, and then all J different. Regarding the value of U^{eff} in (B.11), we have chosen in all cases $U^{eff} = U - J^{eff}$.

In Fig. B.5 we have plotted the exact, HF and $HF + \Sigma^{(2)}$ DOS for the first case ($J = 0$). We can see that this last approximation reproduces better the features of the small peaks around the gap, and the gap is closer to the exact one (5.57 eV versus 5.08 for the HF approximation and 7.12 of exact gap). Moreover, we have tested the importance of off-diagonal elements of self-energy, by calculating the DOS taking into account diagonal terms only (Σ_{ii}). Although the difference is not that high (both reproduce the features of the DOS far from the gap due to correlation, the gap itself is worse than the HF gap). The fact that the second order selfenergy does not reproduce as well as hydrogen (with $J = 0$) second order selfenergy can be related to the fact that $\Sigma^{(2)}$ does not reproduce well the large U limit.

Figure B.6 shows also the exact, HF, and $HF + \Sigma^{(2)}$ results for all J equal to each other. With the inclusion of $\Sigma^{(2)}$ we obtain a gap of 7.69 eV, that compares worse with the exact gap (15.40 eV) than HF (13.55). Although it is able to reproduce qualitatively the small features in the DOS due to the correlation. Due to $J = 3.3t$ we are dealing with a strong correlated system (for hydrogen, the second order selfenergy failed to improve the gap for systems with $J \geq 4t$). In order to improve these poor results we have considered HF density in formula (B.11) ($\rho_{i,j,\sigma}^{(HF)}(E_i)$ instead of $\rho_{i,j,\sigma}^{(0)}(E_i)$). This implies that Dirac deltas are placed at the HF eigenvalues. This slightly improves the pure HF case (the gap is 13.66 eV, compared with pure HF 13.55 eV). We can consider this sigma as a *dressed* sigma with the HF results.

Fig. B.6 DOS of the exact hamiltonian of the benzene molecule (with the same J), the HF hamiltonian and the $\text{HF}+\Sigma^{(2)}$ case. *Black line*: Exact results; *red line*: HF results; *green line*: HF with second order self-energy; *blue line*: HF with *dressed* selfenergy (see text)

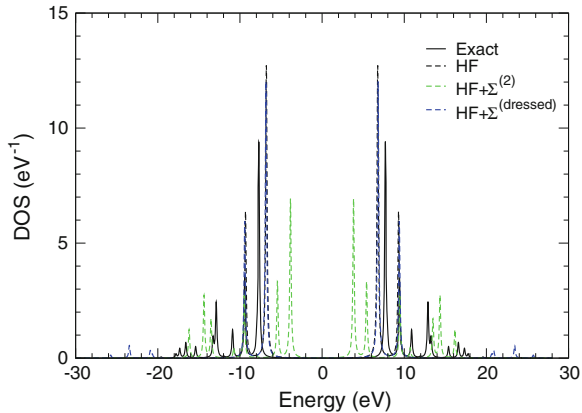
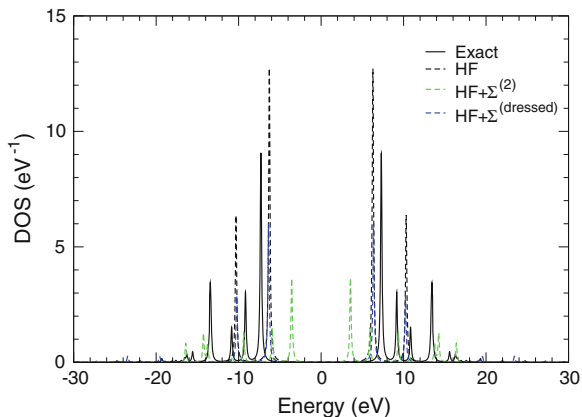


Fig. B.7 DOS of the exact hamiltonian of the benzene molecule ($J \propto 1/d$), the HF hamiltonian and the $\text{HF}+\Sigma^{(2)}$ case. *Black line*: Exact results; *red line*: HF results; *green line*: HF with second order self-energy; *blue line*: HF with *dressed* selfenergy (see text)



Finally, we have calculated the same as the previous case for all J different, that is shown in Fig. B.7. We see again that $\text{HF}+\Sigma^{(2)}$ worsens the gap (7.12 eV compared with exact 14.59 and HF 12.55), and again, if we calculate a *dressed* selfenergy, the gap is slightly improved (12.73 eV) compared with the HF case.

So, the inclusion of the second order selfenergy is a better approximation for the HF gap for systems without strong correlation, but fails to reproduce systems with strong correlation. In that case we can calculate a *dressed* selfenergy using the HF non-diagonal density of states, instead of the DFT one.

B.5 Koopmans' Correction

Finally, we are going to calculate the energy spectra using the Koopmans' correction exposed in Sect. 2.7.4 and comparing it to the exact values for the benzene and hydrogen cases.

B.5.1 Hydrogen

Using formula 2.96 and taking into account that for hydrogen $J^{eff} = J$ and $\delta n_i = \delta n'_i = 1/2$ we get that the Koopmans' gap is:

$$E_g^{Koop.} = 2t + J + \frac{1}{2}f(U - J) \quad (\text{B.16})$$

where f is the fraction of the exchange hole that is taken back to the atomic level due to correlation. We can obtain the value of f by just comparing the Koopmans' gap with the exact one. Then we get:

$$f = 2\sqrt{1 + \left(\frac{4t}{U - J}\right)^2} - \frac{8t}{U - J} \quad (\text{B.17})$$

Note that $f \rightarrow 0$ when $U - J \rightarrow 0$ (as should be expected) but $f \rightarrow 2$ when $U - J \rightarrow \infty$ that makes no sense ($0 < f < 1$). That show us that the Koopmans' correction has only physical meaning in systems where correlation is not very high.

B.5.2 Benzene

For benzene, the simplest case ($J = 0$) enlarges the gap in $\frac{1}{4}fU$. The value of f that makes the Koopmans' and the exact gap coincide is $f = 0.76$, that show us that correlation effects are not negligible in benzene.

If $J \neq 0$ but all $J = J^{eff}$ then the gap ranges from 13.55 to 16.22 (depending on the value of f chosen), the Koopmans' shift and the exact gap coincide when $f = 0.69$. If $U = J$, the gap coincides with the HF one so $f = 0$ (again, there is no correlation when $U = J$).

If all J are different, the gap ranges from 11.85 to 14.53, so $f \simeq 1$. Note that in all cases, correlation is important (f is not far from unity), and that the Koopmans' shift allow us to improve our results (compared with the second-order selfenergy) as long as a suitable choice of f is obtained, or, if we cannot estimate the value, a relatively narrow window (as long as we are not dealing with high correlated systems, where this approximation fails. For example, in benzene, very good results are obtained if we consider $f \sim 0.75$ in all cases.

References

1. P. Pou, Energía de canje y correlación como función de los números de ocupación orbitales: cálculos de energías totales y cuasipartículas. Ph.D. thesis, Universidad Autónoma de Madrid, 2001
2. A. Martín-Rodero, Correlación en sistemas descritos por hamiltonianos LCAO: quimisorción en metales de transición y hamiltoniano de Hubbard. Ph.D. thesis, Universidad Autónoma de Madrid, 1983
3. K. Kaasbjerg, K.S. Thygesen, Benchmarking GW against exact diagonalization for semiempirical models. *Phys. Rev. B* **81**(8), 085102 (2010)

Appendix C

Spin Dependent Extension of McWEDA and Hybrid Functionals

C.1 Generalization of McWEDA for LSDA Functionals

C.1.1 Introduction

Density functional theory consider implicitly that there is no spin polarization and $\rho^\uparrow(\mathbf{r}) = \rho^\downarrow(\mathbf{r}) = 1/2\rho(\mathbf{r})$. However, there is an extension of density functional theory that allows to handle spin polarized density (see [1–4] and references therein). There are also functionals that takes into account this polarization [1, 5]. The analogue for the widely used LDA is the local spin density approximation (LSDA), that is the one that we will consider for McWEDA extension to spin polarized density.

We are going to work in the $(\rho^\uparrow, \rho^\downarrow)$ scheme. However, in literature is also common the (ρ, ρ_s) one. The relationship between both is:

$$\begin{cases} \rho = \rho^\uparrow + \rho^\downarrow \\ \rho_s = \rho^\uparrow - \rho^\downarrow \end{cases} \quad (\text{C.1})$$

$$\begin{cases} \rho^\uparrow = \frac{1}{2}(\rho + \rho_s) \\ \rho^\downarrow = \frac{1}{2}(\rho - \rho_s) \end{cases} \quad (\text{C.2})$$

We need to calculate the following matrix elements:

$$\begin{cases} \langle \alpha, \uparrow | e_{xc}(\rho^\uparrow, \rho^\downarrow) | \alpha, \uparrow \rangle, \langle \alpha, \downarrow | e_{xc}(\rho^\uparrow, \rho^\downarrow) | \alpha, \downarrow \rangle, \langle \alpha, \uparrow | V_{xc}^\uparrow(\rho^\uparrow, \rho^\downarrow) | \beta, \uparrow \rangle, \\ \langle \alpha, \downarrow | V_{xc}^\uparrow(\rho^\uparrow, \rho^\downarrow) | \beta, \downarrow \rangle, \langle \alpha, \uparrow | V_{xc}^\downarrow(\rho^\uparrow, \rho^\downarrow) | \beta, \uparrow \rangle, \langle \alpha, \downarrow | V_{xc}^\downarrow(\rho^\uparrow, \rho^\downarrow) | \beta, \downarrow \rangle \end{cases} \quad (\text{C.3})$$

From now on, we will simplify the notation using $\sigma = \uparrow, \downarrow$.

C.1.2 Energy Matrix Elements

We will begin with the energy matrix elements $\langle \alpha, \sigma | \varepsilon_{xc}(\rho^\uparrow, \rho^\downarrow) | \alpha, \sigma \rangle$ using the same ideas as the McWEDA approximation:

$$\begin{aligned} \langle \alpha, \sigma | \varepsilon_{xc}(\rho^\uparrow, \rho^\downarrow) | \alpha, \sigma \rangle &= \langle \alpha, \sigma | \varepsilon_{xc}(\rho^\uparrow, \rho^\downarrow) | \alpha, \sigma \rangle_{GSN} \\ &\quad + (\langle \alpha, \sigma | \varepsilon_{xc}(\rho_I^\uparrow, \rho_I^\downarrow) | \alpha, \sigma \rangle - \langle \alpha, \sigma | \varepsilon_{xc}(\rho_I^\uparrow, \rho_I^\downarrow) | \alpha, \sigma \rangle_{GSN}) \end{aligned} \quad (C.4)$$

where the GSN matrix element:

$$\begin{aligned} \langle \alpha, \sigma | \varepsilon_{xc}(\rho^\uparrow, \rho^\downarrow) | \alpha, \sigma \rangle_{GSN} &= \varepsilon_{xc}(\overline{\rho_{\alpha,\uparrow}}, \overline{\rho_{\alpha,\downarrow}}) \\ &\quad + \frac{\partial \varepsilon_{xc}(\overline{\rho_{\alpha,\uparrow}}, \overline{\rho_{\alpha,\downarrow}})}{\partial \rho^\uparrow} (\langle \alpha, \sigma | \rho^\uparrow | \alpha, \sigma \rangle - \overline{\rho_{\alpha,\uparrow}}) \\ &\quad + \frac{\partial \varepsilon_{xc}(\overline{\rho_{\alpha,\uparrow}}, \overline{\rho_{\alpha,\downarrow}})}{\partial \rho^\downarrow} (\langle \alpha, \sigma | \rho^\downarrow | \alpha, \sigma \rangle - \overline{\rho_{\alpha,\downarrow}}) \end{aligned} \quad (C.5)$$

and the term $\langle \alpha, \sigma | \varepsilon_{xc}(\rho_I^\uparrow, \rho_I^\downarrow) | \alpha, \sigma \rangle$ is calculated as:

$$\begin{aligned} \langle \alpha, \sigma | \varepsilon_{xc}(\rho_I^\uparrow, \rho_I^\downarrow) | \alpha, \sigma \rangle &= \langle \alpha, \sigma | \varepsilon_{xc}(\rho_I^{\uparrow 0}, \rho_I^{\downarrow 0}) | \alpha, \sigma \rangle \\ &\quad + \langle \alpha, \sigma | \frac{\partial \varepsilon_{xc}(\rho_I^{\uparrow 0}, \rho_I^{\downarrow 0})}{\partial \rho^\uparrow} (\rho_I^\uparrow - \rho_I^{\uparrow 0}) | \alpha, \sigma \rangle \\ &\quad + \langle \alpha, \sigma | \frac{\partial \varepsilon_{xc}(\rho_I^{\uparrow 0}, \rho_I^{\downarrow 0})}{\partial \rho^\downarrow} (\rho_I^\downarrow - \rho_I^{\downarrow 0}) | \alpha, \sigma \rangle \end{aligned} \quad (C.6)$$

Since in literature, it is common to calculate the exchange-correlation energy as a function of ρ, ρ_s , we need to calculate the derivatives $\partial \varepsilon_{xc} / \partial \rho^\sigma$ instead of $\partial \varepsilon_{xc} / \partial \rho_{(s)}$. We can overcome this problem easily using the chain rule:

$$\begin{cases} \frac{\partial \varepsilon_{xc}}{\partial \rho^\uparrow} = \frac{\partial \varepsilon_{xc}}{\partial \rho} \frac{\partial \rho}{\partial \rho^\uparrow} + \frac{\partial \varepsilon_{xc}}{\partial \rho_s} \frac{\partial \rho_s}{\partial \rho^\uparrow} = \frac{\partial \varepsilon_{xc}}{\partial \rho} + \frac{\partial \varepsilon_{xc}}{\partial \rho_s} \\ \frac{\partial \varepsilon_{xc}}{\partial \rho^\downarrow} = \frac{\partial \varepsilon_{xc}}{\partial \rho} - \frac{\partial \varepsilon_{xc}}{\partial \rho_s} \end{cases} \quad (C.7)$$

And if we take $\rho_I^{\uparrow 0} = \rho_I^{\downarrow 0} = \rho_I / 2$ (i.e. neutral charges has no spin polarization), then $\partial \varepsilon_{xc}(\rho_I^0, \rho_{I,s}^0 = 0) / \partial \rho_s = 0$ (since ε_{xc} is an even function of ρ_s). Note that, in that case there is not spin dependence in the formula (since $\partial \varepsilon_{xc} / \partial \rho^\uparrow = \partial \varepsilon_{xc} / \partial \rho^\downarrow$). So if we want to have spin dependence we have to choose different $\rho_I^{\sigma 0}$ for $\sigma = \uparrow, \downarrow$ (i.e. consider a small initial polarization).

C.1.3 Potential Matrix Elements

Now we take care of the potentials:

$$V_{xc}^\uparrow(\rho^\uparrow, \rho^\downarrow) = \frac{\partial(\rho(\mathbf{r})\varepsilon_{xc}(\rho^\uparrow, \rho^\downarrow))}{\partial\rho^\uparrow}, V_{xc}^\downarrow(\rho^\uparrow, \rho^\downarrow) = \frac{\partial(\rho(\mathbf{r})\varepsilon_{xc}(\rho^\uparrow, \rho^\downarrow))}{\partial\rho^\downarrow} \quad (\text{C.8})$$

That are easily related with the chain rule to $V_{xc}(\rho, \rho_s), V_{xc}^s(\rho, \rho_s)$:

$$\begin{cases} V_{xc}^\uparrow(\rho^\uparrow, \rho^\downarrow) = V_{xc}(\rho, \rho_s) + V_{xc}^s(\rho, \rho_s) \\ V_{xc}^\downarrow(\rho^\uparrow, \rho^\downarrow) = V_{xc}(\rho, \rho_s) - V_{xc}^s(\rho, \rho_s) \end{cases} \quad (\text{C.9})$$

Now we calculate the general V_{xc}^σ term

$$\begin{aligned} \langle \alpha, \sigma | V_{xc}^\sigma(\rho^\uparrow, \rho^\downarrow) | \beta, \sigma \rangle &= \langle \alpha, \sigma | V_{xc}^\sigma(\rho^\uparrow, \rho^\downarrow) | \beta, \sigma \rangle_{GSN} \\ &\quad + (\langle \alpha, \sigma | V_{xc}^\sigma(\rho_I^\uparrow, \rho_I^\downarrow) | \beta, \sigma \rangle - \langle \alpha, \sigma | V_{xc}^\sigma(\rho_I^\uparrow, \rho_I^\downarrow) | \beta, \sigma \rangle_{GSN}) \end{aligned} \quad (\text{C.10})$$

The GSN approximation for the potential is:

$$\begin{aligned} \langle \alpha, \sigma | V_{xc}^\sigma(\rho^\uparrow, \rho^\downarrow) | \beta, \sigma \rangle_{GSN} &= V_{xc}^\sigma(\overline{\rho_{\alpha,\beta,\uparrow}}, \overline{\rho_{\alpha,\beta,\downarrow}}) S_{\alpha,\beta} \\ &\quad + \frac{\partial V_{xc}^\sigma(\overline{\rho_{\alpha,\beta,\uparrow}}, \overline{\rho_{\alpha,\beta,\downarrow}})}{\partial\rho^\uparrow} (\langle \alpha, \sigma | \rho^\uparrow | \beta, \sigma \rangle - \overline{\rho_{\alpha,\beta,\uparrow}} S_{\alpha,\beta}) \\ &\quad + \frac{\partial V_{xc}^\sigma(\overline{\rho_{\alpha,\beta,\uparrow}}, \overline{\rho_{\alpha,\beta,\downarrow}})}{\partial\rho^\downarrow} (\langle \alpha, \sigma | \rho^\downarrow | \beta, \sigma \rangle - \overline{\rho_{\alpha,\beta,\downarrow}} S_{\alpha,\beta}) \end{aligned} \quad (\text{C.11})$$

As in standard McWEDA, the correction to the GSN term varies if α, β are orbitals of the same atom or not.

The on-site term (α, β are in the same atom):

$$\begin{aligned} \langle \alpha, \sigma | V_{xc}^\sigma(\rho^\uparrow, \rho^\downarrow) | \beta, \sigma \rangle &= \langle \alpha, \sigma | V_{xc}^\sigma(\rho_I^\uparrow, \rho_I^\downarrow) | \beta, \sigma \rangle \\ &\quad + \langle \alpha, \sigma | \frac{\partial V_{xc}^\sigma(\rho_I^{\uparrow 0}, \rho_I^{\downarrow 0})}{\partial\rho^\uparrow} (\rho_I^\uparrow - \rho_I^{\uparrow 0}) | \beta, \sigma \rangle \\ &\quad + \langle \alpha, \sigma | \frac{\partial V_{xc}^\sigma(\rho_I^{\uparrow 0}, \rho_I^{\downarrow 0})}{\partial\rho^\downarrow} (\rho_I^\downarrow - \rho_I^{\downarrow 0}) | \beta, \sigma \rangle \end{aligned} \quad (\text{C.12})$$

The off-site term (α, β are in different atoms):

$$\begin{aligned}
\langle \alpha, \sigma | V_{xc}^\sigma (\rho_I^\uparrow + \rho_J^\uparrow, \rho_I^\downarrow + \rho_J^\downarrow) | \beta, \sigma \rangle &= \langle \alpha, \sigma | V_{xc}^\sigma (\rho_I^{\uparrow 0} + \rho_J^{\uparrow 0}, \rho_I^{\downarrow 0} + \rho_J^{\downarrow 0}) | \beta, \sigma \rangle \\
&+ \langle \alpha, \sigma | \frac{\partial V_{xc}^\sigma (\rho_I^{\uparrow 0} + \rho_J^{\uparrow 0}, \rho_I^{\downarrow 0} + \rho_J^{\downarrow 0})}{\partial \rho^\uparrow} \\
&(\rho_I^\uparrow - \rho_I^{\uparrow 0} + \rho_J^\uparrow - \rho_J^{\uparrow 0}) | \beta, \sigma \rangle \\
&+ \langle \alpha, \sigma | \frac{\partial V_{xc}^\sigma (\rho_I^{\uparrow 0} + \rho_J^{\uparrow 0}, \rho_I^{\downarrow 0} + \rho_J^{\downarrow 0})}{\partial \rho^\downarrow} \\
&(\rho_I^\downarrow - \rho_I^{\downarrow 0} + \rho_J^\downarrow - \rho_J^{\downarrow 0}) | \beta, \sigma \rangle
\end{aligned} \tag{C.13}$$

C.2 Notes on HF-Like Spin-Dependent Case

C.2.1 The Molecular Case

In the LCAO-OO Hartree-Fock approximation n_{ij} is given by:

$$n_{ij} = 2 \sum_{\mu=1}^{occ.} C_i^{*\mu} C_j^\mu = 2 \sum_{\mu=1}^N F(\mu) C_i^{*\mu} C_j^\mu \tag{C.14}$$

where the factor 2 is due to the spin degeneracy, N is the number of eigenvalues, C_j^μ is the coefficient j of the eigenstate μ ($|\mu\rangle = \sum_{j=1}^N C_j^\mu |\phi_j\rangle$) and $F(i)$ is the occupation function. In an even electron molecule

$$F(\mu) = \begin{cases} 1 & \text{if } \mu \leq \text{HOMO} \\ 0 & \text{if } \mu \geq \text{LUMO} \end{cases} \tag{C.15}$$

Now, what happens when we have a molecule with an odd number of electrons? There will be a level half occupied, the Single Occupied Molecular Orbital (SOMO). So now we need now n_{ij}^\uparrow and n_{ij}^\downarrow that can be defined this way:

$$\begin{aligned}
n_{ij}^\uparrow &= \sum_{\mu=1}^{occ.\uparrow} C_i^{*\mu} C_j^\mu = \sum_{\mu=1}^N F^\uparrow(\mu) C_i^{*\mu} C_j^\mu \\
n_{ij}^\downarrow &= \sum_{\mu=1}^{occ.\downarrow} C_i^{*\mu} C_j^\mu = \sum_{\mu=1}^N F^\downarrow(\mu) C_i^{*\mu} C_j^\mu
\end{aligned} \tag{C.16}$$

In this case, let's suppose that $F^\uparrow(\mu) = F^\downarrow(\mu)$ if $\mu \neq \text{SOMO}$ and $F^\uparrow(\text{SOMO}) = 1$; $F^\downarrow(\text{SOMO}) = 0$. The equation can be rewritten in this way:

$$\begin{aligned}
n_{ij}^{\uparrow} &= \frac{1}{2} \sum_{\mu=1}^N F'(\mu) C_i^{*\mu} C_j^{\mu} + \frac{1}{2} C_i^{*SOMO} C_j^{SOMO} \\
n_{ij}^{\downarrow} &= \frac{1}{2} \sum_{\mu=1}^N F'(\mu) C_i^{*\mu} C_j^{\mu} - \frac{1}{2} C_i^{*SOMO} C_j^{SOMO}
\end{aligned} \tag{C.17}$$

In this case $F'(i)$ is defined as:

$$F'(\mu) = \begin{cases} 2 & \text{if } \mu \leq \text{HOMO} \\ 1 & \text{if } \mu = \text{SOMO} \\ 0 & \text{if } \mu \geq \text{LUMO} \end{cases} \tag{C.18}$$

Is very easy to see that the summation in (C.17) is the non-spin dependent definition of n_{ij} . If we do the following definition:

$$\delta n_{ij}^{\sigma} = \frac{1}{2} C_i^{*SOMO} C_j^{SOMO} \tag{C.19}$$

This way Eq. (C.16) can be easily written as:

$$\begin{aligned}
n_{ij}^{\uparrow} &= \frac{1}{2} n_{ij} + \delta n_{ij}^{\sigma} \\
n_{ij}^{\downarrow} &= \frac{1}{2} n_{ij} - \delta n_{ij}^{\sigma}
\end{aligned} \tag{C.20}$$

C.2.2 Failures of this Model

This model offers an easy way to introduce spin-dependent properties in our system. However, it has several important drawbacks that limit its reliability. First of all, it is not true that the coefficients C_j^{μ} are not spin independent (electrons with spin up and down suffer different potentials on the LSDA approximation). Second, the occupations n_i (that are used by standard FIREBALL) are not changed at this moment, so the sum rule only works in $n_{ij} = n_{ij}^{\uparrow} + n_{ij}^{\downarrow}$. Moreover $n_{ii}^{\uparrow} \neq n_{ii}^{\downarrow} \neq n_i$.

C.2.3 Molecule Over a Surface

In the case of a molecule over a surface, we don't have pure molecular states, so this approach is not suitable *a priori*. We can, however, consider in a first approximation that δn_{ij}^{σ} does not change when the molecule is deposited over the surface, and introduce the δn_{ij}^{σ} calculated for the isolated molecule and obtain $n_{ij}^{\uparrow, \downarrow}$ using (C.20). This method has the advantage that we will obtain a good value for $n_{ij} = n_{ij}^{\uparrow} + n_{ij}^{\downarrow}$ since the contribution of δn_{ij}^{σ} in n_{ij}^{\uparrow} and n_{ij}^{\downarrow} cancel each other.

References

1. U. von Barth, L. Hedin, A local exchange-correlation potential for the spin polarized case. I. *J. Phys. C: Solid State Phys.* **5**(13), 1629 (1972)
2. A. Rajagopal, J. Callaway, Inhomogeneous electron gas. *Phys. Rev. B* **7**(5), 1912 (1973)
3. G. Vignale, M. Rasolt, Current- and spin-density-functional theory for inhomogeneous electronic systems in strong magnetic fields. *Phys. Rev. B* **37**(18), 10685 (1988)
4. R.O. Jones, The density functional formalism, its applications and prospects. *Rev. Mod. Phys.* **61**(3), 689 (1989)
5. S. Vosko, L. Wilk, M. Nusair, Accurate spin-dependent electron liquid correlation energies for local spin density calculations: a critical analysis. *Can. J. Phys.* **58**(8), 1200 (1980)

Curriculum Vitae

Personal data

- Name and surnames: Enrique Abad González
- Birth date: 08/14/1983
- Birth place: Vitoria-Gasteiz, Araba (Spain)
- Nationality: Spanish

Education

- Ph.D., Condensed Matter Physics, Universidad Autónoma de Madrid, November 2011. Advisors: Prof. Fernando Flores, A. Prof. José Ortega. Highest degree obtained
- M. S. (DEA), Condensed Matter Physics. Universidad Autónoma de Madrid, September 2008
- B. S. (Licenciado) Physics degree, Basque Country University (UPV-EHU), Science and Technology Faculty, July 2006. Average qualification: 2.89/4
- High School degree at Colegio Sagrado Corazón-Corazonistas, specialized in Natural and Health Sciences, May 2001. Average qualification 8.3/10

Education (other)

- Hands-on tutorial on electronic structure computations. Trieste (Italy), January 2011
- 5th Summer School in Quantum Phenomena in Low-Dimensional Materials and Nanostructures. Windsor (United Kingdom), August 2010
- 45 h course in Linux for users and for administrators (2006–2007).

Seminars and conferences

- Seminar at the Department of Theoretical Condensed Matter Physics (Universidad Autónoma de Madrid) on April 2008 entitled *Adsorption of organic molecules on metals: C₆₀ on Au(111) surface. The gap problem.*

- Seminar at the Department of Physics (West Virginia University) November 2008, entitled *Dipoles and band alignment for C₆₀/Au(111) or benzene/Au(111) interfaces. The gap problem.*
- Seminar at the Institute of Theoretical Chemistry (University of Stuttgart) August 2011, entitled *Energy level alignment through metal/organic contacts: from interfaces to molecular electronics.*

Sixteen contributions to international conferences (6 talks and 10 posters).

- 2011: XV International Workshop On Computational Physics and Materials Science: Total Energy and Force Methods (Trieste, Italy), International Meeting on Atomic and Molecular Physics and Chemistry 2011 (Rennes, France), 13th International Conference on the Formation of Semiconductor Interfaces (Prague, Czech Republic), CPMD2011: Extending the limits of Ab initio Molecular Dynamics Simulations for Chemistry, Materials Science and Biophysics (Barcelona, Spain)
- 2010: Functional Multiscale Architectures (Bologna, Italy), International Meeting on Atomic and Molecular Physics and Chemistry (Madrid, Spain), MOLMAT 2010 (Montpellier, France), Ψ_k conference 2010 (Berlin, Germany), Passion for Knowledge (San Sebastián, Spain)
- 2009: 12th International Conference on the Formation of Semiconductor Interfaces (Weimar, Germany), Trends in NanoTechnology 2009 (Barcelona, Spain), 10th International Conference on Atomically Controlled Surfaces, Interfaces and Nanostructures (Granada, Spain), Molecular photoreactivity on metal-oxide surfaces from first-principles: photocatalysis and photovoltaics (Madrid, Spain)
- 2008: 7th Iberian Vacuum Meeting (Caparica, Portugal), Materials Science and Engineering 2008 (Nürnberg, Germany)

Participation in research projects

- *First principles simulation of complex materials: molecular materials, organic molecular interfaces and metallic atom nanostructures in semiconductor surfaces* (MAT2004-01271) whose principal investigator was José Ortega Mateo.
- *First principles simulation of nanomaterials* (MAT2007-60966), whose principal investigator was José Ortega Mateo.
- *Mechanical, electrical and catalytic properties of Nanoobjects: synthesis, characterization and modelization* (0505/ MAT/0303) whose principal investigator was Fernando Flores Sintas.
- *Modeling of electronic processes at interfaces in organic-based electronic devices (MINOTOR)* (FP7-NMP-228424) within seventh framework program of European Union, whose coordinators are Roberto Lazzaroni, Jérôme Cornil and David Beljonne.
- *Nanoobjects: From atoms to virus* (S2009/MAT-1467) whose principal investigator is Julio Gómez Herrero.

- *Simulation from first principles of complex materials: organic materials interfaces, photosynthesis and nanocalalysis.* (FIS2010-16046) whose principal investigator is José Ortega Mateo.

Grants and Awards

- Researcher formation grant (from the Basque Country Local Government) 10/01/2006–01/31/2007
- Grant for research personal hiring (from the Madrid Local Government) 02/01/2007–02/01/2011
- Springer thesis prize

Research stays abroad

- West Virginia University (Morgantown, WV, United States) Two months (10/2008–12/2008) in the group of Dr. James P. Lewis.
- Academy of Sciences of Czech Republic (Prague, Czech Republic) One month (05/2008) in the group of Dr. Pavel Jelínek. Three more short stays of less than two weeks on 11/2007, 04/2010, 07/2011.

Teaching Experience

- Teaching assistant from 10/15/2011–1/29/2012. 36 h physics laboratory with first-year chemistry and physics students.
- One week physics laboratory with first-year chemical engineering students (2007, 2008, 2009, 2010)

Computer Skills

- Linux: Advanced user. Familiarized with administrator tasks in OpenSuSe, Ubuntu.
- Windows: Advanced user. Familiarized with administrator tasks in Windows XP, Windows 7.
- Programming: Long experience in Fortran programming (both small and large programs). Contribution of several subroutines in FIREBALL (www.fireball-dft.org) Experience with shell scripting. Basic knowledge of C.
- Productivity applications: LaTeX, Microsoft Office (Word, Excel, Powerpoint), xmgrace, gnuplot, jmol, inkscape, gimp, etc.

Publications

1. F. Flores, E. Abad, J. I. Martínez, B. Pieczyrak, J. Ortega. *On the organic energy gap problem.* Journal of Physics: Condensed Matter (in press).
2. J. I. Martínez, E. Abad, C. González, F. Flores, J. Ortega. *Improved STM Imaging by H-sensitized tips.* Physical Review Letters 108, 246102.
3. E. Abad, J. Ortega, F. Flores (2012). *Metal/organic barrier formation for a C₆₀/Au interface: from the molecular to the monolayer limit.* Physica Status Solidi A 209, 636–646 (Editor's choice).

4. J. I. Martínez, E. Abad, C. González, F. Flores, J. Ortega (2012). *Theoretical characterization of the TTF/Au(111) Interface: STM Imaging, band alignment and charging energy*. Organic Electronics 13, 399.
5. D. Göebel, R. C. Monreal, D. Valdés, E. Abad, D. Primetzhofer and P. Bauer (2011). *Band structure effects in Auger neutralization of He ions at noble metal surfaces*. Physical Review B 84, 165428.
6. J. I. Martínez, E. Abad, F. Flores, J. Ortega, G. Brocks (2011). *Barrier height formation for the PTCDA/Au(111) interface*. Chemical Physics 390, 14.
7. B. Pieczyrak, E. Abad, F. Flores, J. Ortega (2011). *Charging energy and barrier height of pentacene on Au(111): A local-orbital hybrid-functional density functional theory approach*. Journal of Chemical Physics 135, 084702.
8. J. P. Lewis, P. Jelínek, J. Ortega, A. A. Demkov, D. G. Trabada, B. Haycock, H. Wang, G. Adams, J. K. Tomfohr, E. Abad, H. Wang and D. A. Drabold (2011). *Advances and applications in the FIREBALL ab initio tight-binding molecular-dynamics formalism*. Physica Status Solidi B 248, 1989.
9. J. I. Martínez, E. Abad, F. Flores, J. Ortega (2011). *Simulating the organic-molecule/metal interface: TCNQ/Au(111)* Physica Status Solidi B 248, 2044.
10. E. Abad, Y. J. Dappe, J. I. Martínez, F. Flores, J. Ortega (2011). *C₆H₆/Au(111): interface dipoles, band alignment, charging energy and Van der Waals interaction*. Journal of Chemical Physics 134, 044701.
11. E. Abad, J. I. Martínez, J. Ortega, F. Flores (2010). *Barrier formation and charging energy for a variable nanogap organic molecular junction: a tip/C₆₀/Au(111) configuration*. Journal of Physics: Condensed Matter 22, 304007.
12. E. Abad, C. González, J. Ortega, F. Flores (2010). *Charging energy, self-interaction correction and transport energy gap for a nanogap organic molecular junction*. Organic Electronics 11, 332–337.
13. E. Abad, J. Ortega, F. Flores (2009). *Density Functional Theory calculations and the Induced Density of Interface States model for noble metals/C₆₀ interfaces*. Journal of Vacuum Science and Technology B 27(4), 2008–2011.
14. E. Abad, J. Ortega, Y. J. Dappe and F. Flores (2009). *Dipoles and band alignment for benzene/Au(111) and C₆₀/Au(111) interfaces*. Applied Physics A, 95(1), 119–124.